

Computationally-efficient multiscale models for progressive failure and damage analysis of composites

Original

Computationally-efficient multiscale models for progressive failure and damage analysis of composites / Kaleel, Ibrahim; Carrera, Erasmo; Petrolo, Marco; Waas, Anthony M. - (2019).

Availability:

This version is available at: 11583/2728662 since: 2019-03-18T14:42:16Z

Publisher:

Published

DOI:

Terms of use:

openAccess

This article is made available under terms and conditions as specified in the corresponding bibliographic description in the repository

Publisher copyright
thesis

Da definire

(Article begins on next page)



ScuDo
Scuola di Dottorato ~ Doctoral School
WHAT YOU ARE, TAKES YOU FAR



Doctoral Dissertation
Doctoral Program in Mechanical Engineering (31st cycle)

Computationally-efficient multiscale models for progressive failure and damage analysis of composites

By
Ibrahim Kaleel

Supervisors:

Prof. Erasmo Carrera, Politecnico di Torino, Italy

Prof. Anothony M. Waas, University of Michigan, USA

Dr. Marco Petrolo, Politecnico di Torino, Italy

Doctoral committee:

Prof. Sergio De Rosa, University of Naples "Federico II", Italy

Prof. Wenbin Yu, Purdue University, USA

Prof. Paul Weaver, Univeristy of Bristol, UK

Dr. Gaetano Giunta, Luxemborg Institute of Science and Technology, Luxemborg

Dr. Pietro Nali, Thales Alenia Space, Italy

© Ibrahim Kaleel 2019

All rights reserved

To my uppa (father) Abdul Majeed ...

Declaration

I hereby declare that, the contents and organisation of this dissertation constitute my own original work and does not compromise in any way the rights of third parties, including those relating to the security of personal data.

Ibrahim Kaleel

March 2018

Acknowledgements

I extend my deepest gratitude to my advisors, Prof. Erasmo Carrera and Dr. Marco Petrolo, who have guided me through the last three years of my research. Prof. Carrera's invaluable insights into mechanics and his constant persistence on aiming for higher goals has always been inspirational. His never-ending passion and dedication for scientific research shall always inspire me. Dr. Petrolo has been a constant support on every step of the way and I have always been in awe of his organizational skills. His persistently supportive attitude has made this journey an enjoyable one.

I would take this opportunity to thank Prof. Anthony M. Waas for allowing me to conduct research activity at his group in University of Washington. His insight and never-ending zeal has been a constant inspiration. I would like to also thank Dr. Evan Pineda at NASA Glenn Research Center for taking the initiative and hosting me at his research group. It was an invaluable experience to conduct research as well as integrate some of the outcomes of my research work into their framework.

I also owe my gratitude to all my professors and teachers through my life. I would like to especially thank Prof. Alexander Hartmaier at Ruhr Universität Bochum for opening doors for me into the world of scientific research. I am very grateful to have such a wonderful group of office colleagues as well as dear friends: Alberto Garcia de Miguel, Guohong Li and Manish Nagaraj. I always enjoyed all our intense discussions and cherish all the joyful moments in the office. Special thanks to all the member of the MUL² group: Enrico Zappino, Alfonso Pagani, Matteo Filippi, Andrea Viglietti, Daniele Guarnera, Alberto Fiordilino, Riccardo Augello and Nasim Fallahi, without whom this intense and productive year would have not been possible. I sincerely also thank all the administrative staff at Politecnico di Torino for their continued support.

My research work was carried out within the framework of Project FULLCOMP – FULLy integrated analysis, design, manufacturing and health-monitoring of COMPosite structures – funded by European Commission under the Marie Skłodowska Innovative

Training Networks grant for European Training Networks (MSCA-ITN-ETN - 642121). I owe my sincere gratitude to all my fellow FULLCOMPers and I take this opportunity to also thank all the contributors of the project for their continued guidance and support at the project seminars and workshops.

This thesis would not have been possible without the tremendous support of my family. I would like to thank my dearest umma (mother) Zubaida Majeed and my siblings Mansheeda, Althaf, Mashood and Samah for their continued encouragement and for cherishing every small milestone on the way.



Abstract

A class of computationally-efficient tools to undertake progressive failure and damage analysis of composites across scales is presented. The framework is based on a class of refined one-dimensional (1D) theories referred to as the Carrera Unified Formulation (CUF), a generalized hierarchical formulation that generates a class of refined structural theories through variable kinematic description. 1D CUF models can provide accurate 3D-like stress fields at a reduced computational cost, e.g., approximately one to two orders of magnitude of degrees of freedom less as compared to standard 3D brick elements. The effectiveness of 1D CUF models to undertake physically nonlinear simulation is demonstrated through a class of problems with varying constitutive models. The virtual testing platform consists of a variety of computational tools such as failure index evaluations using component-wise modeling approaches (CUF-CW), CUF-CW micromechanics, concurrent multiscale framework, interface, and impact modeling. Failure index evaluation of a class of composite structures underlines the paramount importance of the accurate stress resolutions.

Within the micromechanical framework, the Component-Wise approach (CW) is utilized to represent various components of the RVE. The crack band theory is implemented to capture the damage propagation within the constituents of composite materials and the pre-peak nonlinearity within the matrix constituents is modeled using the J_2 von-Mises theory. A novel concurrent multiscale framework is developed for nonlinear analysis of fiber-reinforced composites. The two-scale framework consists of a macro-scale model to describe the structural level components, e.g, open-hole specimens, coupons, using CUF-LW models and a sub-scale micro-structural model encompassed with a representative volume element (RVE). The two scales are interfaced through the exchange of strain, stress and stiffness tensors at every integration point in the macro-scale model. Explicit finite element computations at the lower scale are efficiently handled by the CUF-CW micromechanics tool. The macro tangent computation based on perturbation method which leads to meliorated performances. A novel numerical framework to simulate progressive delamination in laminated structures based on component-wise models is presented. A class of higher-order cohesive elements

along with a mixed-mode cohesive constitutive law are integrated within the CUF-CW framework to simulate interfacial cohesive mechanics between various components of the structure. A global dissipation energy-based arc -length method to trace the complex equilibrium path exhibited by delamination problem. The capabilities of the framework are further extended through the introduction of contact kinematics to handle impact problems.

A combination of the above tools is used to obtain an accurate material response of the structure in the non-linear regime, from the structural level i.e. macro-scale to the material constituent level i.e. the micro-scale, in a computationally efficient manner, providing a suitable virtual testing environment for the progressive damage analysis of composite structures. The accuracy and efficiency of the proposed computational platform are assessed via comparison against the traditional approaches as well as experimental results found in the literature.

Table of contents

List of figures	xv
List of tables	xxiii
1 Introduction	1
1.1 Motivation	1
1.2 Outline	14
I Physically nonlinear unified formulation	17
2 Unified formulation	19
2.1 Carrera Unified Formulation	19
2.1.1 Taylor Expansion	20
2.1.2 Lagrange Expansion	21
2.2 Finite Element Formulation of 1D CUF	23
2.2.1 Preliminaries	23
2.2.2 Weak formulation of 1D CUF	26
2.2.3 Governing Equation	30
2.3 Numerical cases	34
2.3.1 One-dimensional stress wave propagation	34
2.3.2 Failure index evaluation of a notched composite specimen	36
2.4 Conclusion	45
3 Study on higher-order models for physically nonlinear simulations using elastoplastic models	47
3.1 Elastoplastic material models	47
3.1.1 Numerical aspects of von Mises plasticity model	49
3.2 Numerical results	52

3.2.1	Elasto-Plastic Cantilever Beam	53
3.2.2	Fixed-ended Lipped Channel Beam	59
3.2.3	Clamped Z-beam under pressure load	62
3.3	Conclusion	68

II Micromechanics and Multiscale 71

4 A high-fidelity nonlinear micromechanical framework for hierarchical systems 73

4.1	Micromechanical formulation	73
4.1.1	Component-wise modeling within CUF	74
4.2	Constitutive models	76
4.2.1	Shear-driven plasticity model	76
4.2.2	Crack band model	77
4.3	Numerical results	79
4.3.1	Linear elastic homogenization	80
4.3.2	Modeling pre-peak nonlinearity in composites	89
4.3.3	Progressive failure analysis of fiber-reinforced composite	94
4.4	Conclusion	99

5 A computationally-efficient nonlinear concurrent multiscale framework 101

5.1	Multiscale framework within CUF	101
5.1.1	Computation of consistent macroscopic tangent matrix	102
5.1.2	Implementation aspects	107
5.2	Numerical Results	109
5.2.1	Stiffness prediction of multi-directional laminates	109
5.2.2	Linear multiscale simulation of a randomly distributed large RVE	113
5.2.3	Honeycomb sandwich beam under bending	116
5.2.4	Non linear shear response of multi-layered composite	120
5.2.5	Unnotched laminates under uniaxial tension	123
5.2.6	Open-hole specimen under tension	129
5.3	Conclusion	135

III	Interface and Impact modeling	137
6	Efficient progressive delamination analysis in composite structures	139
6.1	Cohesive zone modeling	139
6.1.1	Boundary value problem	140
6.1.2	Kinematics of interfaces	141
6.1.3	Constitutive modeling of interfaces	142
6.2	Cohesive models within Carrera Unified Formulation	146
6.3	Dissipation-based arc-length solver	147
6.4	Numerical Results	149
6.4.1	Double cantilever test	150
6.4.2	End notch flexure test	151
6.4.3	Mixed-mode bending test	156
6.4.4	Multiple delamination of composite specimen	160
6.5	Conclusion	164
7	Impact modeling in CUF	167
7.1	Contact modeling within CUF	167
7.1.1	Contact Kinematics	167
7.1.2	Weak form of the contact BVP	169
7.1.3	Node-to-Node contact	169
7.2	Numerical results	170
7.2.1	Impact between two rods	170
7.2.2	Impact of a rectangular block	173
7.3	Conclusion	173
8	Summary and Outlook	177
	References	181
IV	Appendices	197
	Appendix A Publications	199

List of figures

1.1	Scanning electron microscopic image of transverse crack formation under tensile transverse loading of cross-ply laminate: (a) debonding of fiber and matrix interface (b) Large transverse cracks are formed by coalescence[80]	7
1.2	The balance of multiscale model efficiency versus fidelity for various classes of multiscale models [5]	10
2.1	Cartesian system for a generic beam	20
2.2	CUF LE elements: (a)L9 cross-section elements and (b) piece-wise discretization of arbitray beam cross-section using L9 elements with local refinement on top flange	22
2.3	Illustration of CW modeling technique for reinforced shell structure [40]	23
2.4	CW modeling adopted for linear static analysis of composites across different scales along with comparison against traditional methods (Ref1 [111], Ref2 [60], Ref3 [40])	24
2.5	Representation of 1D CUF finite element	25
2.6	Illustration of assembly process using fundamental nuclei within CUF [34]	29
2.7	One-dimensional representation of Newton-Raphson iteration with load control: (a) Parametrization of external loading and (c) local iterations within each load increment	31
2.8	Geometry and boundary conditions for 1D stress wave problem	34
2.9	Time history of loading for 1D stress wave problem	35
2.10	Stress and velocity distribution along the beam for time (a) $t = 0.58ms$ (b) $t = 1.01ms$ and (c) $t = 1.2ms$ using 70 B4-elements for one-dimensional stress wave problem	37
2.11	Stress (σ_{yy}) wave propagation in beam at time (a) 0.58ms (b) 1.03ms and (c) 1.2ms for one-dimensional stress wave problem	38

2.12	Comparison of Stress (σ_{yy}) plot along the beam axis for different mesh density at time 0.58ms for 1D stress wave problem	38
2.13	Geometry and boundary conditions for failure evaluation of notched composite specimens	38
2.14	Modeling of notched composite specimens using refined 1D CUF-LW models	40
2.15	Normal stress distribution along the width of notched composite specimen,	41
2.16	Hashin3D matrix tension (MT) failure index for [0] laminate under an applied displacement of 0.2 mm	42
2.17	Hashin3D matrix tension (MT) failure index for [90] laminate under an applied displacement of 0.45 mm	42
2.18	Normal stress distribution σ_{yy} through the thickness of $[0/90]_s$ notched laminate under an applied displacement of 0.125 mm, $x = 16.875$, $y = 69$	43
2.19	In-plane shear stress distribution σ_{xy} through the thickness of $[0/90]_s$ notched laminate under an applied displacement of 0.125 mm, $x = 16.875$, $y = 69$	43
2.20	Transverse shear stress distribution σ_{yz} through the thickness of $[0/90]_s$ notched laminate under an applied displacement of 0.125 mm, $x = 17.04$, $y = 68$	44
2.21	Hashin3D matrix tension (MT) failure index for $[0/90]_s$ laminate under an applied displacement of 0.125 mm	44
2.22	Delamination failure index for $[0/90]_s$ laminate under an applied displacement of 0.125 mm	44
3.1	Elastoplastic material behavior: (a) elastic domain and yield function in stress space and (b) additive split of total strain	48
3.2	Geometrical illustration of Return-Mapping scheme: (a) perfect plasticity and (b) with hardening	50
3.3	Equilibrium path for the elasto-plastic cantilever beam [189]	54
3.4	Geometry and cross-section configurations of the elasto-plastic cantilever beam	54
3.5	Equilibrium path of various beam models for elasto-plastic cantilever beam (30 B4 elements used for TE and LE model)	57
3.6	Comparison of equilibrium path for two-layered and three-layered beam configuration using various models	58
3.7	Geometry of Fixed-ended Lipped Channel Beam	59

3.8	TE and LE models for lipped channel beam	60
3.9	Displacement profile (u_z) along of the beam for fixed-ended lipped channel beam	63
3.10	Deformed configuration (u_z) at $\lambda = 40.98$ for fixed-ended lipped channel beam	63
3.11	von-Mises stress (σ_{xy}) distribution at $\lambda = 40.98$ for fixed-ended lipped channel beam	63
3.12	Equivalent plastic strain ($\bar{\epsilon}_p$) distribution at $\lambda = 40.98$ for fixed-ended lipped channel beam	64
3.13	Transverse stress distribution σ_{xy} at $\lambda = 40.98$ for fixed-ended lipped channel beam	64
3.14	Geometry of clamped Z Beam	64
3.15	TE and LE models for clamped Z Beam	64
3.16	Displacement profile (u_x) along of the beam for clamped Z beam	65
3.17	Deformed configuration (u_x) at $\lambda = 50$ for clamped Z beam	67
3.18	Deformed configuration (u_z) at $\lambda = 50$ for clamped Z beam	67
3.19	von-Mises stress (σ_{vm}) distribution at $\lambda = 50$ for clamped Z beam	67
3.20	Equivalent plastic strain ($\bar{\epsilon}_p$) distribution at $\lambda = 50$ for clamped Z beam	67
3.21	Transverse stress (σ_{xy}) distribution at $\lambda = 50$ for clamped Z beam	68
4.1	A representation of CW modeling of periodic microstructure arbitrary constituents (a) a generic triply-periodic microstructure with three phases, (b) Individual components of RVE modeled via CW technique and (c) Assembled configuration of RVE with cross-section element overlayed on x-z plane and beam elements along the axis of beam	74
4.2	Application of PBC for CUF-CW RVEs: (a) cross-section of the beam and (b) end nodes of the beam	76
4.3	Constitutive modeling of bilinear crack band model [22]	78
4.4	CW modeling of the square-packed RVE for effective moduli prediction of Boron/Aluminium and Graphite/Epoxy material systems	81
4.5	CW modeling of the square-packed and hex-packed RVE for studying the effect of fiber packing architecture	82
4.6	CW discretization of the cross-section of RVE with 13 randomly distributed fibers and a fiber volume fraction of 60%	83
4.7	Maximum principal strain contours ϵ_1^p over the cross-section of the RVE with 13 randomly distributed fibers subjected to transverse tensile strain (a) CW-CUF model and (b) ABAQUS 3D model	84

4.8	Transverse stress contours σ_{22} [MPa] over the cross-section of the RVE with 13 randomly distributed fibers subjected to transverse tensile strain (a) CW-CUF model and (b) ABAQUS 3D model	84
4.9	CW discretization of the circular and square void for analysis of void filled Cu composite	85
4.10	von-Mises stress contours σ_{vm} [MPa] over the cross-section of the RVE of void-filled Cu composite with a void volume fraction of 0.5102 subjected to transverse tensile strain (ϵ_{11}): (a) CUF-CW and (b) ABAQUS 3D .	87
4.11	Architecture of hexagonal honeycomb RVE: (a) Dimensions of the hexagonal honeycomb RVE and (b) CW discretization of the cross-section for hexagonal honeycomb RVE using 18L9 elements	87
4.12	Maximum principal strain contours ϵ_1^p for hexagonal honeycomb RVE with subjected to transverse tensile strain (ϵ_{33}) (a) CW-CUF model and (b) ABAQUS 3D model	88
4.13	von-Mises stress contours σ_{vm} [MPa] for hexagonal honeycomb RVE with subjected to transverse tensile strain (ϵ_{33}) (a) CW-CUF model and (b) ABAQUS 3D model	88
4.14	Hardening curve for three laminate systems with curve parameters . . .	90
4.15	Comparison of in-plane shear responses for three unidirectional material systems	92
4.16	Comparison between 3D FEM and CUF-micro for the in-plane shear response of HTA-6376 material system	93
4.17	Contour plots of inelastic plastic strain for randomly distributed RVE under transverse strain $\bar{\epsilon}_{22}$ of 0.003	93
4.18	Comparison of global stress-strain response for pre-peak nonlinear response of randomly distributed RVE under transverse strain $\bar{\epsilon}_{22}$ of 0.003	94
4.19	CW discretization of the cross-section of RVE with 13 randomly distributed fibers	95
4.20	Transverse tensile stress versus strain for progressive failure analysis under transverse tension for different RVE architecture	97
4.21	Comparison of final damage contour plots for CUF-CW against solutions from literature [160] for square-packed under transverse tension	97
4.22	Damage progression in the randomly distributed fiber composite under transverse tension at global strains (a)0.00225, (b) 0.00275 (c) 0.0035 and (d) 0.004 (Gray: Fiber, Blue: Undamaged matrix, Red: Damaged matrix)	98

5.1	Illustration of multiscale modeling within the CUF framework	102
5.2	Validation test for consistent macroscopic tangent matrix computation using von-Mises theory	105
5.3	Convergence behaviour of various components in homogenized material tangent matrix for different perturbation values	106
5.4	Speed up obtained in the parallel version of multiscale framework for a system with $\sim 130,000$ degrees of freedom	107
5.5	Flowchart for the concurrent multiscale framework based on CUF . . .	108
5.6	Microscale RVE model for stiffness prediction of multi-directional laminates	110
5.7	An illustration of the modeling of composite specimens using refined 1D CUF models for stiffness prediction of multi-directional laminates [60]	111
5.8	Geometry for linear multiscale simulation of a randomly distributed large RVE	113
5.9	von-Mises stress distribution around the hole for linear multiscale simu- lation of a randomly distributed large RVE	114
5.10	Local stress field σ_{11} obtained at location A for linear multiscale simula- tion of a randomly distributed large RVE	115
5.11	Local stress field σ_{12} obtained at location B for linear multiscale simula- tion of a randomly distributed large RVE	115
5.12	Multiscale modeling of honeycomb sandwich using CUF multiscale framework: (a) Interfacing two kinds of micro models for sandwich beam and (b) CW discretization of macro sandwich beam model using L9 cross-section and B4 beam elements	116
5.13	Geometry of the honeycomb core: (a) Repeating core structure and (b) geometrical parameters of RVE	117
5.14	Component-wise modeling of the honeycomb core RVE: (a) CUF beam model of RVE and (b) Cross-section and beam discretization	117
5.15	Geometry and boundary conditions for multiscale modeling of honey- comb sandwich using CUF multiscale framework	119
5.16	Local von-Mises stress field σ_{vm} obtained at a point in core (50.0, 35.0, 16.9) for analysis of honeycomb sandwich beam for different multiscale models	120
5.17	Model information of two-layered composite RVE for multi-layered structure under pure shear loading condition: (a) Boundary conditions for macro model, (b) Cross-section and beam modeling of macro model and (c) Cross-section and beam modeling for micro model	121

5.18	Plastic response of the elasto-plastic phase for two-layered composite RVE for multi-layered structure under pure shear loading condition . .	122
5.19	Comparison of overall macro response of two-layered composite RVE for multi-layered structure under pure shear loading condition against semi analytical solution and FE ² approach [185]	122
5.20	Comparison of convergence between 1D-1D model and CUF-micro model. 1D-1D (Global) refers to the global convergence behavior of the macro 1D model and 1D-1D (Local) refers to the convergence behavior exhibited at the local micro model interfaced to one of the gauss point of macro model	123
5.21	Macro model for off-axis laminates under uniaxial tension	124
5.22	Micro model for 1D-1D multiscale model for off-axis laminates under uniaxial tension	124
5.23	Calibrated hardening curve used for micro RVE model for unnotched laminates under uniaxial tension	126
5.24	Comparison of calibrated CUF-Micro and FE-Micro model against experimental [147] and CDM-Plasticity model [148] for transverse and shear response of the RVE	127
5.25	Accumulated inelastic strain in calibrated RVE at an applied shear strain $\gamma_{12} = 0.05$	127
5.26	Comparison of multiscale model predictions against experimental data [147] and CDM-Plasticity model [148] for off-axis laminates under uniaxial tension	128
5.27	Geometry and boundary condition for open-hole specimen under tension	130
5.28	Material properties for inelastic matrix for the micro model of open-hole specimen under tension	130
5.29	Mesh configuration for various multiscale models for open-hole specimen under tension (Non linear micro model is active only in shaded region)	131
5.30	Remote stress-strain curve for open-hole specimen under tension	132
5.31	Comparison of accumulated inelastic strain at multiple scales for various multiscale models for open-hole specimen under tension at an applied displacement loading of 0.5625 mm	133
5.32	Comparison of von-Mises stress resolution within matrix constituents of the micro scale RVE for various multiscale models for open-hole specimen under tension at an applied displacement loading of 0.5625 mm (Refer to Fig. 5.31 for location of micro RVE)	134

5.33	Convergence behavior of different multiscale model for open-hole specimen under tension	134
6.1	Boundary value problem for cohesive formulation	140
6.2	Boundary value problem for cohesive formulation	141
6.3	Mixed-mode cohesive constitutive law	145
6.4	Cohesive Lagrange cross-section elements	146
6.5	Geometry and loading for double cantilever test	150
6.6	End notch flexure test: Cross-section mesh configuration	151
6.7	Double cantilever test: Comparison of equilibrium curves for different beam elements with same mesh density for (a) 4L9-2CS6 cross-section configuration and (b) 8L9-4CS6 cross-section configuration	152
6.8	Double cantilever test: Three-dimensional displacement contour plot for 8L9-4CS6 with 80B4 model at displacement of (a) 7.2 mm, (a) 33.6 mm and (c) 52.0 mm	153
6.9	Geometry and loading for end notch flexure test	153
6.10	End notch flexure test: Cross-section mesh configuration	153
6.11	End notch flexure test: Comparison of equilibrium curves for (a) linear (B2) and cubic (B4) beam elements using 8L9-4CS6 cross-section configuration and (b) different cross-section configuration using 80 cubic (B4) beam elements	154
6.12	End notch flexure test: Comparison of the no. of iteration required per increment for different models (Gray : Load controlled and Black: Energy-based arc length)	154
6.13	End notch flexure test: Stress σ_{yy} contour plot for 4L9-2CS6 model at (a) $\lambda = 30.08$, (a) $\lambda = 228.4$ and (c) $\lambda = 280.3$	155
6.14	Geometry and loading for mixed-mode bending test	157
6.15	Equilibrium curves for mixed-mode bending test: (a) Results from CUF-CW model using 8L9-4CS6-60B4 is compared against experimental and numerical results from the literature for different mode ratios [17, 30] (b) Comparison of different CUF-CW models against 3D FEM models with varying mesh density for 0.8 mode-mix ratio	159
6.16	Geometry and boundary condition for multiple delamination in composite specimen test	160
6.17	Modeling Multiple delamination of composite specimen using CUF-CW model	161

6.18	Equilibrium curves for multiple delamination of composite specimen test: (a) Comparison of CUF-CW model with experimental and literature results [12, 145, 170] and (b) Comparison between CUF-CW model against 3D FEM results with varying mesh density	162
6.19	Equilibrium curve along with deformed states for CUF-CW model for multiple delamination of composite specimen test	163
6.20	Contour plots of the delamination index - 0: intact, 1: fully delaminated - at the top and bottom cohesive surfaces via CUF for multiple delaminations	163
7.1	Reference and current configuration of two distinct bodies coming into contact	168
7.2	Schematic representation of impact between two rods	171
7.3	Time history of (a) Axial deflection u_y and (b) Axial stress σ_{yy} at the free end of the first rod during the time period of the analysis	171
7.4	Propagation of axial stress σ_{yy} at various points of time during the analysis.	172
7.5	Schematic representation of a rectangular block under impact	172
7.6	Time history of (a) Transverse deflection u_z and (b) Transverse stress σ_{zz} at the point [10.0,10.0, 0.1] of the block	173
7.7	Propagation of transverse stress σ_{zz} through the block at various points of time	174

List of tables

2.1	Mac Laurin's polynomials for TE models	21
2.2	Model information for failure index evaluation of notched composite specimens	39
2.3	Numerical results for load at first ply failure for different models of notched composite specimens	41
3.1	Geometric and material properties of elasto-plastic cantilever beam . .	54
3.2	Comparison of displacement and plastic strength factor (PSF) for various beam models of elasto-plastic cantilever beam	55
3.3	Convergence study of various refined beam models for elasto-plastic cantilever beam	56
3.4	Material properties for multi-layered cantilever beam under bending . .	57
3.5	Comparison of maximum accumulated equivalent plastic strain for different models for multi-layered cantilever beam under bending	58
3.6	Vertical displacement at point A for various models for fixed-ended lipped channel beam	61
3.7	Isotropic hardening data for Clamped Z-beam problem [119]	62
3.8	Displacement for various beam configurations for clamped Z beam . . .	66
4.1	Material properties for effective moduli predictions of fiber-reinforced composite	80
4.2	Predicted effective moduli for Boron/Aluminum composites	81
4.3	Predicted effective moduli for Graphite/Epoxy composites	81
4.4	Comparison of elastic moduli for various RVE architecture for Boron/Aluminium and Graphite/Epoxy material system	82
4.5	Numerical results from de-homogenization of RVE with 13 randomly distributed fibers subjected to transverse tensile strain	83

4.6	Predicted transverse Young modulus E_{22} (GPa) of void-filled Cu composite with varying void volume fraction	86
4.7	Dimensions of hexagonal honeycomb RVE	87
4.8	Predicted transverse Young modulus E_{22} (GPa) of the cellular hexagonal honeycomb RVE	88
4.9	Mechanical properties of fibers	89
4.10	Predicted elastic properties for three unidirectional laminates	90
4.11	Calibrated material properties for matrix along with hardening curve parameters	90
4.12	Numerical results for from 3D FEM and CUF-micro model for the in-plane shear response of HTA-6376	91
4.13	Numerical results for from 3D FEM and CUF-micro model for the in-plane shear response of HTA-6376	91
4.14	Numerical results for pre-peak nonlinear response of randomly distributed RVE under transverse strain $\bar{\epsilon}_{22}$ of 0.003	93
4.15	Material properties of glass fiber and epoxy matrix for progressive failure analysis of fiber-reinforced composite [160, 161]	95
4.16	Model information for progressive failure analysis of fiber-reinforced composite	96
4.17	Numerical results for square-packed RVE under transverse tension . . .	96
4.18	Numerical results for randomly distributed RVE under transverse tension	97
5.1	Convergence behavior for different perturbation strain δE (Relative macro residuum = 10^{-4})	106
5.2	Nomenclature for various models used in multiscale analysis	109
5.3	Calibrated constituent properties of RVE for multiscale analysis for stiffness prediction of multi-directional laminates	110
5.4	Macro model information for stiffness prediction of multi-directional laminates	111
5.5	Stiffness prediction for notched and unnotched multi-directional laminates	112
5.6	Strain computed at two location for dehomogenization linear multiscale simulation of a randomly distributed large RVE	114
5.7	Numerical results for linear multiscale simulation of a randomly distributed large RVE	115
5.8	Geometrical properties of core for multiscale structural analysis of honeycomb sandwich beam [45]	117

5.9	Prediction of effective properties of honeycomb RVE for multiscale structural analysis of honeycomb sandwich beam	118
5.10	Macro model information for analysis of honeycomb sandwich beam . .	119
5.11	Macro model information for analysis of honeycomb sandwich beam . .	119
5.12	Numerical results for analysis of honeycomb sandwich beam under bending load	119
5.13	Material properties for two-layered composite RVE for multi-layered structure under pure shear loading condition	121
5.14	Elastic properties of micro RVE models for off-axis laminates under uniaxial tension	125
5.15	Micro model information for unnotched laminates under uniaxial tension	126
5.16	Numerical results for off-axis laminates under uniaxial tension	126
5.17	Numerical results for open-hole specimen under tension	132
6.1	Material properties for double cantilever test	150
6.2	Model information for DCB specimen test	151
6.3	Material properties for ENF specimen test	152
6.4	Model information for ENF specimen test	155
6.5	Material properties for MMB test	157
6.6	Geometric properties and load values for different mode-mix ratio for MMB test [17, 30]	157
6.7	Model information for MMB test	158
6.8	Comparison of maximum load obtained using 8L9-4CS6-60B4 model for MMB test against experimental and literature	158
6.9	Numerical results for MMB test	159
6.10	Material properties for multiple delamination of composite specimen test [145, 170]	161
6.11	Model information for multiple delamination of composite specimen test	161
6.12	Numerical results for Multiple delamination of composite specimen test	163

Chapter 1

Introduction

1.1 Motivation

Over the last decades, advanced fiber-reinforced composites have extensively penetrated into high-performance products such as primary components of aircraft and racing cars, wind turbine blades and high-performance sports goods. Exponential growth in demand for carbon-reinforced composite is foreseen mainly in aerospace, automotive and wind energy sectors. Stringent government regulations on environmental impact for automobile and aerospace manufactures is yet another driving force for widespread adoption of composite materials. For instance, Advisory Council for Aeronautical Research in Europe (ACARE) has set an ambitious target of a 75% and 90% reduction in CO₂ and NO_x emissions respectively by 2050 [9]. Weight reduction, achieved mainly through the adoption of advanced composite materials, shall play an important role in meeting these targets.

Currently, design and certification of lightweight aircraft composite components depend extensively on experimental testing, which in turn increases the cost as well as the development time [74]. Exhaustive experimental campaigns, currently a mandatory procedure for certification of new composite airframes, are based on the building block approach termed as test pyramid. First introduced by Rouchon [171], testing pyramid consists of different stages starting from elementary coupon to full-scale coupons with progressive design complexity in successive stages. Even though the approach provides a consistent way to analyze and mitigate risk, it relies on extensive amount of testing to cover all critical design features with the budgetary and time constraints. This often leads to restriction of the design space to a limited kind of material or lamination sequences resulting in conservative structural design. Therefore, reducing the number of tests can substantially reduce the development time and cost. In addition, the recent

shift in increased use of composites in commercial products has underlined some of the deficiency in the existing design and modeling capabilities for composites.

The exorbitant cost associated with design and testing of new-age composite structures can be alleviated by supplementing different stages of the pyramid with high-fidelity simulation tools [211]. The activity falls under the paradigm of "virtual testing", which also come under the broad umbrella of activities such as ICME (Integrated Computational Materials science and Engineering) [52] and "Digital-twin" programs (program of creating high-fidelity computational model of entire aircraft to compute structural response in response to flight condition in real-time) [85]. Virtual testing frameworks can expand the design space in early stages of the design and provide a possibility to consider configurations that were too complex to verify with purely empirical methods. Furthermore, these tools can also augment and guide the physical testing of large-scale components. But existing computational tools only account for a fragmented portion of domain covering different length and time scales of composite design with limited reliability and robustness. The challenges associated with virtual testing of composites are two-fold: (1) Understanding the underlying physics which govern the complex deformations across various scales and (2) representation of these physical phenomena through robust and efficient mathematical models leading to a reliable computational framework, which can be exploited by designers and engineers. Former challenge is addressed through continued advances in experimental technology such as non-destructive, in-situ imaging of internal damage of a loaded specimen using state of the art X-ray computed tomography [135]. The inherent multiscale nature of the composite materials along with high complex failure modes pose significant challenges for mathematical modeling [84]. Extensive studies such as World-Wide Failure Exercise (WWFE) have emphasized the challenges associated with developing computational models that yield reliable and accurate results and some of these models still require numerous validation cases [100]. Some of the crucial aspects involve:

1. Proper physics-based constitutive modeling at relevant length scales that are supplemented by experimental validations. Reliable predictions of complex behaviors of composite materials must include interactions accounting for different failure mechanisms such as matrix-cracking, fiber breakage, splitting, and delamination.
2. Need of computationally-efficient numerical models without the loss of fidelity, especially for large-scale structural analysis and simulations involving multiple scales. Often the trade-off between accuracy versus computational efficiency is skewed towards the latter.

3. In case of multiscale analysis, development of numerical methods to resolve displacement and stress fields at lower scales and effectively provide equivalent homogenized properties to subsequent higher-scale with a suitable technique for interfacing across scales

The objective of this thesis is the advancement of numerical tools for modeling progressive failure of composite across scales through development of computationally-efficient advanced structural models. The framework is built using Carrera Unified Formulation, a hierarchical scheme that yields computationally efficient structural models through variable kinematic definitions. A class of tools is presented that can undertake various aspects virtual testing of composite across different stages of test pyramid including micromechanical progressive failure analysis, nonlinear multiscale modeling, delamination modeling and impact analysis. Appropriate damage and failure constitutive models are integrated within the framework to capture various modes of failure including matrix cracking, shear driven pre-peak nonlinearity and interfacial cracking. A brief historical excursus on advanced structural models as well as numerical modeling of composites is presented.

Advanced one-dimensional structural models

Classical structural theories such as Euler-Bernoulli Beam Theory (EBBT) [27, 73] are formulated based on a fixed number of generalized unknowns. For instance, EBBT formulation has three unknowns and describes the bending behavior of slender beam with acceptable accuracy but their usability is restricted to slender prismatic beams. Similarly, beam theory developed by de Saint-Venant for isotropic beam fails to account for transverse shear deformation [61, 62]. Timoshenko Beam Theory (TBT) accounted for rotation about the bending beam axis due to shear deformation through the inclusion of additional terms to the beam kinematics [187, 188], thereby extending the suitability of the formulation to thicker beams. Nonetheless, the applicability of the aforementioned classical models is greatly restricted due to the deficiency in capturing non-classical effects such cross-section warping, torsion-bending coupling, or localized boundary effects. In addition, geometrical restriction including slenderness ratio, material anisotropy, and prismatic nature limit their sphere of applicability. Washizu postulated the following [202]:

"For a complete removal of the inconsistency and an improvement of the accuracy of the beam theory, we may assume a finite number of terms in the kinematic field where the number of terms should be chosen properly "

Several methods have been proposed to extend on the applicability of 1D models for diverse set of problems by overcoming the limitations of classical models. Timoshenko and Goodier improved the global response of classical beam theories by introducing appropriate shear correction factors [186]. Gruttman and coworkers introduced shear correction factors for different structural analysis cases including thin-walled and arbitrary cross-sections [90]. On the theoretical basis of de Saint-Venant solution, Ladavéze and coworkers established *exact* beam theory by reducing the full 3D elasticity equation to beam-like structures [118]. Unlike classical beam models, the formulation is independent of any kinematic assumption. El Fatmi proposed a non-uniform warping beam theory that captured the effect of torsion and shear forces through the introduction of additional warping terms to enhance the normal and shear stresses [68]. Berdichevsky et al. proposed an alternate class of refined models based on asymptotic-type expansions on the basis variational methods where the kinematic field is not assumed a priori and is a result of the analysis [26]. Variational Asymptotic Beam Section Analysis (VABS), developed by Cesnik and Hodges, splits the generalized 3D nonlinear elasticity problem into a 2D linear cross-sectional analysis and a 1D nonlinear beam analysis using variational asymptotic method [46]. The asymptotic series is built using a characteristic parameter related to the structure such as the cross-section thickness of the beam. Schardt proposed a new class of higher-order theory called Generalized Beam Theory (GBT) that describes the kinematic field as a linear combination of cross-sectional deformation modes [173]. Kapania and Raciti provided a comprehensive review of different beam theories for a diverse set of applications including bending, vibration, and buckling [114].

Originally developed by Carrera for two-dimensional structures [32, 33], Carrera Unified Formulation (CUF) provides a structured basis to derive any class of refined beam, plate or shell theories through variable kinematic definition. By means of one- and two-dimensional expansion function for beams and plates/shells respectively, different classes of structural theory can be generated using compact formulation. One-dimensional CUF models were first proposed by Carrera and Giunta which adopted Taylor-like polynomials (TE) as expansion functions [37]. The order (N) of the expansion function is arbitrary and classical models such as EBBT and TBT can be retrieved as special cases of linear expansion (N=1). Carrera and Petrolo extended the capabilities of the 1D CUF model by introducing a new class of theories based on Lagrange-polynomials (LE) [42]. Lagrange-based CUF models are characterized by purely translational unknowns whereas TE models consist of displacement and higher-order derivatives as unknowns. Component-Wise (CW) modeling approach is

an application of 1D LE model to model complex structures by segregating various components of the structure into individual constituents and formulating the problem using 1D LE models in an efficient and concise manner [39]. Purely displacement-based kinematic formulation also permits easy integration of multi-dimensional models (one-, two- or three-) without any ad-hoc techniques [214]. Recently, Pagani et al. extended the capabilities of the CW approach through the introduction of a new class of models based on Hierarchical Legendre-type expansion (HLE) function [153]. Unlike Lagrange-based CUF model, HLE models allowed kinematic enrichment of domain using a single local expansion by altering the polynomial order. Carrera et al. studied the performance of different classes of higher-order 1D models based on polynomial, trigonometric, exponential and zig-zag expansion function [36]. Over the last decade, computational efficiency demonstrated by CUF 1D models have been extensively employed in solving diverse classes of problems including:

1. Failure index evaluation of composite structures using CW technique [123]
2. Linearized buckling [106], large-deflection and post-buckling of composite structures [152]
3. Aeroelastic response of wind structures [194] and Flutter analysis of lifting surface [159]
4. Biomechanics [38] and stoke's flow [195]
5. Rotordynamics [35] and multifield problems [131]
6. Analysis of thermoelastic [70], piezo-electric [44] and functionally graded beams [77]

Carrera et al. provided a comprehensive review of various approaches adopted in developing one-dimensional models along with several applications [41].

Higher-order models for physically nonlinear simulations

Classical beam models (EBBT and TBT) are extensively opted in engineering practice for stress analysis as they offer a good trade-off between accuracy versus computational cost. The validity of these classical models in nonlinear regime remains questionable due to lack of accurate stress resolutions and engineers often resort to computationally expensive 2D or 3D models in such cases. Nevertheless, the added computational demand overshadow their effectiveness in the early design stages and parametric

studies. Over the last few decades, significant effort has led to the development of computationally efficient physically non-linear simulation frameworks based on one-dimensional models and a brief overview follows.

A substantial effort has been diverted towards extending the existing one-dimensional analytical formulation to undertake nonlinear analysis. Timoshenko and Gere extended the TBT to inelastic beam under perfect elasto-plastic assumptions [189]. The formulation was limited to prismatic beams with doubly-symmetric cross-sections and the approach neglected shear effects. Davenne et al. developed an efficient one-dimensional multi-fiber beam FE based for nonlinear dynamic analysis of civil structures that accounts for damage growth in concrete beams [56]. Mata et al. proposed a geometrically exact formulation for 3D beams that account for geometric and physical nonlinearity for analysis of framed structures [125]. Even though the formulation accounted for different kinds of nonlinearity including plasticity and models and exhibited superior computational efficiency, the approach was formulated under the assumption of the planarity of cross-section. Orbison et al. presented an efficient approach for modeling inelastic behavior in 3D beam-column assembly using plastic hinge hypothesis [149]. Most of the analytical and semi-analytical formulation adopts a constrained kinematic, which often restrict their applicability and may even cause non-physical responses in some cases. Recently, Abambres et al. extended Generalized Beam Theory (GBT), originally developed by Schardt [173], for elasto-plastic analysis of thin-walled steel structures exhibiting strain-hardening behavior. Goncalves and Camotim extended the elasto-plastic GBT model to account for geometric nonlinearity [86]. Extension of one-dimensional Variational Asymptotic Beam Section Analysis (VABS) model to physically nonlinear simulation was successfully undertaken by several authors including modeling matrix cracking in helicopter blades [163], modeling hyper-elastic beams subjected to finite deformation [107] and damage analyses of composite structures [108].

Micromechanical analysis

Microscale analysis is an integral part of virtual testing frameworks built within the scheme of Integrated Computational Material Engineering (ICME) [121]. Hierarchical material systems such as composite or polycrystalline metals necessitates their usage in capturing lower scales phenomena for reliable simulation. Figure 1.1 depicts the scanning electron microscopic image of a fiber-reinforced composite under transverse tensile loading characterized by matrix cracking. Micromechanical analysis captures the effective behavior of these heterogeneous systems through homogenization (up-

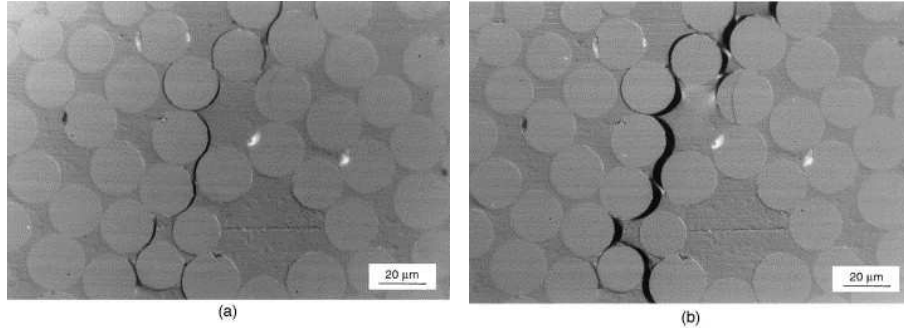


Fig. 1.1 Scanning electron microscopic image of transverse crack formation under tensile transverse loading of cross-ply laminate: (a) debonding of fiber and matrix interface (b) Large transverse cracks are formed by coalescence[80]

scaling) and localization (down-scaling) processes for a given representative volume element (RVE). Such analysis scheme often enrich physically nonlinear simulation phenomena such as progressive failure in composites, as they are greatly stimulated by underlying lower scale features. For example, ply-level damage constitutive models performs well for modeling fiber-reinforced composite with almost brittle failure but their usage remains unreliable in case of composite plies that exhibit significant pre-peak nonlinearity [23]. Constitutive modeling of various constituents at the microscale analysis are often physics-based as their formulation are phenomenologically driven and intends to capture the underlying physics. Over the last decades, significant advances in the field of computation have increased viability of micromechanical simulation within a multiscale modeling context.

Effectiveness of such micromechanical analysis is greatly influenced by proper constitutive modeling at lower scales as well as the ability of these models to generate accurate local fields at the constituent level. The former requires rigorous validation through in-situ experiments whereas latter greatly depends on the mathematical approaches employed to formulate the micromechanical boundary value problem. Mathematical approaches often employed to model such problem can be broadly classified into three categories:

1. Analytical formulations

Analytical formulation provides closed-form solutions for computing elastic effective response of heterogeneous systems in terms of volume fractions and elastic properties of individual constituent such as Rule of mixture by Voigt [200] and Reuss [167], Concentric Cylinder Model (CCM) [94], Eshelby methods[72], Mean-Field Homogenization (MFH) methods of Mori-Tanaka [136] and self-consistent estimate by Hill [98] and G-A

meso-mechanics methods for periodic structures [83]. An analytical micromechanics model based on CCM for the nonlinear composite method was formulated by Zhang and Waas [216]. The method is able to spatially resolve the matrix fields and equip the matrix constituents with an inelastic material model offering a distinct computational advantage over numerical methods. An essential prerequisite for any nonlinear analysis is the accurate resolution of local fields within various constituents. Even though analytical methods are computationally very attractive and effective for moduli predictions, lack of spatially resolved fields often hinders their usage for nonlinear analysis.

2. Semi-analytical approaches

Unlike standard analytical formulation, semi-analytical approaches provide resolution of the local field with a substantial reduction in computational overhead as compared to standard numerical approaches. Significant effort has been dedicated towards extending MFH techniques to nonlinear regimes including analysis of elasto-plastic periodic structures [10, 139, 207], elasto-visco-plastic composites [65]. Accorsi and Nemat-Nasser employed a Fourier series expansion to compute the bounds on overall elastic and elastoplastic moduli along with local fields [10]. Aboudi introduced a closed-form micromechanical theory for nonlinear analysis of repeating unit cell called Method of Cells (MOC) [3, 5]. The generalization of MOC lead to a class of semi-analytical formulations including Generalized Method of Cells (GMC) [156] and High-fidelity-generalized method of cells (HFGMC) [7]. Within GMC, RVE is subdivided into a number of subcells accounting for multiple constituent phases with linearly expanded displacement fields. HFGMC employs second-order displacement field thereby addressing the lack of shear-coupling effect in GMC models but with an increased computational effort. GMC and HFGMC are able to provide accurate local fields within the subcells with significantly reduced computational effort as compared to standard FE approach [5]. GMC and HFGMC have been successfully employed to undertake a class of nonlinear problems including nonlinear composites [92] and progressive failure analysis of composites [23, 161], multiscale analysis [137].

3. Fully-Numerical methods

The generality of full-numerical approaches such as FEM is often exploited to develop micromechanical tools especially for 3D microstructures such as textile composites. Levy and Papazian developed a finite model to predict the tensile stress-strain response of short fiber-reinforced composites with matrix exhibiting elasto-plastic behavior [120]. Sun and Vaidya established FE models for RVE with appropriate periodic boundary conditions and strain energy equivalence for predicting effective moduli of

uni-directional fiber composites [183]. Classical displacement-based FE methods have been widely employed to undertake a class of nonlinear micromechanical problems as versatility exhibited by these model often overshadow the increased computational cost. Fish et al. developed multi-level asymptotic variational formulation to undertake damage analysis in brittle composites [78]. González and Llorca developed an FE based micromechanics toolbox for studying the mechanical behavior of polymer-composites including damage progression, interface decohesion and matrix plastic deformations [87]. Experimentally validated FE-based direct numerical simulation of 3D woven textile composites under tensile loading was developed by Deepak et al. [158]. Vaughan et al. examined the effect of fiber-matrix debonding on the transverse behavior of polymer composites [196]. D'Mello et al. investigated the effects of the manufacturing process on the strength estimation of fiber-reinforced composites [64]. Yu and Tang developed a new class of micromechanics model that could predict effective properties of periodic materials as well as recover local strain and stress fields using variational asymptotic method (VAMUCH) [213]. Implemented within the scheme of FE, VAMUCH has been extensively applied for diverse sets of problems including thermomechanical, piezo-electric and elasto-viscoplastic heterogeneous materials.

A comprehensive review on different varieties of micromechanical approaches can be found in [95, 97, 101]. In addition, Reduced-order modeling techniques are also employed to circumvent exorbitant computational cost associated with large system analysis, where reduced-order technique reduced the size of the global system equations for a given acceptable accuracy [168]. Even though fully-numerical methods provide accurate resolution of the local fields, constraints such as high computational cost often hinder their wide-spread adoption. For instance, commercial packages such as DIGIMAT still rely on analytical or semi-analytical formulations for their micromechanical and multiscale platforms [63]. Within the scheme of multi-scale virtual testing simulation, enhanced efficiency at the lower scales can significantly boost the needed computational overhead.

Multiscale modeling

In order to effectively capture the entire design envelope of hierarchical material structures such as composites, it is fundamental to understand the physics of the material at underlying scales. An integrated multiscale structure and material modeling framework can serve as a vital tool to obtain the best possible physically-realizable engineering designs [121]. Understanding the source of physical behavior at lower scales and

bridging the effect accurately to upper scales can significantly boost the fidelity of such simulations. Despite the fact that continuum-based constitutive modeling has proven to be well suited for predicting the overall response of structures, modeling localized phenomena such as damage and failure propagation using such approaches remains questionable as such mechanisms are heavily influenced by the underlying lower-scale features. Even though multiscale modeling technique effectively increases the fidelity of the simulations, lack of widespread adoption of such technique could be attributed to factors concerning scalability to practical engineering problems. Additionally, exorbitant computational overhead depreciates the overall efficacy of this modeling technique.

Macroscale constitutive modeling assumes the material point as a homogeneous and heterogeneity such as inclusions, voids etc. are accounted through implicit mathematical formulations. Within a multiscale framework, the constitutive response at a material point is interfaced with a lower scale with explicit heterogeneous definitions through homogenization [5]. Thus, effective behavior can be captured by solving a micromechanical boundary value problem (BVP) [5, 96]. In general, micromechanics-based multiscale framework often consists of macro scale modeled using FE models, interfaced with a lower micro scale with explicit heterogeneous material definitions. Based on the coupling scheme adopted to interface different scales, multiscale modeling technique can be broadly classified as (a) Hierarchical, (b) Synergistic and (c) Concurrent methods [5, 181]. Hierarchical strategies are based on one-way coupling

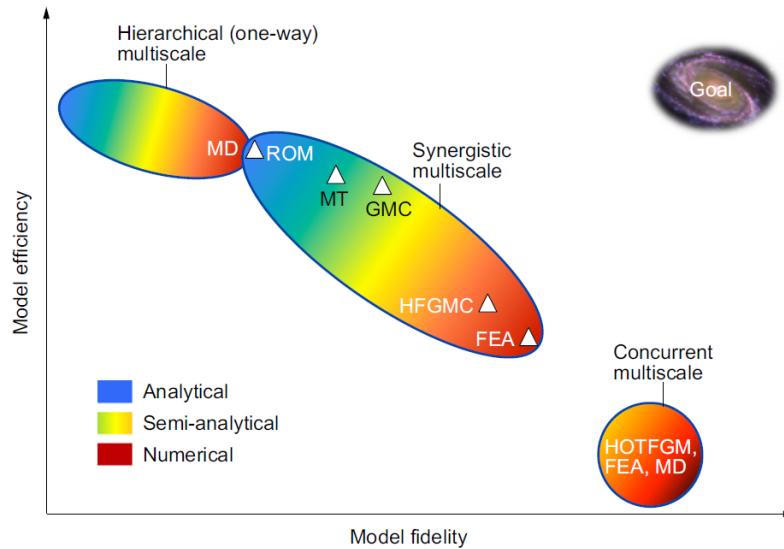


Fig. 1.2 The balance of multiscale model efficiency versus fidelity for various classes of multiscale models [5]

with information passed either bottom-up (homogenization) or top-down (localization). Concurrent methods are characterized by fully-coupled information interfacing with bottom-up and top-down occur concurrently with all scales handled simultaneously in space and time. Synergistic approach is a blend of two approaches where either field variables are handled sequentially in space and concurrently in time or vice versa. Figure 1.2 illustrates the placement of the aforementioned modeling approaches in the model efficiency versus fidelity paradigm. Hierarchical scheme presents with highest computational efficiency but lowest fidelity whereas concurrent approach provides the highest fidelity with the lowest efficiency. As depicted in Fig. 1.2, different kinds of approaches are adopted at the lower scales by various coupling scheme and can be broadly classified into: mean-field (Analytical) and full-field approach (Semi-analytical and Numerical).

Mean-field approach are mostly based on analytical methods such as concentric cylinder model (CCM) [94], Mori-Tanaka method [136] and generalized self-consistent method (GSCM) [104] are utilized to compute the effective response at the microscale. Even though these methods are computationally efficient, lack of spatially resolved information often restricts their usage in the nonlinear regime. Secant-modulus based approaches are employed to extend mean-field theories for nonlinear analysis but often lead to overestimated response due to lack of stress concentration [175]. Zhang and Waas developed an analytical subscale micromechanics model based on two-phase CCM and three-phase GSCM to undertake nonlinear evolution of matrix constituents within composite offering distinct computational advantage [216]. The method was successfully integrated into the multiscale modeling framework for undertaking progressive failure analysis of laminated fiber-reinforced composite and hybrid 3D textile composites [215, 217]. Commercial codes such as DIGIMAT utilizes mean-field methods and its extension for multiscale modeling [63].

A class of semi-analytical methods has been developed to overcome the limitations of mean-field based approaches. Unlike analytical methods, semi-analytical method offers the spatial resolution of fields with a significant computational advantage over fully-numerical approaches. The Method of Cells (MOC) [5] and its extensions including the Generalized Method of Cells (GMC) [155] and High-Fidelity Generalized Method of Cells (HFGMC) [6] are a set of powerful semi-analytical tools to undertake effective behavior of hierarchical materials and structures at the micro scale. These methods are able to provide an anisotropic response of heterogeneous material via semi-closed form solution with high-degree of accuracy. GMC-based multiscale models are extensively applied for undertaking progressive failure and damage modeling for a class of composite

materials and structures [137, 162, 168], where the micromechanics toolbox is integrated with a commercial FE solution for macroscale modeling.

Most commonly adopted fully-numerical approach within the multiscale paradigm are based on finite element models applied at both scale, often referred to as FE^2 method. Introduced by Feyel for modeling elasto-visco-plastic analysis of composite structures [75], FE^2 method has been an active area of research [76, 127, 185, 197]. Ladavèze et al. developed a LATIN based methods, which is a non-incremental iterative computational strategy for multiscale modeling [117], for nonlinear modeling of the composite. FE^2 scheme has been extensively adopted for various classes of multiscale problems such as non linear analysis of composites [164], thermo-mechanical analysis of heterogeneous solids [151], micro-diffusive damage modeling with interface elements [143] and so on. Even though the generality of FE method facilitates application of such methods to complex problems with highly heterogeneous phase, high computational cost associated with solving a large set of nonlinear micromechanical boundary value problem (at every macro gauss point) impedes the use of FE^2 method for practical problems such as impact analysis. To an extent, such exorbitant computational cost can be addressed through parallel implementation [76]. Fritzen et al. developed a massively parallel GPU implementation of a hybrid computational homogenization method for visco-plastic materials using NVIDIA's CUDA framework [79]. An overall speedup in the order of 10^4 with respect to high-performance finite element implementation was achieved.

Reduced-order modeling is yet another powerful technique to scale down the dimensionality of problem using methods such as proper orthogonal decomposition (POD) and proper generalized decomposition (PGD) method [49, 140, 165, 168]. Especially, when implemented at the lower scales, such techniques can significantly boost the computational efficiency within a multiscale framework as well as increase the viability of large-scale problems. Chinesta et al. demonstrated that PGD method scales linearly with the dimension of the problem rather than exponentially-growing characteristics exhibited by mesh-based discretization methods [49]. Néron and Ladevèze integrated PGD techniques within the LATIN method for treating multiscale problems and showed significant gains in terms of computational cost and storage [140]. Recently, Radermacher et al. presented a new multiscale modeling technique FEPOD for non-linear analysis by embedding reduced RVE based on POD method into an FE-based macro-mechanical simulation [165]. Readers are referred to review paper by Kanouté et al. for a comprehensive review on recent developments within multiscale modeling techniques for composites [113].

Delamination modeling in composites

Delamination or interfacial cracking between plies is one of the most dominant forms of failure in laminated composites. It often arises due to unforeseen events such as runway debris impact or tool-drop during maintenance leading to barely visible damage [8, 205]. In addition, high inter-laminar stress leads to through-thickness failures owing to either high localized stress due to geometric (such as stiffener terminations, free-edges) or material discontinuity (such as ply drop-off) [205]. Since delamination can result in a significant altering of the load-bearing capacity of composite structures, especially under compression, understanding and predicting onset and propagation of delamination events in the early stages of design remains crucial.

Within the context of finite element method (FEM), cohesive zone based models are widely adopted for interface modeling in composites. Originally conceived by Dugdale [66] and Barenblatt [19], cohesive fracture concept assumes the existence of a zone around a crack tip which separates the undamaged and delaminated zones of the interface. Hillerborg et al. first introduced the concept of cohesive zone modeling within FEM by developing traction-separation law for estimating the strengths of unreinforced concrete beams [99]. Since then, several contributions addressing cohesive zone modeling technique have followed including application for ductile metals [138], bio-mechanics [51] and mixed-mode delamination in composites [15, 30, 128, 210]. Virtual Crack Closure Technique (VCCT) is yet another technique based on linear elastic fracture mechanics often introduced within the scheme of finite element method [172]. Although VCCT is a computationally effective approach, it is restricted to problems with a predefined initial crack [116].

Precursor to precise delamination analysis involves the accurate resolution of transverse stress-fields. At present, the standard approach involves usage of computationally intensive three-dimensional (3D) FE models or layer-wise two-dimensional (2D) FE models for accurate transverse stress-field predictions, thereby limiting their applicability at early design stages. In addition, cohesive-based finite element analysis incurs few shortcomings including the requirement of extremely refined mesh near the cohesive zone and convergence issues, specifically along the descending branch of the equilibrium path. Turon et al. proposed a set of engineering solutions to overcome some the issue pertaining to cohesive modeling within standard FEM context, including a closed-form expression for penalty stiffness estimation and estimation of cohesive strength based on mesh density [192]. The scalability of the proposed solution to large-scale progressive delamination problems was highlighted. Xie and Waas proposed a discrete cohesive zone model (DCZM) to effectively model delamination analysis [210], where DCZM

uses a rod-type element to enforce cohesive law, unlike the traditional continuum type cohesive elements. A class of finite element models within the scheme of isogeometric analysis using B-splines and NURBS (Non-uniform rational B-splines) are employed to model delamination analysis [103, 142, 145]. Nguyen and co-workers demonstrated the effectiveness and robustness of higher-order FEM built within the isogeometric framework for a variety of class of two- and three- dimensional delamination problems [142, 145].

Some of the attempts at resolving issues related to convergence include the introduction of viscous regularization technique [81] and developing new classes of solver such as arc-length based solvers, catering to the needs of fracture problems [12, 91]. Alfano and Crisfield introduced a new class of local arc-length method in combination with line search technique to significantly improve the robustness and efficiency FE delamination solutions [12]. A numerically efficient solver based on LaTIn-based domain decomposition method was successfully employed by Allix et al. for problems involving multiple simultaneous delamination [14]. A dissipation-based arc-length scheme was developed by Gutiérrez for robust simulation of fracture, where the arc-length constraint was based on the total energy-release rate [91]. Since the energy-dissipated is a global quantity, no a priori selection of zone or degree of freedom is required and the scheme provides stable convergence behavior [198]. The numerical scheme has been successfully adopted for delamination and multiscale analysis of heterogeneous structures [144, 145].

1.2 Outline

The thesis is broadly classified into three parts. Part I focuses on the formulation and implementation of CUF for nonlinear analysis. Micromechanical and multiscale models built within the scheme of 1D CUF is discussed in Part II. Novel numerical modeling of delamination and impact analysis of composites with CUF 1D models is presented in Part III.

Part I: Physically nonlinear unified formulation

Chapter 2 presents the higher-order one-dimensional models employed in this thesis work. One-dimensional models based on Carrera Unified Formulation is formulated within the finite element framework using the principle of virtual work. The capabilities of CUF 1D models are highlighted through numerical examples dealing with wave propagation and failure index evaluation of composite specimens. The chapter intends

to highlight the fundamentals of formulating the higher-order 1D models and their applicability for various classes of problems.

Chapter 3 intends to highlight the effectiveness of 1D CUF models to undertake physically nonlinear simulation. Isotropically work-hardening von-Mises constitutive model is incorporated within the 1D CUF framework to account for material nonlinearity. Numerical results for compact and thin-walled beam members in plastic regime is presented with displacement profiles and beam deformed configuration along with stress contour plots. The results are compared against classical beam models such as EBBT and TBT, reference solutions from literature and three-dimensional solid finite element solution.

Part II: Micromechanics and Multiscale

Chapter 4 presents a novel micromechanics platform formulated within the scheme of Carrera Unified Formulation to undertake linear and nonlinear analyses for various classes of representative volume elements (RVE) architectures. The ability of CUF-CW models to yield accurate local fields along with effective moduli prediction is demonstrated. The capability is extended to nonlinear analysis with integration of different nonlinear constitutive models including crack band for progressive failure analysis and shear driven plasticity model.

Chapter 5 introduces a computationally efficient concurrent multiscale platform to undertake linear and nonlinear analyses. The framework exploits the refined one-dimensional model based on CUF to model various components across multiple scales. The nonlinearity is introduced within individual constituents at the microscale and its effect is scaled up to the macroscale by means of homogenization. The efficiency of the framework is quantified through comparisons with the analysis time and memory requirement against traditional multiscale implementations.

Part III: Interface and Impact modeling

Chapter 6 presents a novel numerical framework to simulate progressive delamination in laminated structures based on component-wise models is presented. Formulated within the Lagrange polynomial based CUF models, Component-wise modeling approach permits modeling of various components of a complex structure through 1D

CUF models at a reduced computational cost. A class of higher-order cohesive elements is integrated within the CUF-CW framework to simulate interfacial cohesive mechanics between various components of the structure. A bilinear constitutive law based on mixed-mode delamination propagation is implemented. The approach makes use of the mixed-mode cohesive constitutive law and a global dissipation energy-based arc-length method to trace complex equilibrium path exhibited by delamination problem. The effectiveness and computational efficiency of CUF-CW models are highlighted through benchmark composite delamination problems and composite structures with multiple delamination fronts.

Chapter 7 presents an application of CUF 1D models for undertaking impact modeling. Formulation of boundary value problem and incorporation of contact modeling technique within CUF is briefly explained. The work considers normal, frictionless contact based on a node-to-node formulation and a penalty approach to enforce the constraints. Explicit time integration scheme is utilized to undertake initial assessment of the capabilities of CUF 1D models for impact simulation of elastic rods and wave propagation on impact in rectangular blocks.

Chapter 8 details summary, concluding remarks and future scope of work. Appendix A lists all the relevant contribution attributed to the thesis including journal publications and conference proceedings.

Part I

Physically nonlinear unified formulation

Chapter 2

Unified formulation

The chapter briefly introduces the higher-order one-dimensional models employed in this thesis work. One-dimensional based on Carrera Unified Formulation is formulated within the finite element framework using principal of virtual work. The capabilities of CUF 1D models are highlighted through numerical examples dealing with wave propagation and failure index evaluation of composite specimens. The chapter intends to highlight fundamentals of formulating the higher-order 1D models and their applicability for different kinds of problems.¹

2.1 Carrera Unified Formulation

The coordinate system adopted for a generic beam is depicted in Fig. 2.1. The cross-section Ω overlayed on the $x - z$ plane with the beam axis lying on along the y axis. A generalized three-dimensional displacement vector is defined as:

$$\mathbf{u}(x, y, z) = \{u_x \quad u_y \quad u_z\}^T \quad (2.1)$$

¹Parts of this chapter has been in published in the following journals:

1. Petrolo M., Kaleel I., Pietro G. D., Carrera E. (2018), "Wave propagation in compact, thin-walled, and layered beams using refined finite element model", International Journal for Computational Methods in Engineering Science and Mechanics 19(3): 207-220
2. de Miguel A.G., Kaleel I., Nagaraj M. H., Petrolo M. Pagani A., Carrera E. (2018), "Accurate evaluation of failure indices of composite layered structure via various FE models", Composite Science and Technology 167(2):174-189

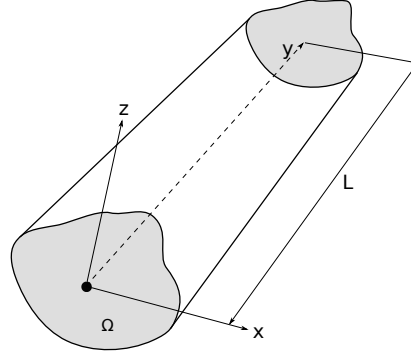


Fig. 2.1 Cartesian system for a generic beam

Carrera Unified Formulation (CUF) is hierarchical scheme that provide a structured basis to generate different classes of axiomatic structural theories [34]. Within one-dimensional CUF (1D CUF) introduced first by Carrera and Giunta [37], theories of structures are defined through the definition of cross-section expansion function $F_\tau(x, z)$:

$$\mathbf{u} = \mathbf{u}_\tau(y)F_\tau(x, z), \quad \forall \quad \tau = 1, \dots, M \quad (2.2)$$

where M is the number of terms in the expansion function and $\mathbf{u}_\tau(y)$ is the generalized displacement vector. Contrary to classical beam models such as EBBT and TBT, the choice of F_τ along with the number of terms M remains arbitrary and determines the theory of structure. Various classes of basis functions including polynomial, harmonic, trigonometric or exponential could be adopted as F_τ without any formal modification to the formulation [34]. Over the past decades, three classes of expansion functions are introduced within the context of 1D CUF, namely: (a) Taylor Expansions (TE) [37], (b) Lagrange Expansions [42] and (c) Hierarchical Legendre Expansion (HLE) [153]. Within the scope of current work, TE and LE models are widely adopted and described in detail in the upcoming section.

2.1.1 Taylor Expansion

Taylor Expansion functions are formulated by using McLaurin's polynomial of kind $x^i z^j$ as F_τ . Originally formulated by Carrera and Giunta [37], TE CUF models are hierarchical in nature with user input N determining the theory of structure. Table 2.1 tabulates the polynomial functions for different orders of TE models.

Table 2.1 Mac Laurin's polynomials for TE models

Order (N)	No. of terms (M)	Expansion function F_τ
TE1	3	$F_1 = 1, \quad F_2 = x, \quad F_3 = z$
TE2	6	$F_4 = x^2, \quad F_5 = xz, \quad F_6 = z^2$
TE3	10	$F_7 = x^3, \quad F_8 = x^2z, \quad F_9 = xz^2, \quad F_{10} = z^3$
...
TEN	$\frac{(N+1)(N+2)}{2}$	$F_{\frac{N^2+N+2}{2}} = x^N, \quad F_{\frac{N^2+N+4}{2}} = x^{N-1}z, \quad \dots, \quad F_{\frac{(N+1)(N+2)}{2}} = z^N$

Classical beam models such as EBBT and TBT can be obtained as special cases of TE1. For instance, kinematic field for TBT with 5 unknowns is expressed as:

$$u_x = u_{x1} \quad (2.3)$$

$$u_y = u_{y1} + xu_{y2} + zu_{y3} \quad (2.4)$$

$$u_z = u_{z1} \quad (2.5)$$

Detailed information on the formulation of TE models can be found in [37]

2.1.2 Lagrange Expansion

Lagrange expansions are formulated using Lagrange-type polynomial thereby circumventing some of the intrinsic limitations with TE models such as inclusion of higher-order terms, which lack physical meaning [42]. With the adoption of iso-parametric formulation, LE models can be employed to model arbitrary cross-sections and permits local refinement of kinematics in the region of interest as shown in Fig. 2.2(b). It is important to emphasize that the each unknown involved in LE model has a precise physical meaning as the unknowns are characterized with purely translational displacements, in contrast to TE models. In the original work by Petrolo and Carrera, three types of LE cross-section elements were introduced, namely (a) three-node L3, (b) four-node L4 and (c) nine-node L9 with linear, bi-linear and bi-quadratic displacement field approximation respectively [42].

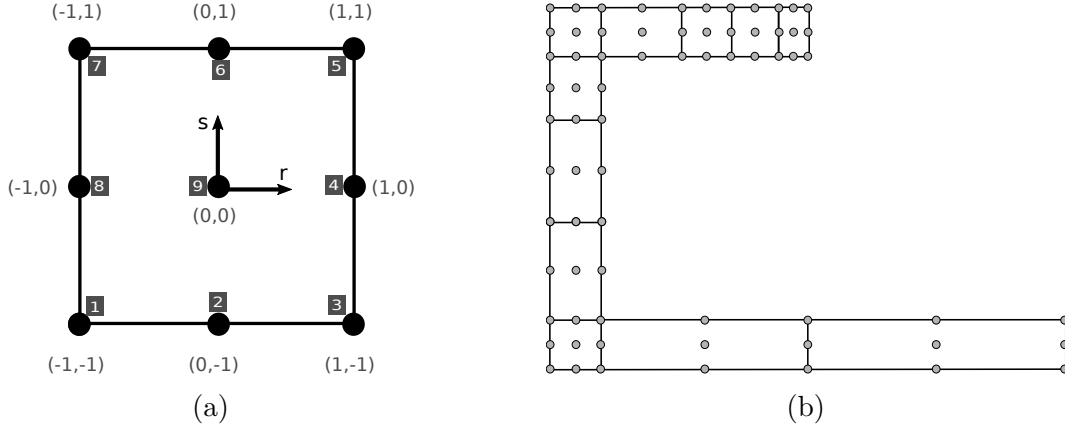


Fig. 2.2 CUF LE elements: (a) L9 cross-section elements and (b) piece-wise discretization of arbitray beam cross-section using L9 elements with local refinement on top flange

The kinematic field within an L9 cross-section element can be expressed as (see Fig. 2.2(a)):

$$\begin{aligned}
 u_x &= F_1 u_{x_1} + F_2 u_{x_2} + \dots + F_9 u_{x_9} \\
 u_y &= F_1 u_{y_1} + F_2 u_{y_2} + \dots + F_9 u_{y_9} \\
 u_z &= F_1 u_{z_1} + F_2 u_{z_2} + \dots + F_9 u_{z_9}
 \end{aligned} \tag{2.6}$$

where u_{i_1}, \dots, u_{i_9} denotes the nine translational displacement unknowns associated with L9 in direction i . The interpolation function for the L9 element is given by:

$$\begin{aligned}
 F_\tau &= \frac{1}{2}(r^2 + rr_\tau)(s^2 + ss_\tau) & \tau &= 1, 3, 5, 7 \\
 F_\tau &= \frac{1}{2}r_\tau^2(r^2 + rr_\tau)(1 - s^2) + \frac{1}{2}s_\tau^2(s^2 + ss_\tau)(1 - r^2) & \tau &= 2, 4, 6, 8 \\
 F_\tau &= (1 - r^2)(1 - s^2) & \tau &= 9
 \end{aligned} \tag{2.7}$$

where r_τ and s_τ are the coordinates of nine nodes of L9 element as depicted in Fig. 2.2(a) and the value of r and s vary from -1 to $+1$. In addition, LE models facilitate integration of various classes of variable kinematic models – one-, two- and three-dimensional models – as kinematic congruence can easily be guaranteed across the interfaces of elements with different kinematics without any ad-hoc mathematical manipulations [214].

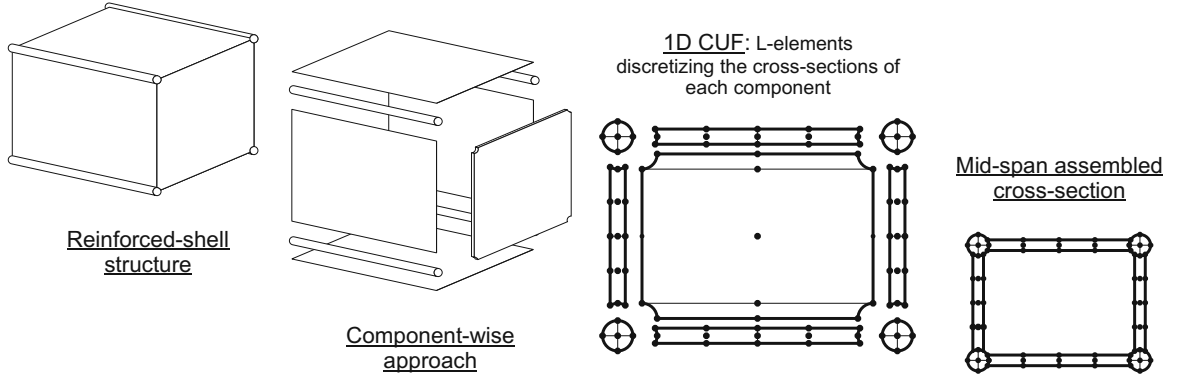


Fig. 2.3 Illustration of CW modeling technique for reinforced shell structure [40]

Component-Wise modeling

Component-Wise (CW) approach is an application of LE based CUF models that allows modeling of multi-component structures through a compact and unique 1D formulation [39, 40]. CW approach facilitates the usage of 1D FE model for various component of a multi-component structure. Figure 2.3 illustrates the CW modeling approach utilized to model a reinforced shell element [40]. Various component of the reinforced-shell including panels and ribs are degenerated into individual 1D finite element. By superimposing the cross-sectional nodes along the interfaces, compatibilities across various components can be enforced. CW approach also enables local tuning of kinematics of components of interest. Since the mathematical models are built using physical boundaries, artificial reference geometric features such as lines for beam axis and surfaces for plate/shell can be omitted. Figure 2.4 depicts the application of CW approach for analysis of composite structures across different scales.

2.2 Finite Element Formulation of 1D CUF

2.2.1 Preliminaries

The strain and stress vectors are expressed as:

$$\boldsymbol{\sigma} = \{\sigma_{xx} \ \sigma_{yy} \ \sigma_{zz} \ \sigma_{yz} \ \sigma_{xz} \ \sigma_{xy}\}^T, \quad \boldsymbol{\epsilon} = \{\epsilon_{xx} \ \epsilon_{yy} \ \epsilon_{zz} \ 2\epsilon_{yz} \ 2\epsilon_{xz} \ 2\epsilon_{xy}\}^T \quad (2.8)$$

Under small strain assumptions, the linear strain-displacement relationship is given by:

$$\boldsymbol{\epsilon} = \mathbf{D} \mathbf{u} \quad (2.9)$$

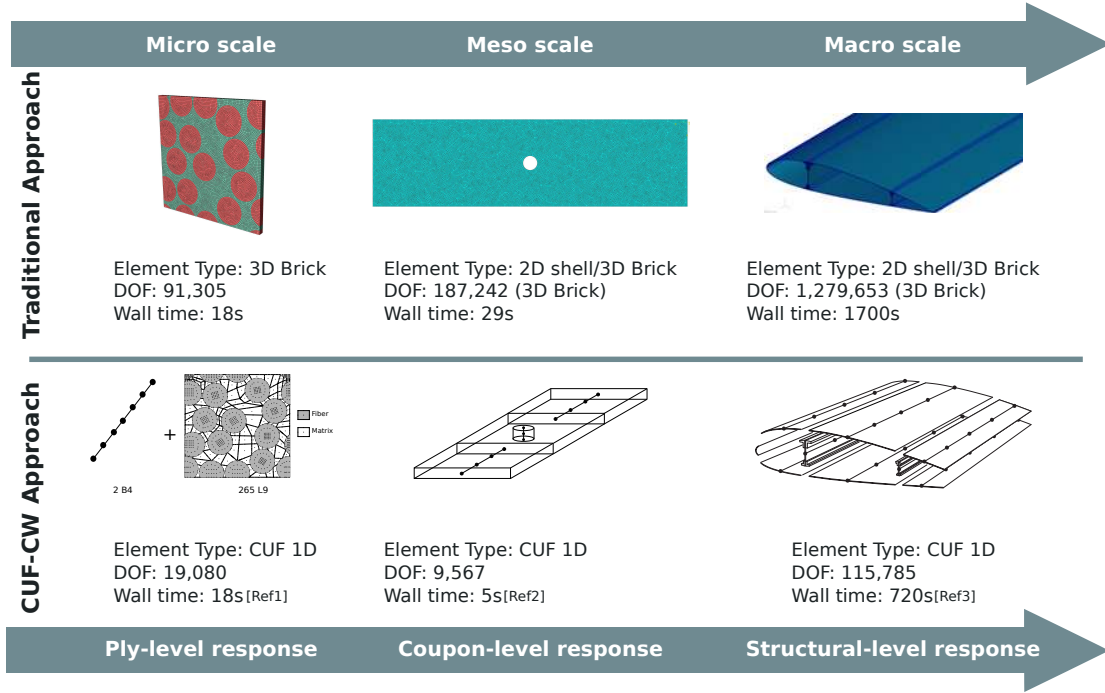


Fig. 2.4 CW modeling adopted for linear static analysis of composites across different scales along with comparison against traditional methods (Ref1 [111], Ref2 [60], Ref3 [40])

where \mathbf{D} is the linear differential operator on displacement vector \mathbf{u} and is given by:

$$\mathbf{D} = \begin{bmatrix} \partial_x & 0 & 0 \\ 0 & \partial_y & 0 \\ 0 & 0 & \partial_z \\ 0 & \partial_z & \partial_y \\ \partial_z & 0 & \partial_x \\ \partial_y & \partial_x & 0 \end{bmatrix} \quad (2.10)$$

$$\partial_x = \frac{\partial(\cdot)}{\partial_x}, \quad \partial_y = \frac{\partial(\cdot)}{\partial_y}, \quad \partial_z = \frac{\partial(\cdot)}{\partial_z} \quad (2.11)$$

By introducing a 6×6 generic constitutive matrix $\tilde{\mathbf{C}}$ with 36 non-zero constants, the stress-strain behavior can be expressed as:

$$\boldsymbol{\sigma} = \tilde{\mathbf{C}}\boldsymbol{\epsilon} \quad (2.12)$$

By adopting conventional finite element approach, the beam axis along y-axis is discretized into discrete number of finite elements. Therefore, the displacement field in

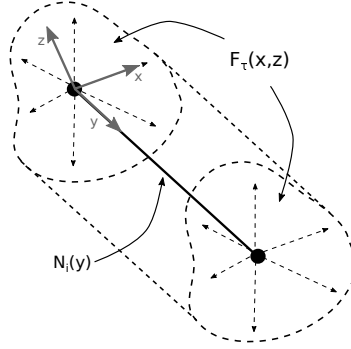


Fig. 2.5 Representation of 1D CUF finite element

Eqn. 2.1 can be reformulated as:

$$\mathbf{u}(x, y, z) = F_\tau(x, z)N_i(y)\mathbf{u}_{\tau i} \quad \forall \quad \tau = 1, \dots, M \quad i = 1, \dots, p+1 \quad (2.13)$$

where N_i stands for i^{th} shape function of order p and $\mathbf{u}_{\tau i}$ denotes generic nodal displacement vector:

$$\mathbf{u}_{\tau i} = [u_{x_{\tau i}} \ u_{y_{\tau i}} \ u_{z_{\tau i}}]^T \quad (2.14)$$

Figure 2.5 depicts a 1D CUF finite element with shape function $N_i(y)$ along the beam axis in y direction and expansion function $F_\tau(x, z)$ overlayed on $x - z$ plane. It is important to emphasize the fact that choice of FE shape function N_i remains independent of kind of expansion function F_τ employed. Standard Lagrange polynomials are adopted as shape functions. Three types of 1D finite elements are extensively adopted in this work, namely (a) two-node B2, (b) three-node B3 and (c) four-node B4 corresponding to linear, quadratic and cubic approximations respectively. The shape functions along with the location of their i^{th} node are expressed as [20]:

B2:

$$\left. \begin{aligned} N_1 &= \frac{1}{2}(1 - \xi) \\ N_2 &= \frac{1}{2}(1 + \xi) \end{aligned} \right\} \begin{aligned} \xi_1 &= -1 \\ \xi_2 &= 1 \end{aligned}$$

B3:

$$\left. \begin{aligned} N_1 &= \frac{1}{2}\xi(1 - \xi) \\ N_2 &= -(1 - \xi)(1 + \xi) \\ N_3 &= \frac{1}{2}\xi(1 + \xi) \end{aligned} \right\} \begin{aligned} \xi_1 &= -1 \\ \xi_2 &= 0 \\ \xi_3 &= 1 \end{aligned} \quad (2.15)$$

B4:

$$\left. \begin{aligned} N_1 &= -\frac{9}{16}(\xi + \frac{1}{3})(\xi - \frac{1}{3})(\xi - 1) \\ N_2 &= \frac{27}{16}(\xi - 1)(\xi - \frac{1}{3})(\xi + 1) \\ N_3 &= -\frac{27}{16}(\xi + 1)(\xi + \frac{1}{3})(\xi - 1) \\ N_4 &= \frac{9}{16}(\xi + \frac{1}{3})(\xi - \frac{1}{3})(\xi + 1) \end{aligned} \right\} \begin{aligned} \xi_1 &= -1 \\ \xi_2 &= -1/3 \\ \xi_3 &= 1/3 \\ \xi_4 &= 1 \end{aligned}$$

2.2.2 Weak formulation of 1D CUF

Consider a domain Ω with essential boundary conditions acting along the boundary Γ_u and traction t_i prescribed along Γ_n . The equilibrium equation for the balance of linear momentum leads to:

$$\sigma_{ij,j} + b_i = \rho \ddot{u}_i, \quad \forall \quad i, j = 1, 2, 3 \quad (2.16)$$

$$\text{with } t_i = \sigma_{ij} n_j \quad \text{in } \Gamma_n \quad (2.17)$$

where σ_{ij} refers to the components of Cauchy stress, ρ denotes the mass density, b_i are body force components and \ddot{u} denotes the second partial derivative of displacement with respect to time. Displacement-based finite element solutions are often formulated on the basis of Principle of Virtual Displacement (PVD) which states that for any imposed virtual displacement on a body in a state of equilibrium, the total internal virtual work equals the total external virtual work [20]:

$$\underbrace{\int_{\Omega} \delta u_i \rho \ddot{u}_i d\Omega}_{\delta L_{ine}} + \underbrace{\int_{\Omega} \delta \epsilon_{ij} \sigma_{ij} d\Omega}_{\delta L_{int}} - \underbrace{\int_{\Omega} \delta u_i b_i d\Omega - \int_{\Gamma_t} \delta u_i t_i d\Gamma}_{\delta L_{ext}} = 0 \quad (2.18)$$

where δ stands for the virtual variation and L_{int} , L_{ext} and L_{ine} stands for internal strain energy, work done by the external loads and work due to inertial loading respectively. The virtual variation of strain energy in the matrix form can be expressed as:

$$\delta L_{int} = \int_V \delta \epsilon \boldsymbol{\sigma} dV \quad (2.19)$$

$$= \int_V \delta \epsilon \tilde{\mathbf{C}} \epsilon dV \quad (2.20)$$

The strain-displacement relationship expressed in Eqn. 2.9 is reformulated using Eqn. 2.13:

$$\boldsymbol{\epsilon} = \mathbf{D}_{\tau i} \mathbf{u}_{\tau i} \quad \mathbf{D}_{\tau i} = \begin{bmatrix} N_i F_{\tau,x} & 0 & 0 \\ 0 & N_{i,y} F_{\tau} & 0 \\ 0 & 0 & N_i F_{\tau,z} \\ 0 & N_i F_{\tau,z} & N_{i,y} F_{\tau} \\ N_i F_{\tau,z} & 0 & N_i F_{\tau,x} \\ N_{i,y} F_{\tau} & N_i F_{\tau,x} & 0 \end{bmatrix} \quad (2.21)$$

Analogously, the virtual variation of strain vector can be expressed in terms of virtual variation of nodal unknowns \mathbf{u}_{sj} :

$$\delta \boldsymbol{\epsilon} = \mathbf{D}_{sj} \delta \mathbf{u}_{sj} \quad (2.22)$$

with

$$\delta \mathbf{u}(x, y, z; t) = F_s(x, z) N_i(y) \delta \mathbf{u}_{sj}(t) \quad \forall \quad s = 1, \dots, M \quad j = 1, \dots, p+1 \quad (2.23)$$

Therefore, the virtual variation of strain energy can be reformulated as:

$$\delta L_{int} = \delta \mathbf{u}_{sj} \int_V \left\{ \mathbf{D}_{sj}^T \tilde{\mathbf{C}} \mathbf{D}_{\tau i} dV \right\} \mathbf{u}_{\tau i} \quad (2.24)$$

$$= \delta \mathbf{u}_{sj} \mathbf{k}_{\tau sij} \mathbf{u}_{\tau i} \quad (2.25)$$

where $\mathbf{k}_{ij\tau s}$ is termed as the Fundamental Nucleus (FN) of the structural stiffness for 1D CUF FE model. The nucleus is a matrix of dimension 3×3 of the form:

$$\mathbf{k}_{\tau sij} = \begin{bmatrix} k_{\tau sij}^{xx} & k_{\tau sij}^{xy} & k_{\tau sij}^{xz} \\ k_{\tau sij}^{yx} & k_{\tau sij}^{yy} & k_{\tau sij}^{yz} \\ k_{\tau sij}^{zx} & k_{\tau sij}^{zy} & k_{\tau sij}^{zz} \end{bmatrix} \quad (2.26)$$

The expansion of indices i, j, τ, s leads to construction of structural stiffness matrix of a single 1D CUF finite element. Diagonal and off-diagonal terms have recurrent expressions stemming from the following:

$$\begin{aligned} k_{\tau sij}^{xx} &= (\tilde{C}_{11} F_{s,x} N_j + \tilde{C}_{51} F_{s,z} N_j + \tilde{C}_{61} F_s N_{j,y}) F_{\tau,x} N_i + (\tilde{C}_{15} F_{s,x} N_j + \tilde{C}_{55} F_{s,z} N_j + \tilde{C}_{65} F_s N_{j,y}) F_{\tau,z} N_i + (\tilde{C}_{16} F_{s,x} N_j + \tilde{C}_{56} F_{s,z} N_j + \tilde{C}_{66} F_s N_{j,y}) F_{\tau} N_{i,y} \\ k_{\tau sij}^{xy} &= (\tilde{C}_{12} F_{s,x} N_j + \tilde{C}_{52} F_{s,z} N_j + \tilde{C}_{62} F_s N_{j,y}) F_{\tau} N_{i,y} + (\tilde{C}_{14} F_{s,x} N_j + \tilde{C}_{54} F_{s,z} N_j + \tilde{C}_{64} F_s N_{j,y}) F_{\tau,z} N_i + (\tilde{C}_{16} F_{s,x} N_j + \tilde{C}_{56} F_{s,z} N_j + \tilde{C}_{66} F_s N_{j,y}) F_{\tau,x} N_i \end{aligned} \quad (2.29)$$

In matrix notation, the expression for virtual variation of work due to inertial loading reads:

$$\delta L_{ine} = \int_V \delta \mathbf{u} \rho \ddot{\mathbf{u}} dV \quad (2.30)$$

Recalling the 1D CUF FE kinematic approximation in Eqn. 2.13, the nodal accelerator vector can be expressed as:

$$\ddot{\mathbf{u}}(x, y, z; t) = F_\tau(x, z) N_i(y) \ddot{\mathbf{u}}_{\tau i}(t) \quad \forall \quad \tau = 1, \dots, M \quad i = 1, \dots, p+1 \quad (2.31)$$

$\ddot{\mathbf{u}}_{\tau i}$ denotes generic nodal displacement vector at given instance of time t . Therefore, the δL_{ine} can be rewritten as:

$$\delta L_{ine} = \delta \mathbf{u}_{sj} \int_V \{N_j F_s \rho \mathbf{I} N_i F_\tau dV\} \ddot{\mathbf{u}}_{\tau i} \quad (2.32)$$

$$= \delta \mathbf{u}_{sj} \mathbf{m}_{\tau sij} \ddot{\mathbf{u}}_{\tau i} \quad (2.33)$$

where \mathbf{I} is the 3×3 identity matrix and $\mathbf{m}_{\tau sij}$ is the fundamental nuclei of the mass matrix for 1D CUF FE model. Analogous to the structural FN, nucleus is a matrix of dimension 3×3 and the complete mass matrix for a 1D CUF finite element can be built by expanding the indices i, j, τ, s . The virtual variation of external work holds

$$\delta L_{ext} = \int_V \delta \mathbf{u}^T \mathbf{g} dV + \int_S \delta \mathbf{u}^T \mathbf{q} dS + \int_l \delta \mathbf{u}^T \mathbf{r} dl + \delta \mathbf{u}^T P_m \quad (2.34)$$

where \mathbf{g} , \mathbf{q} , \mathbf{r} and P_m are body forces per unit volume, surface forces per unit area, line forces per unit line and concentrated force acting at point m respectively. Accounting for Eqn 2.23, the work due to external loading δL_{ext} can be expressed as:

$$\delta L_{ext} = \delta \mathbf{u}_{sj} \left\{ \int_V N_j F_s \mathbf{g} dV + \int_S N_j F_s \mathbf{q} dS + \int_l N_j F_s \mathbf{r} dl + N_j F_s P_m \right\} \quad (2.35)$$

$$= \delta \mathbf{u}_{sj} \mathbf{p}_{sj} \quad (2.36)$$

Detailed information on the derivation of various types of external loadings can found in [193].

The fundamental nuclei formulated is an invariant, i.e formal expressions in the nucleus remains the same irrespective of the choice of shape function or expansion function. For an assembly of generic, arbitrary higher-order beam elements of order p and expansion function with M terms, the global assembly is achieved by expanding

indices of FNs $\tau, s = 1, 2, \dots, M$ and $i, j = 1, 2, \dots, p+1$:

$$\mathbf{K}_{\tau sij} = \sum_{n=1}^{n_{elem}} \sum_{i,j=1}^{p+1} \bigcup_{\tau,s=1}^M \mathbf{k}_{\tau sij} \quad (2.37)$$

$$\mathbf{M}_{\tau sij} = \sum_{n=1}^{n_{elem}} \sum_{i,j=1}^{p+1} \bigcup_{\tau,s=1}^M \mathbf{m}_{\tau sij} \quad (2.38)$$

$$\mathbf{p}_{sj} = \sum_{n=1}^{n_{elem}} \sum_{j=1}^{p+1} \bigcup_{s=1}^M \mathbf{p}_{sj} \quad (2.39)$$

where operator \sum is the finite element assembly operator that sum the corresponding contribution from n_{elem} elements for a given shared degrees of freedom, operator \bigcup is the CUF assembly operator which sums the corresponding contribution based on order of FE and the theory of structure and array $\mathbf{K}_{\tau sij}$, $\mathbf{M}_{\tau sij}$ and $\mathbf{p}_{\tau i}$ are the global assembled stiffness matrix, global mass matrix and global external load vector respectively. Graphical illustration of assembly process is depicted in Fig. 2.6 where fundamental nucleus forms the building block, loop through expansion function indices τ and s leads to a matrix for a given pair of FEM indices i and j , loop through FEM indices of i and j leads to matrix of a given FEM element and loop through all the FEM elements leads to global assembled matrix. Detailed information on the assembly procedure can be found in the book by Carrera et al. [34].

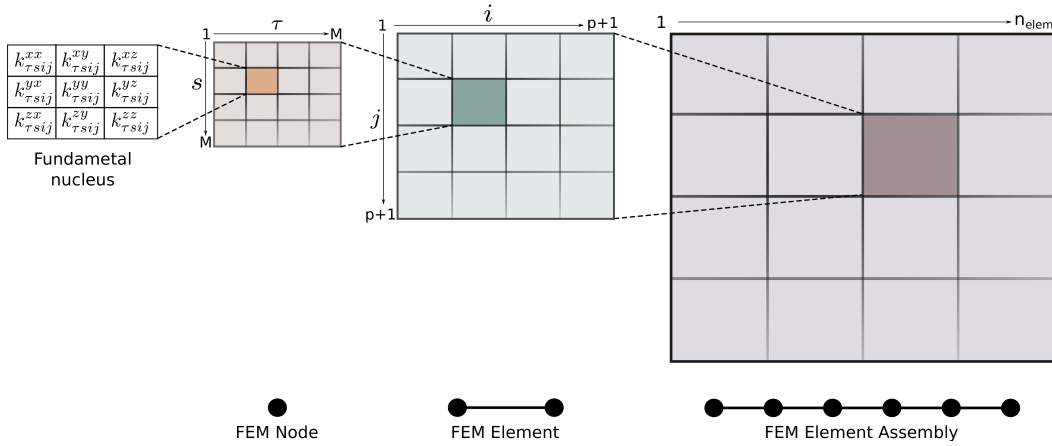


Fig. 2.6 Illustration of assembly process using fundamental nuclei within CUF [34]

2.2.3 Governing Equation

Recalling the weak form of equilibrium equation from Eqn. 2.18:

$$\delta L_{ine} + \delta L_{int} - \delta L_{ext} = 0 \quad (2.40)$$

Introducing fundamental nuclei of structural stiffness matrix (Eqn. 2.24), mass matrix (Eqn. 2.32) and vector of external loadings (Eqn. 2.35) into Eqn. 2.40:

$$\delta \mathbf{u}_{sj} \mathbf{m}_{\tau sij} \ddot{\mathbf{u}}_{\tau i} + \delta \mathbf{u}_{sj} \mathbf{k}_{\tau sij} \mathbf{u}_{\tau i} - \delta \mathbf{u}_{sj} \mathbf{p}_{sj} = 0 \quad (2.41)$$

$$\delta \mathbf{u}_{sj} \{ \mathbf{m}_{\tau sij} \ddot{\mathbf{u}}_{\tau i} + \mathbf{k}_{\tau sij} \mathbf{u}_{\tau i} - \mathbf{p}_{sj} = 0 \} \quad (2.42)$$

$$\forall \quad i, j = 1, \dots, p+1 \quad \tau, s = 1, \dots, M \quad (2.43)$$

Using the global assembled finite element matrix defined in Eqn. 2.37, the compact form of governing equation can be expressed as:

$$\mathbf{M}_{\tau sij} \ddot{\mathbf{u}}_{\tau i} + \mathbf{K}_{\tau sij} \mathbf{u}_{\tau i} = \mathbf{P}_{sj} \quad (2.44)$$

It is important to emphasis the fact that compact formulation expressed in Eqn. 2.44 are invariant to the choice of shape function as well as cross-section expansion functions. Therefore, same numerical implementation can yield a class of structural theories where the choice of expansion function is a free parameter.

Nonlinear incremental quasi-static solver

Within the context of quasi-static nonlinear FEM, the incremental form of equilibrium equation is formulated by neglecting the inertia terms:

$$\mathbf{f}_{int}(\mathbf{u}) - \mathbf{p} = 0 \quad (2.45)$$

where \mathbf{f}_{int} is the global vector of internal force which depends on the global unknowns vector \mathbf{u} and \mathbf{f}_{ext} stands for global external force vector. Using the notation introduced for 1D CUF finite elements in Section 2.2.2, the compact form of Eqn. 2.45 using CUF fundamental nuclei can be expressed as:

$$\mathbf{k}_{\tau sij}^s \mathbf{u}_{\tau i} - \mathbf{p}_{sj} = 0 \quad (2.46)$$

where $\mathbf{k}_{\tau sij}^s$ denotes the fundamental nuclei of secant stiffness matrix obtained using secant material matrix in Eqn. 2.24. Therefore, the compact form of the nonlinear

governing equation can be expressed as:

$$\mathbf{K}_{\tau sij}^s \mathbf{u}_{\tau i} = \mathbf{P}_{sj} \quad (2.47)$$

The incremental finite element scheme is realized through parametrization of external loading by introducing load factor λ (see Fig. 2.7(a)):

$$\mathbf{f}_{int}(\mathbf{u}) - \lambda_n \mathbf{p} = 0 \quad (2.48)$$

where λ_n refers to the prescribed load factor at time instance t_n . Newton-Raphson (N-R) scheme is adopted to obtain step-wise solution from an equilibrium point n to $n + 1$. Using the solution vector at time instance t_{n+1} , the Taylor series expansion of

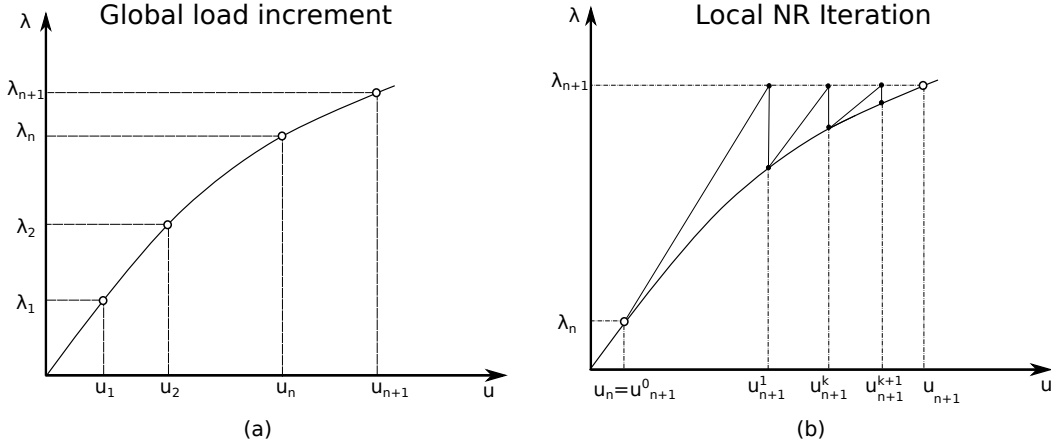


Fig. 2.7 One-dimensional representation of Newton-Raphson iteration with load control: (a) Parametrization of external loading and (c) local iterations within each load increment

internal force vector is given by [20]:

$$\mathbf{f}_{int}(\mathbf{u}_{n+1}^{k+1}) = \mathbf{f}_{int}(\mathbf{u}_{n+1}^k) + \frac{\partial \mathbf{f}_{int}(\mathbf{u}_{n+1}^k)}{\partial \mathbf{u}_{n+1}^k} (\mathbf{u}_{n+1}^{k+1} - \mathbf{u}_{n+1}^k) + \frac{1}{2} \frac{\partial^2 \mathbf{f}_{int}(\mathbf{u}_{n+1}^k)}{\partial \mathbf{u}_{n+1}^{k2}} (\mathbf{u}_{n+1}^{k+1} - \mathbf{u}_{n+1}^k)^2 + \dots \quad (2.49)$$

where k denotes the iteration index for the current increment. By truncating the Taylor series expansion at linear term, N-R scheme for linearized incremental equilibrium equation can be formulated:

$$\mathbf{f}_{int}(\mathbf{u}_{n+1}^{k+1}) = \mathbf{f}_{int}(\mathbf{u}_{n+1}^k) + \underbrace{\frac{\partial \mathbf{f}_{int}(\mathbf{u}_{n+1}^k)}{\partial \mathbf{u}_{n+1}^k}}_{\mathbf{K}^T} \Delta \mathbf{u}; \quad \Delta \mathbf{u} = \mathbf{u}_{n+1}^{k+1} - \mathbf{u}_{n+1}^k \quad (2.50)$$

where $\Delta \mathbf{u}$ is the incremental displacement for a given iteration and \mathbf{K}^T refers to tangent stiffness matrix obtained by taking partial derivative of current internal force with respect to current solution. Compact form of Eqn. 2.50 using CUF matrix notations can be expressed as:

$$\phi_{sj}^{res} = \mathbf{K}_{\tau sij}^T \Delta \mathbf{u}_{\tau i} \quad (2.51)$$

where $\mathbf{K}_{\tau sij}^T$ refers to global tangent stiffness nucleus and ϕ_{sj}^{res} denotes the residual nodal vector of unbalanced forces. As illustrated in Fig. 2.7(b), a new tangent matrix computed at each iteration. In order to achieve asymptotic quadratic convergence exhibited by N-R methods, exact computation of tangent stiffness matrix is crucial. Since current work is limited to physically nonlinear problems, formulation of tangent stiffness nucleus is reduced to obtaining material tangent matrix.

The effectiveness of an incremental solution methods relies on robust and realistic termination criteria. A loose convergence criteria can yield inaccurate results whereas tight convergence criteria can lead to very high computational cost due to increased number of additional iterations. A displacement-based convergence criteria is set:

$$\frac{\|\Delta \mathbf{u}_{n+1}^k\|_2}{\|\mathbf{u}_{n+1}\|_2} \leq TOL \quad (2.52)$$

Dynamic response

Introducing damping contribution into the governing equation (Eqn. 2.44), the equation of motion for dynamic analysis yields:

$$\mathbf{M}_{\tau sij} \ddot{\mathbf{u}}_{\tau i} + \mathbf{C}_{\tau sij} \dot{\mathbf{u}}_{\tau i} + \mathbf{K}_{\tau sij} \mathbf{u}_{\tau i} = \mathbf{P}_{sj} \quad (2.53)$$

where $\dot{\mathbf{u}}_{\tau i}$ refers to the nodal velocity vector and the global damping matrix $\mathbf{C}_{\tau sij}$ is formulated using Rayleigh damping coefficients γ and β as:

$$\mathbf{C}_{\tau sij} = \gamma \mathbf{M}_{\tau sij} + \beta \mathbf{K}_{\tau sij} \quad (2.54)$$

Two classes of solution methods are widely adopted to solve the system of linear differential equation of second order:

1. Direct method

Direct method are characterized with no a priori transformation of equation to different forms with integration of the governing equation using a step-by-step numerical scheme, for instance Central difference scheme (CDS), Newmark scheme

and Houbolt method. The equilibrium equation (2.53) is satisfied at discrete time intervals within the solution interval. Two types of time integration operators are comprised within direct time integration method, namely (a) Implicit and (b) Explicit. The fundamental difference between the operators is that the former computes the current solution based on current as well as previous known solution states whereas the latter computes the new solution purely based on the known quantities. Implicit schemes such as Newmark method are characterized as unconditionally stable thereby allowing large time steps but requires an iterative scheme along with factorization of assembled global matrices at every time step. Explicit scheme such as CDS method are characterized as conditionally stable and the adopted time step size can effect the stability and lead to spurious oscillation. Popularity of explicit schemes can be attributed to the computational efficiency of the method as the computation operations are limited to basic mathematical matrix-vector operations unlike implicit methods.

2. Mode superposition

Mode superposition method involves solving the equilibrium equation by transforming the unknown vector using a finite number of eigen modes. In direct method, the computational cost associated with the solution is directly dependent on the total number of time steps and their effectiveness deteriorates as the system of equation grows larger. Even though mode superposition methods are very powerful, their application is limited to loadings with low frequency contents [20].

Dynamic response analysis for different classes of structures using CUF framework have been widely studied in the past. Carrera and Varello investigated the accuracy of variable kinematic CUF models for compact and thin-walled structures with dynamic loading by employing implicit Newmark scheme [43]. Pagani et al. investigated dynamic response of typical aerospace structure using mode-superposition method within CUF framework [154]. In this work, an explicit time integration method based on the Tchamwa-Wielgosz (TW) scheme, an extension of central difference scheme through introduction of additional damping terms [122]. Finite element solution involving high frequency loading such as wave propagation or impact analysis often exhibits spurious oscillation due to spatial and temporal dispersion error [21, 122, 146]. Some of the attempts at reducing such dispersion error involves introduction of lumped mass matrices [208], adoption of higher-order FE [132], filtering of spurious modes [102] and employing numerical dissipation in time integration scheme such as bulk viscosity

method (BVM) [24] and TW scheme [122]. Since higher-order formulation within CUF naturally addresses the spatial dispersion error, dissipative explicit method based on TW scheme is adopted and can be expressed as follows (for sake of brevity, indices are excluded):

$$\begin{aligned} \mathbf{U}_{t+\Delta t} &= \mathbf{U}_t + \Delta t \dot{\mathbf{U}}_t + \phi \Delta t^2 \ddot{\mathbf{U}}_t \\ \dot{\mathbf{U}}_{t+\Delta t} &= \dot{\mathbf{U}}_t + \frac{1}{2} \Delta t \ddot{\mathbf{U}}_t \\ \ddot{\mathbf{U}}_{t+\Delta t} &= \mathbf{M}^{-1} [\mathbf{F}_{t+\Delta t}^{ext} - \mathbf{C} \dot{\mathbf{U}}_{t+\Delta t} - \mathbf{K} \mathbf{U}_{t+\Delta t}] \end{aligned} \quad (2.55)$$

where Δt is the time increment and the parameter ϕ controls the damping efficiency of the scheme. Since closed-form expression are not readily available to compute critical time step for higher-order finite elements, power iteration is used to compute the highest-frequency ω_n of the system [134]. Therefore, the critical time step size is defined as:

$$\Delta t_{cr} = \frac{2}{\omega_n} \quad (2.56)$$

2.3 Numerical cases

2.3.1 One-dimensional stress wave propagation

The accuracy and stability of the CUF 1D formulation to undertake linear dynamic problem is analyzed by modeling the classic 1D stress wave problem. The 1D numerical case is commonly adopted in the literature to validating and benchmarking new numerical frameworks as analytical solutions are available [122, 146]. An isotropic beam with a square cross-section of 0.2 m and length of 5.0 m is considered. The Young's modulus (E) of beam is taken as 207 GPa with a Poisson's ratio of zero and density (ρ) of 7800 kgm⁻³ is assumed. Figure 2.8 depicts the geometry and boundary conditions of the problem. A pulse load $p_0 = 0.1$ MPa was applied for a duration from 0 (t_0) - 0.19 (t_1) ms.

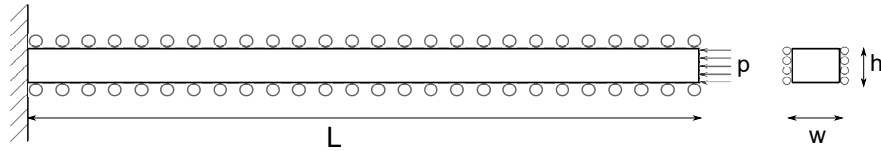


Fig. 2.8 Geometry and boundary conditions for 1D stress wave problem

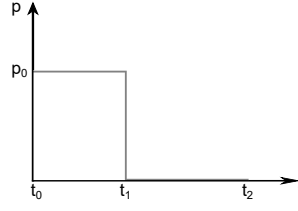


Fig. 2.9 Time history of loading for 1D stress wave problem

A cross-section model with 1L9 element is associated to the beam assembly with a varying number of B4 elements. An explicit Tchamma-Wielgosz numerical scheme is employed to run the analysis for a duration of 1.2 ms. The damping parameter ϕ is set as 1.013. In addition, stiffness proportional damping is also introduced into the system. A similar model is developed in ABAQUS using 250 linear brick element with a BVM based explicit scheme for time integration.

For a 1D wave propagation problem, the governing wave equation reads:

$$\frac{\partial^2 u}{\partial y^2} = \frac{1}{c_0^2} \frac{\partial^2 u}{\partial t^2}, \quad c_0 = \sqrt{\frac{E}{\rho}} \quad (2.57)$$

where c_0 denotes the wave speed of the material. Using the method of d'Alembert, solution for the wave equation can be written as:

$$u(y, t) = f(y - c_0 t) + g(y + c_0 t) \quad (2.58)$$

where f and g are arbitrary functions representing right-traveling and left-traveling waves, respectively [88]. The solution obtained using CUF models are compared against analytical and ABAQUS results. Figure 2.10 compares the stress and velocity distribution along the axis of the beam at various time instances obtained using CUF-CW model with 70B4 elements against analytical and ABAQUS solution. The contour plot stress wave (σ_{yy}) at various time instances for CUF-CW model with 70B4 element is depicted in Fig. 2.11. The effect of mesh density along the axis on the stress distribution is studied in Fig. 2.12.

Following observations can be drawn:

1. CUF models are able to capture the wave propagation with great accuracy
2. As the mesh density is increased, the spurious oscillations are easily mitigated, even at the reflected wave front

3. From Fig. 2.12, it is evident that the dispersion error gets almost nullified with 70 B4 elements along the beam axis whereas ABAQUS models required 250 elements.

2.3.2 Failure index evaluation of a notched composite specimen

The numerical example focuses on the importance of accurate stress fields for evaluating failure indices. A rectangular plate with a hole under axial displacement is investigated. Three sets of lamination sequences are considered: (a) [0], (b) [90] and (c) [0/90]_s. Figure 2.13 depicts the geometry and boundary condition of the notched specimen.

Figure 2.14 illustrates the CW modeling technique employed to model the CUF-LW notched specimen as a three-component beam assembly. In order to compare the accuracy of the obtained results, various 3D FEM models based on standard 3D brick elements with varying mesh density is built using ABAQUS. Information regarding the mesh configuration along with the problem size and analysis time is tabulated in Table 2.2. The far-notch beam configuration is modeled with a combination of B4 beam elements along with L9 cross-section elements, where the beam is oriented in the y-direction. Each far-notch zone spans 49 mm in length. A combination of B3 beam elements along with L9 elements is employed to model the near-notch region. Since CW models contain only displacement unknowns, various components can be easily interfaced. Detailed information on the integration of 1-, 2- and 3-dimensional refined models within the CUF framework can be found in the [214].

Hashin 3D failure criteria is employed to evaluate intra-laminar failure indices with 1- denoting the fiber direction and 2-3 represents the transverse directions of the ply [93]:

1. Fibre Tension:

$$\left(\frac{\sigma_{11}^2}{X_T^2}\right)^2 + \frac{\sigma_{12}^2 + \sigma_{13}^2}{S_{12}^2} \geq 1 \quad (2.59)$$

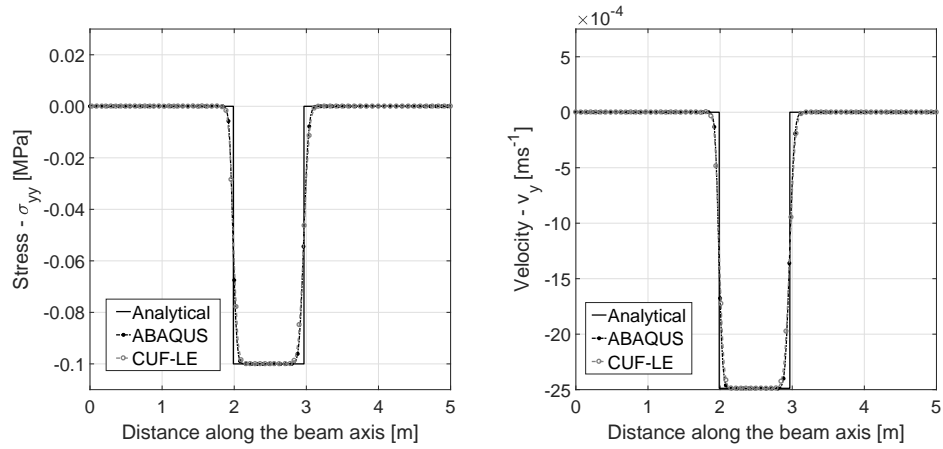
2. Fibre Compression:

$$\left(\frac{\sigma_{11}^2}{X_C^2}\right)^2 \geq 1 \quad (2.60)$$

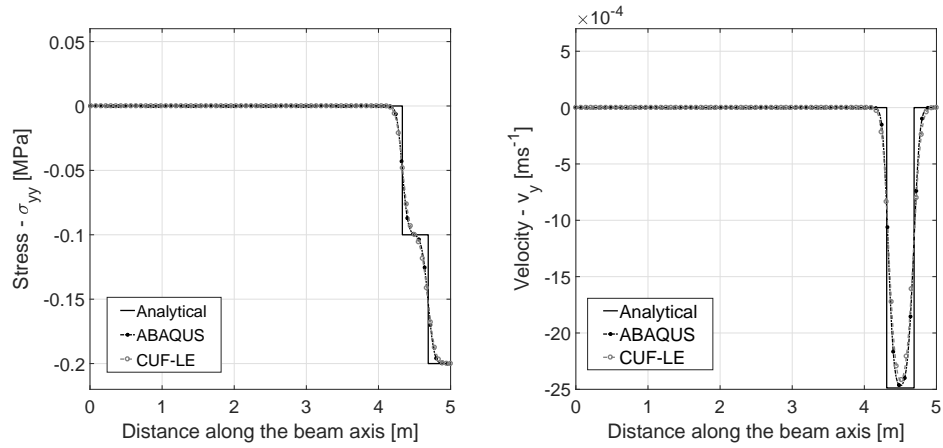
3. Matrix Tension:

$$\frac{(\sigma_{22} + \sigma_{33})^2}{Y_T^2} + \frac{\sigma_{23}^2 - \sigma_{22}\sigma_{33}}{S_{23}^2} + \frac{\sigma_{12}^2 + \sigma_{13}^2}{S_{12}^2} \geq 1 \quad (2.61)$$

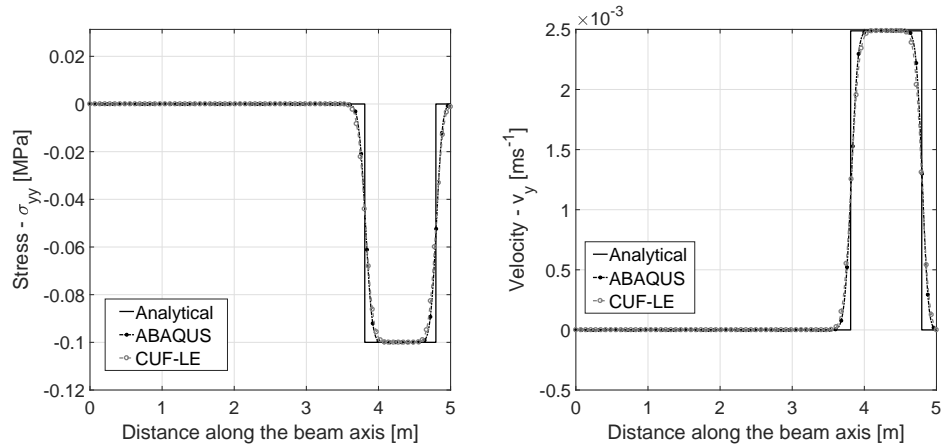
(a) Propagating wave



(b) At boundary - superposition of waves



(c) Reflecting wave



(a) Stress distribution

(b) Velocity distribution

Fig. 2.10 Stress and velocity distribution along the beam for time (a) $t = 0.58ms$ (b) $t = 1.01ms$ and (c) $t = 1.2ms$ using 70 B4-elements for one-dimensional stress wave problem

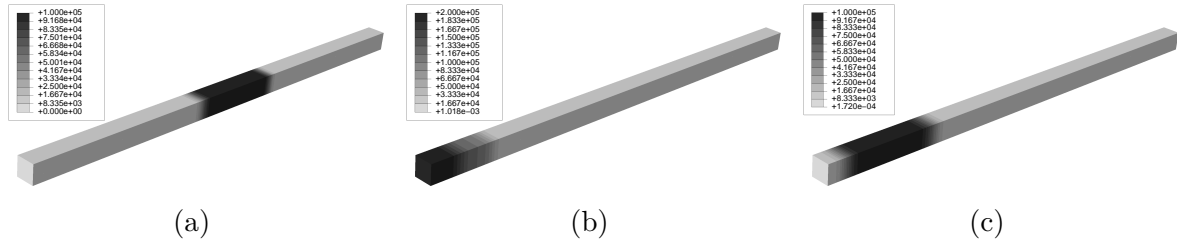


Fig. 2.11 Stress (σ_{yy}) wave propagation in beam at time (a) 0.58ms (b) 1.03ms and (c) 1.2ms for one-dimensional stress wave problem

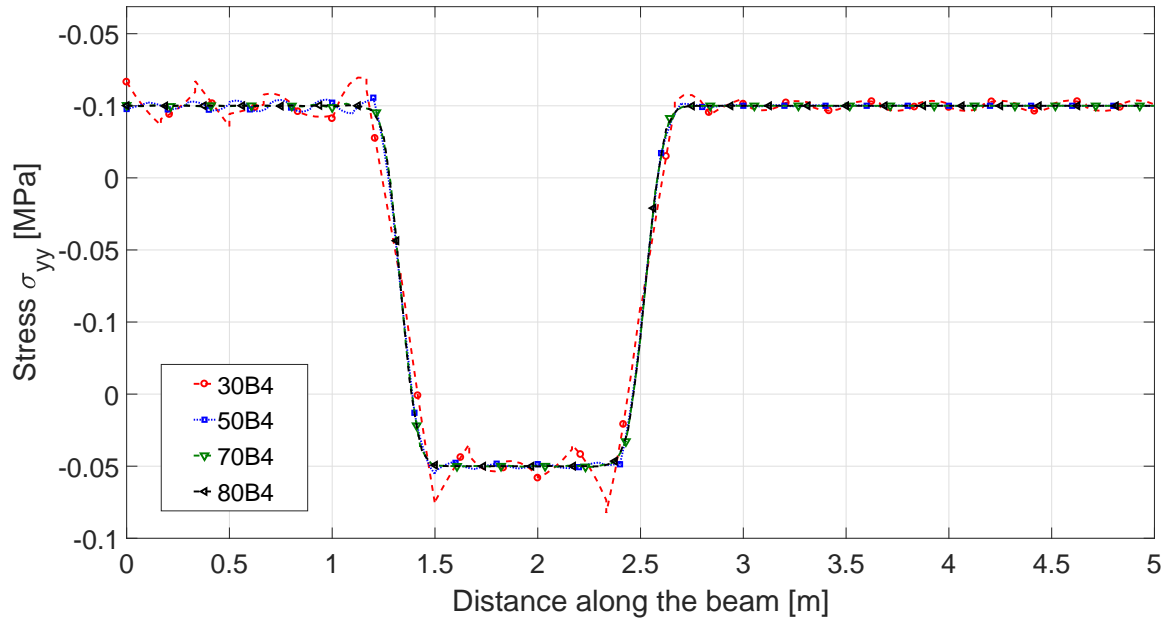


Fig. 2.12 Comparison of Stress (σ_{yy}) plot along the beam axis for different mesh density at time 0.58ms for 1D stress wave problem

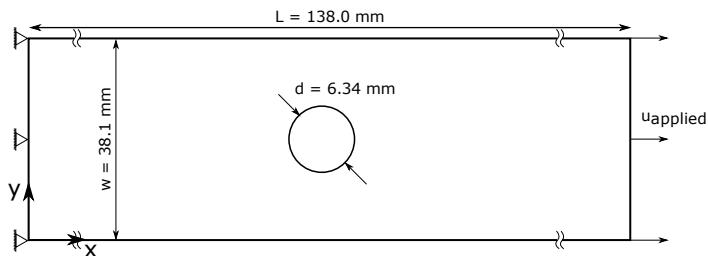


Fig. 2.13 Geometry and boundary conditions for failure evaluation of notched composite specimens

Table 2.2 Model information for failure index evaluation of notched composite specimens

Model	Discretization	DOF	CPU Time (s)
Laminate 1 : [0]			
CUF-LW	C2: 7L9-10B4 and C1:136L9-1B3 (One element per layer)	9,414	4
ABQ3D-Coarse	Linear brick elements (C3D8) with an average element size of 0.275 around the notch. Two elements per layer.	25,632	6
ABQ3D-Refined	Linear brick elements (C3D8) with an average element size of 0.2 around the notch. Two elements per layer.	39,348	12
Laminate 2 : [90]			
CUF-LW	C2: 7L9-10B4 and C1:136L9-1B3 (One element per layer)	9,414	4
ABQ3D-Coarse	Linear brick elements (C3D8) with an average element size of 0.275 around the notch. Two elements per layer.	25,632	6
ABQ3D-Medium	Linear brick elements (C3D8) with an average element size of 0.2 around the notch. Two elements per layer.	39,348	7
ABQ3D-Refined	Linear brick elements (C3D8) with an average element size of 0.1 around the notch. Two elements per layer.	93,960	15
Laminate 3 : [0/90]_s			
CUF-LW1	C2: 28L9-10B4 and C1:136L9-4B3 (One element per layer)	28,242	19
CUF-LW2	C2: 28L9-10B4 and C1:136L9-12B3 (Two elements per layer)	53,346	42
ABQ3D-1L	Linear brick elements (C3D8) with an average element size of 0.1 around the notch. One element per layer.	187,320	42
ABQ3D-2LQ	Quadratic brick elements (C3D20) with an average element size of 0.2 around the notch. Two element per layer.	265,782	68
ABQ3D-4LR	Linear brick elements (C3D8) with an average element size of 0.05 around the notch. Four elements per layer.	1,306,977	602

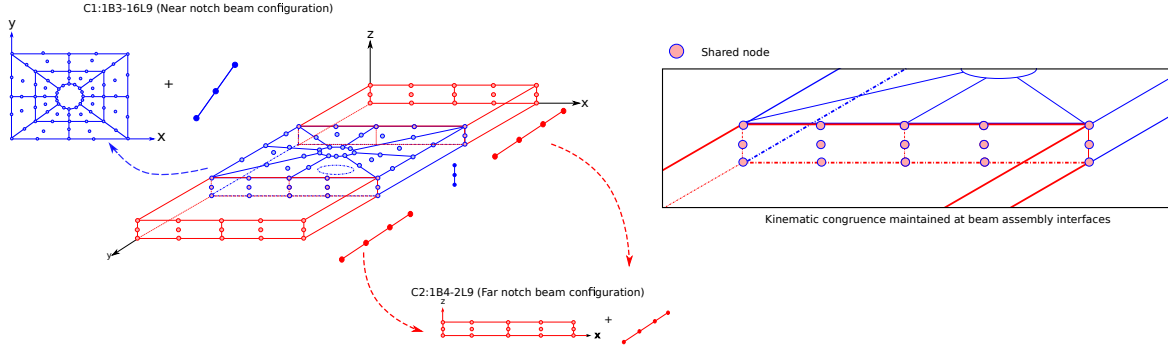


Fig. 2.14 Modeling of notched composite specimens using refined 1D CUF-LW models

4. Matrix Compression:

$$\left[\left(\frac{Y_C}{2S_{23}} \right)^2 - 1 \right] \left(\frac{\sigma_{22} + \sigma_{33}}{Y_C} \right) + \frac{(\sigma_{22} + \sigma_{33})^2}{4S_{23}^2} + \frac{\sigma_{23}^2 - \sigma_{22}\sigma_{33}}{S_{23}^2} + \frac{\sigma_{12}^2 + \sigma_{13}^2}{S_{12}^2} \geq 1 \quad (2.62)$$

where σ_{ij} represents the components of the stress tensor in the material coordinate system. X, Y represents that of the material strengths in fiber and transverse direction, with the subscripts T and C denoting tensile and compressive loading, respectively. The material shear strengths is denoted by S_{ij} . A mixed-mode quadratic criteria proposed by Brewer and Lagace is used to determine the delamination index [28]:

$$\left(\frac{\langle \sigma_{33} \rangle}{Z_T} \right)^2 + \left(\frac{\sigma_{23}}{S_{23}} \right)^2 + \left(\frac{\sigma_{13}}{S_{13}} \right)^2 \geq 1 \quad (2.63)$$

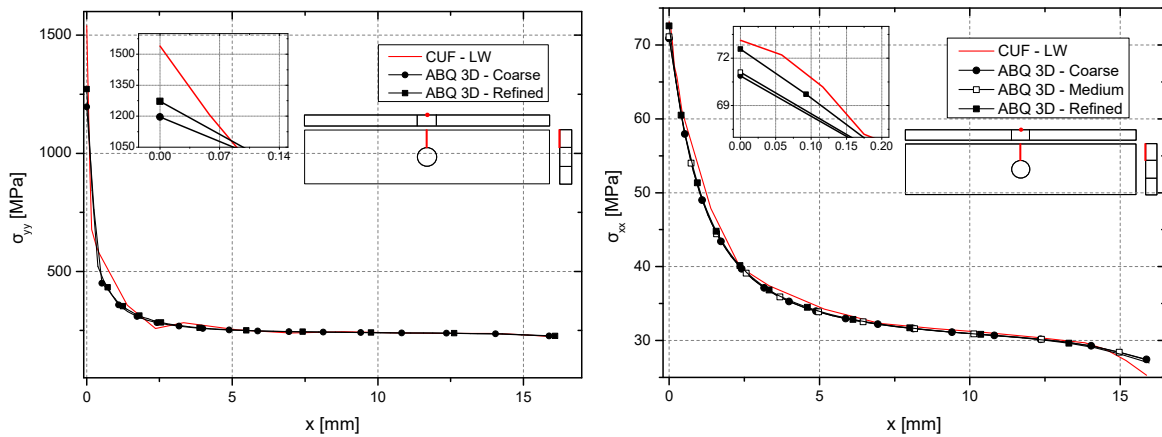
where σ_{33} denotes the transverse normal stress in the material coordinate system, S_{13} and S_{23} are the transverse shear stresses with Z_T being the inter-laminar normal strength while S_{13} and S_{23} are the transverse shear strengths.

The first ply failure load is computed as the load at which one of the failure indices attains the unity. Table 2.3 tabulates the first ply failure load for different models along with the mode of failure. Figures 2.15a and 2.15b depicts the in-plane stress distribution along the width of the [0] and [90] notched specimens respectively. The Hashin 3D matrix tension contour plot for [0] and [90] laminates are depicted in Fig. 2.16 and Fig. 2.17 respectively, where an applied displacement of 0.2 mm corresponded to first ply failure for [0] whereas an applied displacement of 0.45 mm was required for [90] laminate.

Figures 2.18, 2.19 and 2.20 depicts the through-the-thickness axial stress σ_{yy} , the transverse shear stresses σ_{xy} and σ_{yz} for [0/90]_s notched laminate respectively. The contour plots in Fig. 2.21 and Fig. 2.22 refers to Hashin-3D matrix tension and the

Table 2.3 Numerical results for load at first ply failure for different models of notched composite specimens

Model	DOF	Load at first ply failure [N]	First ply failure mode
Laminate 1 : [0]			
CUF-LW	9,414	1,120	Matrix Tension
ABQ3D-Coarse	25,632	1,142	
ABQ3D-Refined	39,348	1,120	
Laminate 2 : [90]			
CUF-LW	9,414	141	Matrix Tension
ABQ3D-Coarse	25,632	147	
ABQ3D-Medium	39,348	146	
ABQ3D-Refined	93,960	141	
Laminate 3 : [0/90]_s			
CUF-LW1	28,242	1,531	Matrix Tension
CUF-LW2	53,346	1,500	
ABQ3D-1L	187,320	2,097	
ABQ3D-2LQ	265,782	1,737	
ABQ3D-4LR	1,306,977	1,797	



(a) σ_{yy} for [0] laminate under an applied displacement of 0.2 mm (b) σ_{xx} for [90] laminate under an applied displacement of 0.4 mm

Fig. 2.15 Normal stress distribution along the width of notched composite specimen,

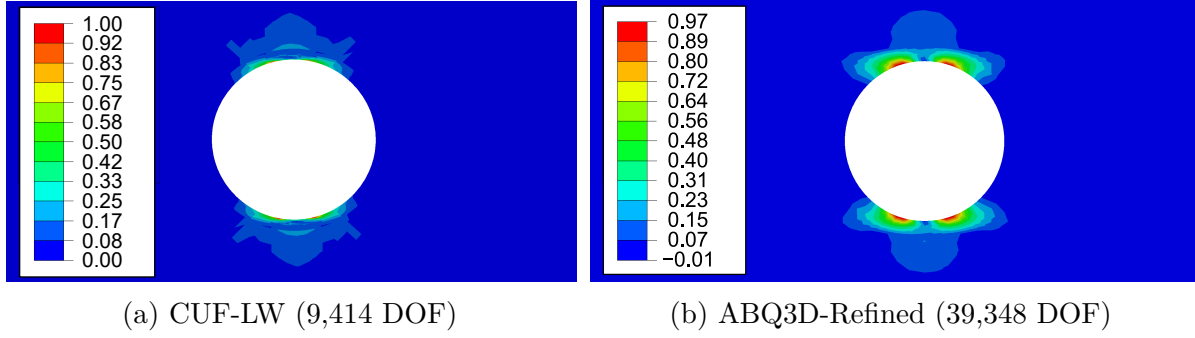


Fig. 2.16 Hashin3D matrix tension (MT) failure index for $[0]$ laminate under an applied displacement of 0.2 mm

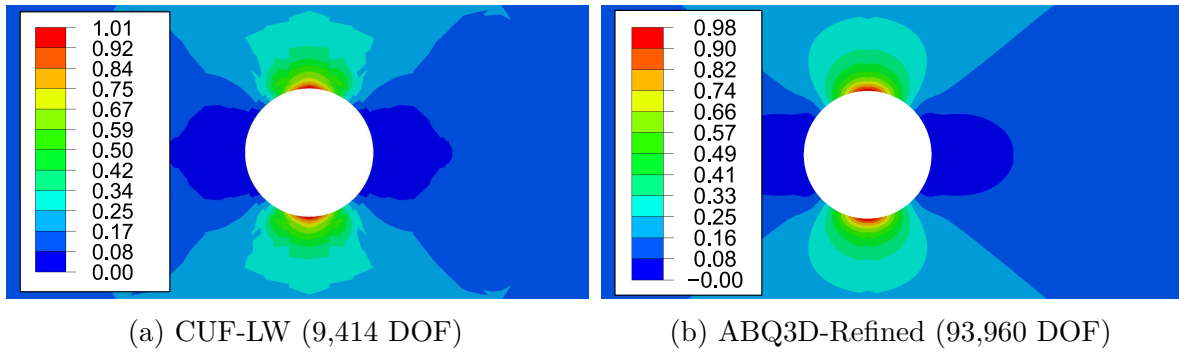


Fig. 2.17 Hashin3D matrix tension (MT) failure index for $[90]$ laminate under an applied displacement of 0.45 mm

delamination failure indices, for the $[0/90]_s$ laminate under an applied displacement of 0.125 mm

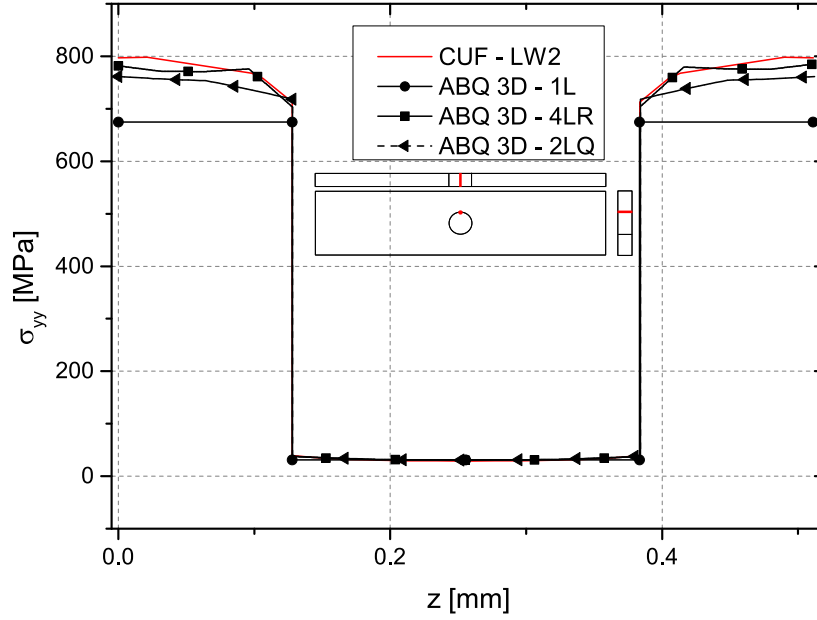


Fig. 2.18 Normal stress distribution σ_{yy} through the thickness of $[0/90]_s$ notched laminate under an applied displacement of 0.125 mm, $x = 16.875$, $y = 69$

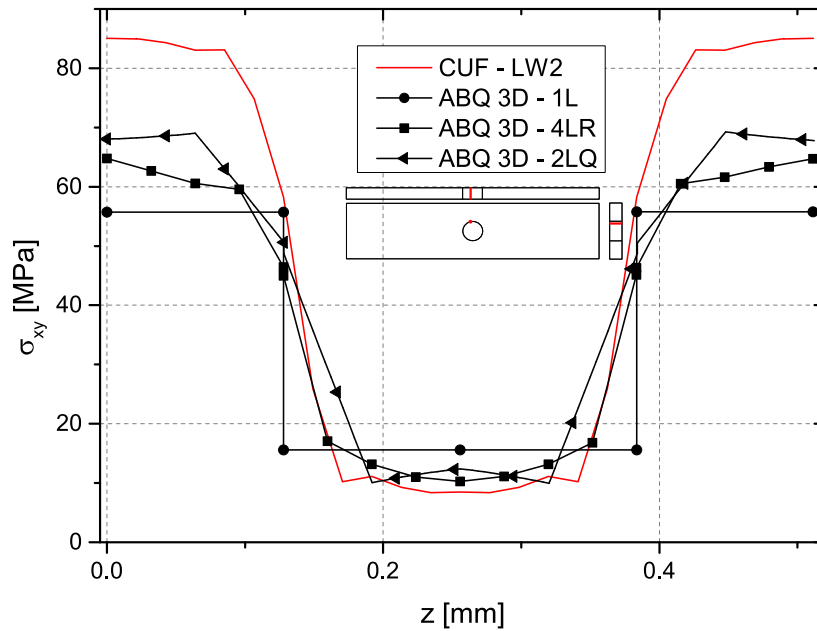


Fig. 2.19 In-plane shear stress distribution σ_{xy} through the thickness of $[0/90]_s$ notched laminate under an applied displacement of 0.125 mm, $x = 16.875$, $y = 69$

Following observations can be made:

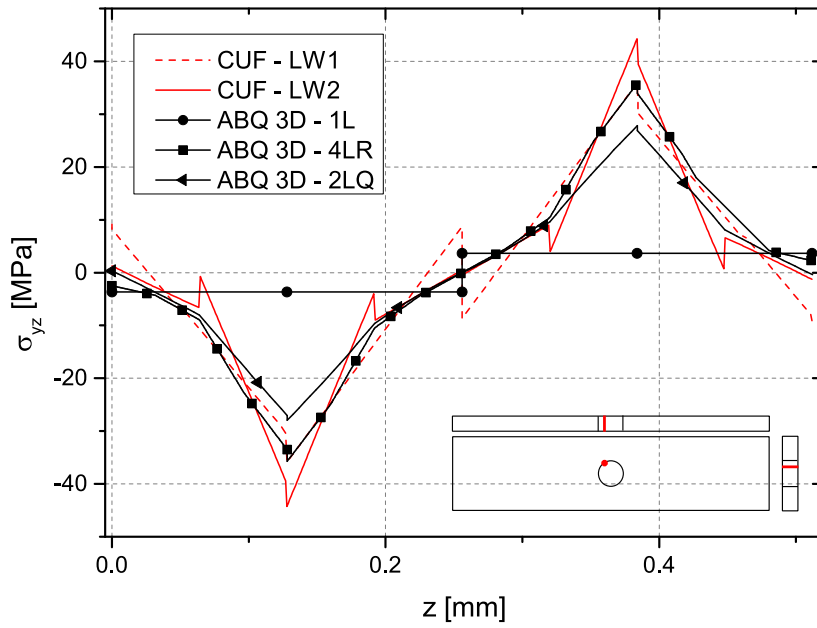


Fig. 2.20 Transverse shear stress distribution σ_{yz} through the thickness of $[0/90]_s$ notched laminate under an applied displacement of 0.125 mm, $x = 17.04$, $y = 68$

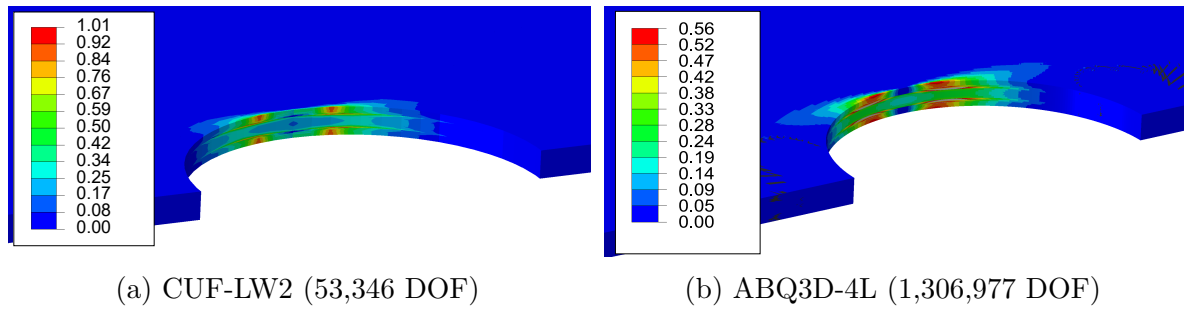


Fig. 2.21 Hashin3D matrix tension (MT) failure index for $[0/90]_s$ laminate under an applied displacement of 0.125 mm

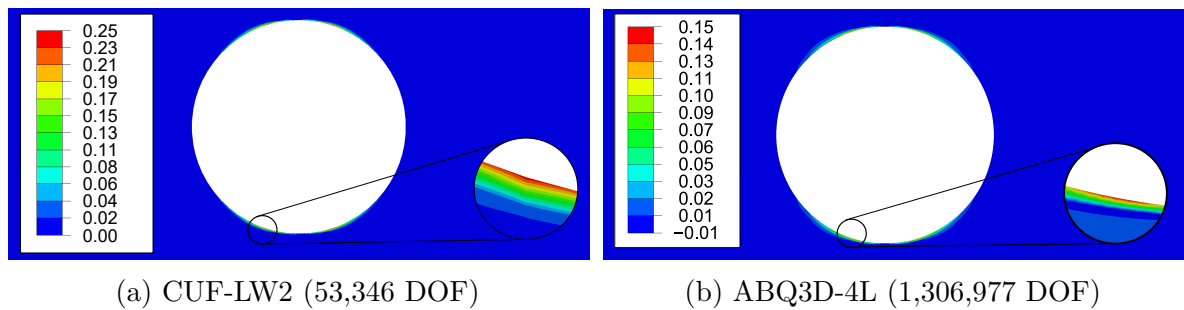


Fig. 2.22 Delamination failure index for $[0/90]_s$ laminate under an applied displacement of 0.125 mm

1. In comparison to ABAQUS 3D solutions, CUF models are able to accurately capture in-plane stress predictions (See Fig. 2.15a and Fig. 2.15a for the [0] and [90] ply laminates respectively)
2. In case of [0] and [90] ply laminates, load at first ply failure tends to agree well for ABAQUS and CUF models.
3. For $[0/90]_s$, ABAQUS models severely underestimates the out-of-plane stresses as compared to CUF models as seen in Fig. 2.20. The effect of under-predictions is significantly reflected in the failure index evaluations as shown in Fig. 2.21 and 2.22 for matrix tension delamination index predictions. The predictions from ABAQUS models tends to improve as the through-the-thickness mesh density is improved.
4. From Table 2.3, it is evident that failure to capture accurate stress fields can substantially over-predict the load at first ply failure.

2.4 Conclusion

The chapter presented the higher-order one-dimensional formulation adopted in the thesis work. The one-dimensional models are based on Carrera Unified Formulation (CUF), a hierarchical formulation that provide a structured basis to derive any class of refined beam, plate or shell theories through variable kinematic definition. Using the principle of virtual work, the governing equation for CUF models are formulated in concise manner though the definition of fundamental nuclei. Special emphasis placed on the invariant nature of the formulation as the same numerical implementation can be employed for generating different classes of higher-order models. The ability of CUF-1D model to accurately capture three-dimensional fields at a reduced computational cost is highlighted through two numerical case. Stress wave propagation in an isotropic beam underlined the CUF models to efficiently capture severe stress gradients at the wave fronts. The efficiency can be exploited in modeling impact problems . Failure index evaluation of notched composite specimen emphasized the importance of higher-order models in resolving three-dimensional stress fields for computing failure indexes. For instance, the inability of standard 3D FEM to capture out-of-plane stresses highlights the importance of non-traditional higher-order models for high-fidelity analysis in composites. Since accurate resolution of displacement and stress fields is a precursor for reliable nonlinear simulations, proposed higher-order 1D models are apt for undertaking physically nonlinear simulation with an added benefit of computational efficiency.

Chapter 3

Study on higher-order models for physically nonlinear simulations using elastoplastic models

*The present chapter intends to highlight the effectiveness of 1D CUF models to undertake physically nonlinear simulation. Isotropically work-hardening von-Mises constitutive model is incorporated within the 1D CUF framework to account for material nonlinearity. Numerical results for compact and thin-walled beam members in plastic regime is presented with displacement profiles and beam deformed configuration along with stress contour plots. The results are compared against classical beam models such as EBBT and TBT, reference solutions from literature and three-dimensional solid finite element solution.*¹

3.1 Elastoplastic material models

The theory of elastoplasticity provides a realistic mathematical description of inelastic behavior in metals. The von-Mises theory is based on the hypothesis that metal yields when the J_2 stress deviator reaches the critical value [133]. The inelastic deformations

¹Parts of this chapter has been in published in the following journal:

1. Carrera E., , Petrolo M. (2017), "Elastoplastic analysis of compact and thin-walled structures using classical and refined beam finite element models", Mechanics of Advanced Materials and Structures
2. Kaleel I., Petrolo M., Carrera E., Waas A., (2019) "On the effectiveness of higher-order models for physically non linear analysis", in "Advances in Predictive Models and Methodologies for Numerically Efficient Linear and Nonlinear analysis of Composites"

are accompanied by dissipation of energy, which in turn leads to permanent deformation when completely unloaded. Within the context of geometrically linear theorem, the classical theory of plasticity can be defined based on a set of equations, which determine the elastic material behaviour and inelastic deformation evolution:

1. Additive split of strain tensor

An important hypotheses within the small strain theory of plasticity is the decomposition of total strain into sum of elastic strain, ϵ^e , (reversible) and plastic strain, ϵ^p , (permanent),

$$\epsilon = \epsilon^e + \epsilon^p \quad (3.1)$$

2. Elastic domain

Elastic domain is the range of stress within which the behavior is completely elastic and the domain is delimited by the yield boundary. Therefore, the yield function Φ is of the form

$$\Phi(\sigma, \zeta) \leq 0 \quad (3.2)$$

The hardening parameter ζ determines the extent of yield function in the continued process of plastification. Therefore the boundary of elastic domain is given by $\Phi(\sigma, \zeta) = 0$ and stress states outside the elastic domain is not admissible.

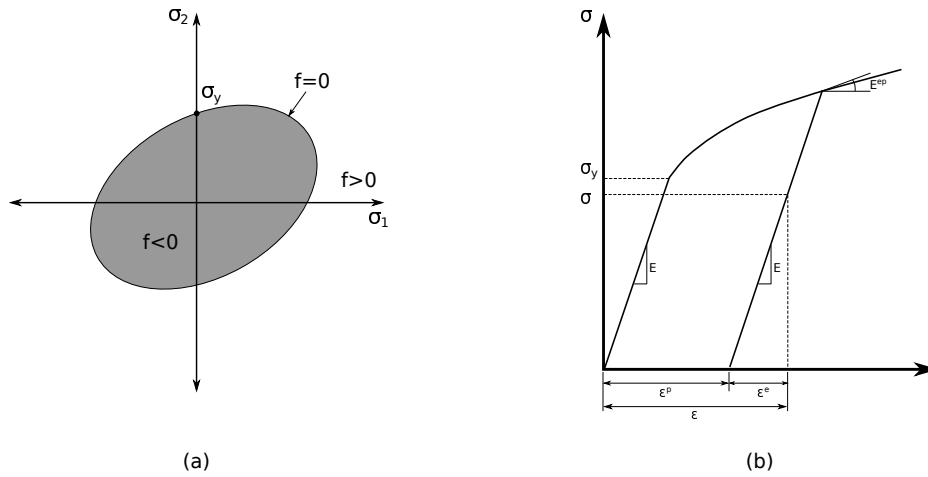


Fig. 3.1 Elastoplastic material behavior: (a) elastic domain and yield function in stress space and (b) additive split of total strain

3. Plastic flow rule

The plastic yielding occurs when the yield function $\Phi = 0$ with a nonzero plastic strain rate $\dot{\epsilon}_p$, which is given by:

$$\dot{\epsilon}_p = \dot{\gamma} \text{sign}(\sigma) \quad (3.3)$$

where $\dot{\gamma}$ is the plastic multiplier and sign function decides the sign of the plastic strain rate (positive for tension and negative for compression). The criteria for plastic flow (loading/unloading) condition is formulated in a concise manner based on Kuhn-Tucker condition:

$$\Phi \leq 0, \quad \dot{\gamma} \geq 0, \quad \Phi \dot{\gamma} = 0 \quad (3.4)$$

4. Hardening law

Hardening law describes the evolution of yield stress based on the evolution of plastic strain. Isotropic hardening is characterized with expanding yield surface in the stress space, which can be expressed as:

$$\sigma_y = \sigma_y(\bar{\epsilon}^p) \quad (3.5)$$

where $\bar{\epsilon}^p$ is the accumulated plastic strain. Based on the plastic flow rule, accumulated plastic strain can be expressed as:

$$\bar{\epsilon}^p = \int_0^t |\dot{\epsilon}^p| dt = \int_0^t |\dot{\gamma}| dt \quad (3.6)$$

3.1.1 Numerical aspects of von Mises plasticity model

The condition for von Mises plasticity model with an isotropic hardening case can be expressed as:

$$f = q(\boldsymbol{\sigma}) - \sigma_y(\bar{\epsilon}_p) \quad (3.7)$$

with

$$q(\boldsymbol{\sigma}) = \sqrt{3J_2} = \sqrt{\frac{1}{2} [(\sigma_{xx} - \sigma_{yy})^2 + (\sigma_{yy} - \sigma_{zz})^2 + (\sigma_{zz} - \sigma_{xx})^2 + 6(\sigma_{xy}^2 + \sigma_{xz}^2 + \sigma_{yz}^2)]} \quad (3.8)$$

where f is the von-Mises yield locus, $q(\boldsymbol{\sigma})$ is the von-Mises stress, σ_y is the yield stress (elastic limit), J_2 is the second invariant of deviatoric stress and $\bar{\epsilon}_p$ is the isotropic hardening parameter. The flow rule is given by the Prandtl-Reuss equation, which

is obtained by considering the von-Mises yield function (see Eqn. 4.7) as the flow potential. The flow vector reads:

$$\mathbf{N} = \frac{\partial f}{\partial \boldsymbol{\sigma}} = \sqrt{\frac{3}{2}} \frac{\mathbf{s}}{\|\mathbf{s}\|} \quad (3.9)$$

where \mathbf{s} is the deviatoric stress tensor. Hardening is a phenomenological aspect of plastic yielding which is characterized by the dependence of the critical yield value on the history of plastic strains.

For the current framework, a rate-independent isotropic hardening is considered. It is incorporated into the formulation by making the yield stress as a function of accumulated plastic strain as given in Eqn. 4.7 and corresponds to uniform expansion of initial yield locus. On the other hand, a perfectly plastic behavior is characterized with no hardening. The yield stress does not depend on the accumulated plastic strain. In the current framework, strain hardening approach is utilized to treat the isotropic hardening behavior. Taking into account the associative flow rule, the rate evolution equation can be formulated as

$$\bar{\epsilon} = \sqrt{\frac{2}{3}} \|\boldsymbol{\epsilon}_p\| \quad (3.10)$$

The implementation of constitutive model is based on the book by Neto et. al. [141].

Implicit numerical integration scheme

Two essential material specific operations involved are: (1) the state update procedure, where stress σ_{n+1}^k and hardening variable $\bar{\epsilon}_p^k$ are computed at every gauss point and (2) computing the tangent stiffness matrix for solving the nonlinear finite element equations. In the state update procedure presented here, backward Euler scheme is

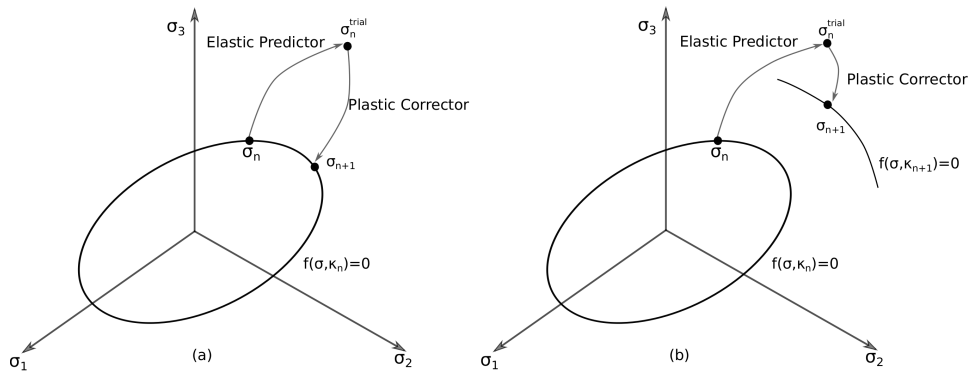


Fig. 3.2 Geometrical illustration of Return-Mapping scheme: (a) perfect plasticity and (b) with hardening

utilized. This leads to a two-step algorithm for the state update as follows:

1. Elastic Predictor Step

In a given increment $[t_n - t_{n+1}]$ with a strain increment $\Delta\epsilon$, solution is assumed to be elastic and leads to an elastic trial solution

$$\epsilon_{n+1}^{e,trial} = \epsilon_n^e + \Delta\epsilon \quad (3.11)$$

$$\bar{\epsilon}_{p_{n+1}} = \bar{\epsilon}_{p_n} \quad (3.12)$$

The corresponding elastic trial stress is computed and solution is accepted, if the elastic trial stress lies within the yield locus. In case the elastic trial stress exceeds the yield locus, Plastic Corrector Step is initiated

2. Plastic Corrector Step

A scalar nonlinear equation with incremental plastic multiplier $\Delta\gamma$ as the unknown is solved using Newton-Raphson (NR) method

$$\bar{f}(\Delta\gamma) = q_{n+1}^{trial} - 3G\Delta\gamma - \sigma_y(\bar{\epsilon}_n^p + \Delta\gamma) \quad (3.13)$$

where q_{n+1}^{trial} is the trial von-Mises stress. With solution $\Delta\gamma$ at hand, state variables are updated

$$\mathbf{s}_{n+1} = \left(1 - \frac{\Delta\gamma 3G}{q_{n+1}^{trial}}\right) \mathbf{s}_{n+1}^{trial} \quad (3.14a)$$

$$\boldsymbol{\sigma}_{n+1} = \mathbf{s}_{n+1} + p_n^{trial} \mathbf{I} \quad (3.14b)$$

$$\epsilon_{n+1}^e = \frac{1}{2G} \mathbf{s}_{n+1} + \frac{1}{3} \epsilon_v^{e,trial} \mathbf{I} \quad (3.14c)$$

$$\bar{\epsilon}_{n+1}^p = \bar{\epsilon}_{n+1}^p + \Delta\gamma \quad (3.14d)$$

Geometrical interpretation of return-mapping scheme is illustrated in Fig. 3.2. It should be noted that each iteration step consists of a global Newton-Raphson step for computing the global incremental solution and local Newton-Raphson step at every gauss point to compute the incremental plastic multiplier as shown in Eqn. 3.13.

Consistent elastoplastic tangent operator

Newton-Raphson scheme is often characterized with good convergence qualities. Quadratic rate of asymptotic convergence of the global iteration procedure can only be guaranteed when a full tangent matrix is used. In order to ensure robustness of Newton-Raphson

iterative scheme, it is important to compute the elastoplastic tangent modulus (\mathbf{C}^{ep}) correctly. The elastoplastic tangent modulus is a fourth-order tensor, which is obtained by taking variations of integrated equations with respect to the solution variables. An elastoplastic consistent tangent operator is defined as follows:

$$\mathbf{C}^{ep} = \frac{\partial \boldsymbol{\sigma}}{\partial \boldsymbol{\epsilon}_{n+1}^{e,trial}} \quad (3.15)$$

After straightforward manipulation of Eqns. 3.14-3.15, following expression can be obtained

$$\mathbf{C}_{ep} = \mathbf{C}_e - \frac{\Delta\gamma}{q_{n+1}^{trial}} 6G^2 \mathbf{I}_d + 6G^2 \left(\frac{\Delta\gamma}{q_{n+1}^{trial}} - \frac{1}{3G + H} \right) \bar{\mathbf{N}}_{n+1} \otimes \bar{\mathbf{N}}_{n+1} \quad (3.16)$$

where G and H are the hardening and bulk modulus respectively [141]. The elastoplastic consistent tangent operator (see Eqn. 3.16) is consistent with the implicit return-mapping scheme employed for state update procedure and is based on the works of Simo and Taylor [178]. Based on the consistent tangent material operator (Eqn. 3.16), we can formulate the tangent fundamental nucleus for CUF (2.24) as follows

$$k_{ij\tau s}^{tan} = \int_l \int_{\Omega} \mathbf{D}^T \mathbf{C}_{ep} \mathbf{D} dl d\Omega \quad (3.17)$$

Additionally, the isotropic hardening curve ($\sigma_y(\bar{\epsilon}_p)$) is assumed to be piece-wise linear. The framework accepts a set of data points that approximate the arbitrarily nonlinear hardening curve. Linear interpolation is employed to approximate between the data points. This allows the use of experimental hardening curve directly into the simulation.

3.2 Numerical results

The section encompasses three sets of numerical results illustrating advanced capabilities of non-linear CUF framework for solving elastoplastic problems. First, an elastoplastic cantilever beam with compact cross-section under a bending load is investigated. An analytical solution is available for the proposed problem and the example serves a good benchmark to evaluate the accuracy of refined-beam models. The second and third numerical examples investigate the refined capabilities of CUF models to analyze thin-walled beams. A lipped channel beam and Z-beam is investigated and complex mechanical behaviors such as coupled bending -torsion and localized plasticity growth is efficiently analyzed by the CUF models. For each set of numerical example, a

classical three-dimensional finite element model is built in ABAQUS [2] and the results serve as a benchmark to assess the accuracy and efficiency of the refined beam models. Displacement profiles, three-dimensional deformed configuration, accumulated plastic growth contour and stress contours are presented for validation purposes.

3.2.1 Elasto-Plastic Cantilever Beam

A cantilever beam with rectangular cross-section under a vertical load at the tip is investigated. Two classes of cantilever beam are considered, namely (a) Single-layered and (b) Multi-layered beam.

Single-layered cantilever beam

The material and geometric properties of the beam is illustrated in Table 3.1 and the example is based on the work of Wen et al. [203]. An ideal elastic-perfect plastic stress-strain model is adopted, where the stress remains the same beyond the yield point.

Timoshenko and Gere developed an analytical solution for deflection of isotropic elastoplastic beam of rectangular cross-section under bending load [189]. The non-dimensional form of the solution is given as follows:

Elastic Region

$$\frac{\delta}{\delta_y} = \frac{P}{P_y} \quad \left(0 \leq \frac{P}{P_y} \leq 1\right) \quad (3.18a)$$

Plastic Region

$$\frac{\delta}{\delta_y} = \left(\frac{P}{P_y}\right)^2 \left[5 - \left(3 + \frac{P}{P_y}\right) \sqrt{3 - \frac{2P}{P_y}}\right] \quad \left(1 \leq \frac{P}{P_y} \leq \frac{3}{2}\right) \quad (3.18b)$$

where δ_y is the displacement at the yield load P_y . The equilibrium path is depicted in Fig. 3.3. The ratio between the limit load and yield load is termed as plastic strength factor. The geometry of the beam is illustrated in Fig. 3.4. The beam is discretized using B4 elements. A vertical load is applied at the tip of the beam in increments. The cross-section of the beam is modeled using LE and TE models as illustrated in Fig. 3.4. The results from various models are tabulated in Table 3.2. The results are given in terms of vertical displacement at limit load and yield load and plastic strength

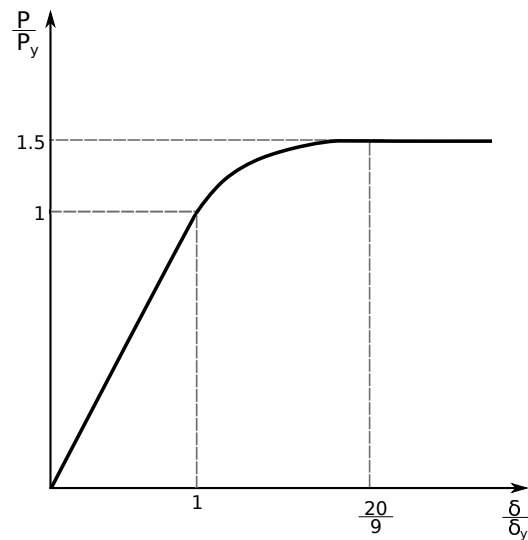


Fig. 3.3 Equilibrium path for the elasto-plastic cantilever beam [189]

Table 3.1 Geometric and material properties of elasto-plastic cantilever beam

Parameters	Values	Units
Geometrical Properties		
Beam Length (L)	50.0	m
Cross-section width (w)	1000.0	mm
Cross-section height (h)	800.0	mm
Material Properties		
Young's modulus	210.0	GPa
Poisson's Ratio	0.3	-
Yield Stress	210.0	MPa

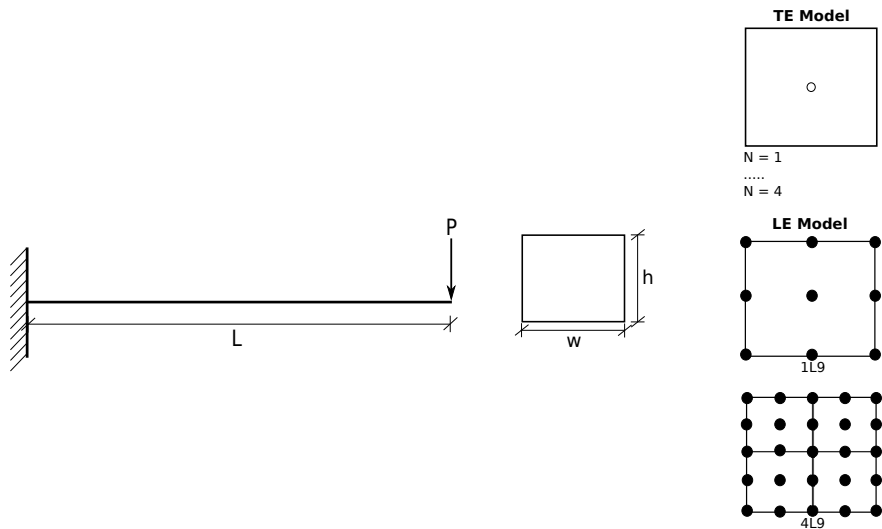


Fig. 3.4 Geometry and cross-section configurations of the elasto-plastic cantilever beam

factor. Classical models such as EBBT and TBT as well as refined beam models are compared against ABAQUS 1D beam and 3D solid results. Comparison of equilibrium path for various beam models is illustrated in Fig. 3.5. Convergence study for various beam with number of elements along the beam is tabulated in Table 3.3.

Table 3.2 Comparison of displacement and plastic strength factor (PSF) for various beam models of elasto-plastic cantilever beam

Type	NDOF	u_z at yield force		u_z at limit load		PSF	
		Value (m)	Error (%)	Value (m)	Error (%)	Value	Error (%)
Analytical	-	2.08	-	4.622	-	1.5	-
Secant Stiff. Form. [203]	-	-	-	4.82	4.28	1.51	0.67
ABAQUS							
1D Beam	606	2.084	0.18	3.612	21.87	1.51	0.43
3D Solid (Coarse)	22,590	2.067	0.62	4.281	7.38	1.55	3.57
3D Solid (Refined)	148,797	2.077	0.14	4.467	3.35	1.54	2.38
Classical Models							
EBBT	549	2.083	0.16	6.406	38.60	3.08	105.00
TBT	549	2.084	0.18	6.407	38.61	3.08	105.00
TE							
N = 1	549	2.084	0.18	6.407	32.38	3.08	105.00
N = 2	1098	2.079	0.07	4.937	6.81	1.55	3.33
N = 3	1830	2.079	0.06	4.735	2.44	1.53	2.00
N = 4	2745	2.079	0.06	4.624	0.03	1.52	1.29
LE							
1L9	1647	2.0787	0.06	3.623	21.61	1.35	10.00
4L9	4575	2.0789	0.05	4.534	1.90	1.52	1.29

Multi-layered cantilever beam

Two types of multi-layered configuration are considered: (a) unsymmetric two-layered and (b) symmetric three-layered. The material properties for the multi-layered beam are tabulated in Table 3.4. As depicted in Fig. 3.4, the length of the beam is taken as 0.5 m and a square cross-section of side 10 mm is considered. The beam is discretized using 40 B4 elements. Figure 3.6 compares the equilibrium path for two-layered and three-layered beam configuration using different models. Table 3.5 enlists the maximum accumulated equivalent plastic strain for different models for multi-layered cantilever beam under bending.

Following observations can be made

1. All models provide accurate results within the elastic regime. It is clear that classical beam models as well as ABAQUS 1D Beam model fail, when the load

Table 3.3 Convergence study of various refined beam models for elasto-plastic cantilever beam

Type	NDOF	Displacement at yield force		Displacement at limit load		Plastic Strength Factor	
		Value [m]	Error [%]	Value [m]	Error [%]	Value	Error [%]
B4 - 10 elements							
TE							
EBBT	155	2.0833	0.16	6.501	40.64	3.10	106.67
TBT	155	2.0837	0.18	6.502	40.68	3.10	106.67
N=1	279	2.0837	0.18	6.502	40.68	3.10	106.67
N=2	558	2.0717	0.40	5.052	9.30	1.57	4.33
N=3	930	2.0719	0.39	4.852	4.97	1.56	3.67
N=4	1395	2.0719	0.39	4.729	2.30	1.55	3.00
LE							
1L9	837	2.0718	0.39	3.062	33.76	1.35	10.00
4L9	2325	2.0719	0.39	4.514	2.34	1.52	1.66
B4 - 20 elements							
TE							
EBBT	305	2.0833	0.16	6.407	38.60	3.08	105.00
TBT	305	2.0837	0.18	6.408	38.64	3.08	105.00
N=1	549	2.0837	0.18	6.408	38.64	3.08	105.00
N=2	1098	2.0770	0.14	4.909	6.20	1.55	3.33
N=3	1830	2.0772	0.13	4.695	1.58	1.54	2.67
N=4	2745	2.0772	0.13	4.659	0.77	1.53	2.00
LE							
1L9	1647	2.0771	0.14	3.623	21.61	1.35	10.00
4L9	4575	2.0773	0.13	4.534	1.90	1.52	1.29
B4 - 30 elements							
TE							
EBBT	455	2.0833	0.16	6.407	38.60	3.08	105.00
TBT	455	2.0837	0.18	6.408	38.61	3.08	105.00
N=1	819	2.0837	0.18	6.408	38.63	3.08	105.00
N=2	1638	2.0786	0.07	4.937	6.81	1.55	3.33
N=3	2730	2.0788	0.06	4.735	2.44	1.53	2.00
N=4	4095	2.0788	0.06	4.624	0.03	1.52	1.33
LE							
1L9	2457	2.0787	0.06	3.579	22.56	1.35	10.00
4L9	6825	2.0789	0.05	4.591	0.69	1.52	1.32

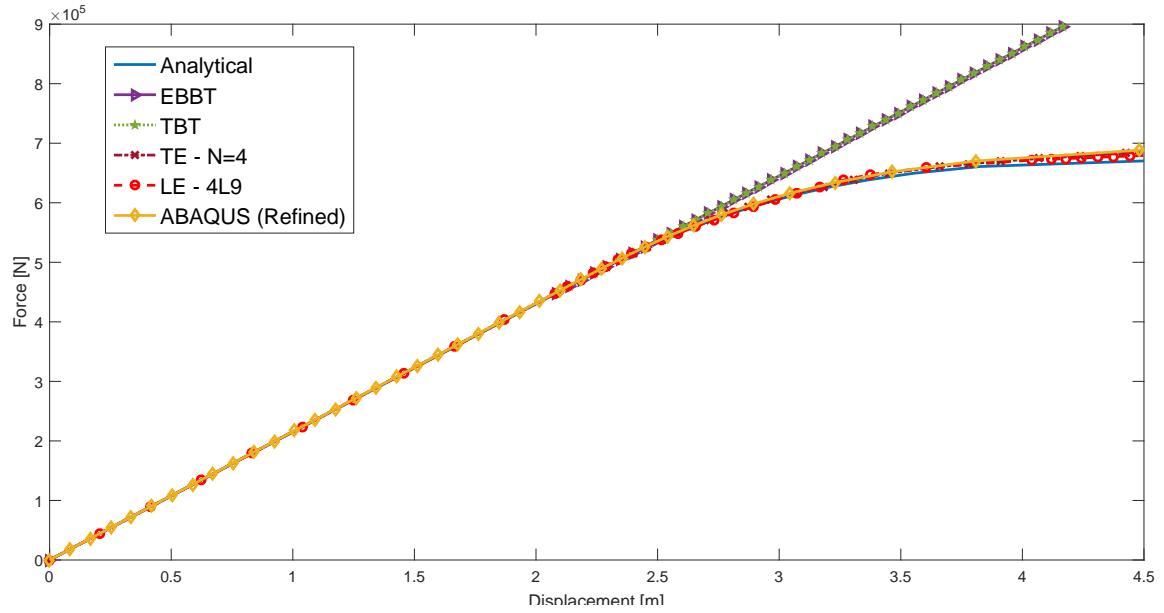


Fig. 3.5 Equilibrium path of various beam models for elasto-plastic cantilever beam (30 B4 elements used for TE and LE model)

Table 3.4 Material properties for multi-layered cantilever beam under bending

	Young's modulus (GPa)	Poisson's ratio (-)	Yield stress (MPa)
Mat1	210.0	0.3	210.0
Mat2	70.0	0.3	110.0

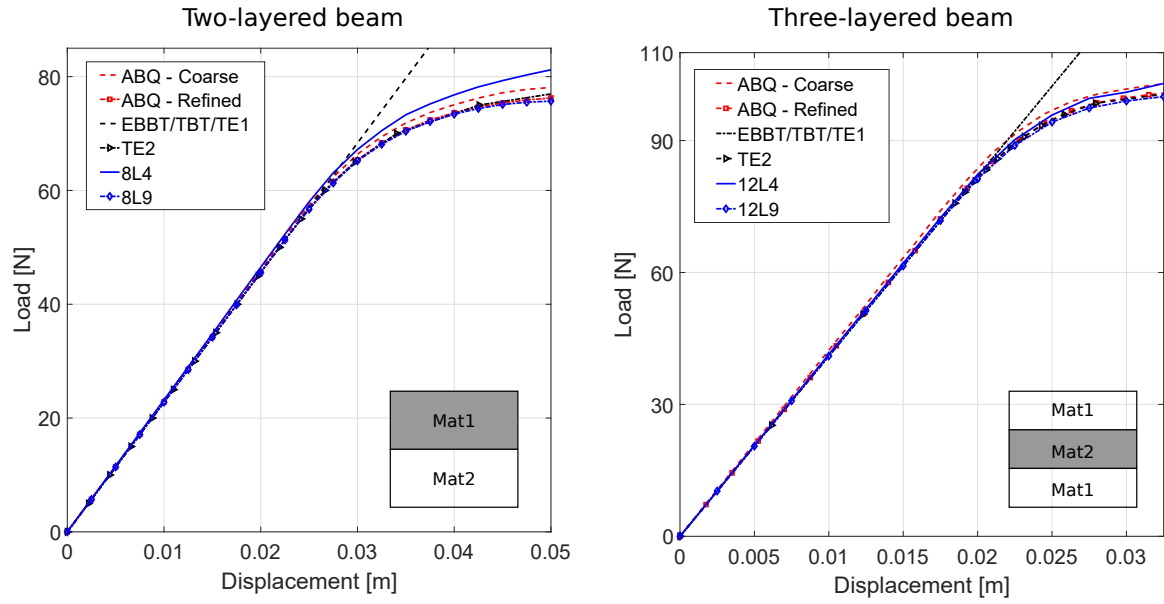


Fig. 3.6 Comparison of equilibrium path for two-layered and three-layered beam configuration using various models

Table 3.5 Comparison of maximum accumulated equivalent plastic strain for different models for multi-layered cantilever beam under bending

Model	Two-layered		Three-layered	
	DOF	$\bar{\epsilon}_p^{max} [\times 10^{-3}]$	DOF	$\bar{\epsilon}_p^{max} [\times 10^{-3}]$
3D FE models				
ABQ-Coarse	21,084	7.66	42,210	4.79
ABQ-Refined	64,260	8.07	63,210	4.89
TE models				
EBBT	363	-	363	-
TBT	605	-	605	-
TE1	1,089	-	1,089	-
TE2	2,178	5.65	2,178	3.57
LE models				
8L4 ¹ /12L4 ²	5,445	5.35	7,623	3.99
8L9 ¹ /12L9 ²	16,335	8.56	23,595	4.87

¹Two-layered beam ²Three-layered beam

exceeds the elastic limit. In case of single-layered beam, classical beam models fail to attain plasticity at the given load, whereas ABAQUS 1D underestimates the displacement at limit load by 21% (see Table 3.2).

2. For different classes of layered beams, higher order CUF 1D models are able to capture plastic behavior very accurately at a very reduced computational cost as compared to ABAQUS 3D solution.
3. From Table 3.3 and Table 3.5, it is evident further refinement of CUF models lead to increased accuracy in results
4. Failure of classical beam models such as EBBT and TBT and the lower-order models to capture plasticity is due to that fact that these models lack accurate description of stress fields.

3.2.2 Fixed-ended Lipped Channel Beam

The current example demonstrates the advanced capability of CUF for analyzing thin-walled metallic structures with material nonlinearity. The problem statement is based on the works of Abambres et al. [1]. The geometry and boundary conditions of the beam are illustrated in Fig. 3.7. Two vertical line loads of $\lambda N/mm$ is applied at the mid-span of the beam along the top and bottom flanges. The material behavior is assumed to be elasto-plastic with a Young's modulus, $E = 200GPa$, Poisson's ratio, $\nu = 0.3$ and yield stress, $\sigma_y = 450MPa$. A perfect plastic case is considered with strain-hardening slope $H = 0$. TE and LE models are used to model the problem as

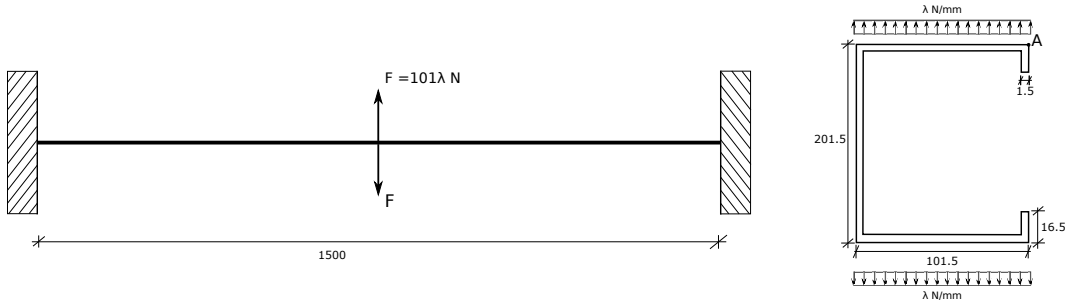


Fig. 3.7 Geometry of Fixed-ended Lipped Channel Beam

illustrated in Fig. 3.8. For the sake of comparison, additional FE model are developed in ABAQUS using shell elements (full integration with 5 Gauss points through the thickness) and 3D linear elements (linear elements with full integration) with degrees of freedom of 69,948 and 1,342,656 respectively [2].

The displacements are evaluated at point A (see Fig. 3.7) at two load points: (1) $\lambda = 12.69$ (elastic regime) and (2) $\lambda = 40.94$ (elasto-plastic regime), henceforth referred to as elastic and elasto-plastic point respectively. Table 3.6 comprises the

computed displacement at point A (see Fig. 3.7) for various beam models. The results are compared against reference solution obtained from the work of Abambres et al [1] and ABAQUS solutions. Three-dimensional deformation configuration obtained from LE-44L9 model and ABAQUS 3D model is illustrated in Fig. 3.10. Displacement profile (U_z) at point A along the length of the beam is depicted in Fig. 3.9. Figures 3.11-3.13 consists of contour plots at elasto-plastic point for von-Mises stress (σ_{vm}) distribution, equivalent plastic strain ($\bar{\epsilon}_p$) distribution and transverse stress (σ_{xy}) distribution.

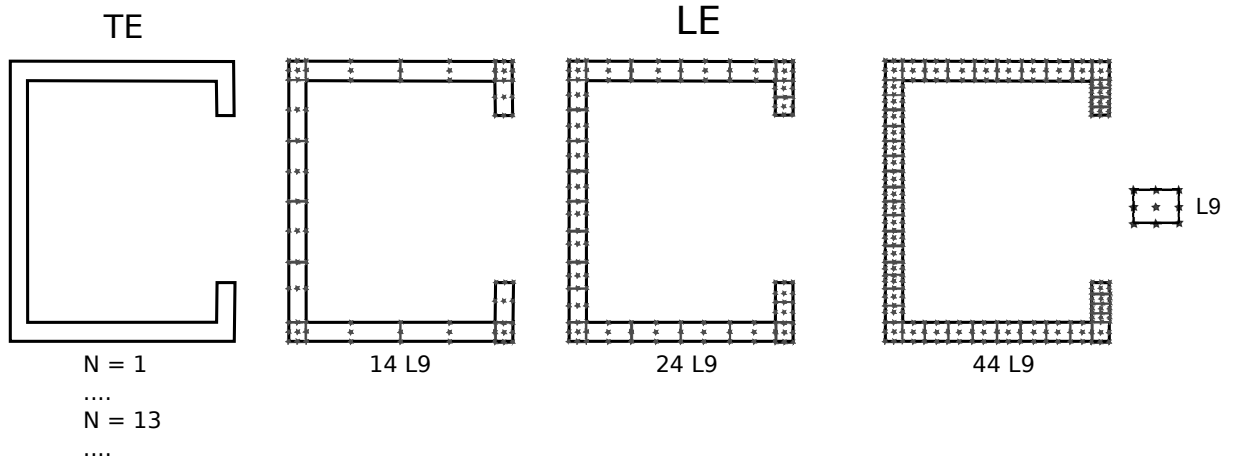


Fig. 3.8 TE and LE models for lipped channel beam

Following observations can be made:

1. CUF beam models - especially LE models - demonstrates the ability to produce accurate displacement and stress fields for thin-walled beams and their applicability for plasticity analysis
2. From Fig. 3.9, it is evident that displacement profiles for 44L9 and ABAQUS 3D model are similar and within the acceptable limits.
3. Local accumulation of plasticity can be observed at mid-span of the beam along the tip of the lip, flange and web-flange intersection.
4. From Table 3.6, it is evident that continued enrichment of the displacement field yields accurate results. LE-44L9 model requires only about 5.42% of the total degrees of freedom of that of an ABAQUS 3D model to provide similar results.
5. Since the deformation is localized at the mid-span of the beam, TE models fail to provide accurate displacement and stress fields

6. LE models tend to perform better as it is able to capture the local deformation and stress field more accurately.

Table 3.6 Vertical displacement at point A for various models for fixed-ended lipped channel beam

	NDOF	Displacement (u_z)	
		$\lambda = 12.69$	$\lambda = 40.94$
GBT [1]	3,222	13.63	77.6
ABAQUS - Shell	69,948	13.47	74.93
ABAQUS - 3D Brick	1,342,656	13.31	69.92
B4-10 elements			
TE			
EBBT	155	0.002	0.006
TBT	155	0.002	0.006
N=1	279	0.002	0.006
N=2	558	0.004	0.120
N=3	930	0.011	0.036
N=4	1,395	0.088	0.285
N=5	1,953	0.139	0.448
N=6	2,604	1.724	5.699
N=7	3,348	2.344	8.308
N=8	4,185	7.632	28.324
N=9	5,115	9.411	36.542
N=10	6,138	10.262	42.096
N=11	7,254	11.221	48.179
N=12	8,463	11.768	53.037
LE			
14L9	8,091	13.143	68.110
24L9	13,671	13.270	69.630
44L9	24,831	13.300	70.850
B4-20 elements			
TE			
EBBT	305	0.002	0.006
TBT	305	0.002	0.006
N=1	549	0.002	0.006
N=2	1,098	0.004	0.012
N=3	1,830	0.011	0.036
N=4	2,745	0.088	0.285
N=5	3,843	0.139	0.448
N=6	5,124	1.724	5.713
N=7	6,588	2.345	8.315
N=8	8,235	7.638	29.076
N=9	10,065	9.421	37.621
N=10	12,678	10.273	42.678
N=11	14,274	11.234	49.376

N=12	16,653	11.783	54.473
LE			
14L9	15,921	13.160	71.910
24L9	26,901	13.280	74.156
44L9	48,861	13.320	76.009
B4-30 elements			
TE			
EBBT	455	0.002	0.006
TBT	455	0.002	0.006
N=1	819	0.002	0.006
N=2	1,638	0.004	0.012
N=3	2,730	0.011	0.036
N=4	4,095	0.088	0.285
N=5	5,733	0.139	0.448
N=6	7,644	1.725	5.708
N=7	9,828	2.345	8.317
N=8	12,285	7.640	29.004
N=9	15,015	9.424	37.619
N=10	18,018	10.277	43.409
N=11	21,294	11.238	50.266
N=12	24,843	11.786	55.495
LE			
14L9	23,751	13.170	73.220
24L9	40,131	13.285	75.947
44L9	72,891	13.321	78.340

3.2.3 Clamped Z-beam under pressure load

A clamped Z - beam is acted upon by a pressure load along its length $L = 1000$ mm and at both flanges as depicted in Fig. 3.14. The pressure load acts in opposite directions, thereby inducing bending and torsional displacement effects in the structure. The cross-section of the beam is modeled using TE and LE models are depicted in Fig. 3.15. The material behavior of Aluminium is assumed with a Young's modulus, $E = 70 \text{ GPa}$, Poisson's ratio, $\nu = 0.3$ and nominal yield stress, $\sigma_y = 300 \text{ MPa}$. An isotropic elastoplastic with isotropic hardening is modeled with hardening data as tabulated in Table 3.7.

Table 3.7 Isotropic hardening data for Clamped Z-beam problem [119]

Stress (MPa)	300	340	355	375	390	410	430	450	470	484
Plastic Strain	0.000	0.00047	0.0012	0.0045	0.01036	0.0213	0.0344	0.0513	0.0800	0.147

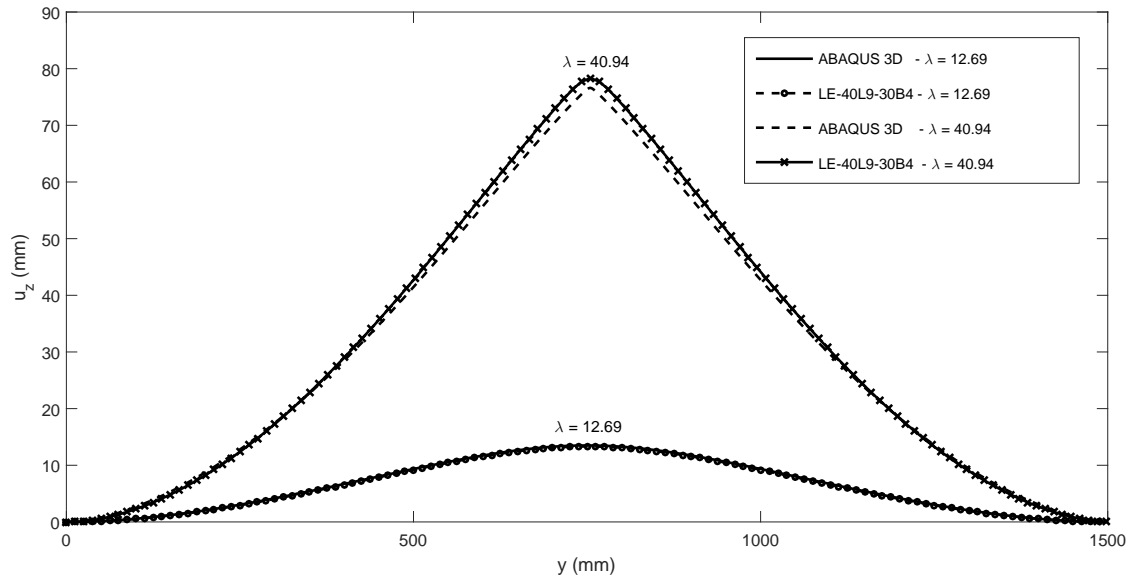


Fig. 3.9 Displacement profile (u_z) along of the beam for fixed-ended lipped channel beam

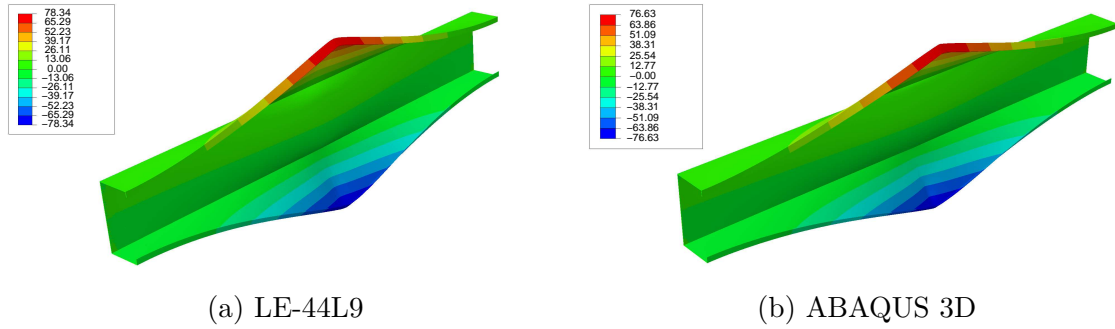


Fig. 3.10 Deformed configuration (u_z) at $\lambda = 40.98$ for fixed-ended lipped channel beam

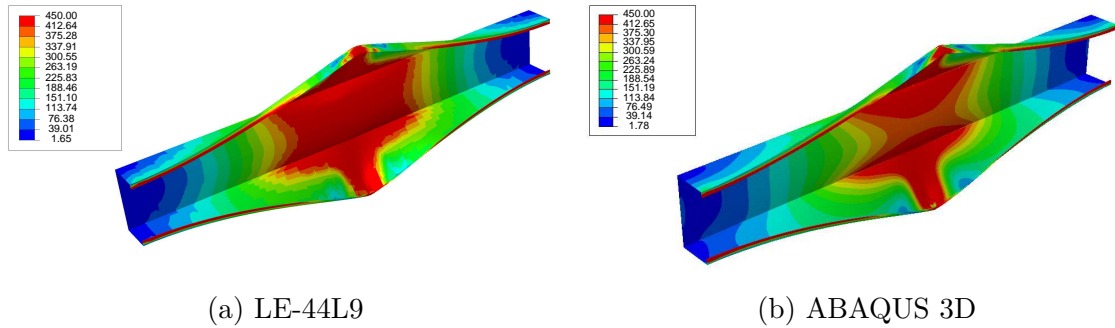


Fig. 3.11 von-Mises stress (σ_{xy}) distribution at $\lambda = 40.98$ for fixed-ended lipped channel beam

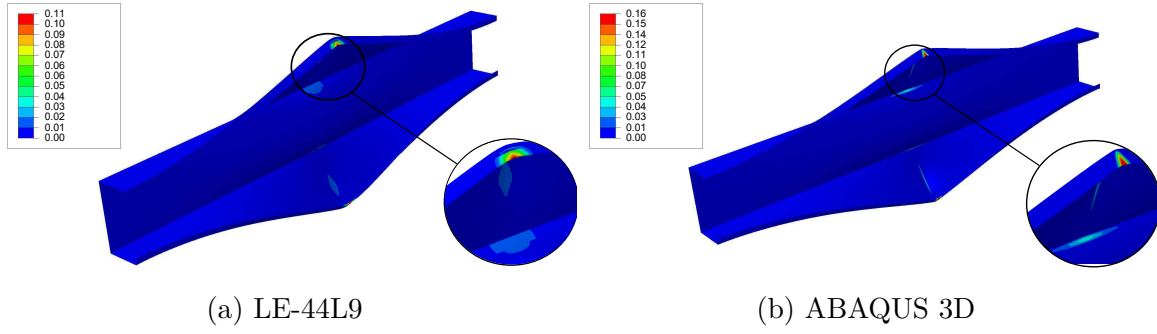


Fig. 3.12 Equivalent plastic strain ($\bar{\epsilon}_p$) distribution at $\lambda = 40.98$ for fixed-ended lipped channel beam

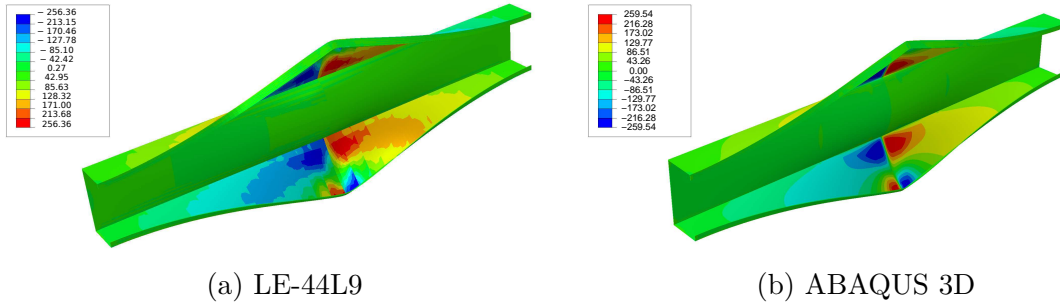


Fig. 3.13 Transverse stress distribution σ_{xy} at $\lambda = 40.98$ for fixed-ended lipped channel beam

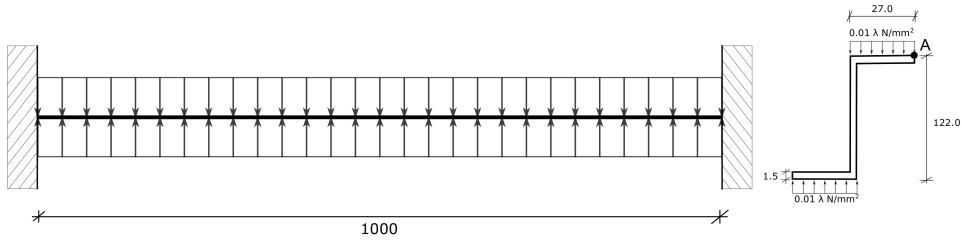


Fig. 3.14 Geometry of clamped Z Beam

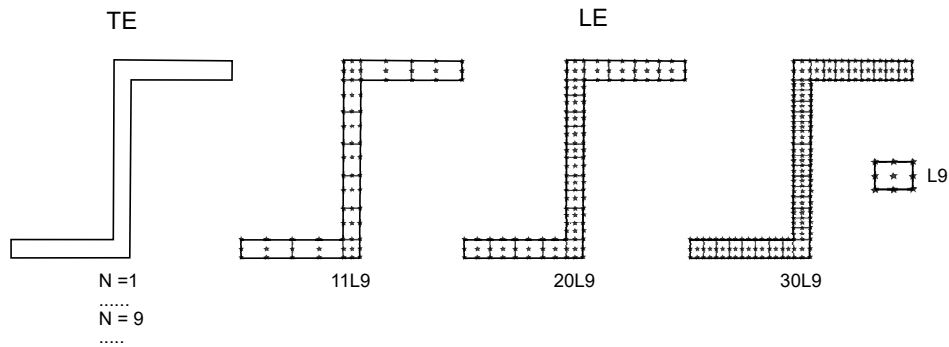


Fig. 3.15 TE and LE models for clamped Z Beam

A similar model was developed in ABAQUS using shell elements (full integration with 5 Gauss points through the thickness) and 3D linear elements (linear elements with full integration) with degrees of freedom 697,392 and 42,210 respectively [2]. Two load points are considered for evaluation: (1) $\lambda = 12$ (elastic regime) and (2) $\lambda = 50$ (elasto-plastic regime), henceforth referred to as elastic and elasto-plastic point respectively. The displacement u_x and u_z is evaluated at point A and tabulated for different beam models in Table 3.8. Contour plots of the LE-30L9 with 30 B4 elements models are compared against the reference ABAQUS 3D solutions. All the contour plots are evaluated at elasto-plastic point. The displacement profile (u_x) at point A along the beam is given in Fig. 3.16. Three-dimensional deformation configuration of the beam at elasto-plastic point for u_x and u_z are depicted in Fig. 3.17 and Fig. 3.18 respectively. von-Mises stress (σ_{vm}) distribution, equivalent plastic strain ($\bar{\epsilon}_p$) distribution and transverse stress (σ_{xy}) distribution are depicted in Figs. 3.19-3.21.

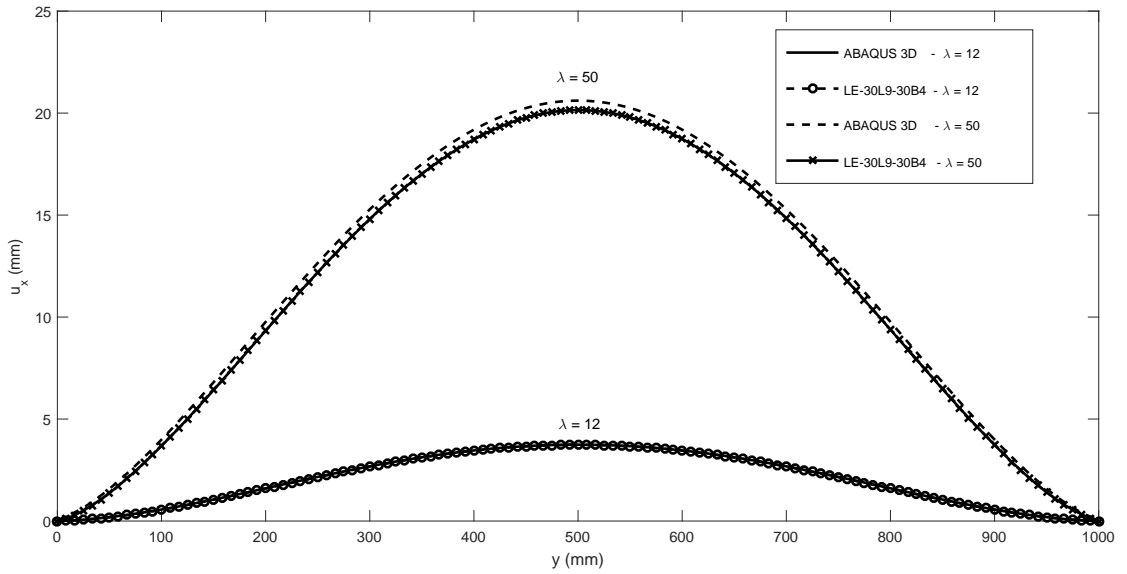


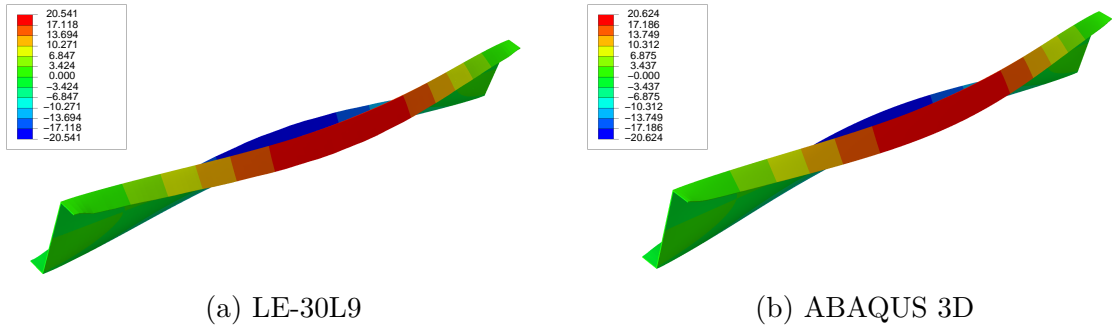
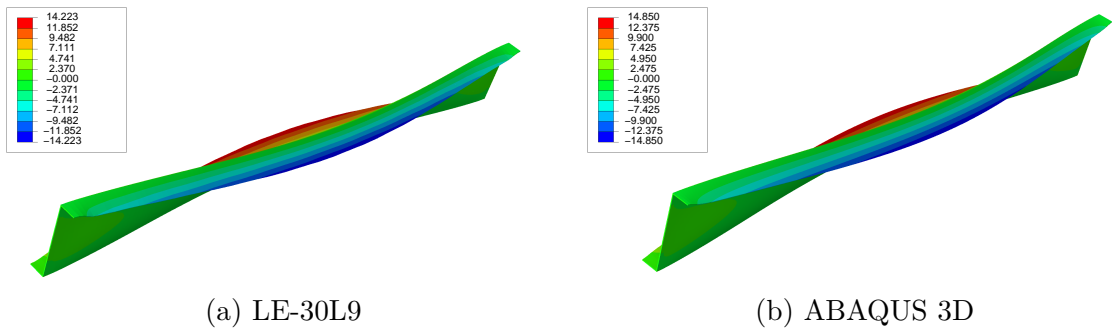
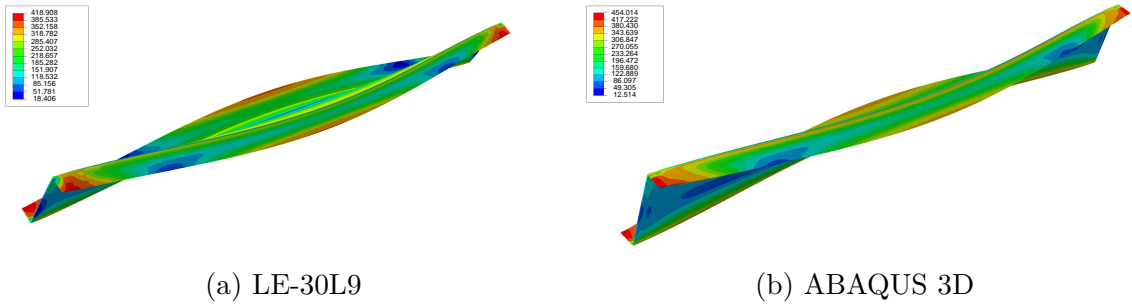
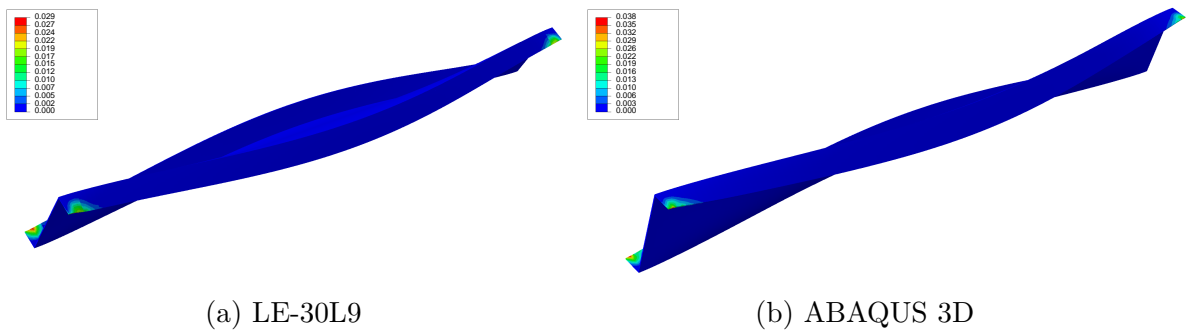
Fig. 3.16 Displacement profile (u_x) along of the beam for clamped Z beam

Following observations can be made

1. In contrast to classical models, higher order CUF models can capture displacement mechanisms and produces accurate stress field.
2. Local accumulation of plastic growth can be observed at clamped end of the beam at the flange-end

Table 3.8 Displacement for various beam configurations for clamped Z beam

Type	NDOF	Displacement at $\lambda = 12$		Displacement at $\lambda = 50$	
		u_x	u_z	u_x	u_z
ABAQUS 3D	697,392	3.74	3.046	20.62	14.85
ABAQUS 2D	42,210	3.79	2.803	21.02	13.89
B4 - 10 elements					
TE					
EBBT	155	0.045	0.021	0.186	0.086
TBT	155	0.045	0.021	0.186	0.086
N=1	279	0.045	0.021	0.186	0.086
N=2	558	0.466	0.202	1.942	0.841
N=3	930	0.476	0.207	1.981	0.864
N=4	1,395	2.710	1.173	11.589	5.015
N=5	1,953	2.736	1.312	11.765	5.613
N=6	2,604	3.436	1.694	15.958	7.775
N=7	3,348	3.425	2.025	15.852	9.101
N=8	4,185	3.642	2.164	17.756	10.131
N=9	5,115	3.646	2.417	17.458	11.045
LE					
11L9	6,417	3.703	2.786	17.902	12.673
20L9	11,439	3.704	2.835	17.930	12.880
33L9	18,693	3.705	2.852	17.940	12.962
B4 - 20 elements					
TE					
EBBT	305	0.045	0.021	0.186	0.086
TBT	305	0.045	0.021	0.186	0.086
N=1	549	0.045	0.021	0.186	0.086
N=2	1,098	0.466	0.202	1.943	0.841
N=3	1,830	0.477	0.208	1.987	0.866
N=4	2,745	2.723	1.178	11.857	5.129
N=5	3,843	2.750	1.318	12.058	5.734
N=6	5,124	3.457	1.703	17.103	8.266
N=7	6,588	3.446	2.033	17.023	9.592
N=8	8,235	3.665	2.174	19.114	10.714
N=9	10,065	3.669	2.427	19.066	11.733
LE					
11L9	12,627	3.726	2.796	19.599	13.399
20L9	22,509	3.728	2.845	19.627	13.609
33L9	36,783	3.727	2.869	19.710	13.758
B4 - 30 elements					
TE					
EBBT	455	0.045	0.021	0.186	0.086
TBT	455	0.045	0.021	0.186	0.086
N=1	819	0.045	0.021	0.186	0.086
N=2	1,638	0.466	0.202	0.186	0.086
N=3	2,730	0.477	0.208	0.186	0.086
N=4	4,095	2.727	1.180	1.943	0.841
N=5	5,733	2.755	1.319	1.988	0.867
N=6	7,644	3.463	1.706	12.035	5.206
N=7	9,828	3.452	2.036	18.089	10.041
N=8	12,285	3.672	2.177	20.445	11.288
N=9	15,015	3.676	2.430	20.577	12.379
LE					
11L9	18,837	3.733	2.799	20.056	13.596
20L9	33,579	3.735	2.848	20.160	13.840
33L9	54,873	3.735	2.886	20.541	14.223

Fig. 3.17 Deformed configuration (u_x) at $\lambda = 50$ for clamped Z beamFig. 3.18 Deformed configuration (u_z) at $\lambda = 50$ for clamped Z beamFig. 3.19 von-Mises stress (σ_{vm}) distribution at $\lambda = 50$ for clamped Z beamFig. 3.20 Equivalent plastic strain ($\bar{\epsilon}_p$) distribution at $\lambda = 50$ for clamped Z beam

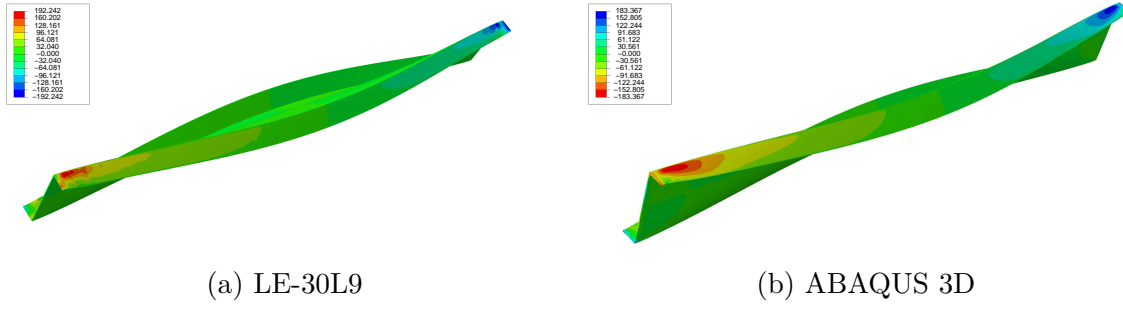


Fig. 3.21 Transverse stress (σ_{xy}) distribution at $\lambda = 50$ for clamped Z beam

3. In the case of TE models, only TE with $N=9$ or higher are able to capture the deformation mechanism quite accurately. This is because, unlike LE models, Taylor expansion functions have a global description of the cross-section.
4. Even the less-refined LE models (11L9) can capture the deformation mechanism quite accurately. It requires less than 2% of the total degrees of freedom of a 3D ABAQUS model to provide an accuracy within 7%.
5. LE-30L9 model requires only about 7.8% of the total degrees of freedom of that of an ABAQUS 3D model to provide similar displacement and stress fields.

3.3 Conclusion

A computationally efficient framework for physically non-linear structural simulation based on refined beam model is presented. von-Mises plasticity theory was incorporated along with Carrera Unified Formulation (CUF) to undertake non-linear finite element simulation. Isotropic non-linear strain-hardening is integrated into the constitutive model to account for material non-linearity. Modeling approaches based on TE (Taylor Expansion) and LE (Lagrange Expansion) are considered. Using the principle of virtual work, the nonlinear governing equations and related finite element approximation were formulated. Numerical results related to compact and thin-walled isotropic beam structures demonstrates the versatility and effectiveness of the CUF framework. Classical beam models such as Euler-Bernoulli Beam Theory (EBBT) and Timoshenko Beam Theory (TBT) fails to capture accurate stress field, which in turn leads to an inaccurate description of non-linear deformation state. CUF 1D models are able to detect 3D like effects and capture phenomena such as cross-section warping, bending-torsion coupling and localized deformation and plasticity growth, among the others, with great computational efficiency. The need of iterative schemes for physically

nonlinear problem leads to prohibitive computational cost and CUF 1D models can reduce such an overhead given that 10-100 times less unknown variables than traditional 2D/3D models are required.

Part II

Micromechanics and Multiscale

Chapter 4

A high-fidelity nonlinear micromechanical framework for hierarchical systems

The chapter presents a novel micromechanics platform formulated within the scheme of Carrera Unified Formulation to undertake linear and nonlinear analysis for various classes of representative volume elements (RVE) architectures. The ability of CUF-CW models to yield accurate local fields along with effective moduli prediction is demonstrated. The capability is extended to nonlinear analysis with integration of different nonlinear constitutive models including crack band for progressive failure analysis and shear driven plasticity model.¹

4.1 Micromechanical formulation

Within continuum mechanics, the homogeneous continuum is assumed to retain its bulk material properties irrespective of the scale. In case of real materials, the

¹Parts of this chapter has been in published in the following journals:

1. Kaleel I., Petrolo M., Waas A.M., Carrera E. (2017), "Computationally efficient, high-fidelity micromechanics framework using refined 1D models", Composite Structures 181:358-367
2. Kaleel I., Petrolo M., Waas A. M., Carrera E. (2017), Micromechanical Progressive Failure Analysis of Fiber-Reinforced Composite using Refined Beam Models. ASME. J. Appl. Mech. 85(2)
3. Kaleel I., Petrolo M., Carrera E. (2018), "Elastoplastic and progressive failure analysis of fiber-reinforced composites via an efficient nonlinear microscale model", Aerotecnica Missili and Spazio 97(2):103-110

assumption starts to fade at lower scales as they turn heterogeneous in nature [5]. The micromechanical formulations intends to capture the explicit heterogeneous nature of the microstructure and provide an effective continuum to the higher-scale by defining representative volume elements (RVE). RVE is defined as a volume of element that is large enough to effectively capture the nature of the microstructure from a statistical viewpoint. Homogenization provides effective properties based on the individual constituents of the RVE whereas de-homogenization (or localization) intends to capture the response of local constituents based on the response of the structure. Under an imposed deformation state, homogenization is achieved through volume averaging the stress and strain fields:

$$\bar{\epsilon}_{ij} = \frac{1}{V} \int_V \epsilon_{ij} dV \quad (4.1)$$

$$\bar{\sigma}_{ij} = \frac{1}{V} \int_V \sigma_{ij} dV \quad (4.2)$$

where V is the volume of RVE, σ_{ij} and ϵ_{ij} are the local stress and local strain within the individual constituents of the RVE, respectively.

4.1.1 Component-wise modeling within CUF

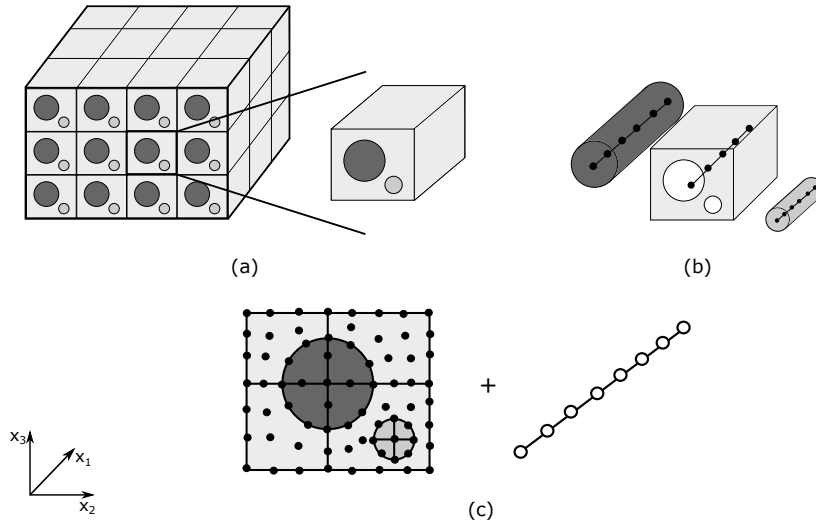


Fig. 4.1 A representation of CW modeling of periodic microstructure arbitrary constituents (a) a generic triply-periodic microstructure with three phases, (b) Individual components of RVE modeled via CW technique and (c) Assembled configuration of RVE with cross-section element overlaid on x-z plane and beam elements along the axis of beam

A heterogeneous triply-periodic microstructure RVE is formulated using the CW modeling technique elaborated in Chapter 2. Various constituents of the RVE is degenerated into individual component beams and assembled to construct the overall RVE. The CW also enable displacement continuity across the interface of different constituents. As illustrated in Fig. 4.1(c), multiple Lagrange elements are overlayed on the x_2 - x_3 plane attributing different constituents of the RVE. The cross-section extends along the span of the beam in x_1 direction.

The micromechanical formulation is postulated based on the assumption of periodicity. A Representative Volume Element (RVE) is assumed based on heterogeneous distribution of the constituent at the micro-scale. Sun and Vaidya laid out a rigorous mechanical foundation for periodic 3D RVE using strain energy equivalence [183]. In order to maintain compatibility of displacement along different faces of RVE, periodic boundary conditions (PBCs) need to be applied, which must maintain the energy equivalence [183, 209]. Therefore, displacements along the opposing boundary faces read:

$$u_i^{j+}(x, y, z) - u_i^{j-}(x, y, z) = \bar{\epsilon}_{ik}(x_k^{j+} - x_k^{j-}) \quad (4.3)$$

where $\bar{\epsilon}_{ik}$ is the average strains, indices $j+$ and $j-$ represent the positive and negative directions along x_k . As formulated by Sun and Vaidya [183], the average strains ($\bar{\epsilon}_{ij}$) and stresses ($\bar{\sigma}_{ij}$) the RVE are given by: The effective material matrix of the homogenized RVE can be formulated as

$$\bar{\sigma}_{ij} = \bar{\mathbf{C}}_{ijkl} \bar{\epsilon}_{ij} \quad (4.4)$$

where $\bar{\mathbf{C}}_{ijkl}$ is the homogenized material matrix of the RVE. The components of $\bar{\mathbf{C}}_{ijkl}$ matrix is populated by applying six individual unit strain. The homogenized stress for an applied unit strain corresponds to the respective column in the $\bar{\mathbf{C}}_{ijkl}$ matrix.

Introduction of PBC within a 3D RVE often requires tedious tracking and manipulation of degrees of freedom corresponding to boundary faces. CW modeling technique simplifies the PBC assignment by classifying them into two types: (1) PBC over the cross-section DOFs and (2) PBC over the end nodes of the beam, as illustrated in Fig. 4.2. For an applied macro strain $\bar{\epsilon}_{ij}$, explicit terms for PBC associated with cross-section of the RVE can be formulated as:

$$\begin{aligned} u_{2+}^1 - u_{2-}^1 &= \bar{\epsilon}_{22} l_2 & u_{3+}^1 - u_{3-}^1 &= \bar{\epsilon}_{33} l_3 \\ u_{2+}^2 - u_{2-}^2 &= 2 \bar{\epsilon}_{21} l_2 & u_{3+}^2 - u_{3-}^2 &= 2 \bar{\epsilon}_{31} l_3 \\ u_{2+}^3 - u_{2-}^3 &= 2 \bar{\epsilon}_{23} l_2 & u_{3+}^3 - u_{3-}^3 &= 2 \bar{\epsilon}_{32} l_3 \end{aligned} \quad (4.5)$$

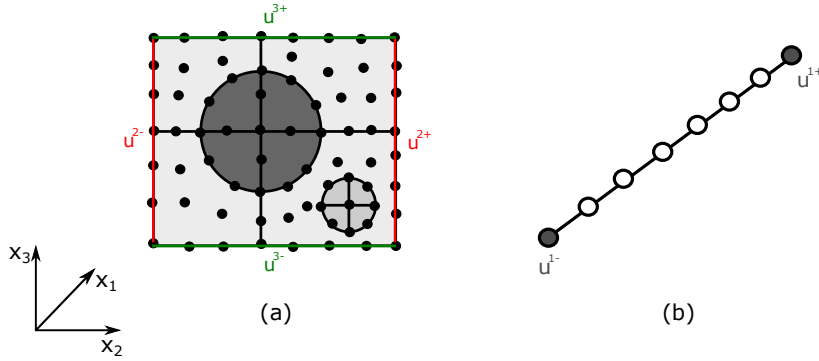


Fig. 4.2 Application of PBC for CUF-CW RVEs: (a) cross-section of the beam and (b) end nodes of the beam

where u_{x+}^k and u_{x-}^k represents the degrees of freedom associated with dimension x along the positive and negative direction of k respectively, l_2 and l_3 are the lengths of the cross-section along x_2 and x_3 , respectively. These constraints are applied for all corresponding cross-section degrees of freedom corresponding to every beam node in the RVE. PBCs associated with end beam nodes reads:

$$\begin{aligned} u_{1+}^1 - u_{1-}^1 &= \bar{\epsilon}_{11}L \\ u_{1+}^2 - u_{1-}^2 &= 2\bar{\epsilon}_{12}L \\ u_{1+}^3 - u_{1-}^3 &= 2\bar{\epsilon}_{13}L \end{aligned} \quad (4.6)$$

where u_{1-}^k and u_{1+}^k are the degrees of freedom associated with negative and positive end nodes of the beam element along the direction k and L is the length of the beam element. PBCs are inserted into the global system of arrays through penalty approach.

4.2 Constitutive models

Two classes of nonlinear constitutive models are integrated within the CUF-CW framework. Shear-driven inelastic nature of matrix constituents in polymer composites is modeled through plasticity based models. Progressive failure modeling of matrix constituents is achieved through crack band model implementations.

4.2.1 Shear-driven plasticity model

Non linear shear response exhibited by unidirectional laminates is usually associated with inelastic deformation within the matrix constituents of the composite. Experimental observations highlights the existence of ductile behavior of epoxy resin, especially

under shear loading conditions [71]. Ductile nature of the matrix implies the presence of pronounced plastic behavior under matrix-dominant deformations. Phenomenological material models based on plasticity formulations are often utilized to model the shear-driven pre-peak nonlinearity of polymer composites. Plasticity based inelastic models are often utilized to simulate the shear-driven non-linear behavior of polymer for meso-level and microscale analysis [182, 199, 219].

Recalling von-Mises J_2 theory from Section 3.1, the yield function reads:

$$\Phi = q(\boldsymbol{\sigma}) - \sigma_y(\bar{\epsilon}_p) \quad (4.7)$$

where $q(\boldsymbol{\sigma})$ is the equivalent von-Mises stress and $\sigma_y(\bar{\epsilon}_p)$ is the hardening function which is a function of accumulated plastic strain $\bar{\epsilon}_p$. In order to accurately characterize experimental curves, a four-parameter hardening model based on the work of Zhou et al is employed [219]:

$$\sigma_y(\bar{\epsilon}_p) = \sigma_0 + \sigma_\infty(1 - \eta e^{\beta \epsilon_p})(1 - \eta e^{\mu \epsilon_p}) \quad (4.8)$$

where σ_0 is the initial threshold often referred to yield stress, β , η and μ are parameters used to fit the hardening curve. Detailed information on constitutive model of the von-Mises model along with numerical implementation and tangent material matrix can found in Section 3.1.1.

4.2.2 Crack band model

Physical behaviour of crack band

Proposed by Bazant and Oh for heterogeneous aggregate materials (such as concrete), the crack band model captures the progressive micro-cracking in heterogeneous material systems characterized with strain-softening behavior by smearing the gradual effect of micro-cracking over a band of material with known dimension [22]. The theory combines concept of cohesive zone modeling within the classical continuum mechanics framework by characterizing the crack band growth on three parameters, namely fracture energy, the material strength and the dimension of the band. The formulation assumes linear elastic behavior until initiation of crack band, followed by linear degradation of stiffness until final failure. The tangent slope of post-peak softening curve is scaled by a characteristic length (band dimension) to ensure the total energy release upon complete failure corresponds to prescribed fracture toughness. The fracture toughness G_c of the material is estimated as the area under the traction-separation law, which governs the

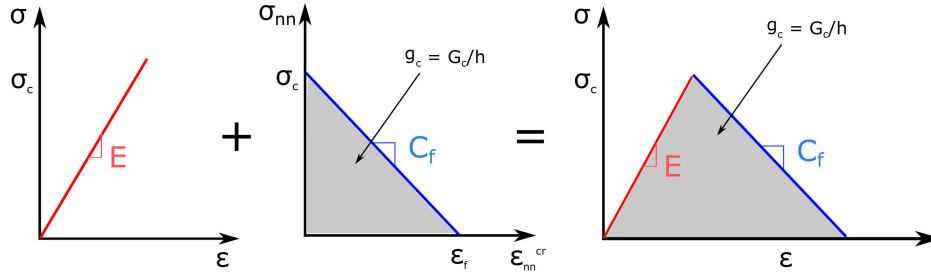


Fig. 4.3 Constitutive modeling of bilinear crack band model [22]

cohesive behavior of the crack growth.

$$G_c = \int_0^{\delta_f} \sigma \, du \quad (4.9)$$

where u is the crack displacement within the fracture zone. The original formulation hypothesized the orientation of the band perpendicular to the direction of maximum principal stress (pure mode I). Further reformulation of the crack band theory can be found extensively in found in literature [59, 124, 161]. de Borst and Nauta reformulated smeared crack band model to incorporate non orthogonal cracks [59]. The formulation also accounted for other non-linear phenomena such as plasticity, creep, thermal dilation and shrinkage. Maimí et al. extended the crack theory for prediction of failure mechanisms in laminated composite by incorporating sophisticated initiation criteria [124]. Pineda et al. implemented a variation of crack band model within the HFGMC micromechanics framework to model failure in fiber-reinforced polymer matrix composite [161].

Numerical implementation of crack band

The crack band model for mode I under tensile principal stress state is implemented within the CUF-CW micromechanics framework. The nature of the crack band mode is determined by the principal stress state $[\sigma_1^m, \sigma_2^m, \sigma_3^m]$ along with principal directions $[\mathbf{n}_1^m, \mathbf{n}_2^m, \mathbf{n}_3^m]$ computed at every gauss point of the RVE. The spurious mesh dependency is mitigated by rationally scaling fracture energy as depicted in Fig. 4.3. As proposed by Bazant [22], a characteristic length scale l_c computed based on the unit normal vector \mathbf{n}_1 to the crack band is introduced. The crack band is assumed to be in Mode I when the largest magnitude of the principal stress is tensile in nature. Therefore, the

crack band initiation criteria is set as [184]:

$$\frac{\sigma_1^m}{\sigma_c^m} = 1 \quad (4.10)$$

where σ_c^m is the cohesive strength of the crack band. The orientation of the crack band is fixed after the crack is initiated. The post-peak softening slope E_{IT} and the strain at failure is computed based on characteristic length l_c and matrix fracture toughness G_c [22]

$$\epsilon_f = \frac{2G_c}{\sigma_c^m l_c} \quad (4.11)$$

$$E_{IT} = \left(\frac{1}{E_m^0} - \frac{\epsilon_f}{\sigma_c^m} \right)^{-1} \quad (4.12)$$

where E_m^0 is the undamaged Youngs modulus of the matrix. Since E_{IT} must remain less than zero, an upper limit is enforced on the characteristic length l_c^{max} :

$$l_c^{max} < \frac{2G_c E_m^0}{\sigma_c^m} \quad (4.13)$$

The damage variable D_I is calculated as:

$$D_I = 1 + \frac{E_{IT}(\epsilon_c^m - \epsilon_1^m)}{E_m^0} \quad (4.14)$$

where rotated strain state ϵ_1^m is computed based on the rotation matrix for principal frame \mathbf{T} :

$$\epsilon_1^m = T_{1i}^m \epsilon_{ij}^m T_{1i}^m \quad (4.15)$$

The secant material matrix due to damage growth is computed as:

$$\mathbf{S}^d = \frac{1}{(1 - D_I)} \mathbf{S} \quad (4.16)$$

4.3 Numerical results

Three sets of numerical results are discussed in the section. First set of numerical examples pertains to linear elastic homogenization of different types of RVE architectures. Pre-peak nonlinearity exhibited by various kinds of composite material systems is studied in second set of numerical cases. Progressive failure analysis of a square-packed and randomly distributed RVE is investigated in the third set of numerical cases.

4.3.1 Linear elastic homogenization

Effective moduli of fiber-reinforced composite

The predictive capabilities of CUF-CW micromechanics framework is examined through evaluation of effective module for composite material systems. Two types of material systems are considered, namely Boron/Aluminum (Br/Al) and Graphite/Epoxy (Gr/Ep) material systems. The material properties for the material systems are tabulated in Table 4.1 with fiber volume fraction of 47% and 60% for Br/Al and Gr/Ep respectively. The CW discretization of the cross-section for different material systems

Table 4.1 Material properties for effective moduli predictions of fiber-reinforced composite

Material	E_{11} [GPa]	E_{22} [GPa]	G_{12} [GPa]	ν_{12} [-]	ν_{23} [-]
Graphite fiber	235.0	14.0	28.0	0.20	0.25
Boron fiber	379.3	379.3	172.41	0.10	0.10
Epoxy matrix	4.8	4.8	1.8	0.34	0.34
Aluminum matrix	68.3	68.3	26.3	0.30	0.30

is illustrated in Fig. 4.4. The beam of the RVE is discretized with 2 B4 element along with a cross section containing 20 L9 elements. The total degrees of freedom amounts to 1869. The predicted results are compared against literature including solution based on

1. Finite element approach by Sun et al [183]
2. CCM by Rotem et al. [94]
3. Method of Cells (MOC) by Aboudi [4]
4. Generalized Method of Cells (GMC) by Paley et al. [157]
5. High Fidelity Generalized Method of Cells (HFGMC) by Aboudi et al. [7],
6. Elasticity based Cell Method (ECM) by Williams [204]
7. Variational Asymptotic Method for Unit Cell Homogenization (VAMUCH) by Yu et al. [213]

The predicted effective properties for two material systems along with literature comparisons are enlisted in Table 4.2 and Table 4.3.

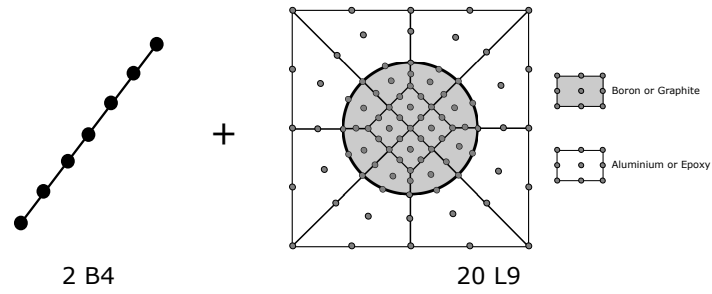


Fig. 4.4 CW modeling of the square-packed RVE for effective moduli prediction of Boron/Aluminium and Graphite/Epoxy material systems

Table 4.2 Predicted effective moduli for Boron/Aluminum composites

Models	E_{11} [GPa]	E_{22} [GPa]	G_{12} [GPa]	G_{23} ([GPa]	ν_{12} [-]	ν_{23} [-]
CUF-CW	215.2	144.3	54.4	46.0	0.195	0.253
FEM [183]	215.0	144.0	57.2	45.9	0.190	0.290
CCM [94]	231.9	127.3	54.0	49.6	0.193	0.282
MOC [4]	215.0	142.6	51.3	43.7	0.200	0.250
GMC [157]	215.0	141.0	51.2	43.7	0.197	0.261
HFGMC [7]	215.4	144.0	54.3	45.8	0.195	0.255
ECM (3^{rd}) [204]	215.0	143.4	54.3	45.1	0.190	0.260
VAMUCH [213]	215.0	144.1	54.4	45.9	0.195	0.255

Table 4.3 Predicted effective moduli for Graphite/Epoxy composites

Models	E_{11} [GPa]	E_{22} [GPa]	G_{12} [GPa]	G_{23} [GPa]	ν_{12} [-]	ν_{23} [-]
CUF-CW	142.8	9.6	6.10	3.13	0.252	0.349
FEM [183]	142.6	9.6	6.00	3.10	0.250	0.350
CCM [94]	144.6	8.9	5.8	3.3	0.252	0.361
MOC [4]	143.0	9.6	5.47	3.08	0.250	0.350
GMC [157]	143.0	9.5	5.68	3.03	0.253	0.358
HFGMC [7]	142.9	9.6	6.09	3.10	0.252	0.350
ECM (3^{rd}) [204]	143.0	9.6	5.85	3.07	0.250	0.350
VAMUCH [213]	142.9	9.6	6.10	3.12	0.252	0.350

Effect of fiber packing architecture

A study on the effect of fiber-packing architecture on the effective moduli is investigated. Two types of RVE architectures are taken into consideration: (a) square-packed and (b) hex-packed RVE. As depicted in Fig. 4.5, square-packed RVE is modeled with 20 L9 element whereas 44 L9 elements are utilized to model hex-packed RVE. A 2B4 beam configuration is used for both architecture. As tabulated in Table 4.4, predicted results are compared against solutions of Sun and Vaidya [183].

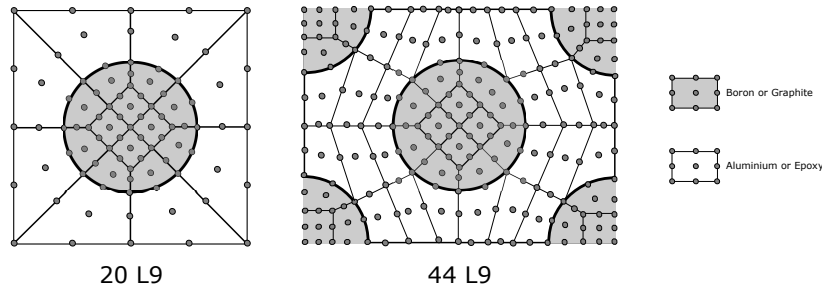


Fig. 4.5 CW modeling of the square-packed and hex-packed RVE for studying the effect of fiber packing architecture

Table 4.4 Comparison of elastic moduli for various RVE architecture for Boron/Aluminium and Graphite/Epoxy material system

	Boron/Aluminium (Fiber VF=47%)				Graphite/Epoxy (Fiber VF=60%)			
	Square-packed		Hex-packed		Square-packed		Hex-packed	
	CUF-CW	FEM [183]	CUF-CW	FEM [183]	CUF-CW	FEM [183]	CUF-CW	FEM [183]
E_1	215.22	215.0	215.19	215.0	142.83	142.60	142.83	142.6
E_2	144.29	144.0	132.91	136.5	9.63	9.60	9.17	9.20
ν_{12}	0.19	0.19	0.19	0.19	0.25	0.25	0.25	0.25
ν_{23}	0.25	0.29	0.31	0.34	0.35	0.35	0.38	0.38
G_{12}	54.44	57.2	54.18	54.0	6.10	6.00	5.86	5.88
G_{23}	46.03	45.9	51.13	52.5	3.13	3.10	3.34	3.35

De-homogenization of randomly distributed fiber reinforced composite

The following numerical case emphasizes on the ability of CUF-CW models to produce accurate 3D fields at a reduced computational overhead. A randomly distributed

fiber-reinforced RVE with a volume fraction of 60% is considered. The size of the RVE is $21.25\mu m \times 21.25\mu m$ and it is based on the work of Pineda et al. [161]. The material properties for fiber and matrix are enlisted in 4.1 and the cross-section of the RVE is modeled with 265 L9 elements (see Fig. 4.6). A beam configuration of 2 B4 element is utilized to model the RVE, thereby amounting to a total degree of freedom of 19,080. For the sake of comparison, a similar RVE is modeled in ABAQUS using 24,765 3D linear elements. The mesh density of 3D FE model was chosen post a mesh convergence analysis. A global transverse strain $\bar{\epsilon}_{22}$ of 0.001 is applied to the RVE. Table 4.5 compares the numerical results for CUF-CW and ABAQUS 3D models

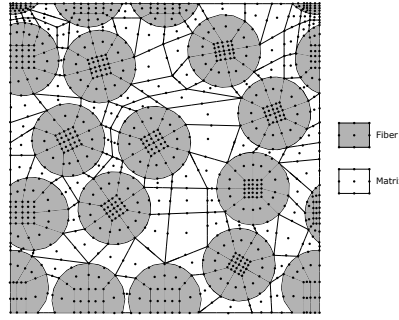


Fig. 4.6 CW discretization of the cross-section of RVE with 13 randomly distributed fibers and a fiber volume fraction of 60%

along with the total analysis time. Comparisons are made between contour plots of maximum principal strain (ϵ_1^p) and transverse stress (σ_{22}) for CUF-CW and ABAQUS 3D for as depicted in Fig. 4.7 and Fig. 4.8 respectively.

Table 4.5 Numerical results from de-homogenization of RVE with 13 randomly distributed fibers subjected to transverse tensile strain

	DOF (-)	Maximum principal strain $\epsilon_1^{max} \times 10^{-3}$	Maximum transverse stress σ_{22}^{max} (MPa)	Analysis time (s)
CUF-CW	19,080	2.08	14.92	18
ABAQUS 3D	91,305	2.11	14.22	324

Results suggests:

1. The effective moduli of different composite material systems are accurately predicted by CUF-CW models
2. CUF-CW are able to capture the effect of different RVE architecture on the effective moduli

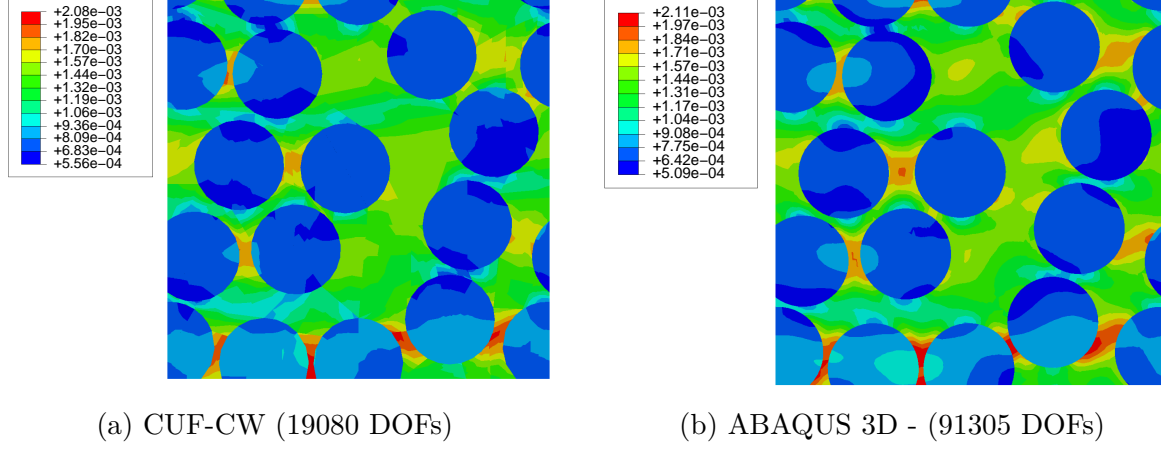


Fig. 4.7 Maximum principal strain contours ϵ_1^p over the cross-section of the RVE with 13 randomly distributed fibers subjected to transverse tensile strain (a) CW-CUF model and (b) ABAQUS 3D model

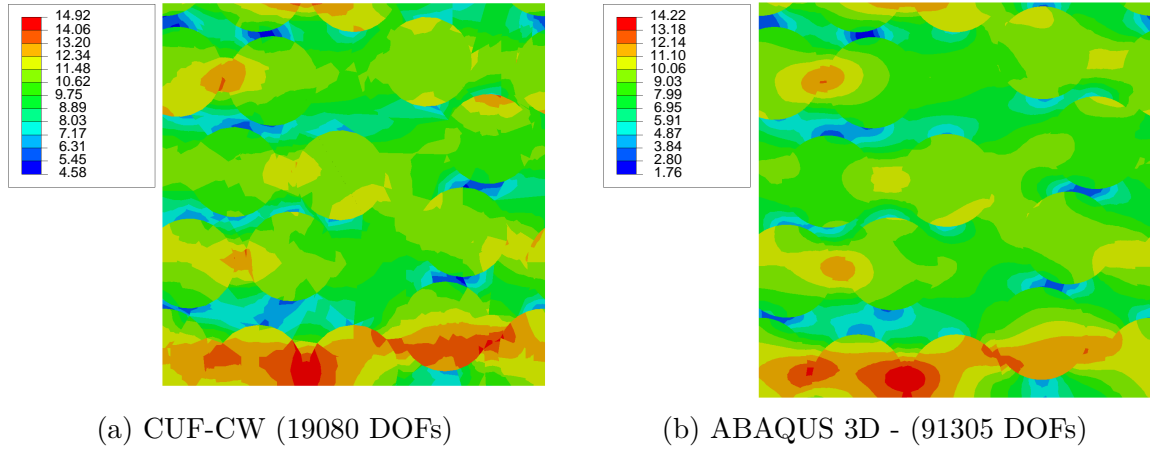


Fig. 4.8 Transverse stress contours σ_{22} [MPa] over the cross-section of the RVE with 13 randomly distributed fibers subjected to transverse tensile strain (a) CW-CUF model and (b) ABAQUS 3D model

3. Comparison of contour plots obtained by CUF-CW models against ABAQUS 3D solution demonstrates the high-fidelity of the framework.
4. In addition, the analysis time taken by CUF-CW models are 18s whereas ABAQUS 3D model requires 324s, thereby demonstrating computational efficiency of CUF-CW framework.

Effective moduli of Void filled composite

CUF-CW framework is utilized to investigate global and local behaviour of void-filled composite RVEs. The void-filled RVE is assigned with a material properties of Copper with Young's modulus of 127 GPa and Poisson ratio of 0.34. Two classes of inclusion shapes are investigated, namely (a) square and (b) circular. A 2B4 beam configuration is used and the total degrees of freedom amounts to 4,032 and 3,780 for circular and square voided composite RVE respectively. Figure 4.9 depicts the CW modeling of two void-filled Cu composite. The effective transverse Young's modulus is predicted

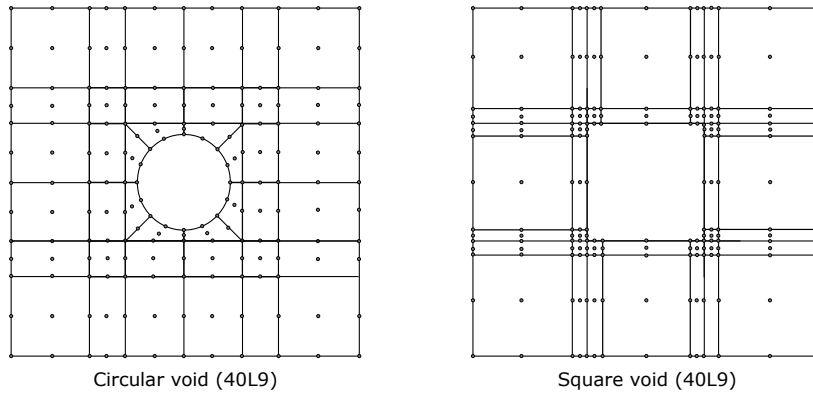


Fig. 4.9 CW discretization of the circular and square void for analysis of void filled Cu composite

for different void volume fractions of 0.0204, 0.1837, 0.5102 and 0.7511. As tabulated in Table 4.6, the predicted results are compared against solutions from the literature including

1. Method of Cells (MOC) by Aboudi [4]
2. Elasticity-based Cell Method (ECM) (3^{rd} and 5^{th} order) by Williams [204],
3. Variational Asymptotic Method for Unit Cell Homogenization (VAMUCH) by Yu et al. [213]

For sake of comparison, a similar 3D FEM model using linear brick element is developed for square voided Cu composite RVE with volume fraction of 0.5102. The ability of CUF-CW models to capture strong stress gradients around the corner on square voided Cu composite is demonstrated by comparing the von-Mises stress contour plot against ABAQUS 3D solution. The von-Mises stress contour plot for an applied transverse tensile strain ($\bar{\epsilon}_{11}$) of 0.001 is depicted in Fig. 4.10. The total degrees of freedom for ABAQUS 3D model amounted to 72,225 with analysis time of 201s whereas CUF-CW model requires only 3456 degrees of freedom with analysis time of 5s.

Table 4.6 Predicted transverse Young modulus E_{22} (GPa) of void-filled Cu composite with varying void volume fraction

	Void volume fraction			
	0.0204	0.1837	0.5102	0.7511
Circular void				
CUF-CW	120.36	82.27	39.57	10.32
VAMUCH [213]	120.34	82.67	39.08	10.31
FEM [213]	120.34	82.64	39.08	10.31
Square void				
CUF-CW	120.22	82.02	39.85	18.28
MOC [4]	110.20	75.27	38.22	17.99
G-F [201]	120.63	83.50	40.48	18.40
ECM (3rd)[204]	110.20	75.38	38.23	17.99
ECM (5th)[204]	118.90	80.97	39.64	18.20
VAMUCH [213]	120.22	81.73	39.75	18.25
FEM [213]	120.22	81.70	39.75	18.25

The results suggest that

- In comparison to reference solutions, the CUF-CW models accurately predicts the transverse Young modulus
- Strong stress-gradients exhibited by square voided composite is efficiently captured by CUF-CW models.

Effective moduli of Periodical cellular material

The effective moduli of a peridical cellular material is predicted using CUF-CW models. The architecture of RVE under investigation is hexagonal (see Fig. 4.11(a)) with an isotropic material of Young's modulus E_0 of 0.91 GPa and Poisson ratio ν of 0.3. Table

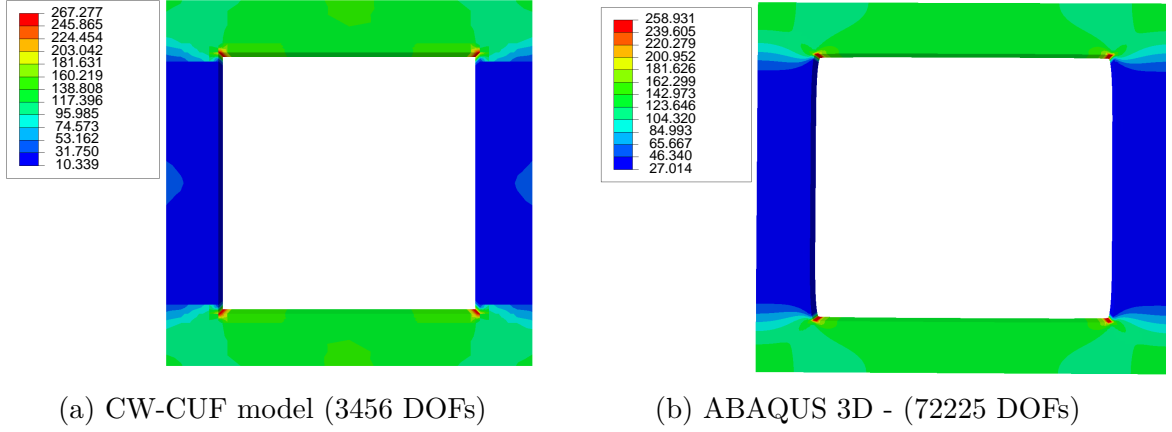


Fig. 4.10 von-Mises stress contours σ_{vm} [MPa] over the cross-section of the RVE of void-filled Cu composite with a void volume fraction of 0.5102 subjected to transverse tensile strain (ϵ_{11}): (a) CUF-CW and (b) ABAQUS 3D

4.7 lists the dimensions of the hexagonal honeycomb RVE. As depicted in Fig. 4.11(b), the RVE is modeled using 28L9 elements. The micromechanical formulation dictates the insertion of elements in the void areas (white areas in Fig. 4.11(b)) with a weak material of very low stiffness ($E_{void}/E_0 = 10^{-5}$). The RVE is discretized with 2B4 elements along the axis. Accounting for additional degrees of freedom due to void elements, the total degrees of freedom amounts to 6,993. A similar ABAQUS 3D model is developed using 3D linear element with a total degrees of freedom of 79,104.

Table 4.7 Dimensions of hexagonal honeycomb RVE

a	t/a	ϕ
$3^{-3/4}$	$\sqrt{3}/12$	60°

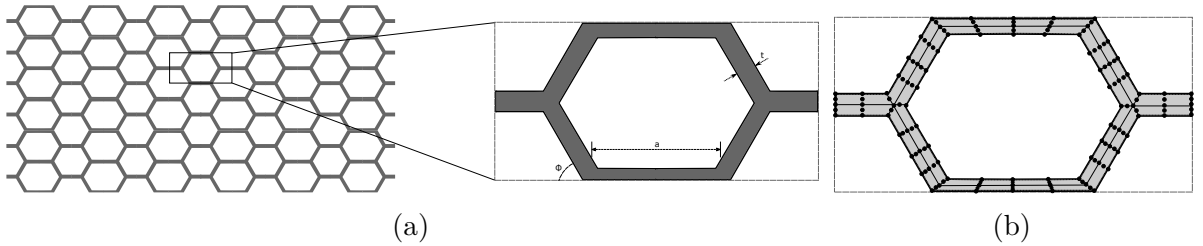


Fig. 4.11 Architecture of hexagonal honeycomb RVE: (a) Dimensions of the hexagonal honeycomb RVE and (b) CW discretization of the cross-section for hexagonal honeycomb RVE using 18L9 elements

The predicted transverse Young's modulus for different models are tabulated in Table 4.8 along with reference solution by Gibson and Ashby [83]. A de-homogenization analysis is undertaken with RVE being subject to transverse strain (ϵ_{33}) of 0.001. Maximum principal strain (ϵ_1^p) contour and von-Mises stress (σ_{vm}) are depicted in Fig. 4.12 and Fig. 4.13, respectively. Results suggests that

Table 4.8 Predicted tranverse Young modulus E_{22} (GPa) of the cellular hexagonal honeycomb RVE

CUF-CW	G-A MMM [83]	FEM 3D
0.0504	0.0498	0.0485

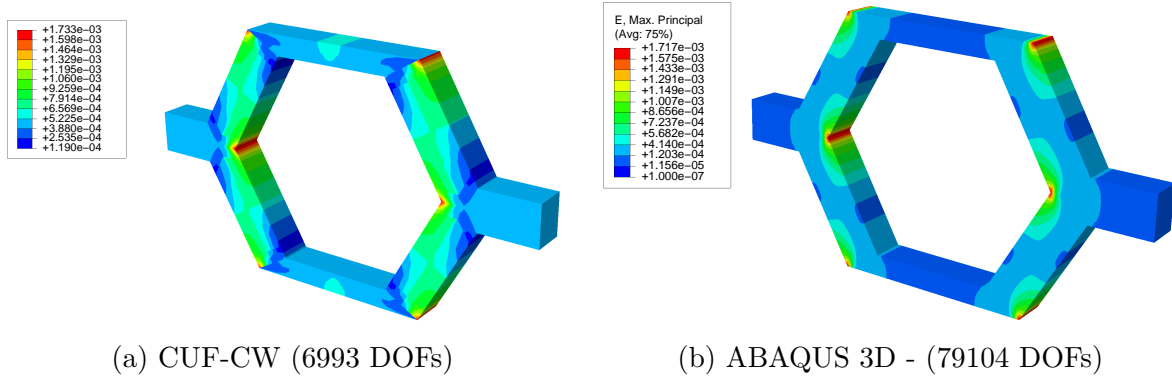


Fig. 4.12 Maximum principal strain contours ϵ_1^p for hexagonal honeycomb RVE with subjected to transverse tensile strain (ϵ_{33}) (a) CW-CUF model and (b) ABAQUS 3D model

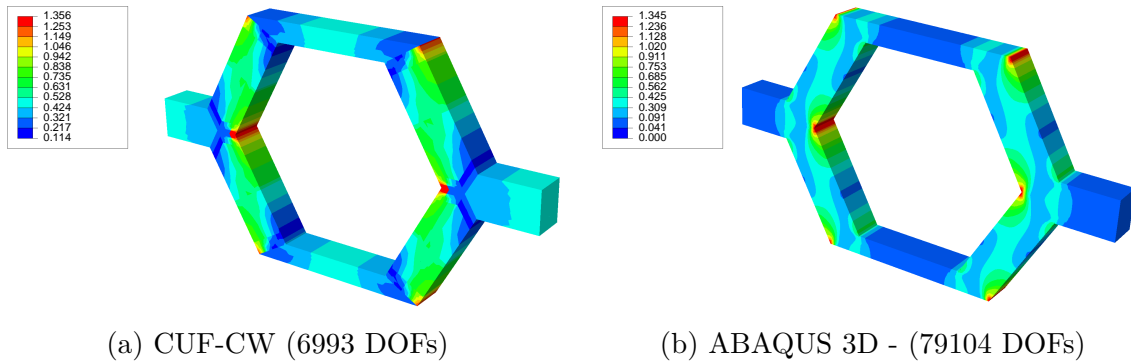


Fig. 4.13 von-Mises stress contours σ_{vm} [MPa] for hexagonal honeycomb RVE with subjected to transverse tensile strain (ϵ_{33}) (a) CW-CUF model and (b) ABAQUS 3D model

- In comparison to the reference solution and FEM 3D results, CUF-CW can predict the transverse Young modulus accurately.
- CUF-CW can effectively capture strong gradients within the honeycomb RVE.

4.3.2 Modeling pre-peak nonlinearity in composites

Nonlinear shear behavior of unidirectional composites

In-plane shear response of three different material systems are investigated. The material system under consideration are:

1. E-Glass-MY750
2. HTA-6376
3. IM7-8552

Table 4.9 Mechanical properties of fibers

Fiber type	E-Glass [179]	HTA [147]	IM7 [109]
V_f (%)	60	62	60
E_1^f (GPa)	74.0	223.0	272.5*
E_2^f (GPa)	74.0	23.0	15.5*
G_{12}^f (GPa)	30.8	32.0	29.0*
G_{23}^f (GPa)	30.8	7.0	7.0
ν_{12}^f (-)	0.20	0.28	0.2

* Calibrated values

The calibrated elastic material properties various constituents of the material system are enlisted in Table 4.9 and Table 4.10. A four-parameter hardening model is employed to simulate the pre-peak nonlinearity within the matrix constituents. Table 4.11 tabulates the calibrated hardening properties for different matrices (see Fig. 4.14 for the hardening curves). The cross-section configuration of the square-packed RVE is similar to the one presented in Section 4.3.1 with a dimension of $10\mu m \times 10\mu m \times 0.1\mu m$ (length \times width \times thickness).

In Fig. 4.15, the in-plane shear response obtained using CUF-CW is compared against experimental and reference literature solution for three different material system. In order to emphasis on the efficiency of the CUF-CW model, an additional assessment on comparison of shear response prediction is undertaken. The assessment employs a

Table 4.10 Predicted elastic properties for three unidirectional laminates

Fiber Type	E-Glass	HTA	IM7
Matrix Type	MY750	6376	8552
E_1 (GPa)	46.1	139.6	165.0
E_2 (GPa)	15.9	10.1	9.0
G_{12} (GPa)	5.9	5.9	5.6
G_{23} (GPa)	4.3	3.1	3.1
ν_{12} (-)	0.2	0.19	0.34

Table 4.11 Calibrated material properties for matrix along with hardening curve parameters

Matrix	E (GPa)	ν (-)	R_0 (MPa)	R_∞ (MPa)	β (-)	η (-)	μ (-)
MY750	4.3	0.27	60.0	115.0	-3.5	0.56	-170.0
6376	3.7	0.20	40.3	120.0	-12.5	0.40	-170.0
8552	4.1	0.29	65.0	120.0	-10.0	0.60	-250.0

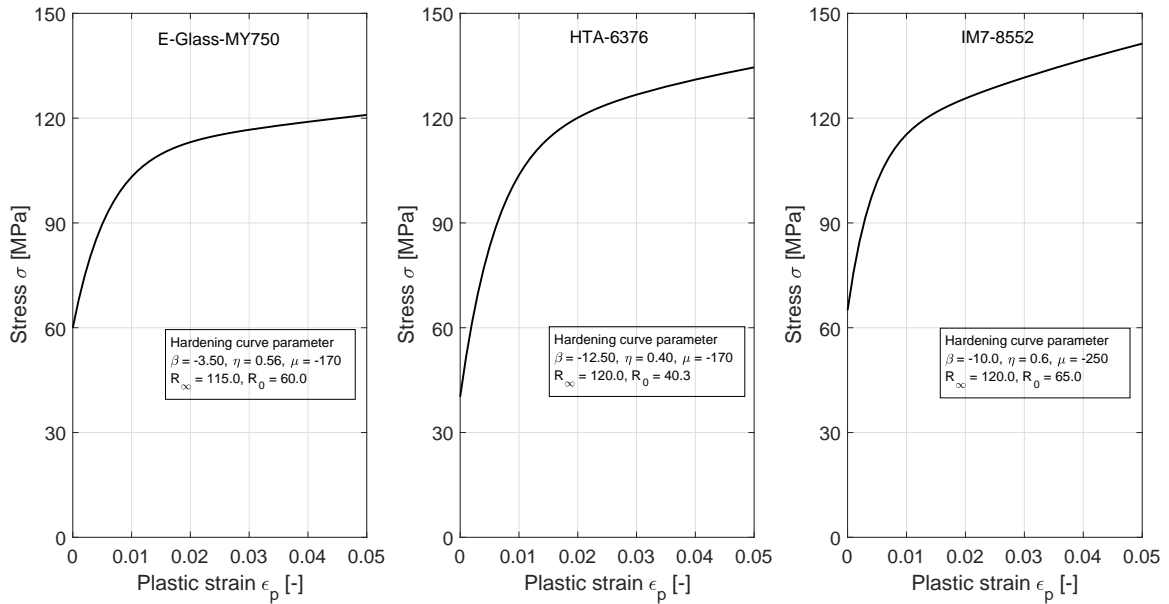


Fig. 4.14 Hardening curve for three laminate systems with curve parameters

square-packed RVE modeled using 1656 standard 3D brick element for comparison. The in-plane shear response of HTA-6376 material response using CUF-CW and FEM 3D models are depicted in Fig. 4.16. Table 4.12 compares the modeling information including total degrees of freedom, number of gauss points within each model and total analysis time for CUF-CW and 3D FEM model.

Table 4.12 Numerical results for from 3D FEM and CUF-micro model for the in-plane shear response of HTA-6376

	DOF	Number of gauss points	Total analysis time [s]
CUF-micro	1,869	1,440	130
FE-micro	6,405	13,248	271

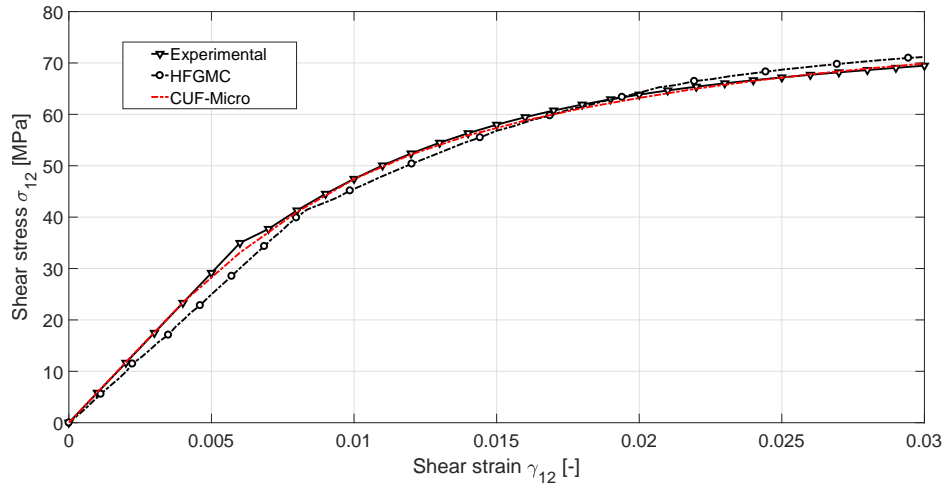
Modeling pre-peak nonlinearity in randomly distributed fiber RVE

The numerical example focuses on simulating pre-peak nonlinearity within a randomly distributed fiber RVE. Current example is an extension of the dehomogenization analysis for a randomly distributed RVE undertaken in Section 4.3.1. The architecture of the RVE is depicted in Fig. 4.6. The fiber is assumed to be transversely isotropic elastic and matrix constituents of the RVE exhibits inelastic deformations based on plasticity model. The material properties of fiber and matrix constituents of the RVE is tabulated in Table 4.13. The matrix is assumed to exhibit perfect plasticity with a yield stress σ_y of 5 MPa. A transverse strain $\bar{\epsilon}_{22}$ of 0.003 is applied across the faces of RVE. A similar model using ABAQUS 3D linear brick elements is developed using 24,765 C3D8 elements.

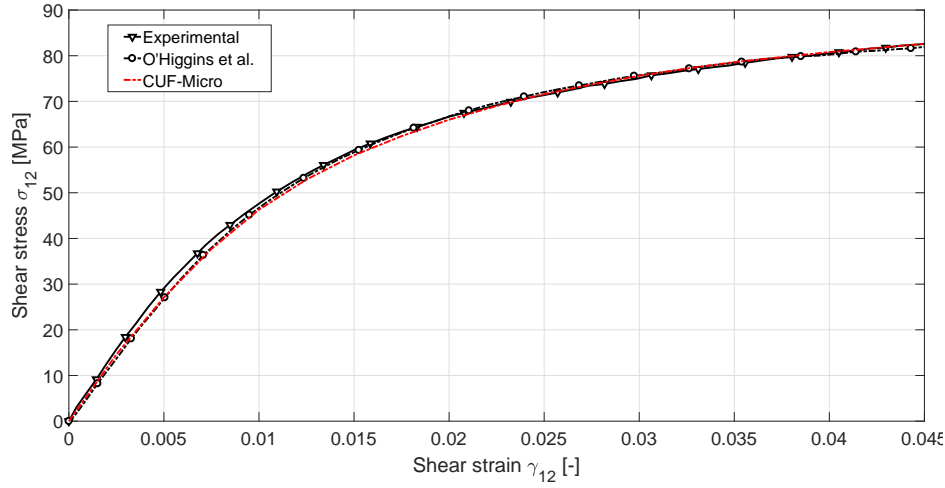
Table 4.13 Numerical results for from 3D FEM and CUF-micro model for the in-plane shear response of HTA-6376

	E_{11} (GPa)	E_{22} (GPa)	ν_{12} (-)	G_{12} (GPa)	G_{13} (GPa)
Fiber	126	7.5	0.263	4.98	2.97
Matrix	4.65	4.65	0.35	1.72	1.72

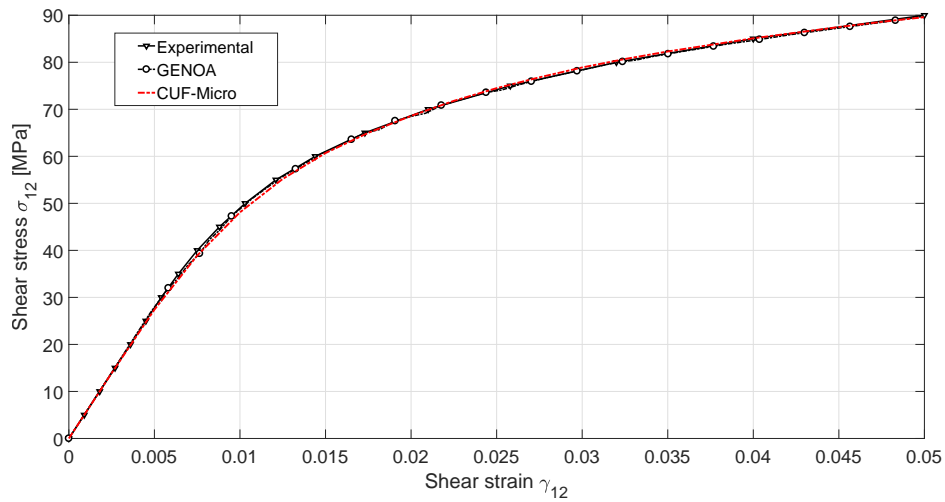
Figure 4.17 compares the contour plots for inelastic plastic strain for CUF-CW and ABAQUS 3D models. The global nonlinear stress-strain response of randomly distributed RVE for CUF-CW and ABAQUS 3D model are compared in Fig. 4.18. Table 4.14 enlists the numerical results including maximum plastic strain, model size and analysis time for different models.



(a) E-Glass/MY750 (Experimental [179] and HFGMC [23])



(b) HTA-6376 (Experimental [126] and Higgins et al. [147])



(c) IM7-8552 (Experimental [109] and GENOA [47])

Fig. 4.15 Comparison of in-plane shear responses for three unidirectional material systems

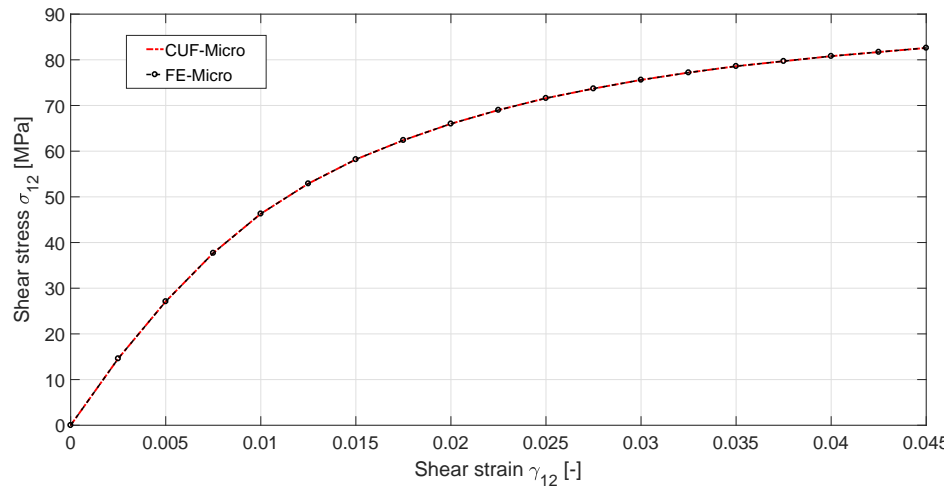


Fig. 4.16 Comparison between 3D FEM and CUF-micro for the in-plane shear response of HTA-6376 material system

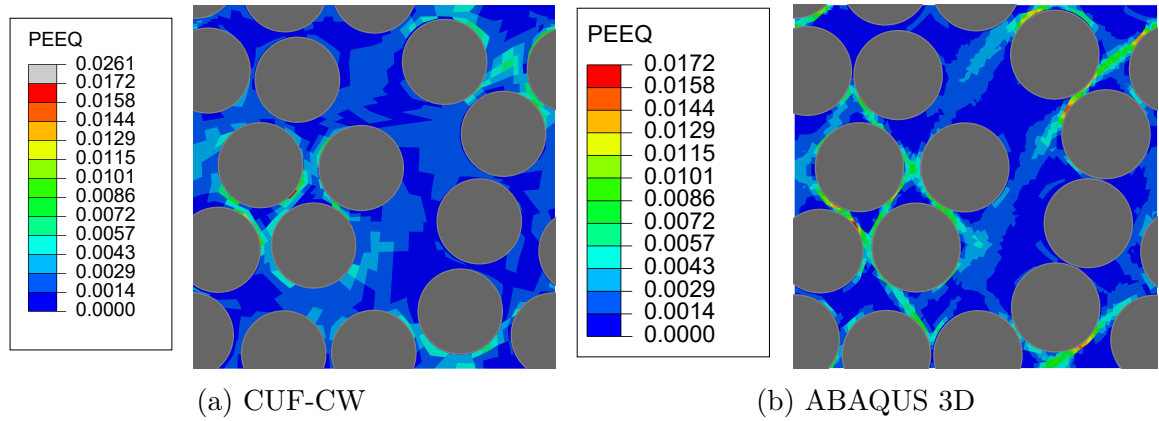


Fig. 4.17 Contour plots of inelastic plastic strain for randomly distributed RVE under transverse strain $\bar{\epsilon}_{22}$ of 0.003

Table 4.14 Numerical results for pre-peak nonlinear response of randomly distributed RVE under transverse strain $\bar{\epsilon}_{22}$ of 0.003

Models	DOF	No. of gauss points	ϵ_p^{max} ($\times 10^{-2}$)	Total analysis time [s]	Average iters per NR step	Time per increment [s]
CUF-CW	13,644	9,540	2.61	1,109	4	36
ABAQUS 3D	91,305	99,060	1.72	4,034	4	134

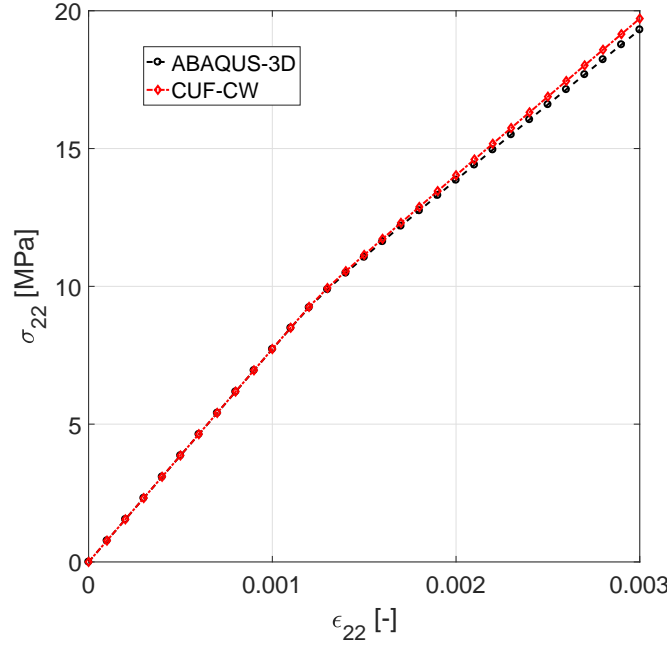


Fig. 4.18 Comparison of global stress-strain response for pre-peak nonlinear response of randomly distributed RVE under transverse strain $\bar{\epsilon}_{22}$ of 0.003

Following observations can be drawn:

1. In comparison to reference experimental and numerical solution, CUF-CW models provides accurate nonlinear shear behavior.
2. For randomly distributed fiber RVE, in addition to capturing the global stress-strain curve accurately, CUF-CW models provide accurate resolution of local inelastic strain contour plot within the RVE.
3. On average, CUF-CW models provide a reduction in total analysis time by a factor of 3.
4. In addition, CUF-CW exhibits multi-fold reduction in the required number of gauss points within the RVE, which can lead to great reduction in memory overhead within a multiscale framework.

4.3.3 Progressive failure analysis of fiber-reinforced composite

The post-peak softening behavior exhibited by uni-directional E-Glass/MY750 Epoxy composite under transverse loading due to matrix cracking is simulated. Based on the

work of Pineda et al., two classes of RVE architecture are considered in the current study: (a) Square-packed and (b) Randomly distributed fiber-reinforced RVE [160, 161]. The fiber is assumed to be linear elastic and bi-linear crack band model is employed for matrix constituents. Material properties including fracture properties are tabulated in Fig. 4.15.

Table 4.15 Material properties of glass fiber and epoxy matrix for progressive failure analysis of fiber-reinforced composite [160, 161]

	Young's modulus	Poisson Ratio	Shear modulus	Fracture properties	
	E (GPa)	ν (-)	G (GPa)	σ_c (MPa)	G_c (N/mm)
Fiber	74.00	0.20	30.80	-	-
Matrix	4.65	0.35	1.79	66.5	0.000563

In addition to CUF-CW model, 3D FEM model using standard 3D linear brick element is developed for the randomly distributed RVE. Table 4.16 enlists numerical details including the total degrees of freedom and number of gauss points for different models used for both RVE architecture. As listed in Table 4.16, two CUF-CW models, namely CUF-CW (265L9) and CUF-CW (276L9), are developed for analyzing randomly-distributed RVE with the latter model having increased kinematics within the matrix zone with additional L9 elements (see Fig. 4.19). A global transverse strain $\bar{\epsilon}_{22}$ of 0.008 and 0.004 is applied for square-packed and randomly distributed fiber RVE respectively.

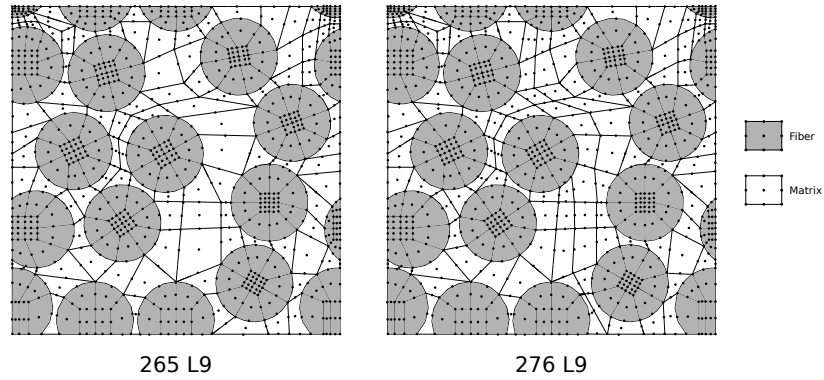


Fig. 4.19 CW discretization of the cross-section of RVE with 13 randomly distributed fibers

Figure 4.20 depicts the global transverse stress-strain curve for different RVE architectures. In case of square-packed RVE, the results are compared against the solutions of Pineda et al. [160] whereas the CUF-CW results for randomly distributed RVE is compared against solutions obtained using 3D FEM model. Numerical results

Table 4.16 Model information for progressive failure analysis of fiber-reinforced composite

Models	Model information	DOF	No. of GP
Square-packed RVE (Dimension: $0.8 \mu m \times 8 \mu m \times 8 \mu m$, VF: 58%)			
CUF-CW	The cross-section is modeled using 20L9 along with 2 B4 element along the beam axis (see Fig. 4.5).	1,869	1,440
Randomly distributed RVE (Dimension: $(3\mu m \times 21.25\mu m \times 21.25\mu m)$, VF: 59%)			
CUF-CW (265L9)	The cross-section is modeled using 265L9 along with 2 B4 element along the beam axis (see Fig. 4.19).	23,877	19,080
CUF-CW (276L9)	The cross-section is modeled using 276L9 along with 2 B4 element along the beam axis (see Fig. 4.19). Additional L9 elements are added in the matrix zone to enrich the kinematic field within matrix constituents.	24,843	19,872
FEM -3D	24,765 standard linear 3D brick elements. Mesh density is chosen after a convergence study with respect to elastic fields	91,305	198,120

including the ultimate transverse stress and strain are tabulated in Table 4.17 and Table 4.18 for square-packed and randomly distributed RVE respectively. The final damage contour plot obtained using CUF-CW for square-packed RVE is compared against the solutions of Pineda et al. [160] in Fig. 4.21. Various stages of damage progression for different models of randomly distributed RVE is depicted in Fig. 4.22.

Table 4.17 Numerical results for square-packed RVE under transverse tension

	Ultimate transverse stress (MPa)	Strain at ultimate transverse stress (-)
GMC [160]	54.6	0.00310
HFGMC [160]	56.8	0.00313
FEM-2D [160]	51.3	0.00267
CUF-CW	59.7	0.00314

Results suggests:

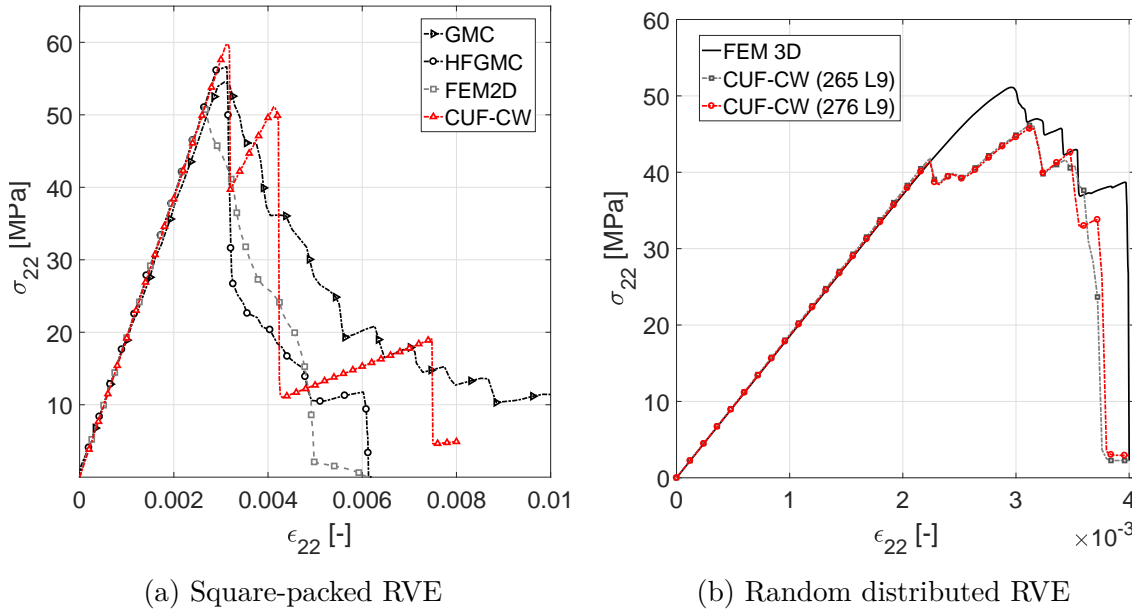


Fig. 4.20 Transverse tensile stress versus strain for progressive failure analysis under transverse tension for different RVE architecture

Table 4.18 Numerical results for randomly distributed RVE under transverse tension

	Ultimate global stress	Strain at ultimate stress	Strain at complete failure	Total CPU time
	(MPa)	(-)	(-)	(min)
CUF-CW (265 L9)	46.15	0.0031	0.0037	36
CUF-CW (276 L9)	45.71	0.0031	0.0038	48
FEM 3D	51.11	0.0029	0.0040	108

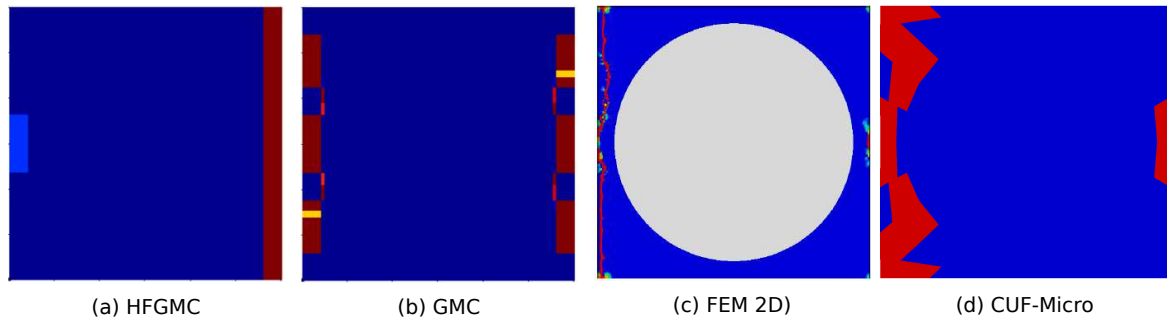


Fig. 4.21 Comparison of final damage contour plots for CUF-CW against solutions from literature [160] for square-packed under transverse tension

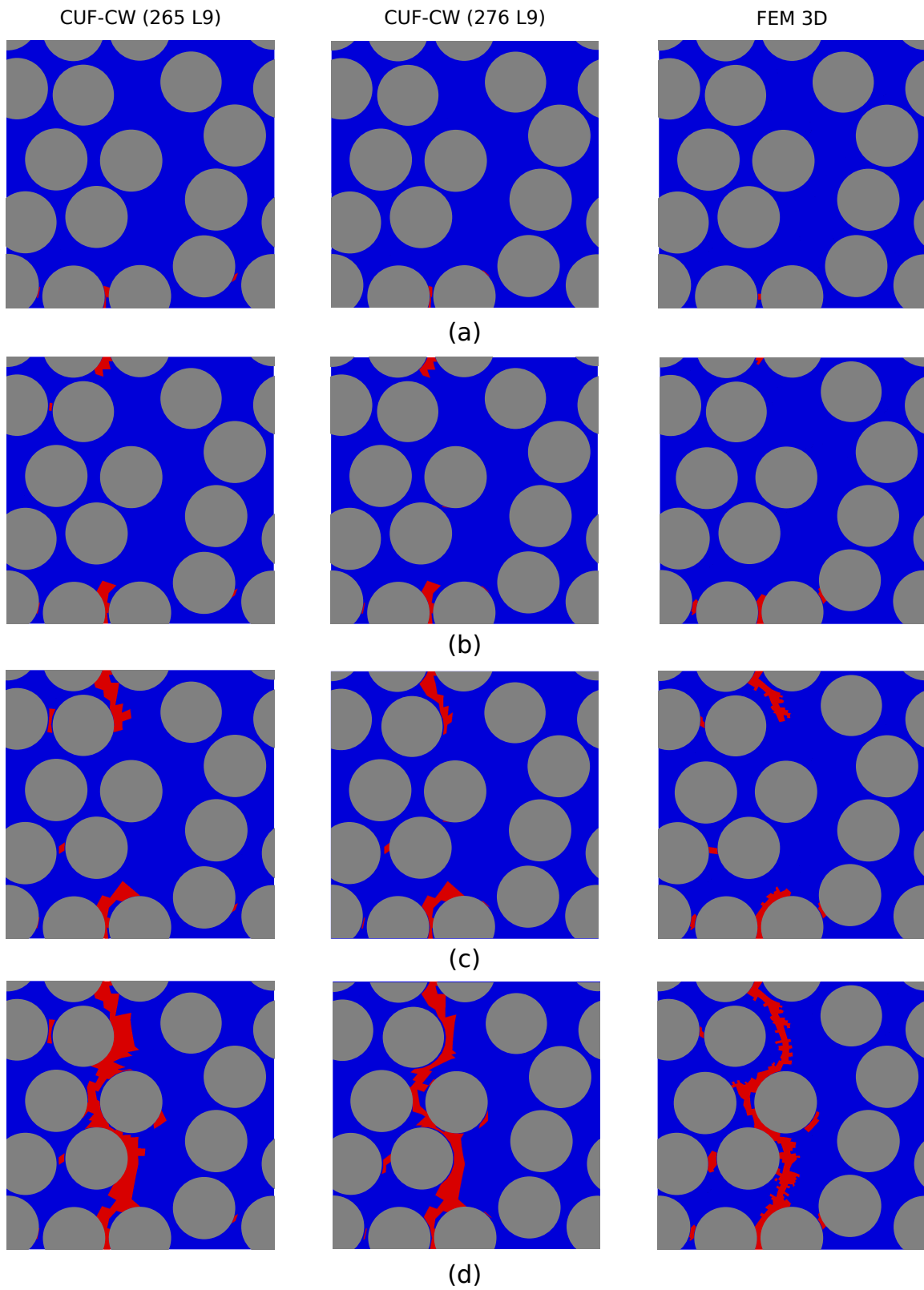


Fig. 4.22 Damage progression in the randomly distributed fiber composite under transverse tension at global strains (a) 0.00225, (b) 0.00275 (c) 0.0035 and (d) 0.004 (Gray: Fiber, Blue: Undamaged matrix, Red: Damaged matrix)

1. The capability of CUF-CW to capture various stages of damage progression is successfully illustrated.
2. It is evident from Fig. 4.21 and Fig. 4.22 that the CUF-CW models captures the brittle nature of failure by losing its load-carrying capacity in steps, evidenced in experimental observations.
3. The global stress-strain curves for different RVE architectures are comparable to reference solutions as well as the results obtained using 3D FEM models. The predicted ultimate global transverse stress by CUF-CW models are within the acceptable limits of accuracy.
4. In case of randomly distributed RVE, lack of first load drop within 3D FEM model can be ascribed to the stagnation of the first crack band at the top of RVE.
5. In case of randomly distributed RVE, the total analysis time for two CUF-CW models are 36 and 48 minutes whereas 3D FEM model requires 108 minutes for the analysis. A three-fold reduction in total computational time and a ten-fold reduction in the terms of memory requirement can be observed. analysis.

4.4 Conclusion

A novel and computationally-efficient micromechanics framework, built within the scheme of Carrera Unified Formulation (CUF), for physically nonlinear analysis is presented. The representative volume element (RVE) is modeled using the Component-Wise approach (CW), an extension of CUF beam model based on Lagrange type polynomials. Nonlinear constitutive models such as crack band for progressive failure analysis and shear driven plasticity model is incorporated into the framework. The versatility of the framework is demonstrated through numerical results taken from literature for fiber-reinforced composite, void-filled composite and periodic cellular material. CUF-CW models are able to accurately predict the effective moduli in tandem with accurate 3D fields recovery.

Pre-peak nonlinearity within the matrix constituent is modeled using von-Mises plasticity model. CUF-CW models accurately predicted the nonlinear shear behavior for different material systems in comparison to experimental and literature reference solutions. For randomly distributed RVE, CUF-CW provided accurate resolution of inelastic strain within matrix constituents of the RVE. Micromechanical progressive

failure analysis of a square-packed and randomly distributed RVE under transverse tension is undertaken. The predicted failure modes using CUF-CW corresponds well with the analogous FEM 3D model and observations made in the experiments. On average, CUF-CW models are able to produce solutions in the range of 3D FE models with a three-fold decrease in terms of analysis time and ten-fold reduction in the memory requirement. In the view of multi-fold efficiency, these models serve as an ideal candidates for computationally-intensive concurrent multiscale framework. Employing CUF-CW at the lower scale in such frameworks can significantly boost the overall efficiency both in terms of analysis time and memory requirements.

Chapter 5

A computationally-efficient nonlinear concurrent multiscale framework

A computationally efficient concurrent multiscale platform to undertake linear and nonlinear analysis is presented in the chapter. The framework exploits refined one-dimensional model based on CUF to model various components across multiple scales. The nonlinearity is introduced within individual constituents at the micro scale and its effect is scaled up to the macroscale by means of homogenization. The efficiency of the framework is quantified through comparisons with the analysis time and memory requirement against traditional multiscale implementations.¹

5.1 Multiscale framework within CUF

The CUF micromechanics framework is interfaced with a macro scale CUF framework as schematically illustrated in Fig. 5.1. In the proposed multiscale scheme, the material response of each integration point in the macro model is established by applying macroscopic strain on micro RVE model through periodic boundary conditions. Scale transition between the scales is achieved through homogenization technique, i.e, volume

¹Parts of this chapter has been in published in the following journals:

1. Kaleel I., Petrolo M., Carrera E., Waas A.M. (2019), "A computationally efficient concurrent multiscale framework for the nonlinear analysis of composite structures" (Under review)
2. Kaleel I., Petrolo M., Carrera E., Waas A.M. (2019), "A computationally efficient concurrent multiscale framework for the linear analysis of composite structures" (Under review)

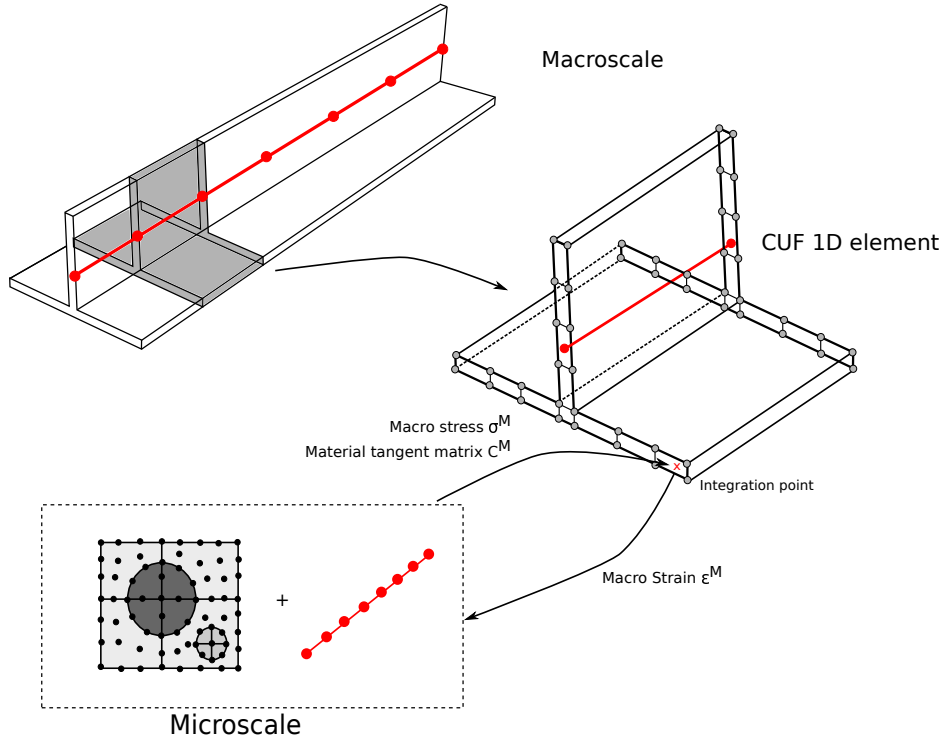


Fig. 5.1 Illustration of multiscale modeling within the CUF framework

averaging of the microscopic quantities in the microscale RVE. The generality within the CUF framework facilitates the usage of same implementation at multiple scales. Additionally, variable kinematic nature of the framework aids in integrating various classes of finite element in a competent manner. Detailed information on the formulation of micromechanical problem can be found in Chapter 4. Algorithm 1 outlines the steps involved for every micromechanical update call received from the macro scale.

5.1.1 Computation of consistent macroscopic tangent matrix

The efficiency and convergence behavior of a multiscale iterative scheme hinges on accurate computation of macroscopic tangent matrix, which must be consistent with the macroscopic stress evolution. In case of numerical microscale model, lack of explicit macroscale constitutive formulation necessitates the extraction of macroscopic stress and material tangent matrix in an ensemble averaged sense. Numerical tangent matrix computation within a multi-level FE framework was first formulated by Kouznetsova et al. [115], where fourth-order consistent macroscopic tangent tensor was derived from condensing the micro finite element tangent matrix. The procedure involves computation of Schur complement for matrix inversion, which could be memory

Algorithm 1 Iterative algorithm for non linear CUF-CW micromechanics toolbox**Input:** $\Delta\epsilon_{ij}^t, \Delta t$ **Output:** $\mathbf{C}_{tan}^t, \bar{\sigma}^t, HistM^t$

1. Recall last converged state macro solution state
 $\bar{\sigma}_{ij}^{t-\Delta t}; \bar{\epsilon}_{ij}^{t-\Delta t}; HistM^{t-\Delta t}; NLFlag^{t-\Delta t}$ ▷ NLFlag is true for nonlinear RVEs
2. **if** .not. NLFlag **then** ▷ RVE is in elastic regime
 - (a) Computing the deformation state of RVE based on input total and incremental macro strain $\Delta\epsilon_{ij}^t$ ▷ Eqn1
 - (b) Evaluate incremental and total strains at all integration points in the RVE
 - (c) Evaluate stress updates at all integration points in the RVE and check for non linear initiation
 - (d) **if** (Initiation condition satisfied) **then**
 $NLFlag \leftarrow \text{True}$
 - (e) Compute and update the macro stress and state variables
 $\bar{\sigma}^t \leftarrow \langle \sigma_{ij}^{(\alpha\beta)^i} \rangle; HistM^t \leftarrow \langle Histm^{(\alpha\beta)^i} \rangle$
3. **if** NLFlag **then** ▷ RVE is in non-linear regime
 - (a) Recall last converged state micro solution state
 $U^{(\alpha\beta)^{t-\Delta t}}; \sigma_{ij}^{(\alpha\beta)^{t-\Delta t}}; \epsilon_{ij}^{(\alpha\beta)^{t-\Delta t}}; Histm^{(\alpha\beta)^{t-\Delta t}}$
 - (b) **while** ($\|R\| \leq tol$) **do** ▷ Iterative Newton-Raphson iteration
 - i. Assemble the overall global tangent stiffness matrix $K_{tan}^{(\alpha\beta)^{i-1}}$ with incremental strain applied as PBC
 - ii. Compute the global incremental displacement of the RVE
 $K_{tan}^{(\alpha\beta)^{i-1}} \delta U^{(\alpha\beta)^i} = R^{i-1}; \Delta U^{(\alpha\beta)^i} = \Delta U^{(\alpha\beta)^{i-1}} + \delta U^{(\alpha\beta)^i}$
 $U^{(\alpha\beta)^i} = U^{(\alpha\beta)^{i-1}} + \Delta U^{(\alpha\beta)^i}$
 - iii. Evaluate incremental and total strain at all integration points in the RVE based on current displacement field
 $\Delta\epsilon_{ij}^{(\alpha\beta)^i} \leftarrow \Delta U^{(\alpha\beta)^i}; \epsilon_{ij}^{(\alpha\beta)^i} \leftarrow U^{(\alpha\beta)^i}$
 - iv. Perform non linear stress updates at all integration points in the RVE to obtain updated stress and history variables
 $\sigma_{ij}^{(\alpha\beta)^i}; Histm^{(\alpha\beta)^i}$
 - v. Compute and assemble global residual error R based on current micro stress $\sigma_{ij}^{(\alpha\beta)^i}$
 - (c) Update the micro solution variables
 $U^{(\alpha\beta)^t} \leftarrow U^{(\alpha\beta)^i}; \sigma_{ij}^{(\alpha\beta)^t} \leftarrow \sigma_{ij}^{(\alpha\beta)^i}; \epsilon_{ij}^{(\alpha\beta)^t} \leftarrow \epsilon_{ij}^{(\alpha\beta)^i}; Histm^{(\alpha\beta)^t} \leftarrow Histm^{(\alpha\beta)^i}$
 - (d) Compute effective tangent stiffness
 - i. Incremental unit strain is applied as PBC to the current global stiffness matrix $K_{tan}^{(\alpha\beta)^t}$
 - ii. Populate the effective macro tangent matrix by using perturbation scheme (See Section 5.1.1)
 - (e) Compute and update the macro stress and state variables
 $\bar{\sigma}^t \leftarrow \langle \sigma_{ij}^{(\alpha\beta)^i} \rangle; HistM^t \leftarrow \langle Histm^{(\alpha\beta)^i} \rangle$

expensive for large micro models. In this work, macroscopic tangent matrix is computed numerically using perturbation technique based on forward difference approximation developed by Miehe and Koch [130]. This numerical scheme has been successfully adopted in a wide range of non linear multiscale problems for computing material tangent [82, 129, 180].

The macroscopic material tangent matrix is computed by numerical linearization around the current macroscopic loading. The numerical tangent is computed by applying six infinitesimally small perturbation strain $\delta\epsilon$ on the current equilibrium strain field:

$$\delta\sigma = \mathbf{C}_{\delta\epsilon}\delta\epsilon \quad (5.1)$$

where $\delta\sigma$ is the perturbed stress due to applied perturbed strain $\delta\epsilon$. The perturbation value depends on the machine precision, as too small value may lead to numerical problems and error would accumulate in case of large values [129]. During the perturbation step, the internal variables \mathbb{H} must be able to evolve in order to obtain a consistent numerical tangent [129]. Therefore, the perturbation is done by adding the perturbation strain to the current macro strain. Thus the internal variables H evolve unconstrained and inelastic during perturbation procedure. At step Δt^{n+1} , macroscopic stress and internal variables are obtained through volume averaging the micro stresses and internal variables respectively. The perturbed stress $\delta\bar{\sigma}$ increment can be computed as

$$\delta\bar{\sigma}^{n+1} = \bar{\sigma}(\epsilon^{n+1} + \delta\epsilon, \mathbb{H}^{n+1} + \delta\mathbb{H}) - \bar{\sigma}(\epsilon^{n+1}, \mathbb{H}^{n+1}) \quad (5.2)$$

Each column of the numerical tangent matrix $\mathbf{C}_{\delta\epsilon}$ is populated by solving six non linear microscopic boundary value problems. Therefore, each micro call procedure involves one nonlinear BVP solution to compute the macro stress and six nonlinear BVP solution to compute the tangent stiffness matrix.

In order to investigate the effectiveness and accuracy of the method, a validation test is undertaken. A specimen with a hole is modeled using 12L9 and 1B2 CUF element. As illustrated Fig. 5.2a, the macro model is interfaced with a microstructure modeled with a homogeneous isotropic material exhibiting von-Mises plasticity. A single scale analysis of the same problem with von-Mises plasticity model is undertaken to compare the overall response of the structure as well the global convergence behavior (see Fig. 5.2b).

Table 5.1 tabulates the number of iterations required for each load step for different perturbation values. The effectiveness of the algorithm can be examined by comparing

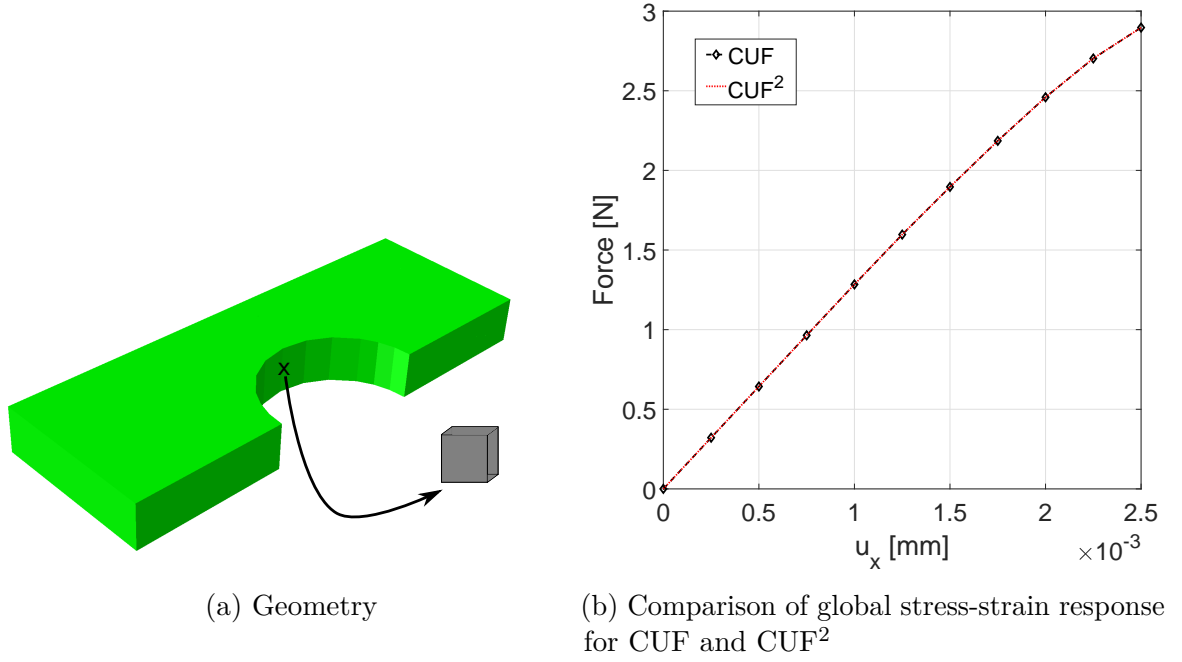


Fig. 5.2 Validation test for consistent macroscopic tangent matrix computation using von-Mises theory

the homogenized tangent matrix against the analytical tangent matrix of von-Mises model for a perturbation value of 10^{-6} :

$$\begin{aligned}
 \mathbf{C}_{analytical} &= \begin{bmatrix} 6179.1670 & 4682.6240 & 4638.2090 & -80.3894 & 45.2823 & -23.0188 \\ 4682.6240 & 7066.4530 & 3750.9230 & 41.6662 & -23.4701 & 11.9308 \\ 4638.2090 & 3750.9230 & 7110.8690 & 38.7232 & -21.8123 & 11.0880 \\ -80.3894 & 41.6662 & 38.7232 & 1663.9490 & 3.0005 & -1.5253 \\ 45.2823 & -23.4701 & -21.8123 & 3.0005 & 1667.5860 & 0.8592 \\ -23.0188 & 11.9308 & 11.0880 & -1.5253 & 0.8592 & 1668.8390 \end{bmatrix} \\
 \mathbf{C}_{\delta E} &= \begin{bmatrix} 6178.3770 & 4681.9150 & 4637.4760 & -80.3608 & 45.2666 & -23.0105 \\ 4681.7960 & 7065.9650 & 3750.1660 & 41.6634 & -23.4686 & 11.9299 \\ 4637.3200 & 3750.1870 & 7110.2600 & 38.7186 & -21.8099 & 11.0867 \\ -80.6796 & 41.8166 & 38.8630 & 1663.8320 & 3.0114 & -1.5308 \\ 44.9858 & -23.3163 & -21.6694 & 2.9809 & 1667.5690 & 0.8535 \\ -23.3154 & 12.0845 & 11.2309 & -1.5449 & 0.8703 & 1668.7720 \end{bmatrix}
 \end{aligned}$$

Table 5.1 Convergence behavior for different perturbation strain δE (Relative macro residuum = 10^{-4})

Load Step	Number of Newton-Raphson iterations					
	Analytical	10^{-7}	10^{-6}	$\ \delta E\ $ 10^{-5}	10^{-4}	10^{-3}
3	2	2	2	2	2	2
4	3	3	3	3	3	3
5	2	2	2	2	3	5

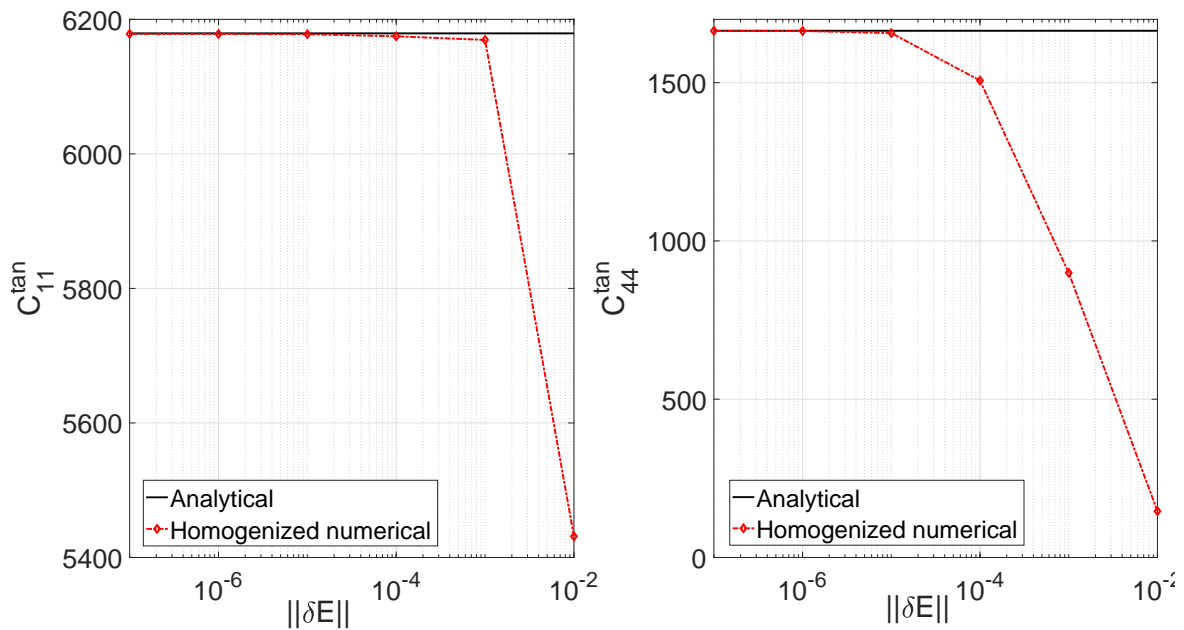


Fig. 5.3 Convergence behaviour of various components in homogenized material tangent matrix for different perturbation values

Figure 5.3 depicts the convergence behavior two different components of tangent matrix for different perturbation values. A perturbation value $||\delta\epsilon||$ of 10^{-6} for further computations.

5.1.2 Implementation aspects

A standard single-scale finite implementation spends a significant amount of time on stiffness matrix computations and global matrix decomposition for solution [48]. As the system grows larger, the contribution from the latter tends to increase. In case of multiscale framework, due to the requirement of solving significantly large set of local problems associated with micro solutions, majority of the computational effort is spent on macro gauss point update procedures. Such significant computational effort is often addressed through parallel implementations.

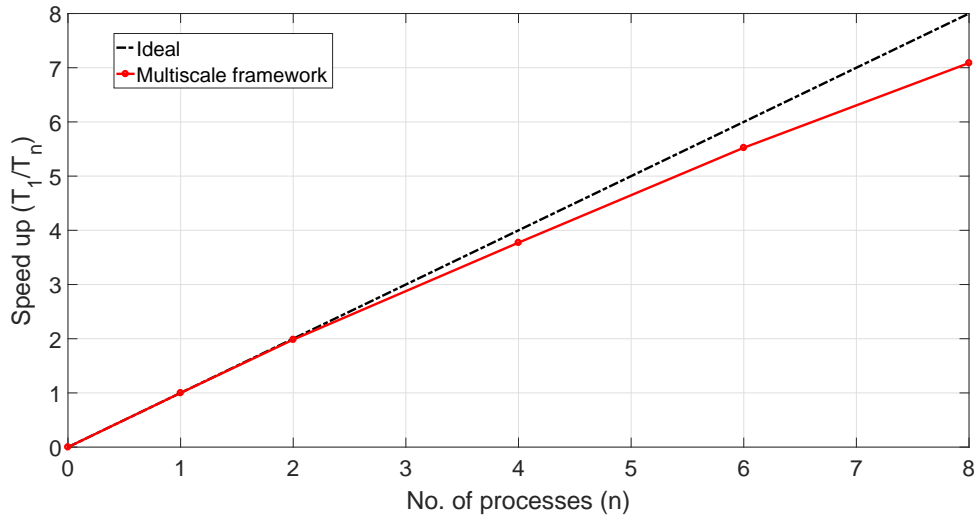


Fig. 5.4 Speed up obtained in the parallel version of multiscale framework for a system with $\sim 130,000$ degrees of freedom

As depicted in Figure 5.5, macro scale is interfaced with the micro framework through the *update macro gauss point* subroutine, where the micro framework receives the current incremental macro strain as the input. The micro framework computes the updated macro tangent matrix, macro stress and solution variables and sends it back to the *macro gauss point update* subroutine. Due to the iterative nature of the framework, the solution variables of every gauss point within the micro RVE associated with a macro gauss points needs to be stored. This may lead to exponential increase in the memory usage as the size of the numerical problem grows. The current framework

manages memory in an efficient manner by storing the solution variables for micro RVEs only when it enters the nonlinear regime.

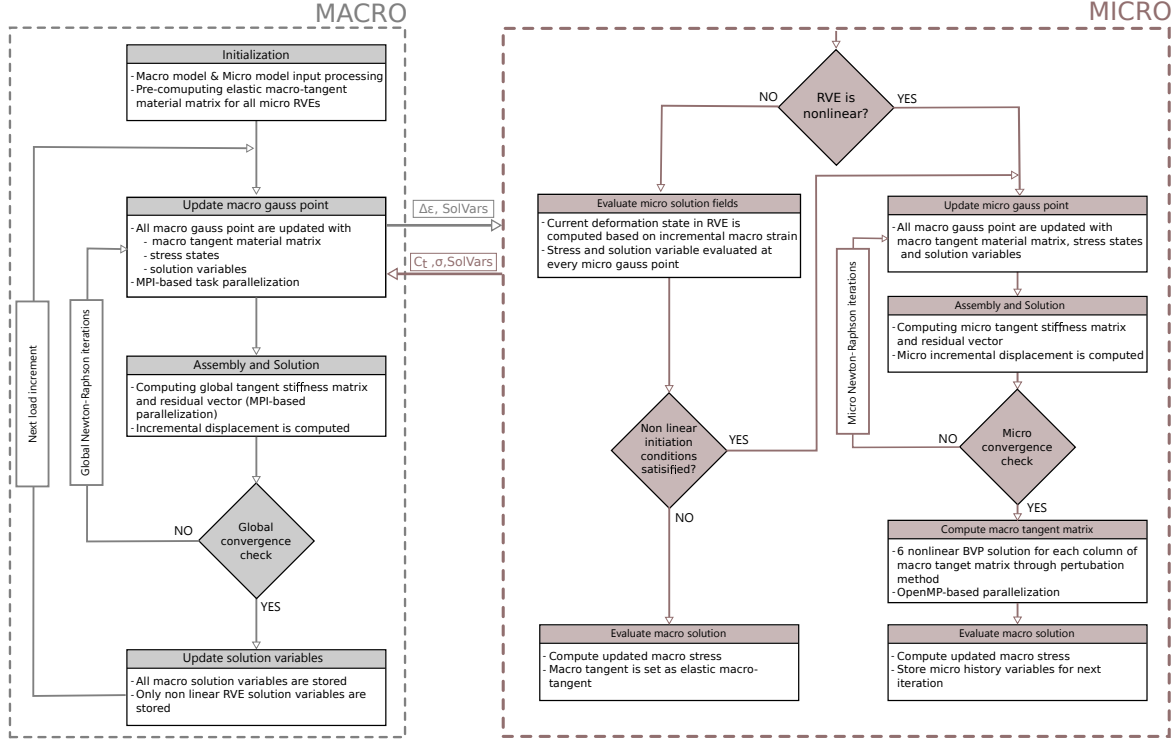


Fig. 5.5 Flowchart for the concurrent multiscale framework based on CUF

A hybrid MPI-OpenMP based parallelization strategy is adopted at multiple phases within the framework [55]. MPI based constructs are employed to parallelize the global level operations such as updating solution variables at macro gauss points and global stiffness assembly. OpenMP commands are utilized at the local level operations such as macro tangent computation, where all six nonlinear BVP solutions are carried out in a parallel manner. Within multiscale framework, since majority of the analysis time is spent on solving the micromechanical BVP at every macro gauss point, the parallelization strategy adopted above yields a near-ideal speedup as depicted in Fig. 5.4. Since tangent computation is associated with additional 6 nonlinear BVP solution at micro scale per macro gauss point, a modified Newton scheme is adopted to solve all the numerical cases. Therefore tangent material matrix is computed only at the beginning of each load increment.

5.2 Numerical Results

The robustness and effectiveness of the proposed concurrent multiscale framework is demonstrated through numerical cases for linear and nonlinear analysis. The framework is also able to handle standard three-dimensional eight-node brick finite elements, commonly used in literature for FE² framework based multiscale analysis. Based on the kind of finite elements used in the two scales, different multiscale models are used to solve the problem as enlisted in Table 5.2.

Table 5.2 Nomenclature for various models used in multiscale analysis

Model name	Macro scale	Micro scale
1D-1D	CUF beam element	CUF beam element
1D-3D	CUF beam element	Standard 3D brick element
3D-1D	Standard 3D brick element	CUF beam element
3D-3D	Standard 3D brick element	Standard 3D brick element

The first three sets of numerical cases deals with linear elastic multiscale analysis. First example predicts the stiffness for notched and un-notched specimens for various multidirectional laminate system. Linear elastic analysis of an open-hole composite specimen under tension with a large randomly distributed fiber RVE in the microscale is taken as the second numerical case. The third example deals with analysis of simply supported honeycomb sandwich beam under bending load. In order to validate and assess the robustness of the framework to undertake nonlinear multiscale analysis, multi-layered structure under pure shear loading condition is simulated as the fourth numerical case. The last two sets of numerical cases deals with investigation of nonlinearity exhibited by off-axis laminates with comparison against experimental results and prediction of nonlinear response of open-hole composite specimen.

5.2.1 Stiffness prediction of multi-directional laminates

The numerical example evaluates the stiffness of three different multi-directional laminate systems: (1) Layup 1: $[0/45/90/-45]_{2s}$, (2) $[60/0/-60]_{3s}$ and (3) $[30/60/90/-30/-60]_{2s}$. The laminates are made up of uni-directional IM7/977-3 graphite epoxy material system. The static tensile and compressive stiffness of above mentioned laminate system for un-notched and notched specimens are evaluated. Clay et al. conducted a study on exploring existing state of the art in composite damage analysis [50, 69]. This study is limited to stiffness prediction for above mentioned laminate

system. The architecture of the microscale RVE is taken as square-packed with a

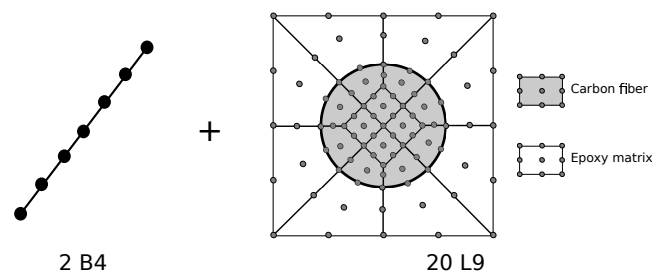


Fig. 5.6 Microscale RVE model for stiffness prediction of multi-directional laminates

volume fraction of 65% (see Fig. 5.6). Based on the experimental results for uniaxial tension and compression, the elastic material properties of the RVE are calibrated [50, 137] (see Table 5.3). As depicted in Fig. 5.6, the square-packed RVE is modeled using 2B4 beam elements along with 20L9 elements across the section. The macro-scale models for un-notched and notched specimens are modeled through the CW modeling approach as illustrated in Fig. 5.7. The details pertaining to CUF models for different layups with total analysis time for static analysis is tabulated in Table 5.4. Table 5.5 enlists the predicted stiffness values for different laminate system for notched and un-notched specimens along with comparison against experimental and literature results.

Table 5.3 Calibrated constituent properties of RVE for multiscale analysis for stiffness prediction of multi-directional laminates

	E_1	E_2	E_3	ν_{12}	ν_{23}	G_{12}
	[GPa]	[GPa]	[GPa]	[—]	[—]	[GPa]
IM7 Fiber	256.0 ^T /215.0 ^C	15.0	15.0	0.28	0.19	15.0
Epoxy 977-3	3.2	3.2	3.2	0.38	0.38	1.16

T: Tension C: Compression

Following observations can be drawn:

1. The predicted stiffness by multiscale models for a variety of multi-directional coupons are of great accuracy
2. It is evident from Table 5.5 that the error obtained by 1D-1D models for coupons under tension and compression are within 4% and 8% respectively.
3. CUF multiscale framework are able to efficiently model non-prismatic structures

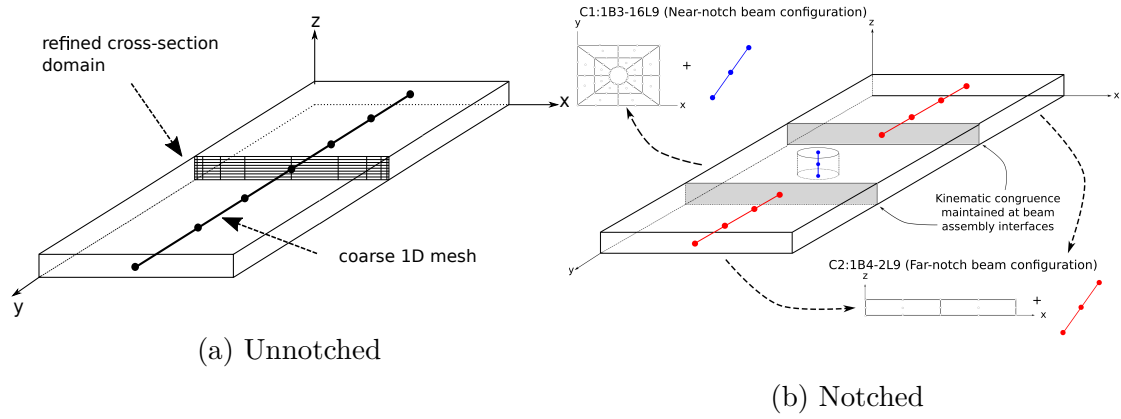


Fig. 5.7 An illustration of the modeling of composite specimens using refined 1D CUF models for stiffness prediction of multi-directional laminates [60]

Table 5.4 Macro model information for stiffness prediction of multi-directional laminates

Model	Information	DOF	CPU Time (s)
Layup1 : $[0/45/90/-45]_{2s}$			
Un-notched	48L9-4B4	21,483	7.5
Notched	C2: 64L9-4B4 and C1:80L9-16B3	45,540	19.1
Layup2 : $[60/0/-60]_{3s}$			
Un-notched	54L9-10B4	24,087	7.8
Notched	C2: 72L9-4B4 and C1:80L9-18B3	48,708	20.3
Layup3 : $[30/60/90/-30/-60]_{2s}$			
Un-notched	60L9-10B4	26,691	8.9
Notched	C2: 80L9-4B4 and C1:80L9-20B3	51,060	21.0

Table 5.5 Stiffness prediction for notched and unnotched multi-directional laminates

		Experimental [50]	MAC/GMC [137]	NCYL [215]	1D-1D
Unnotched Tensile					
Layup	1:	60.5	59.6 (1.49%)	60.6 (0.17%)	59.4 (1.82%)
[0/45/90/ - 45] _{2s}					
Layup 2:	[60/0/ -	59.5	59.8 (0.50%)	61.5 (3.36%)	59.2 (0.50%)
60] _{3s}					
Layup	3:	38.0	39.0 (2.63%)	39.7 (4.47%)	39.1 (2.89%)
[30/60/90/ -					
30/ - 60] _{2s}					
Unnotched Compression					
Layup	1:	48.0	51.0 (6.25%)	52.3 (8.96%)	50.9 (6.17%)
[0/45/90/ - 45] _{2s}					
Layup 2:	[60/0/ -	48.9	51.2 (4.70%)	52.3 (6.95%)	51.0 (4.29%)
60] _{3s}					
Layup	3:	33.5	33.3(0.60%)	34.8 (3.88%)	34.11 (1.82%)
[30/60/90/ -					
30/ - 60] _{2s}					
Notched Tension					
Layup	1:	48.3	49.1 (1.66%)	50.3 (4.14%)	49.4 (2.28%)
[0/45/90/ - 45] _{2s}					
Layup 2:	[60/0/ -	48.8	48.9 (0.20%)	51.1 (4.71%)	50.44 (3.36%)
60] _{3s}					
Layup	3:	32.4	33.7 (4.01%)	34.5 (6.48%)	33.25 (2.62%)
[30/60/90/ -					
30/ - 60] _{2s}					
Notched Compression					
Layup	1:	44.5	41.6 (6.52%)	41.9 (5.84%)	41.2 (7.42%)
[0/45/90/ - 45] _{2s}					
Layup 2:	[60/0/ -	44.4	41.9 (5.63%)	41.9 (5.63%)	41.0 (7.70%)
60] _{3s}					
Layup	3:	30.1	29.2 (3.00%)	29.8 (1.00%)	28.63 (4.88%)
[30/60/90/ -					
30/ - 60] _{2s}					

All units in GPa. Quantities in parenthesis represent error with respect to experimental result

5.2.2 Linear multiscale simulation of a randomly distributed large RVE

The following numerical case demonstrates the capability of the multiscale framework to efficiently compute the local micro stress fields. Ricks et al. [168] undertook a linear elastic multiscale analysis of notched rectangular specimen with dimensions $304.8 \text{ mm} \times 38.1 \text{ mm} \times 3.5 \text{ mm}$ (length \times width \times height) with a circular notch of diameter 6.35 mm . As depicted in Fig. 5.7 (b), an equivalent model is developed using CW technique with configuration: C2: 4L9-2B4 and C1:80L9-1B3. Fibers are oriented in parallel along the length of specimen and a displacement of 6.9 mm is applied at one end of the specimen with the other end clamped. The macro model is interfaced with randomly distributed fiber RVE as illustrated in Fig. 5.8 (b). The architecture of the RVE is based on work undertaken by Kaleel et al. [111, 112]. The micro model RVE is modeled using 265 L9 with 2 B4 elements and the material properties are same as the previous numerical example (Table 5.3). A similar RVE model is developed using 24,765 3D brick finite elements. Two classes of multiscale models are developed, namely (a) 1D-1D: Both micro and macro scale is modeled using CUF beam elements and (b) 1D-3D: Macro CUF model is interfaced with a standard FE based micro model. The mesh configuration for the 3D FE micro model is based on convergence study and details of the same can be found in paper by Kaleel et al. [111].

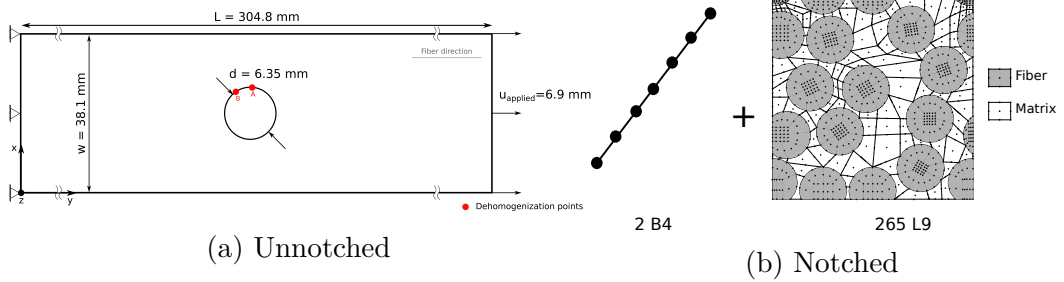


Fig. 5.8 Geometry for linear multiscale simulation of a randomly distributed large RVE

Figure 5.9 depicts the global von-Mises stress distribution around the notch for 1D-1D and 1D-3D models. Local fields are plotted at locations *A* and *B* (see Fig. 5.8) around the notch in Fig. 5.10 and Fig. 5.11 respectively. The macro strain at the aforementioned macro gauss points locations used for dehomogenization is tabulated in Table 5.6. Numerical results enlisted in Table 5.7 provides information regarding the model size, analysis time and memory requirements. The analysis time is compared for two cases: one with computation and storage of local stress fields in micro RVEs and other one without it. Local stress fields in micro RVE is obtained by undertaking

dehomogenization at every gauss point in the macro structure. Memory required to store the local micro stress field is also computed.

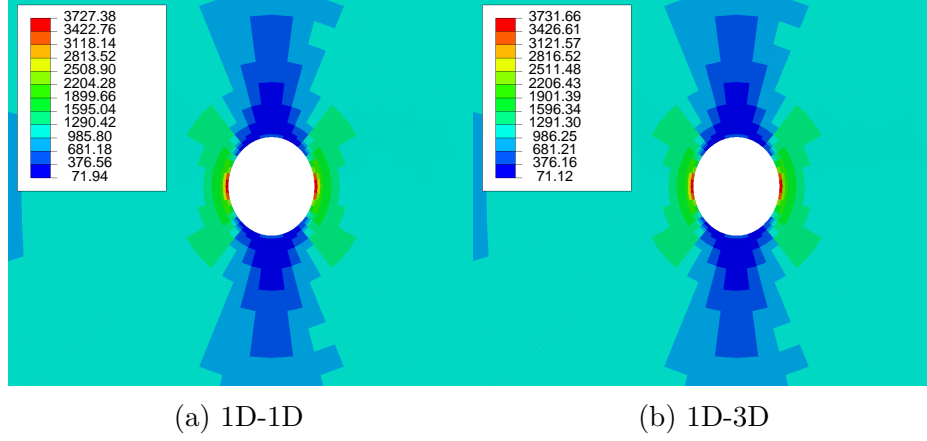


Fig. 5.9 von-Mises stress distribution around the hole for linear multiscale simulation of a randomly distributed large RVE

Table 5.6 Strain computed at two location for dehomogenization linear multiscale simulation of a randomly distributed large RVE

	ϵ_{22} $\times 10^{-2}$	ϵ_{11} $\times 10^{-2}$	ϵ_{33} $\times 10^{-2}$	ϵ_{23} $\times 10^{-3}$	ϵ_{13} $\times 10^{-3}$	ϵ_{12} $\times 10^{-2}$
Location A (23.2, 152.4, 0.0)						
1D-1D	-1.297	8.412	1.703	1.155	0.919	1.914
1D-3D	-1.309	8.478	-1.725	1.390	1.128	-1.936
Location B (23.0, 151.9, 0.0)						
1D-1D	1.011	3.553	-1.253	-3.136	-6.367	9.695
1D-3D	1.020	3.551	-1.261	-3.082	-7.771	9.745

Results suggests the following:

1. In comparison to 3D models at the microscale, 1D models are able to effectively capture the local fields with great accuracy.
2. The capability of the multiscale framework to interface different kinds of higher-order finite element models at micro scale is highlighted.
3. In comparison with the analysis time for 1D-3D model, it is evident from Table 5.7 that the 1D-1D models requires only one-third of the time for analysis without local fields and one-fourth of the time for analysis with local fields.

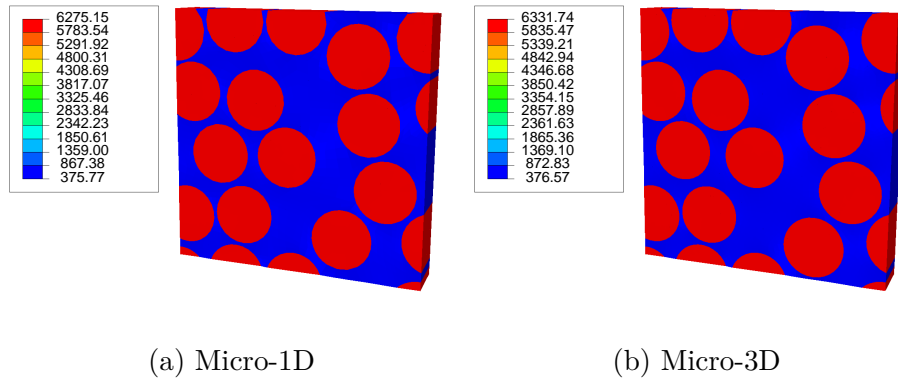


Fig. 5.10 Local stress field σ_{11} obtained at location A for linear multiscale simulation of a randomly distributed large RVE

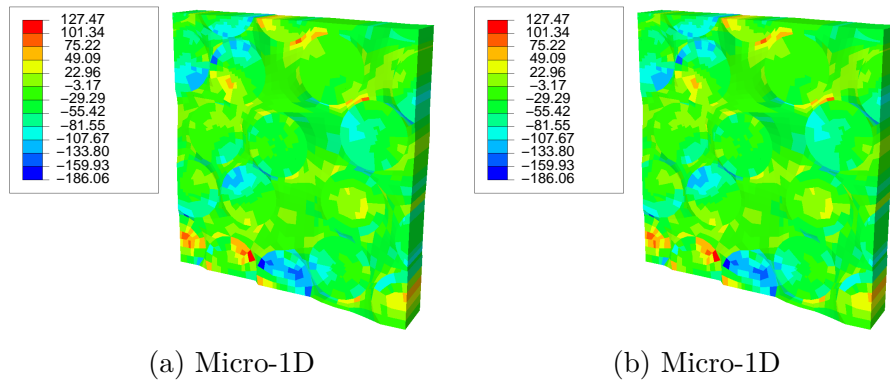


Fig. 5.11 Local stress field σ_{12} obtained at location B for linear multiscale simulation of a randomly distributed large RVE

Table 5.7 Numerical results for linear multiscale simulation of a randomly distributed large RVE

	Macro Model		Micro Model		Analysis time (s)		Memory required per macro GP ¹ [MB]
	DOF	No. of GPs	DOF	No. of GPs	Without local micro fields	With local micro fields	
1D-1D	4,140	2,736	13,642	9,540	3.0	10.1	1.5
1D-3D	4,140	2,736	31,524	61,008	9.6	42.7	9.8

DOF: Degrees of freedom. GP: Gauss point.

¹ Required memory per each macro GP is calculated as 20 state variables stored per each gauss point in the micro RVE using double precision real (8 bytes)

4. The efficiency of the 1D-1D models can be further exemplified by comparing the memory requirements for the two models. A 6.5 times savings in terms of total memory required to store the local fields are obtained for 1D-1D models.

5.2.3 Simply-supported honeycomb sandwich beam under bending loading

The current numerical example highlights the capabilities of CUF multiscale framework to handle multiple types of RVE efficiently through multiscale modeling of honeycomb sandwich beam. The numerical example consists of a simply supported honeycomb sandwich structure with an aluminium core and composite face sheet under bending loading. The face sheets consists of a laminate $[0]_2$ modeled through RVE described in the previous example (Section 5.2.1).

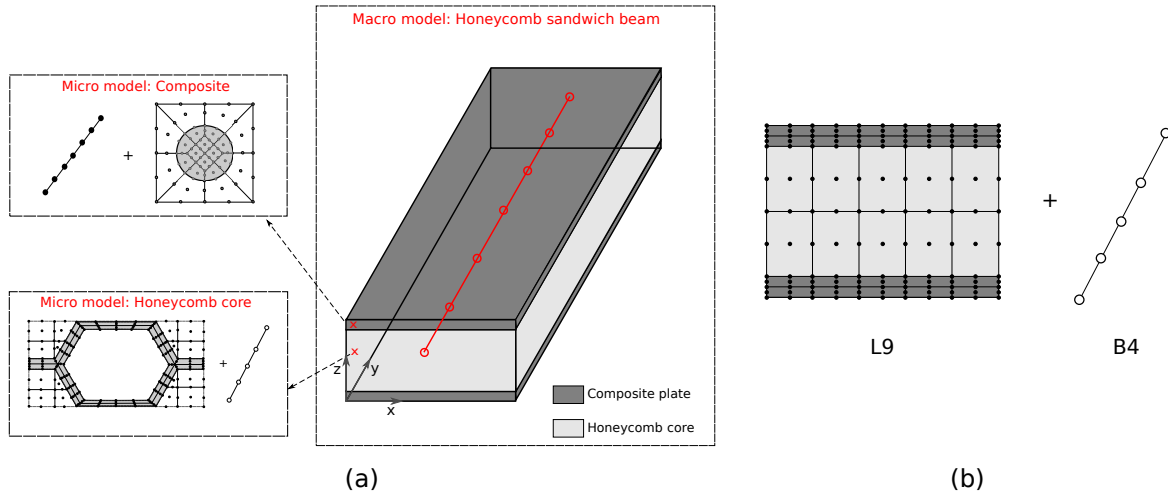


Fig. 5.12 Multiscale modeling of honeycomb sandwich using CUF multiscale framework: (a) Interfacing two kinds of micro models for sandwich beam and (b) CW discretization of macro sandwich beam model using L9 cross-section and B4 beam elements

Based on the work of Catapano and Montemurro [45], the honey comb core is modeled using properties enlisted in Table 5.8 (see Fig. 5.13). The honeycomb core is made of aluminium with Young's modulus E of 70 GPa, Poisson's ratio ν of 0.33 and density ρ of $2.7 \times 10^{-6} \text{ kg/mm}^3$. As discussed in the original paper on CUF micromechanics [111], additional void elements (elastic air) are added to the RVE to remain consistent with the micromechanical homogenization formulation. As depicted in Fig. 5.14, the RVE is discretized using 286 L9 elements and 2 B4 elements amounting to a total degrees of freedom of 25,389. Table 5.9 enlists the predicted elastic properties of the honeycomb with comparison against results from the literature.

Table 5.8 Geometrical properties of core for multiscale structural analysis of honeycomb sandwich beam [45]

l_1	l_2	t_c	θ	h_c
(mm)	(mm)	(mm)	(deg)	(mm)
3.66	1.833	0.0635	60	20

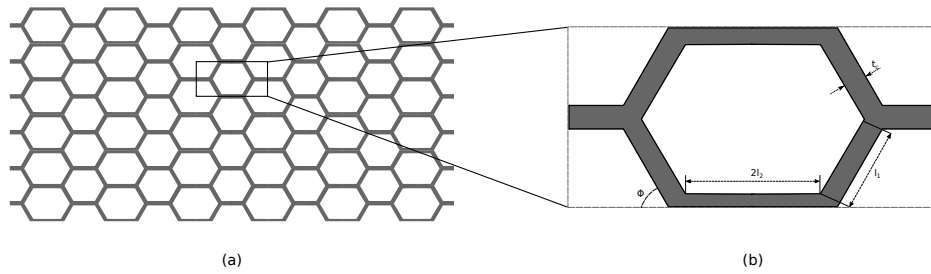


Fig. 5.13 Geometry of the honeycomb core: (a) Repeating core structure and (b) geometrical parameters of RVE

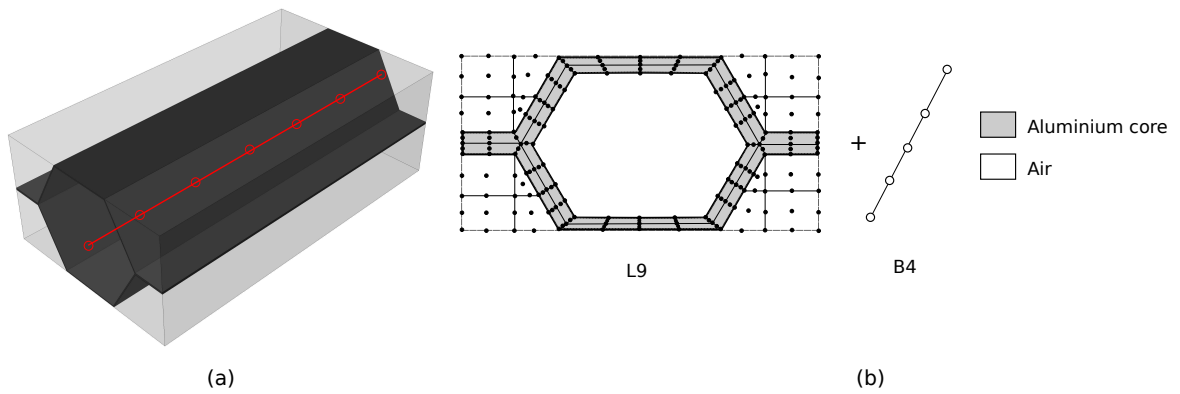


Fig. 5.14 Component-wise modeling of the honeycomb core RVE: (a) CUF beam model of RVE and (b) Cross-section and beam discretization

Table 5.9 Prediction of effective properties of honeycomb RVE for multiscale structural analysis of honeycomb sandwich beam

	CUF-Micro	MSG2D [218]	Catapano et al. [45]	Burton et al. [29]	Grediac [89]
E_1 (MPa)	0.935	0.884	0.884	0.815	0.815
E_2 (MPa)	0.969	0.918	0.918	0.815	0.815
E_3 (MPa)	1814.8	1812.3	1812.3	1848.2	1848.2
G_{12} (MPa)	0.591	0.565	0.640	0.489	0.489
G_{23} (MPa)	263.8	262.6	262.9	260.6	260.6
G_{13} (MPa)	386.4	384.5	390.8	156.3 (LB) 434.3 (UB)	397.1
ν_{12} (-)	0.98	0.98	0.98	1.00	1.00
ν_{23} (-)	1.70×10^{-4}	1.67×10^{-4}	1.61×10^{-4}	1.45×10^{-4}	1.45×10^{-4}
ν_{13} (-)	1.76×10^{-4}	1.61×10^{-4}	1.67×10^{-4}	1.45×10^{-4}	1.45×10^{-4}
ρ (kgmm ⁻³)	7.02×10^{-8}	6.99×10^{-8}	6.99×10^{-8}	7.12×10^{-8}	-

LB: Lower bound, UB: Upper bound

A simply supported sandwich honeycomb beam of length 700mm is modeled. As depicted in Fig. 5.15, a uniform pressure of 0.01MPa acts on the top surface of the beam. As discussed earlier, gauss points belonging to composite face sheet is interfaced with fiber-reinforced micro CUF RVE model using 20 L9 and 2 B4 elements (see Fig. 5.6). The honeycomb aluminum core gauss points are interfaced with the honeycomb core RVE micro model. Table 5.10 enlists the three classes of multiscale models used for the example. All the macro models are interfaced with the same micro RVE configuration, details of which are furnished in Table 5.11. Numerical results including maximum displacement and von-Mises stress σ_{vm} at mid-span, analysis time and memory requirement for total storage of micro state solutions are listed in Table 5.12. Comparison between analysis time with and without local micro fields are also tabulated. Local von-Mises stress field at point (50.0, 35.0, 16.9) in the core of sandwich honeycomb beam is illustrated in Fig. 5.16.

Following observations are drawn:

1. Multiple 1D micro models are effectively interfaced with macro 1D models and 3D brick models. Maximum von-Mises stress observed at the midspan in the

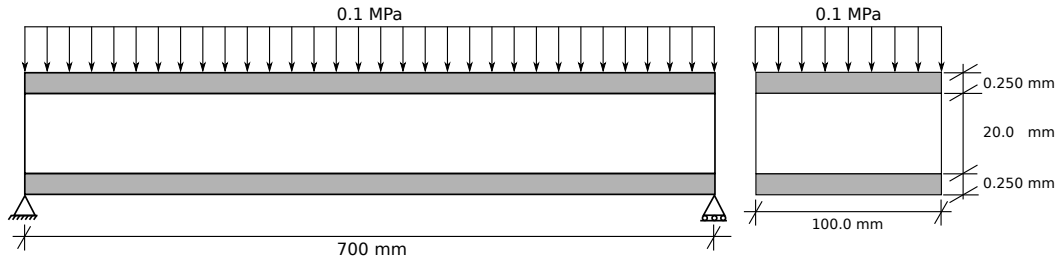


Fig. 5.15 Geometry and boundary conditions for multiscale modeling of honeycomb sandwich using CUF multiscale framework

Table 5.10 Macro model information for analysis of honeycomb sandwich beam

Model	Information	DOF	NGP
1D-1D	CUF beam element (36L9-15B4)- 1L9 per layer for composite and 2L9 per layer for core	19,734	16,200
3D-1D (Coarse)	12500 standard 3D brick element ¹ - Mesh seed along the beam : 50 - One brick element per layer for composite and 4 brick element for core	43,758	100,000
3D-1D (Refined)	20000 standard brick element ¹ - Mesh seed along the beam: 80 - One brick element per layer for composite and 4 brick element for core	69,498	160,000

DOF: Degrees of freedom. NGP: Number of gauss points. ¹ Full integration (8 gauss points per element)

Table 5.11 Macro model information for analysis of honeycomb sandwich beam

RVE Model	Information	DOF	NGP
Composite face sheet	CUF beam element (20L9-2B4)	1,869	1,440
Honeycomb core	CUF beam element (1209-2B4)	25,389	20,596

Table 5.12 Numerical results for analysis of honeycomb sandwich beam under bending load

Model	Number of CPUs	Macro model		Analysis time (s)		Memory required for all macro GPs [GB] ¹
		Max disp (mm)	Max σ_{vm} (MPa)	without local fields	with local fields	
1D-1D	1	4.61	121.7	14.9	64.0	2.95
3D-1D (Coarse)	4	4.50	118.8	27.9	181.2	19.8
3D-1D (Refined)	4	4.56	120.5	44.0	287.0	31.6

DOF: Degrees of freedom. GP: Gauss point.

¹ Required memory for all macro GP is calculated as 10 state variables (double precision real - 8 bytes) stored per each gauss point in the micro RVE multiplied by total number of macro GP. Micro gauss points for elastic air in micro core RVE is not included.

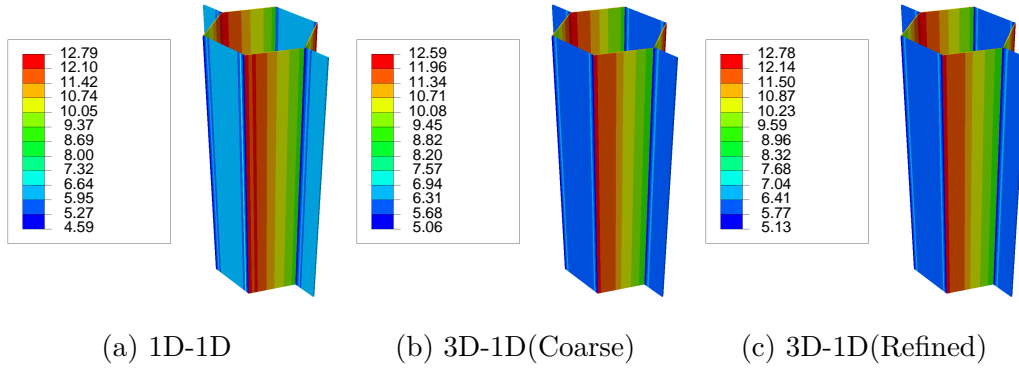


Fig. 5.16 Local von-Mises stress field σ_{vm} obtained at a point in core (50.0, 35.0, 16.9) for analysis of honeycomb sandwich beam for different multiscale models

macro model for 1D-1D model is 4.61 MPa and coarse and refined configuration of 3D-1D models are 118.8 MPa and 120.5 MPa respectively.

2. From Table 5.12, it can be seen that 1D-1D models utilizes 1 CPU to obtain the results with and without local micro fields in 14.9s and 64.0s respectively, whereas the analysis runtime for 3D-1D model (refined) for with and without micro fields is 44.0s and 287.0s respectively by utilizing 4 CPUs. The stark difference can be attributed to the fact that macro 3D require higher number of gauss points, which in turn increases the time required for the analysis drastically.
3. Table 5.10 shows that 1D macro model requires 16,200 gauss points but 3D macro models required 100,000 and 160,000 for coarse and refined configurations respectively. The difference in required gauss point translates to large variation in the memory required to store micro state solutions at all macro gauss points. 1D-1D models require only 2.95 GB to store all the micro solutions whereas coarse and refined configuration of 3D-1D models require 19.8 GB and 31.6 GB respectively (see Table 5.12).
4. Dehomogenization of the core at a given point by different multiscale models exhibit similar von-Mises stress fields as shown in Fig. 5.16.

5.2.4 Non linear shear response of multi-layered composite

In order to validate the proposed concurrent multiscale framework for nonlinear analysis, a multi-layered structure under pure shear loading condition is simulated. The problem definition is based on the work of Tikarrouchine et al. [185]. The microscale is modeled using a periodic stack of two composite layers with volume fraction of 0.5 each. As

illustrated in Fig. 5.17(c), the first layer is modeled as an elastic material whereas the second layer exhibits an elasto-plastic response with material parameters tabulated in Table 5.13. Figure 5.18 depicts the plastic response of elasto-plastic phase, based on the power-law hardening function.

Table 5.13 Material properties for two-layered composite RVE for multi-layered structure under pure shear loading condition

	Volume fraction	Young's modulus	Poisson' ratio	Yield Stress
	[-]	[GPa]	[-]	[MPa]
Elastic phase	0.5	6.0	0.2	-
Elasto-plastic phase	0.5	2.0	0.3	10.0

The boundary conditions imposed on the macrostructure corresponds to a pure shear loading case (see Fig. 5.17(a)). An additional node is constrained in the y direction to mitigate rigid-body motion. The cuboidal macro structure is modeled using 1 L9 element along the cross-section and 1 B4 element along the beam axis as depicted in Fig. 5.17(b). The dimensions of the cube is taken as 1.0. Since the boundary conditions imposed on the macro model yields pure shear loading (all strain components except ϵ_{23} are zero), the overall response of the macro structure must be identical to a micromechanical analysis of the RVE with an imposed non zero shear strain ϵ_{23} . The macro stress σ_{23} for the 1D-1D macro model is computed by dividing the total reaction force along one of the faces by face area.

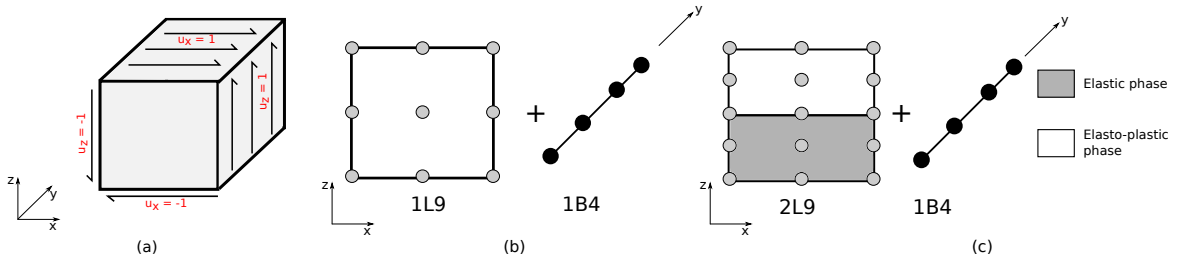


Fig. 5.17 Model information of two-layered composite RVE for multi-layered structure under pure shear loading condition: (a) Boundary conditions for macro model, (b) Cross-section and beam modeling of macro model and (c) Cross-section and beam modeling for micro model

The overall macro response is depicted in Fig. 5.19 along with results from CUF-micromechanical analysis, semi-analytical solution as well as reference FE^2 solution from the work of Tikarrouchine et al. [185]. In order to assess the convergence behavior of the framework, another set of analysis is carried out with a total strain of the 5% is

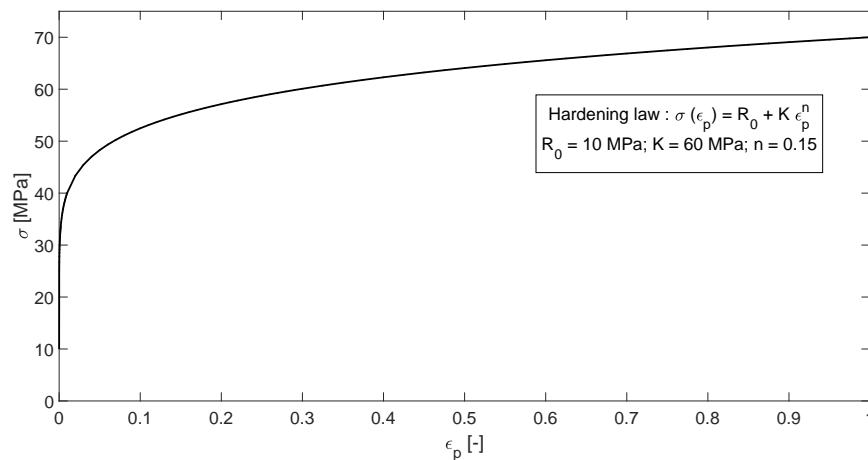


Fig. 5.18 Plastic response of the elasto-plastic phase for two-layered composite RVE for multi-layered structure under pure shear loading condition

applied in one large increment. Similar to the study undertaken by Haj-Ali and Aboudi in [92], this study aims at evaluating the robustness of the framework to handle severe non-linearity. Figure 5.20 shows the convergence behavior of 1D-1D model versus the CUF-micro model, where 1D-1D (Global) refers to the global convergence behavior of the macro 1D model and 1D-1D (Local) refers to the convergence behavior exhibited at the local micro model interfaced to one of the gauss point of macro model. Results

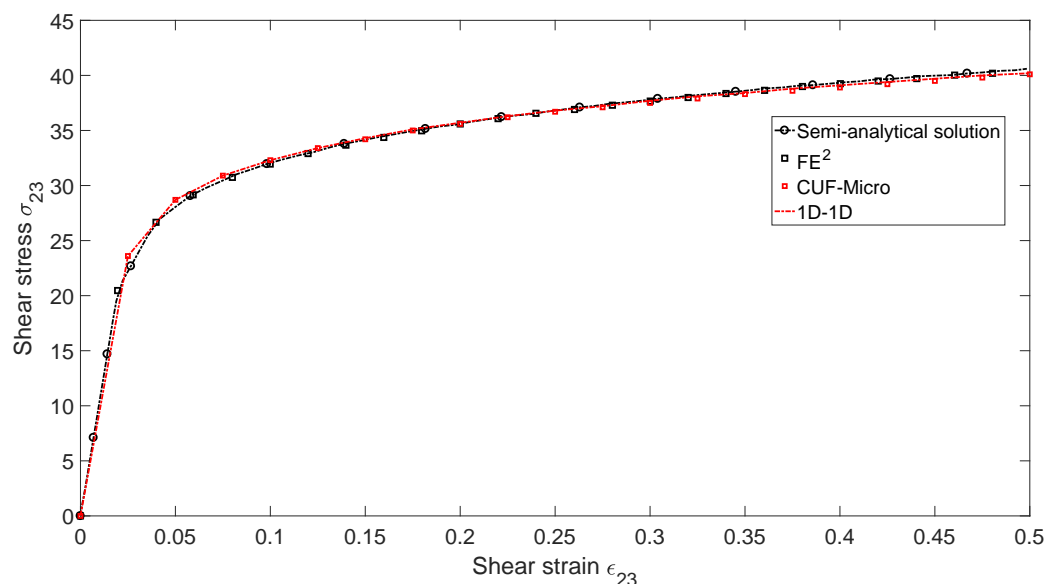


Fig. 5.19 Comparison of overall macro response of two-layered composite RVE for multi-layered structure under pure shear loading condition against semi analytical solution and FE^2 approach [185]

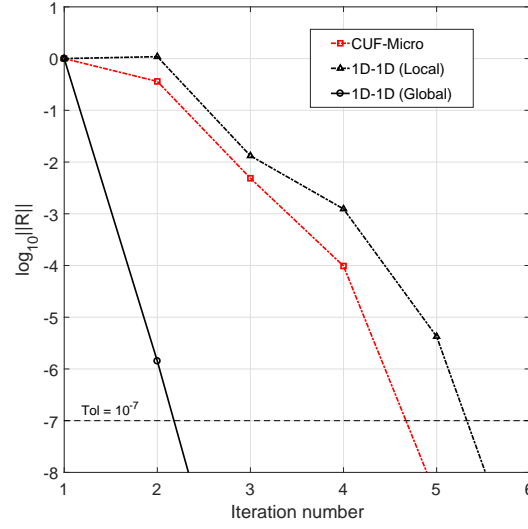


Fig. 5.20 Comparison of convergence between 1D-1D model and CUF-micro model. 1D-1D (Global) refers to the global convergence behavior of the macro 1D model and 1D-1D (Local) refers to the convergence behavior exhibited at the local micro model interfaced to one of the gauss point of macro model

suggest the following:

1. From Fig. 5.19 it is evident that the overall macro response for 1D-1D model corresponds well with CUF-micromechanics and reference solutions.
2. It can be observed that the multiscale framework exhibits superior convergence, even for severe nonlinear increment (see Fig. 5.20)
3. The robustness and capability of the framework has been successfully validated.

5.2.5 Unnotched laminates under uniaxial tension

O'Higgins et al. conducted experimental and numerical investigation on the effect of transverse and shear non-linear response for off-axis glass fiber-reinforced composite laminates under tension [147, 148]. Emergence of permanent strains in specimens during cyclic loading revealed plastic like behavior of laminates. Authors also developed a lamina level CDM based plasticity model for undertaking numerical analysis of off-axis laminates under tension [148], which shall serve as a reference solution for the following study. In this study, predictive capabilities of CUF multiscale framework is exploited in analyzing off-axis laminated CFRP composite under uniaxial tension. Inelastic deformation phenomena is captured through modeling plastic deformation in

the matrix constituents at micro scale. Three different laminates sequences are studied, namely $[10]_{2s}$, $[55]_{2s}$ and $[67.5]_{2s}$ and material system under consideration is HTA-6376.

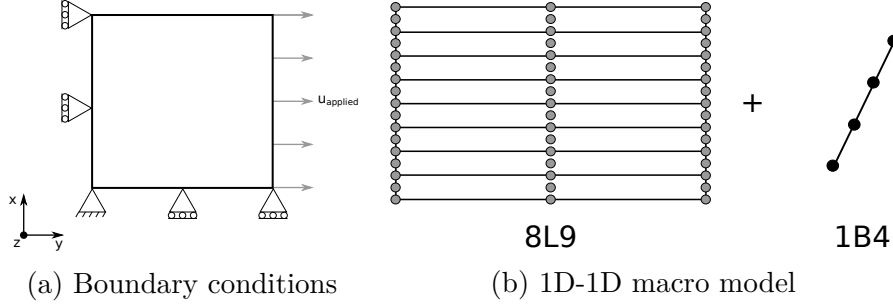


Fig. 5.21 Macro model for off-axis laminates under uniaxial tension

Two classes of multiscale models are considered, namely:

- (a) 1D-1D: Micro scale and macro scale models are modeled using CUF 1D elements using 1B4 element with 1L9 element per layer (see Fig. 5.21a). Total number of gauss points in the macro structure accounted to 288.
- (b) 3D-3D: Analogous to traditional FE^2 method, both scale are modeled using 2 linear 3D brick element per layer, similar to the modeling technique undertaken by O'Higgins et al. for the coupon [148]. Total number of gauss points in the macro structure amounted to 1152.

The thickness of each layer is taken as 0.125 mm. The boundary condition for the macro structure is depicted in Fig. 5.21b. As depicted in Fig. 5.22, the microstructure

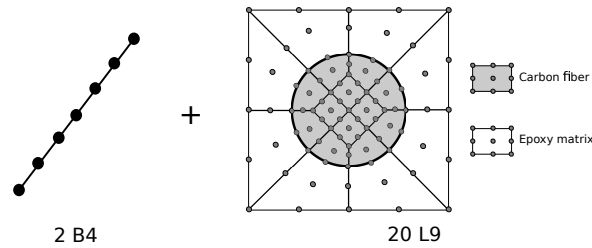


Fig. 5.22 Micro model for 1D-1D multiscale model for off-axis laminates under uniaxial tension

of RVE is assumed to be square-packed. The micro model for 1D-1D model consists of 20L9 element along the cross-section and 2B4 along the beam with total degrees of freedom of 1869 (see Fig. 5.22). The mesh configuration for the micro model for

Table 5.14 Elastic properties of micro RVE models for off-axis laminates under uniaxial tension

	E_1 (GPa)	E_2 (GPa)	G_{12} (GPa)	G_{23} (GPa)	ν_{12} (-)
HTA Fiber	223.0	23.0	32.0	7.0	0.28
MY750 matrix	4.3	4.3	1.7	1.7	0.27

3D-3D model was chosen based on a convergence study and details of the same can be found in paper by Kaleel et al. [111]. The 3D model consists of 1656 brick elements amounting to a total degrees of freedom of 5796. The model information for micro scale models are furnished in Table 5.15 along with analysis time comparison with and without macro tangent material matrix computation. The fiber is modeled as transversely isotropic linear elastic material and von-Mises plasticity model is used to model inelastic deformation in matrix constituents. The transverse and shear response of the RVE is calibrated to experimental data available for $[90]$ and $[\pm 45]$ coupons [147]. Calibrated elastic material properties for the micro RVE models are tabulated in Table 5.14. The hardening curve of matrix plasticity model is calibrated using a four parameter model [110] and depicted in Fig. 5.23. Figure 5.24 depicts the overall response of 1D-1D micro model and 3D-3D micro model under transverse and shear response loading with comparison against experimental [147] and literature solutions [148]. Accumulated plastic strain in calibrated RVE models at an applied shear strain $\gamma_{12} = 0.05$ are depicted in Fig. 5.25.

The calibrated micro scale RVE models are interfaced with the macro models for three different laminate systems. Figure 5.26 compares the tensile stress versus strain for three laminate systems with comparison against experimental [147] and CDM-plasticity model results [148]. It is important to emphasis that both the reference results includes the final failure point whereas the current simulation is restricted to only modeling the nonlinear behavior. The final failure point for both the reference models are denoted with " \times " in the Fig. 5.26. Table 5.16 enlists the total time taken for the analysis as well as the memory usage for different multiscale models.

Following observations can be drawn:

1. It is evident from Fig. 5.24 that the micro mechanical calibration of the RVEs leads to accurate representation of the shear response of the laminate. Calibrated RVEs tends to exhibit reduced non-linear response under transverse loading condition. Figure 5.25 shows that 1D micro model exhibit similar accumulated inelastic strain field in comparison to 3D micro model under shear loading

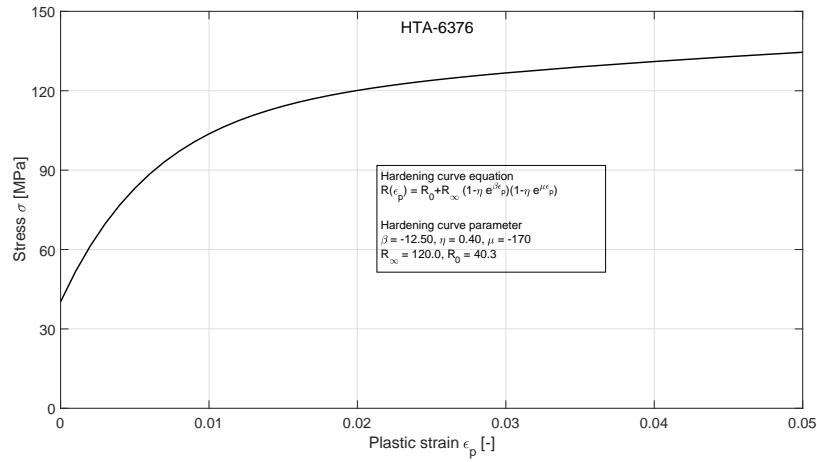


Fig. 5.23 Calibrated hardening curve used for micro RVE model for unnotched laminates under uniaxial tension

Table 5.15 Micro model information for unnotched laminates under uniaxial tension

Micro model	Information	DOF	NGP	Analysis time per increment [s]	
				Without tangent	With tangent
1D-1D	CUF beam element - 20L9 cross section elements with 2 B4 beam elements	1,869	1,440	0.45	2.90
3D-3D	1656 brick elements (2 elements per layer)	6,405	13,248	0.75	5.24

Table 5.16 Numerical results for off-axis laminates under uniaxial tension

Laminates Model	[10] _{2s}		[55] _{2s}		[67.5] _{2s}		Average	
	1D-1D	3D-3D	1D-1D	3D-3D	1D-1D	3D-3D	1D-1D	3D-3D
Total analysis time (hh:mm)	0:47	2:32	0:50	2:12	0:39	2:20	0:46	2:22
Average memory usage per core (GB)	1.52	28.1	1.51	28.0	1.51	28.1	1.51	28.1

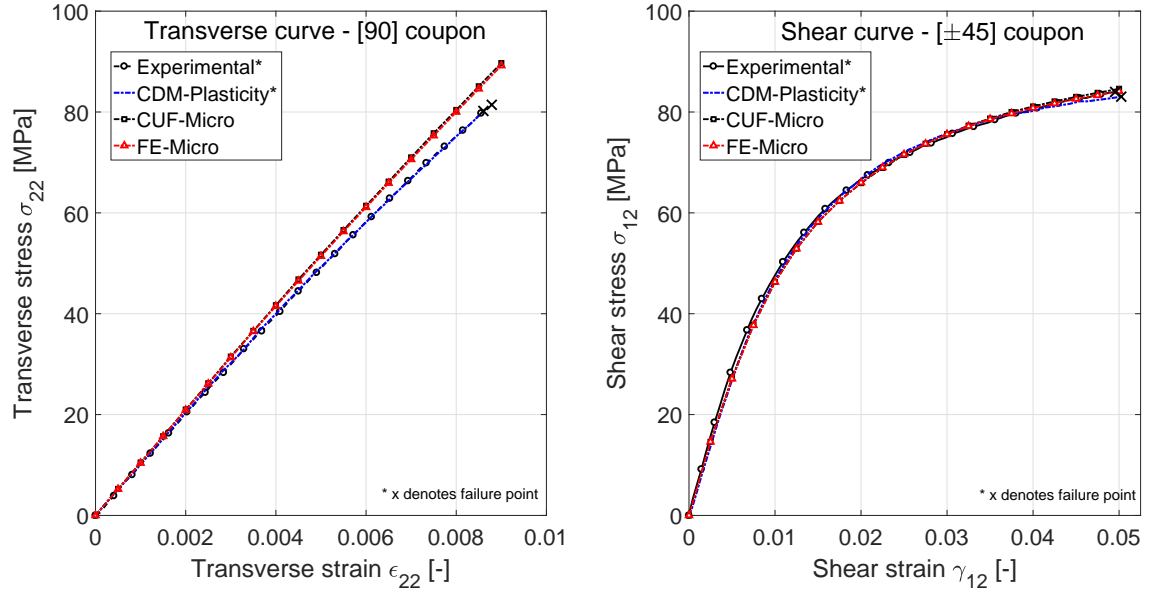


Fig. 5.24 Comparison of calibrated CUF-Micro and FE-Micro model against experimental [147] and CDM-Plasticity model [148] for transverse and shear response of the RVE

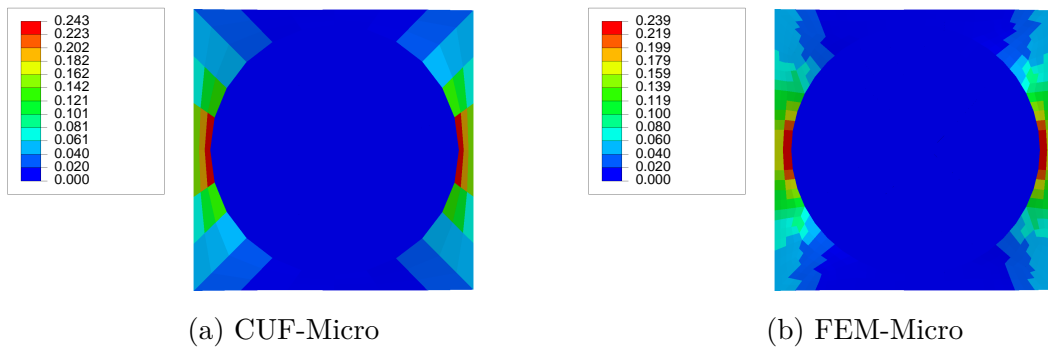


Fig. 5.25 Accumulated inelastic strain in calibrated RVE at an applied shear strain $\gamma_{12} = 0.05$

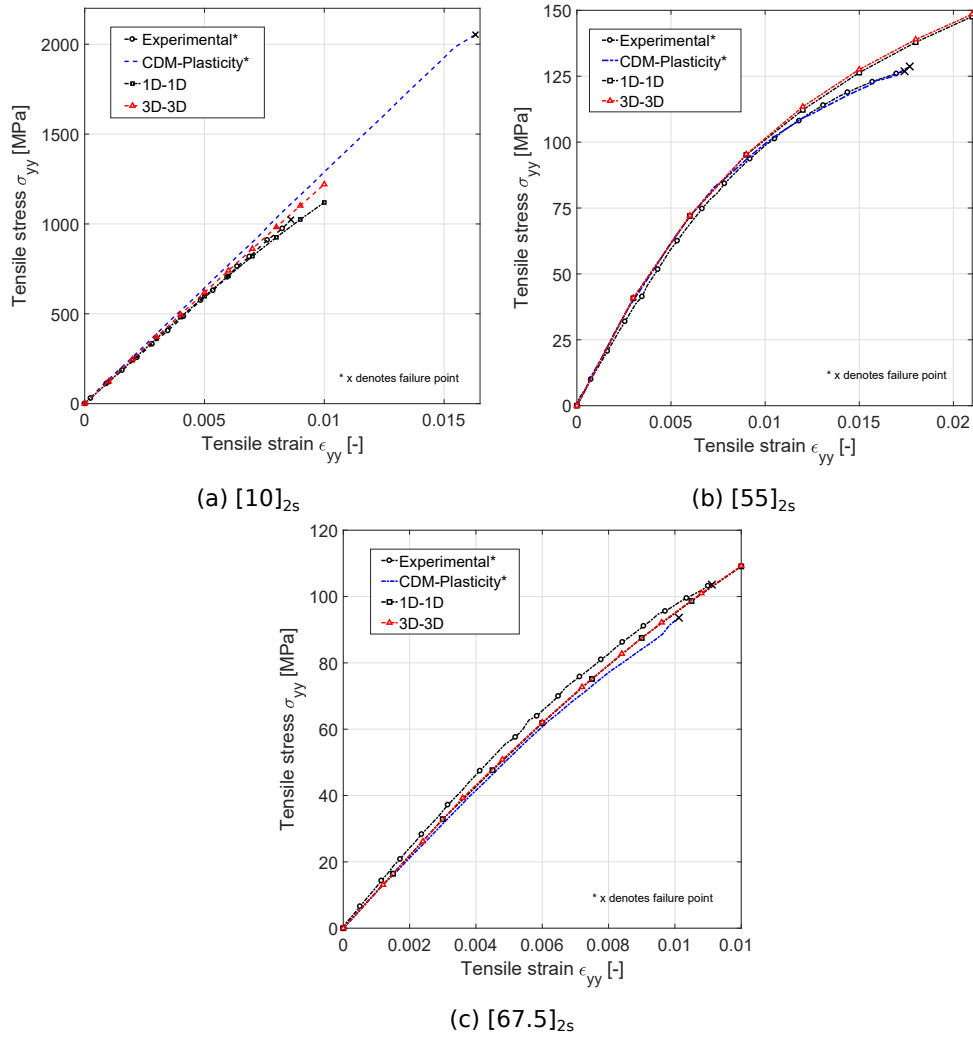


Fig. 5.26 Comparison of multiscale model predictions against experimental data [147] and CDM-Plasticity model [148] for off-axis laminates under uniaxial tension

2. In comparison to experimental and reference results, both the multiscale captures varying degree of nonlinearity exhibited by different laminates with acceptable accuracy (see Fig. 5.26)
3. Table 5.15 shows that 3D-3D micro models requires twice the time to undertake a single micro RVE analysis in comparison to 1D-1D model. The speed-up obtained is carried over to the overall analysis time for the multiscale analysis with 1D-1D models requires only 46 minutes whereas 3D-3D needs 2 hours and 22 minutes on average (see Table 5.16).
4. Stark difference is observed in terms of memory usage between both the multiscale model (see Table 5.16). The difference can be attributed to the large variation in required number of gauss points in the micro scale for both models. 1D micro RVE is modeled using 1,440 gauss points whereas 3D micro model requires 13,248 gauss points. On average, 1D-1D models are 18 times memory efficient than the respective 3D-3D models.

5.2.6 Open-hole specimen under tension

A numerical case with an open-hole specimen exhibiting nonlinearity under tension is undertaken to further exemplify the potential of the proposed multiscale framework. As illustrated in Fig. 5.27, a quarter of the open-hole specimen is modeled with symmetric boundary conditions. The specimen is subjected to a displacement loading of 0.5625 mm applied in 20 incremental steps. The dimensions of the specimen along with the boundary conditions are depicted in Fig. 5.27. Three classes of multiscale models are employed, namely:

- (a) 1D-1D : The cross-section of macro model is modeled using 37 L9 elements with each layer modeled with B2 beam elements.
- (b) 3D-1D Coarse: The macro model is built using 792 3D brick elements. One element is used to represent each layer.
- (c) 3D-1D Refined: The mesh density is increased around the hole region, thereby raising the total number of 3D brick element used to model the specimen to 1088. One element is used to represent each layer.

It should be noted that all the multiscale model described above are interfaced with the same CUF 1D beam micro model. The micro model consists of a fiber-reinforced

composite system with an elasto-plastic matrix. Fiber is assumed to be linear isotropic material with a Young's modulus $E = 414 \text{ GPa}$ and Poisson's ratio $\nu = 0.15$ and has a volume fraction of 0.6. The material properties of matrix are listed in Fig. 5.28 with yield stress and post-yield hardening curve. The mesh configurations for the different multiscale models are depicted in Figure 5.29. Due to high stress gradient within the zone around the hole, material nonlinearity in the micro model is activated only in the integrations points within this zone (shaded regions in Fig. 5.29).

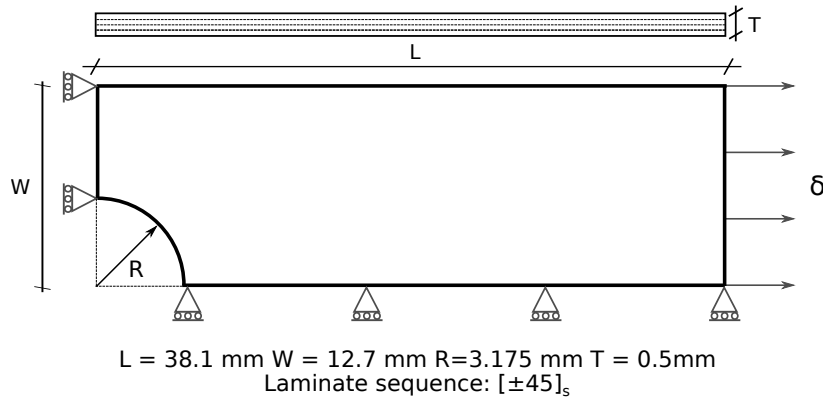


Fig. 5.27 Geometry and boundary condition for open-hole specimen under tension

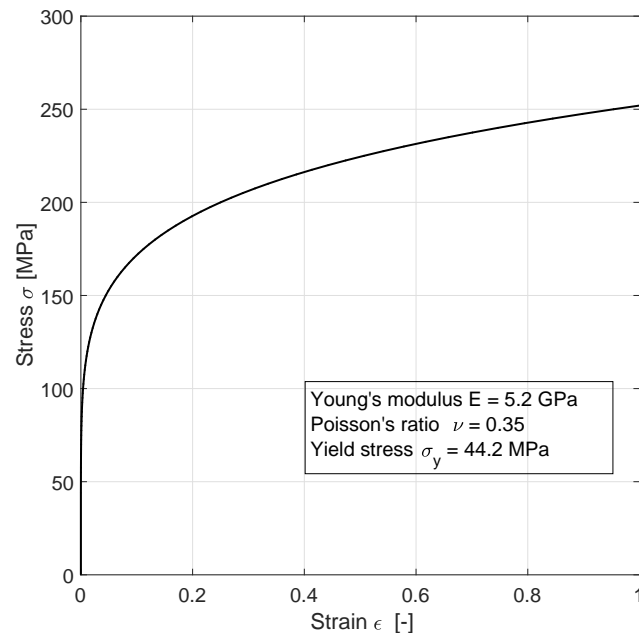
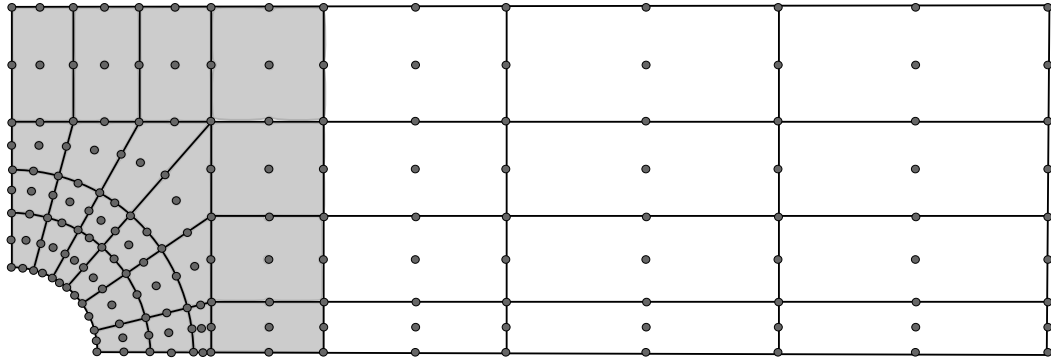
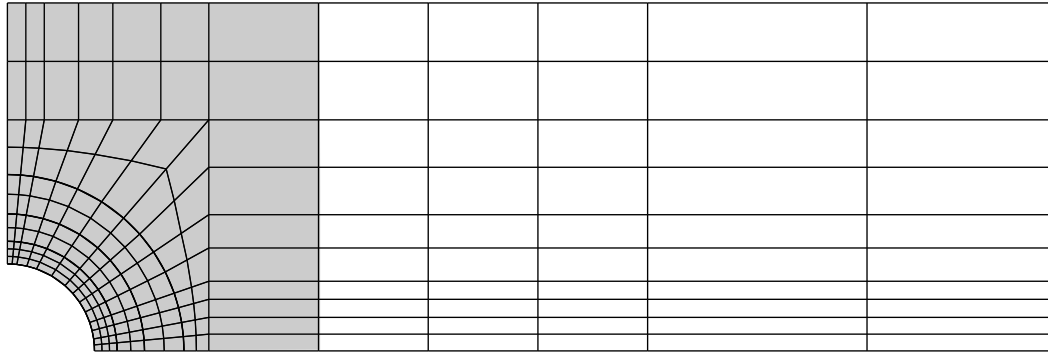


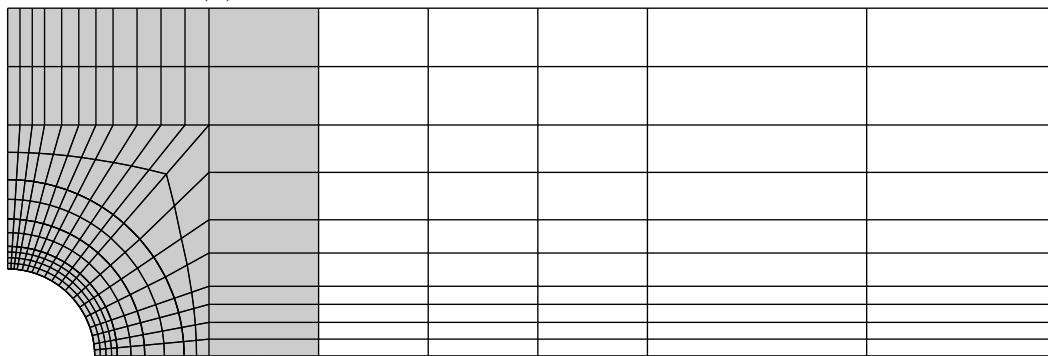
Fig. 5.28 Material properties for inelastic matrix for the micro model of open-hole specimen under tension



(a) 1D Macro model: 37 L9 cross-section elements - 1 B2 beam element per layer



(b) 3D Coarse macro model: 1088 3D brick element



(c) 3D Refined macro model : 792 3D brick element

Fig. 5.29 Mesh configuration for various multiscale models for open-hole specimen under tension (Non linear micro model is active only in shaded region)

Figure 5.30 depicts the remote stress-strain response for different multiscale models. Remote stress is computed by the dividing the reaction force at the applied displacement end by its area whereas ratio of applied displacement to the length of the specimen is taken as remote strain. Table 5.17 enlists the model information of different multiscale models along with analysis time and memory requirements. The accumulated inelastic strain for different multiscale models are compared in Fig. 5.31 including spatial resolution of the equivalent inelastic strain at the micro scale. Figure 5.32 depicts the von-Mises stress distribution within the matrix constituent of the micro RVE for various multiscale models. As depicted in Fig. 5.33, the convergence behavior of different multiscale model is studied by comparing the number of iterations required in each loading increment.

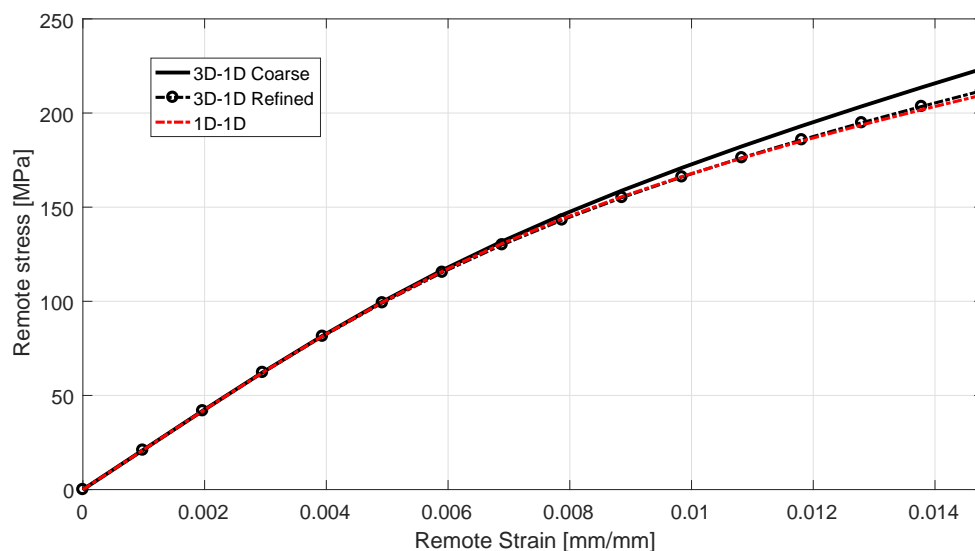


Fig. 5.30 Remote stress-strain curve for open-hole specimen under tension

Table 5.17 Numerical results for open-hole specimen under tension

Model	Information	DOF	NGP	Total analysis time [hh:mm:ss]	Memory usage [Gb]
1D-1D	37 L9 cross-section element with 4 B2 beams	2,655	2,664	01:53:38	2.02
3D-1D Coarse	792 3D brick elements with one element per layer	3,450	6,336	05:27:12	7.28
3D-1D Refined	1088 brick elements with one element per layer.	4,650	8,704	08:24:37	8.75

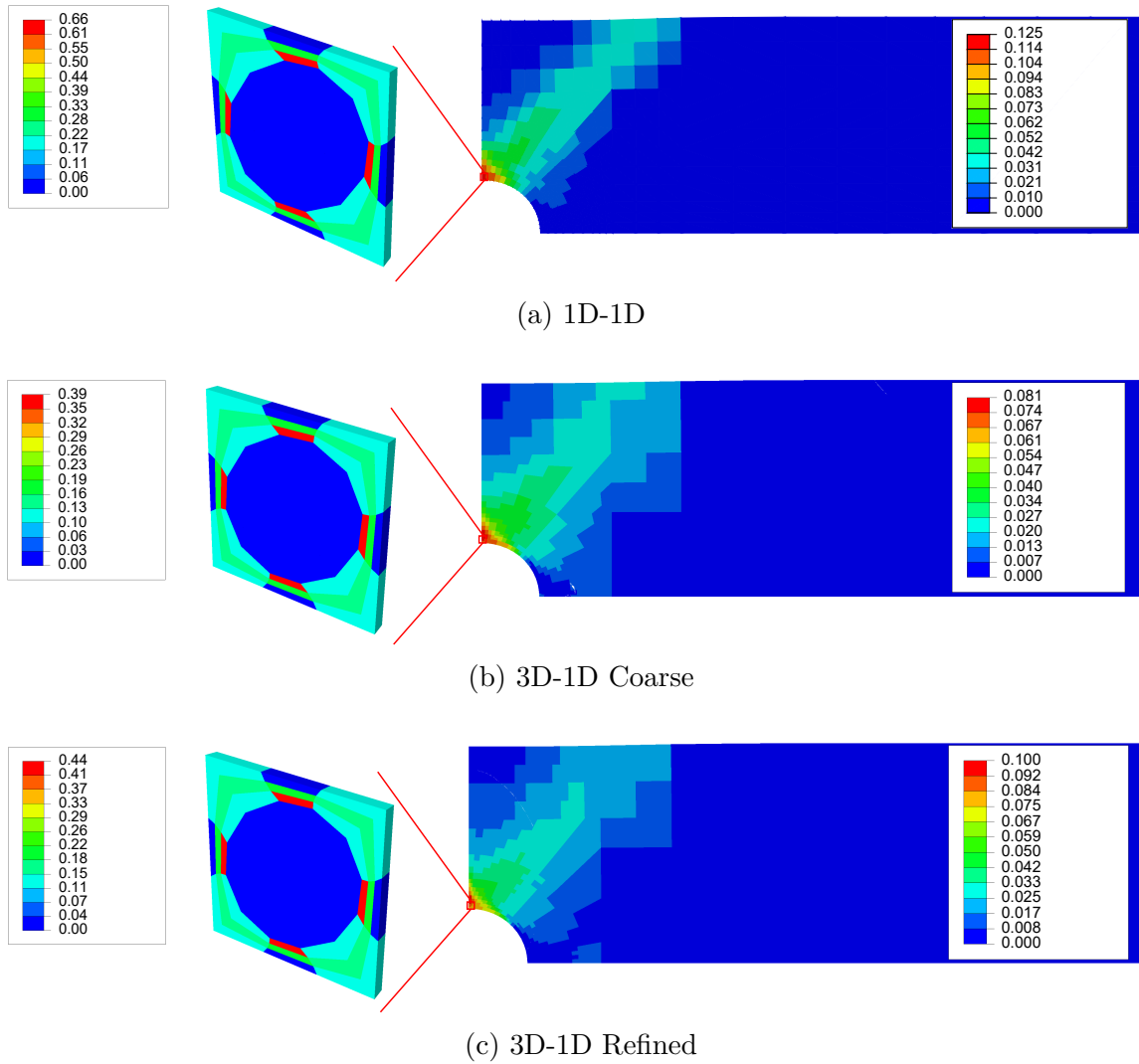


Fig. 5.31 Comparison of accumulated inelastic strain at multiple scales for various multiscale models for open-hole specimen under tension at an applied displacement loading of 0.5625 mm

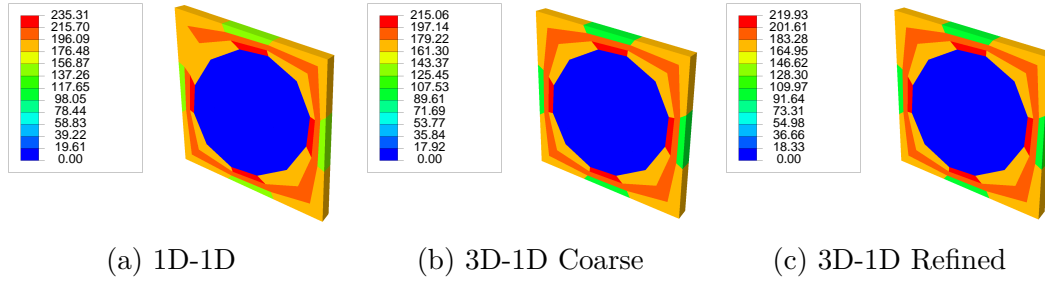


Fig. 5.32 Comparison of von-Mises stress resolution within matrix constituents of the micro scale RVE for various multiscale models for open-hole specimen under tension at an applied displacement loading of 0.5625 mm (Refer to Fig. 5.31 for location of micro RVE)

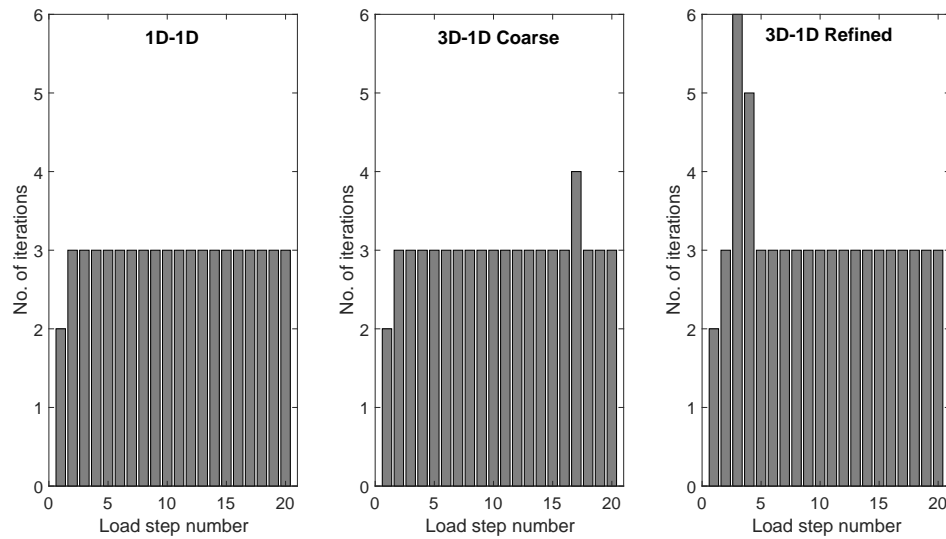


Fig. 5.33 Convergence behavior of different multiscale model for open-hole specimen under tension

Results suggests:

1. From Fig. 5.30 it can be stated that 1D-1D model and 3D-1D Refined exhibit similar remote stress- strain response. Underdeveloped stress fields within the 3D-1D Coarse macro model leads to a reduced nonlinear response.
2. Contour plots for accumulated inelastic strain at both scales illustrates superior capability of 1D-1D model to capture nonlinear behavior across scales (see Fig. 5.30). Figure 5.32 further emphasizes the capabilities of the framework by comparing the von-Mises stress field at the micro scale.
3. It can be inferred from Table 5.17 that 1D-1D models exhibit multifold efficiency in terms of analysis time.
4. Even though all multiscale models are interfaced with the same micro 1D model, 1D-1D model requires only 2,664 macro gauss points whereas 3D-1D Coarse and 3D-1D Refined models need 6,336 and 8,704 gauss points respectively. Therefore, total memory requirement for 1D-1D models is confined to 2.02 Gb whereas 3D-1D Coarse and 3D-1D Refined models need 7.28 Gb and 8.75 Gb respectively.
5. Figure 5.33 shows that framework exhibits superior convergence behavior as full tangent matrix is computed numerically for the macro model through perturbation method. For the current analysis, the framework requires on average 3 iterations per load increment.

5.3 Conclusion

A computationally-attractive concurrent multiscale framework for modeling linear and non-linear behavior for hierarchical and multi-layered structures is presented. Built within the scheme of Carrera Unified Formulation (CUF), the framework exploits CUF models at macro scale to model the structural level components (e.g: open-hole specimens, coupons etc) interfaced through concurrent modeling approach with an efficient CUF-micromechanics toolbox. The latter can model different classes of RVE with various architectures and material compositions with a reduced computational cost with significant reductions of the overall computational overhead of the multiscale analysis. Further efficiency stems from the adoption of a hybrid MPI-OpenMP based parallelization strategy for numerical implementation. Nonlinearity is introduced at the constituent level within the micro scale and the effect is scaled up to the macro structure

through homogenization. A perturbation based numerical homogenization scheme is utilized to obtain the macro tangent matrix, leading to a numerically robust framework. The variable kinematic nature of the formulation permits balancing the efficiency versus fidelity trade-off in a pragmatic manner. The numerical results suggests:

1. A multi-fold improvement of efficiency with respect to analysis time and memory requirement as compared to traditional multiscale implementations based on 3D FE, thereby addressing the scalability issues associated with multiscale modeling.
2. In comparison to reference literature and results from 3D FE, the accuracy of the solutions obtained are high
3. Present methodology presents an elegant way of employing 1D formulation at every scale independent of the geometric complexity or material heterogeneity, thus reducing the computational overhead at multiple scales.

Part III

Interface and Impact modeling

Chapter 6

Efficient progressive delamination analysis in composite structures

*A novel numerical framework to simulate progressive delamination in laminated structures based on component-wise models is presented. Formulated within the Lagrange polynomial based CUF models, Component-wise modeling approach permits modeling of various components of a complex structure through 1D CUF models at reduced computational cost. A class of higher-order cohesive elements are integrated within the CUF-CW framework to simulate interfacial cohesive mechanics between various components of the structure. A bilinear constitutive law based on mixed-mode delamination propagation is implemented. The approach makes use of the mixed-mode cohesive constitutive law and a global dissipation energy-based arc -length method to trace complex equilibrium path exhibited by delamination problem. The effectiveness and computational efficiency of CUF-CW models are highlighted through benchmark composite delamination problems and composite structures with multiple delamination fronts.*¹

6.1 Cohesive zone modeling

Cohesive zone modeling technique is an effective and extensively applied numerical tool for investigating fracture process in materials and structures [58, 150, 192, 210]. Based

¹Parts of this chapter has been in published in the following journals:

1. Kaleel I., Carrera E., Petrolo M. (2019), "Novel structural models for the progressive delamination of laminated composites"
2. Kaleel I., Petrolo M., Carrera E., Waas A., (2019) "On the effectiveness of higher-order models for physically non linear analysis", in "Advances in Predictive Models and Methodologies for Numerically Efficient Linear and Nonlinear analysis of Composites"

on the pioneering work by Dugdale [67] and Barenblatt [18], cohesive zone modeling technique hypothesizes the existence of a narrow band of vanishing thickness ahead of a crack tip. The narrow band is decomposed into two virtual surfaces (upper and lower) across the crack tip with presence of resistive cohesive forces. The cohesive constitutive law relates the cohesive traction to the separating distance between the surfaces. The traction-separation relation defines the constitutive behavior of the fracture, which imitates the non linear fracture process. The cohesive traction can attain a critical value, then reduces to zero thereby creating new free surfaces.

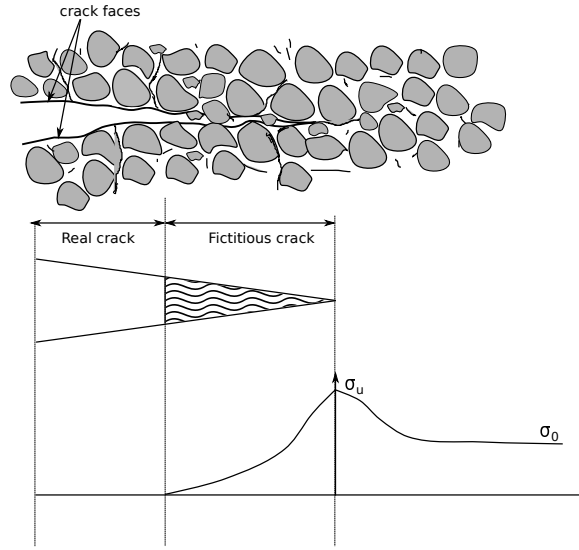


Fig. 6.1 Boundary value problem for cohesive formulation

6.1.1 Boundary value problem

Consider a domain Ω with a crack zone Γ_c as shown in Fig. 6.2. Essential boundary conditions are imposed along boundary Γ_u and prescribed tractions τ_i act along the boundary Γ_n . The domain Ω is subdivided into two domain, Ω_+ and Ω_- along the crack boundary Γ_c as depicted in Fig. 6.2. The equilibrium equations within the domain Ω can be expressed as follows:

$$\sigma_{ij,j} + \rho b_i = 0 \quad \text{in } \Omega \quad (6.1a)$$

$$\sigma_{ij} n_j = t_i \quad \text{in } \Gamma_n \quad (6.1b)$$

$$\sigma_{ij} n_j^+ = \tau_i^+ = -\tau_i^- = -\sigma_{ij} n_j^- \quad \text{in } \Gamma_c \quad (6.1c)$$

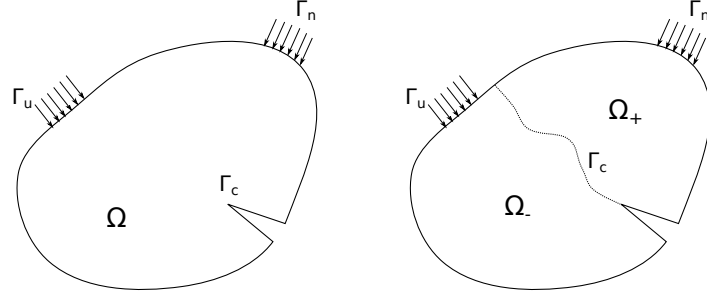


Fig. 6.2 Boundary value problem for cohesive formulation

where σ_{ij} is the stress field within the domain due to external loading τ_i , b_i are the body forces, ρ is the density of the material and τ_i^+ , τ_i^- are the closing tractions acting along the cohesive surface.

6.1.2 Kinematics of interfaces

The kinematics of the interface is established based on displacement jump across the interface boundary [11, 13]. The displacement jump across the interface can be expressed as:

$$[[u_i]] = u_i^+ - u_i^- \quad (6.2)$$

where u_i^+ and u_i^- denotes the displacement of the given point i on the upper (Ω_+) and lower surface (Ω_-) of the interface. In a three-dimensional cartesian coordinate system, the deformed position of a point x_i^\pm on the cohesive surface can be expressed as:

$$x_i^\pm = X_i^\pm + u_i^\pm \quad (6.3)$$

where X_i^\pm is the undeformed position of the point and u_i^\pm is the displacement at the given point. The tangential plane at a given point is spanned by two vectors v_{ξ_i} and v_{η_i} , expressed as:

$$v_{\xi_i} = \bar{x}_{i,\xi} \quad v_{\eta_i} = \bar{x}_{i,\eta} \quad (6.4)$$

where \bar{x} is the mid-surface position. Therefore, the local normal and tangential coordinate vector can be obtained as:

$$\mathbf{v}_n = \mathbf{v}_\xi \times \mathbf{v}_\eta \|\mathbf{v}_\xi \times \mathbf{v}_\eta\|^{-1} \quad (6.5a)$$

$$\mathbf{v}_s = \mathbf{v}_\xi \|\mathbf{v}_\xi\|^{-1} \quad (6.5b)$$

$$\mathbf{v}_t = \mathbf{v}_n \times \mathbf{v}_s \quad (6.5c)$$

The directional cosine forms an orthogonal rotation tensor Θ_i relating the local system to global system. The displacement jump in local system is given by

$$\Delta_i = \Theta_i [[u_i]] \quad (6.6)$$

The rotation tensor Θ_i is populated using the components of \mathbf{v}_n , \mathbf{v}_s and \mathbf{v}_t .

6.1.3 Constitutive modeling of interfaces

Cohesive constitutive law relates the cohesive traction τ_i to the displacement jump Δ_i across the interface surface, which can be expressed as follows:

$$\tau_i = \tau(\Delta_i) \quad (6.7)$$

The thermodynamically consistent cohesive constitutive formulation is based on the works of Simo and Ju for continuum damage models (CDM) [177] and extension of the CDM model within the context of cohesive formulation by Turon et al. [190, 191]. The free energy for a unit interface surface can be expressed as follows:

$$\Psi(\Delta, d) = (1 - d)\Psi^0(\Delta) - d\Psi^0(\delta_{3i}\langle -\Delta_3 \rangle) \quad (6.8)$$

where d is the scalar variable accounting for damage, δ_{ij} is the Kronecker delta and Ψ^0 is a convex function defined as follows:

$$\Psi^0(\Delta) = \frac{1}{2}\Delta_i D_{ij}^0 \Delta_j \quad \forall \quad \{i, j = 1, 2, 3\} \quad (6.9)$$

where D_{ij}^0 is the undamaged stiffness tensor. The second term in Eqn. 6.8 accounts for preventions of inter-penetration of adjacent cohesive surfaces after decohesion. The free energy equation is differentiated to obtain the constitutive relation, which is expressed as:

$$\tau_i = \frac{d\Psi}{d\Delta_i} = (1 - d)D_{ij}^0 \Delta_j - dD_{ij}^0 \delta_{3j} \langle -\Delta_3 \rangle \quad (6.10)$$

The undamaged stiffness tensor, D_{ij}^0 expressed in terms of scalar penalty stiffness K in each direction:

$$D_{ij}^0 = \begin{bmatrix} K_{11} & 0 & 0 \\ 0 & K_{22} & 0 \\ 0 & 0 & K_{33} \end{bmatrix} \quad (6.11)$$

Two classes of decohesion mechanism is considered in the current study, namely, (1) Pure mode and (2) Mixed-mode. In case of Pure mode I, mode II or mode III loading cases, delamination initiates when the inter-laminar traction attains the respective inter-laminar strength $(\tau_3^0, \tau_1^0, \tau_2^0)$.

$$\frac{\tau_i}{\tau_i^0} = 1 \quad i = 1, 2, 3 \quad (6.12)$$

The area under the traction-separation curve corresponds to their respective fracture toughness $(G_{IC}, G_{IIC}, G_{IIIC})$ as follows:

$$\begin{aligned} \text{Mode I} : \int_0^{\delta_3^f} \tau_3 d\delta_3 &= G_{IC} \\ \text{Mode II} : \int_0^{\delta_1^f} \tau_1 d\delta_1 &= G_{IIC} \\ \text{Mode III} : \int_0^{\delta_2^f} \tau_2 d\delta_2 &= G_{IIIC} \end{aligned} \quad (6.13)$$

As demonstrated by Cui et al. [54], non-interactive criteria can lead to poor delamination onset prediction. Therefore, a mixed-mode loading is utilized that account for coupling of different loading modes. Based on the quadratic criteria proposed by Ye [212], mixed-mode delamination onset can be expressed as:

$$\left(\frac{\langle \tau_3 \rangle}{\tau_3^0} \right)^2 + \left(\frac{\tau_1}{\tau_1^0} \right)^2 + \left(\frac{\tau_2}{\tau_2^0} \right)^2 = 1 \quad (6.14)$$

Since only tensile normal traction contributes to delamination onset, $\langle . \rangle$ operator is used in Eqn. 6.14 which can be expressed as $\langle x \rangle = \frac{1}{2}(x + |x|)$.

Damage Criteria

Based on the works of Simu et al.[177] and Turon [190, 191], the damage initiation criteria is formulated in the displacement jump space:

$$f(\lambda^t, r^t) = G(\lambda^t) - G(r^t) \leq 0 \quad \forall \quad t \in \mathbb{R}_+ \quad (6.15)$$

where t indicates the given instance of time, r^t is the damage threshold at the given instance t and λ^t is the equivalent displacement jump norm at the given instance t expressed as:

$$\lambda = \sqrt{\langle \Delta_3 \rangle^2 + \Delta_1^2 + \Delta_2^2} \quad (6.16)$$

The function $G(\cdot)$ in Eqn. 6.15 is a monotonic scalar function that define the evolution of damage variables. The initiation condition is met when the displacement jump norm λ exceeds the initial damage threshold r^0 , which is an input material property.

Damage Propagation

Analogous to rate equation introduced in [177], damage evolution of the variable d is defined using the rate equation

$$\dot{r} = \dot{\mu} \quad (6.17)$$

where $\dot{\mu}$ is the damage consistency parameter used to define the loading/unloading conditions based on Kuhn-Tucker relations:

$$\dot{\mu} \geq 0 \quad ; \quad f(\lambda^t, r^t) \leq 0 \quad ; \quad \dot{\mu} f(\lambda^t, r^t) = 0 \quad (6.18)$$

The rate equation for damage variable can be expressed as

$$\dot{d} = \dot{\mu} \frac{\partial f(\lambda, r)}{\partial \lambda} = \dot{\mu} \frac{\partial G(\lambda)}{\partial \lambda} \quad (6.19)$$

By integrating the rate equations for internal variables, damage threshold r^t and the damage variable d^t can be expressed as

$$r^t = \max \left\{ r_0, \max_{s \in [0, t]} \lambda^s \right\} \quad ; \quad d^t = G(r^t) \quad (6.20)$$

The scalar function $G(\cdot)$ determines the evolution of the damage variable based on bilinear constitutive equation and can be defined as follows:

$$G(\lambda) = \frac{\Delta^f(\lambda - \Delta^0)}{\lambda(\Delta^f - \Delta^0)} \quad (6.21)$$

where Δ^0 is the onset displacement jump equaling the initial damage threshold r^0 and Δ^f is the final displacement jump corresponding to full damage. Benzeggagh and Kenane proposed a semi-empirical formulation to compute the critical energy release rate for delamination under mixed-mode loading [25]:

$$G_c = G_I^c + (G_{II}^c - G_I^c) \left(\frac{G_I^c}{G_T^c} \right)^\eta, \quad G_T = \frac{G_{II}}{G_I + G_{II}} \quad (6.22)$$

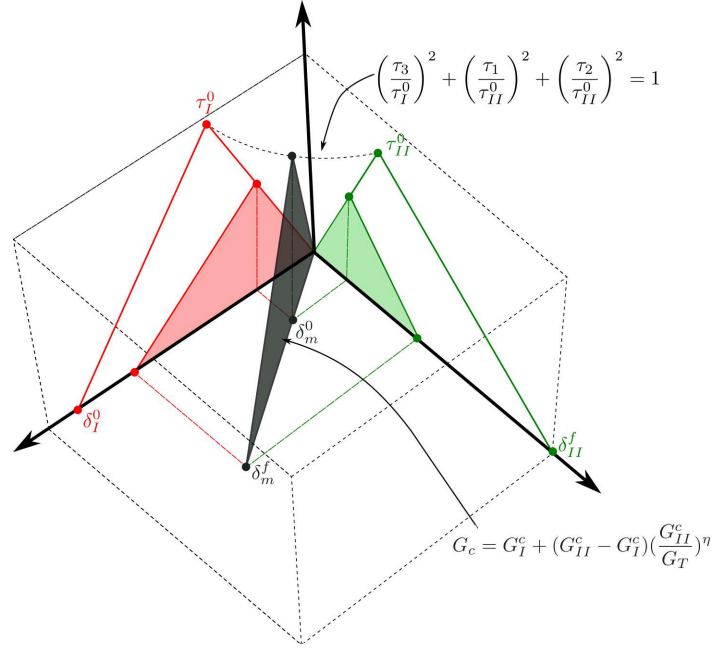


Fig. 6.3 Mixed-mode cohesive constitutive law

Therefore the displacement jump criterion is defined as:

$$\Delta^0 = \sqrt{\Delta_3^2 + (\Delta_{shear}^2 - \Delta_3^2)B^\eta} \quad (6.23)$$

$$B = \frac{G_{shear}}{G_T}, \quad \Delta_{shear} = \sqrt{\Delta_I^2 + \Delta_{II}^2}, \quad G_{shear} = G_I + G_{II} \quad (6.24)$$

The tangent constitutive matrix is formulated by differentiation the traction-displacement relation in Eqn. 6.7 [191]:

$$\begin{aligned} \dot{t} &= D_{ij}^{tan} \dot{\Delta}_j \\ D_{ij}^{tan} &= \begin{cases} \left\{ D_{ij} - K \left[1 + \delta_{3j} \frac{\leq -\Delta_j \geq}{\Delta_j} \right] \left[1 + \delta_{3j} \frac{\leq -\Delta_i \geq}{\Delta_i} \right] H \Delta_i \Delta_j, & r < \lambda < \Delta^f \right\} \\ D_{ij}, & r > \lambda \text{ or } \Delta^f < \lambda \end{cases} \end{aligned} \quad (6.25)$$

where H is the scalar parameter defined as:

$$H = \frac{\Delta^f \Delta^0}{(\Delta^f - \Delta^0) \lambda^3} \quad (6.26)$$

6.2 Cohesive models within Carrera Unified Formulation

The displacement field on the upper and lower face of the cohesive surface (6.2) can be expressed:

$$\mathbf{u}^+ = F_\tau N_i \mathbf{u}_{\tau i}^+, \quad \mathbf{u}^- = F_\tau N_i \mathbf{u}_{\tau i}^-, \quad [[\mathbf{u}]] = F_\tau N_i (\mathbf{u}_{\tau i}^+ - \mathbf{u}_{\tau i}^-) \quad (6.27)$$

where \mathbf{u}^+ and \mathbf{u}^- are the displacement along the upper and lower edge of the CS element respectively. As depicted in Fig. 6.4, three types of cohesive Lagrange cross-section

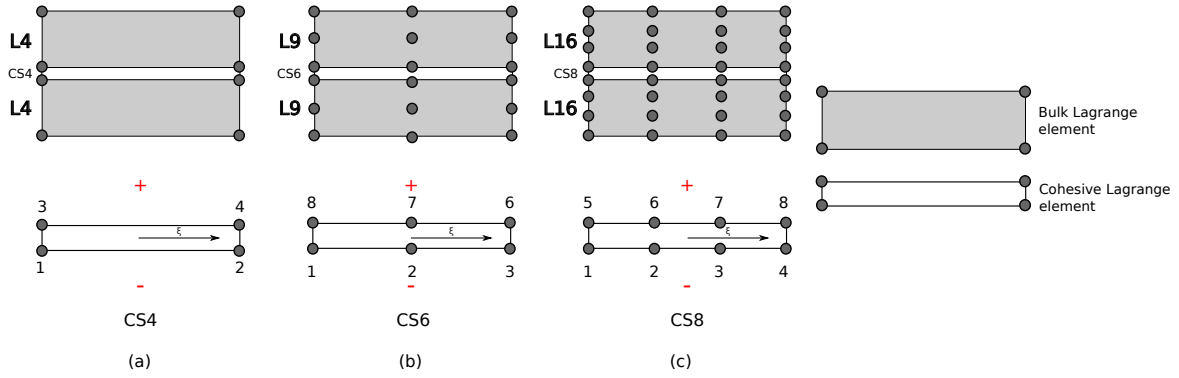


Fig. 6.4 Cohesive Lagrange cross-section elements

elements are introduced with expansion function expressed as:

Linear: CS4:

$$\begin{aligned} \mathbf{u}^+ &= F_1 \mathbf{u}_3 + F_2 \mathbf{u}_4 \\ \mathbf{u}^- &= F_1 \mathbf{u}_1 + F_2 \mathbf{u}_2 \end{aligned} \quad \left. \begin{aligned} F_1 &= \frac{1}{2}(1 - \xi) \\ F_2 &= \frac{1}{2}(1 + \xi) \end{aligned} \right\} \begin{aligned} \xi_1 &= -1 \\ \xi_2 &= 1 \end{aligned}$$

Quadratic: CS6:

$$\begin{aligned} \mathbf{u}^+ &= F_1 \mathbf{u}_4 + F_2 \mathbf{u}_5 + F_3 \mathbf{u}_6 \\ \mathbf{u}^- &= F_1 \mathbf{u}_1 + F_2 \mathbf{u}_2 + F_3 \mathbf{u}_3 \end{aligned} \quad \left. \begin{aligned} F_1 &= \frac{1}{2}\xi(1 - \xi) \\ F_2 &= -(1 - \xi)(1 + \xi) \\ F_3 &= \frac{1}{2}\xi(1 + \xi) \end{aligned} \right\} \begin{aligned} \xi_1 &= -1 \\ \xi_2 &= 0 \\ \xi_3 &= 1 \end{aligned}$$

Cubic - CS8:

$$\begin{aligned} \mathbf{u}^+ &= F_1 \mathbf{u}_5 + F_2 \mathbf{u}_6 + F_3 \mathbf{u}_7 + F_4 \mathbf{u}_8 \\ \mathbf{u}^- &= F_1 \mathbf{u}_1 + F_2 \mathbf{u}_2 + F_3 \mathbf{u}_3 + F_4 \mathbf{u}_4 \end{aligned} \quad \left. \begin{aligned} F_1 &= -\frac{9}{16}(\xi + \frac{1}{3})(\xi - \frac{1}{3})(\xi - 1) \\ F_2 &= \frac{27}{16}(\xi - 1)(\xi - \frac{1}{3})(\xi + 1) \\ F_3 &= -\frac{27}{16}(\xi + 1)(\xi + \frac{1}{3})(\xi - 1) \\ F_4 &= \frac{9}{16}(\xi + \frac{1}{3})(\xi - \frac{1}{3})(\xi + 1) \end{aligned} \right\} \begin{aligned} \xi_1 &= -1 \\ \xi_2 &= -1/3 \\ \xi_3 &= 1/3 \\ \xi_4 &= 1 \end{aligned} \quad (6.28)$$

By accounting for contributions due to cohesive matrix, the equilibrium equation (Eqn. 2.47) can be reformulated in terms of finite element matrices of a generic structural theory:

$$\mathbf{k}_{ij\tau s}^{bulk} \mathbf{u}_{\tau i} + \mathbf{k}_{ij\tau s}^{coh} [[\mathbf{u}_{\tau i}]] - \mathbf{p}_{\tau i} = 0 \quad (6.29)$$

where $k_{ij\tau s}^{bulk}$ and $k_{ij\tau s}^{coh}$ refers to fundamental nuclei of bulk and cohesive stiffness matrix respectively and fundamental nuclei for the external loading is expressed as $p_{\tau i}$. The expression for $k_{ij\tau s}^{bulk}$ and $p_{\tau i}$ has already been discussed in Chapter 2. Based on Eqn. 6.29, the fundamental nuclei of cohesive force can be formulated as follows:

$$f_{coh\tau i}^+ = \int_{\Gamma_c} F_{\tau} N_i \mathbf{u}_{\tau i}^+ t^+ d\Gamma_c \quad f_{coh\tau i}^- = \int_{\Gamma_c} F_{\tau} N_i \mathbf{u}_{\tau i}^- t^- d\Gamma_c \quad (6.30)$$

In order to formulate the fundamental nuclei of cohesive tangent nucleus, the rate form of the cohesive constitutive law is recalled (Eqn 6.25):

$$\dot{\mathbf{t}}^c = \mathbf{Q} \mathbf{D}^{tan} \mathbf{Q}^T [[\dot{\mathbf{u}}]] = \mathbf{Q} \mathbf{D}^{tan} \mathbf{Q}^T F_{\tau} N_i (\mathbf{u}_{\tau i}^+ - \mathbf{u}_{\tau i}^-) \quad (6.31)$$

where \mathbf{Q} is the orthogonal transformation matrix used for transformation between local and global system for cohesive elements. The fundamental nuclei for the cohesive tangent matrix is formulated by linearization of cohesive force vector (Eqn. 6.30):

$$k_{ij\tau s}^{coh} = \int_{\Gamma_c} F_{\tau} N_i \mathbf{Q} \mathbf{D}^{tan} \mathbf{Q}^T F_s N_j d\Gamma_c \quad (6.32)$$

Integration of cohesive elements with standard Gauss Quadrature leads to responses with spurious oscillations, especially when large stress gradients are present across a cohesive element [174]. In this work, Newton-Cotes integration scheme is adopted for integrating the FNs tangent stiffness matrix and internal force vector. The discrete equation of the weak form can be expressed as:

$$\mathbf{f}^{int} + \mathbf{f}^{coh} - \mathbf{f}^{ext} = 0 \quad (6.33)$$

where \mathbf{f}^{int} , \mathbf{f}^{coh} and \mathbf{f}^{ext} denotes the global vectors for internal, cohesive and external force respectively.

6.3 Dissipation-based arc-length solver

On the basis of the pioneering work by Riks [169] and others [53, 166], arc-length based numerical solution strategies are widely adopted to trace complex equilibrium path for

structural analysis with limit points. The methodology introduces an additional loading parameter as an unknown through constrain equation, thereby removing singularities associated with tangent matrix at limit points. Therefore, the system of equations read:

$$\begin{bmatrix} \mathbf{f}^{int}(\mathbf{u}) - \lambda \mathbf{f}^{ext} \\ g(\mathbf{u}, \lambda) \end{bmatrix} = 0 \quad (6.34)$$

where $\mathbf{f}^{int}(\mathbf{u})$ includes contribution from bulk as well cohesive finite elements and g is the constraint equation. The type of arc-length method depends on the kind of constraint equation g employed. A comprehensive review on different arc-length strategies along with their operation failure can be found in [31]. Even though traditional arc-length methods perform well in solving elastic nonlinear problems, they run into convergence issue in dealing with problems involving material instabilities, especially with the ones with localized failures such as delamination [12, 57].

Gutiérrez proposed a path-following constraint based on the energy release rate for geometrically linear problems with damage mechanics based material instabilities [91]. Since the constraint is based on the total energy dissipated, a global quantity, no a priori selection of degrees of freedom is required, a requirement commonly found in arc-length techniques for failure analysis [12, 57]. Based on the assumption that unloading behavior remains elastic, the dissipation-based arc-length constraint equation can be expressed as [91]:

$$g = \frac{1}{2} \mathbf{f}_{ext}^T (\lambda_0 \Delta \mathbf{u} - \Delta \lambda \mathbf{u}_0) - \Delta \tau \quad (6.35)$$

where \mathbf{f}_{ext}^T is the global unit external force vector, $\Delta \tau$ is the dissipation path parameter, λ_0 and \mathbf{u}_0 are the last converged load factor and displacement vector.

Implementation Aspects

At each Newton-Raphson iteration, the system of equation need to be solved is of the form (Eqn. 6.34):

$$\begin{bmatrix} \mathbf{K}^{tan} & -\mathbf{f}_{ext} \\ \mathbf{h}^T & s \end{bmatrix} \begin{bmatrix} d\mathbf{u} \\ d\lambda \end{bmatrix} = \begin{bmatrix} \phi_{res}^k \\ -g^k \end{bmatrix}; \quad \begin{bmatrix} d\mathbf{u} \\ d\lambda \end{bmatrix} = \begin{bmatrix} \Delta \mathbf{u} \\ \Delta \lambda \end{bmatrix}^{k+1} - \begin{bmatrix} \Delta \mathbf{u} \\ \Delta \lambda \end{bmatrix}^k \quad (6.36)$$

where k refers to the previous iteration and $\Delta \mathbf{u}$ and $\Delta \lambda$ is the displacement and load increments respectively. It is evident from the Eqn. 6.36 that the banded structure

of global consistent tangent matrix is deteriorated due to the presence of additional data pertaining to constraint equations. Using the Sherman-Morrison formula, the global consistent tangent (Eqn. 6.36) can be reformulated as [176, 198]:

$$\begin{bmatrix} d\mathbf{u} \\ d\lambda \end{bmatrix} = \begin{bmatrix} \mathbf{d}^I \\ -g^k \end{bmatrix} - \frac{1}{\mathbf{h}^T \mathbf{d}^{II} - s} \begin{bmatrix} (\mathbf{h}^T \mathbf{d}^I + g^k) \mathbf{d}^{II} \\ -\mathbf{h}^T \mathbf{d}^I - g^k(1 + \mathbf{h}^T \mathbf{d}^{II} - s) \end{bmatrix} \quad (6.37)$$

where the vectors \mathbf{d}^I and \mathbf{d}^{II} are obtained by factorizing the same structural tangent matrix \mathbf{K}^{tan} :

$$\mathbf{K}^{tan} \mathbf{d}^I = \phi_{res} \quad \mathbf{K}^{tan} \mathbf{d}^{II} = -\mathbf{p} \quad (6.38)$$

Based on the constraint equation (Eqn. 6.35), the derivatives required for the construction of global consistent tangent matrix (Eqn. 6.37) reads [198]:

$$\mathbf{h} = \frac{\partial g}{\partial \mathbf{u}} = \frac{1}{2} \lambda_0 \mathbf{p}^T, \quad s = \frac{\partial g}{\partial \lambda} = -\frac{1}{2} \mathbf{p}^T \mathbf{u}_0 \quad (6.39)$$

The amount of energy dissipated during a given load increment is always monotonically increasing quantity. However, the solver can run into numerical issues at non-dissipative regions (such as pure elastic loading) on the equilibrium path as the path parameter can get close to machine precision. This is addressed through addition of a robust switching algorithm by introduction of threshold values. The algorithm switches to displacement/force controlled loading during non-dissipative regions and switches back to dissipation-controlled when the energy threshold is met.

In addition, the path parameter $\Delta\tau$ needs to be adjusted during the course of computation to limit the number of steps required to minimum without any cut-backs. The adjustment is achieved automatically by setting the optimal value of iterations per increment k_{opt} . The path parameter for a given increment i is set as [91]:

$$\Delta\tau^i = \Delta\tau^{i-1} \frac{k_{opt}}{k^{i-1}} \quad (6.40)$$

where k^{i-1} refers to the number of iterations required in the last converged load step. In this work k_{opt} is set as 6.

6.4 Numerical Results

Four sets of numerical results are discussed in this section. The first three sets of numerical examples pertains to simulation of benchmark test including Double

Cantilever Test with pure Mode I delamination propagation, End Notch Flexure test with pure mode II delamination propagation and numerical modeling of mixed-mode bending test with two different mode-mix ratios. The fourth numerical case deals with simulation of composite specimen with multiple delamination fronts.

6.4.1 Double cantilever test

The numerical case intends to highlight the effectiveness of higher-order beam models to accurately capture the equilibrium path for DCB test. The DCB problem exhibits pure mode I fracture. The material properties for the DCB specimen is tabulated in Table 6.1. As illustrated in Fig. 6.5, the length of the beam is 10 m with an initial crack length of 2.5 m. Component-wise modeling approach adopted with two-cross section configuration as depicted in Fig. 6.6. In order to compare different classes

Table 6.1 Material properties for double cantilever test

E_1 (GPa)	E_2/E_3 (GPa)	G_{12} (GPa)	G_{23} (GPa)	ν_{12}/ν_{13} (-)	G_{IC} (Nmm ⁻¹)	τ_1 (MPa)	K (Nmm ⁻³)
135.3	9.0	5.2	3.1	0.24	0.46	2.0	1.0×10^6

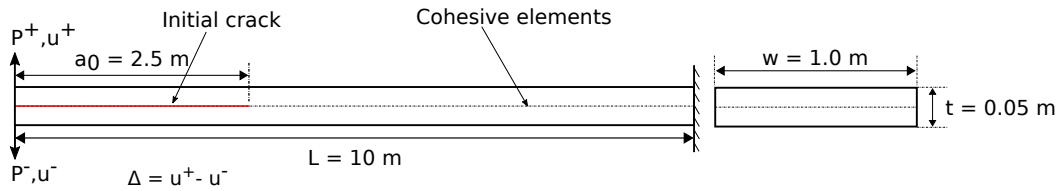


Fig. 6.5 Geometry and loading for double cantilever test

of beam elements, two sets of beam element configurations are considered as listed in Table 6.2. The first set consists 120 B2 (linear), 60 B3 (cubic) and 40 B4 (cubic) beam elements with 4L9-2CS6 cross-section configuration. A finer mesh configuration with 240 B2 (linear), 120 B3 (cubic) and 80 B4 (cubic) beam elements with 8L9-4CS6 cross-section configuration is considered as the second set. The configurations for the beam in each set were chosen in such a way that the total degrees of freedom remained the same. Energy-based arc length method with an initial lambda λ_0 of 25 along with unit force applied as P^+ and P^- . The analysis is terminated when the displacement u reaches 0.055 m. The equilibrium path obtained using different beam configurations are compared against analytical solution based beam theory proposed by Mi et al. [128].

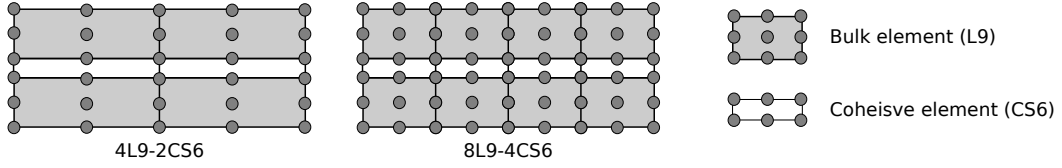


Fig. 6.6 End notch flexure test: Cross-section mesh configuration

Table 6.2 Model information for DCB specimen test

Model	Information	DOF
4L9-2CS6	Cross-section is modeled using 4L9 bulk elements with 2 CS6 cohesive elements (see Fig. 6.6). Beam configurations used to model are (a) 120 B2, (b) 60 B3 and (c) 40 B4	10,890
8L9-4CS6	Cross-section is modeled using 8L9 bulk elements (four per each layer) with 4 CS6 cohesive elements (see Fig. 6.6). Beam configurations used to model are (a) 240 B2, (b) 120 B3 and (c) 80 B4	39,042

Figure 6.7 compares the equilibrium path for different classes of beam configuration to the analytical solution. Mismatch in the initial stiffness of undamaged laminate can be attributed to the fact the beam is not perfectly built-in and can rotate at the delamination front. Three-dimensional contour plot for propagation of delamination front at various load instances 8L9-4CS6 cross-section configuration with 80 B4 beam elements are depicted in Fig. 6.8.

Following observations can be drawn:

1. It is evident from Fig. 6.7a that B2 elements tend to overestimate the response whereas B3 elements show spurious oscillations for 4L9-2CS6 cross-section configuration. Even though all the beam configuration amounts to same degrees of freedom, cubic B4 beam configuration tends to capture the equilibrium quite accurately, even in case of coarser configuration
2. Cubic beam element B4 tends to perform well for both coarse and finer mesh configurations. In case of refined cross-section mesh (see Fig. 6.7b), B3 and B4 beam configurations compare well with the analytical solution.

6.4.2 End notch flexure test

End Notch Flexure (ENF) test are often adopted to characterize the mode II delamination test method and it is employed as benchmark test to evaluate the accuracy and performance of cohesive based implementation. The ENF specimen is modeled using

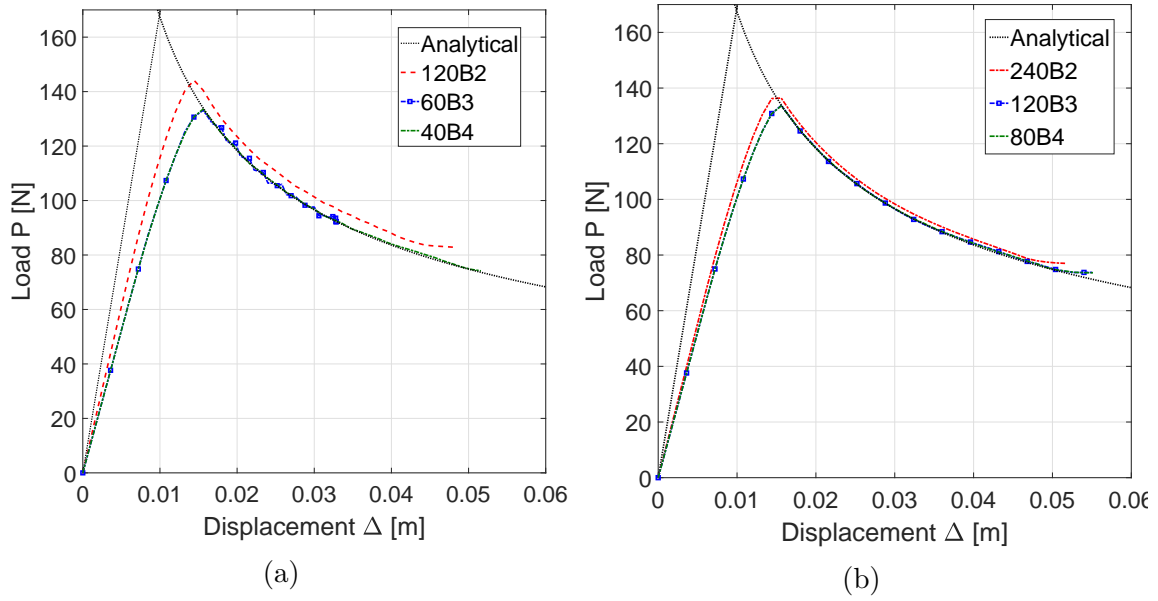


Fig. 6.7 Double cantilever test: Comparison of equilibrium curves for different beam elements with same mesh density for (a) 4L9-2CS6 cross-section configuration and (b) 8L9-4CS6 cross-section configuration

an isotropic material as analytical solution are valid only for isotropic material [128]. The material properties of the specimen is tabulated in Table 6.3. Figure 6.9 illustrates the geometry and boundary conditions of the specimen. Additionally, inter-penetration along the initial crack surface is prevented by placing contact elements along the initial crack surface (see Fig. 6.9). Energy-based arc length method is utilized to solve the numerical problem with an initial lambda λ_0 of 50 with a unit force applied as P . The analysis is terminated when the displacement u reaches 3.5 mm.

Table 6.3 Material properties for ENF specimen test

Bulk material		Cohesive material		
E	ν	τ_1	K	G_{IIC}
(GPa)	(-)	(MPa)	(Nmm ⁻³)	Nmm ⁻¹
150.0	0.25	80.0	10^6	1.45

Two classes of CUF models are developed, namely (a) 4L9-2CS6 and (b) 2L9-3CS6 as shown in Fig. 6.10. In order to highlight the efficiency of the higher-order component-wise models, two additional sets of model based on standard linear brick elements are developed as tabulated in Table 6.4. The total degrees of freedom as well as the total analysis time for different models are also enlisted in Table 6.4. The

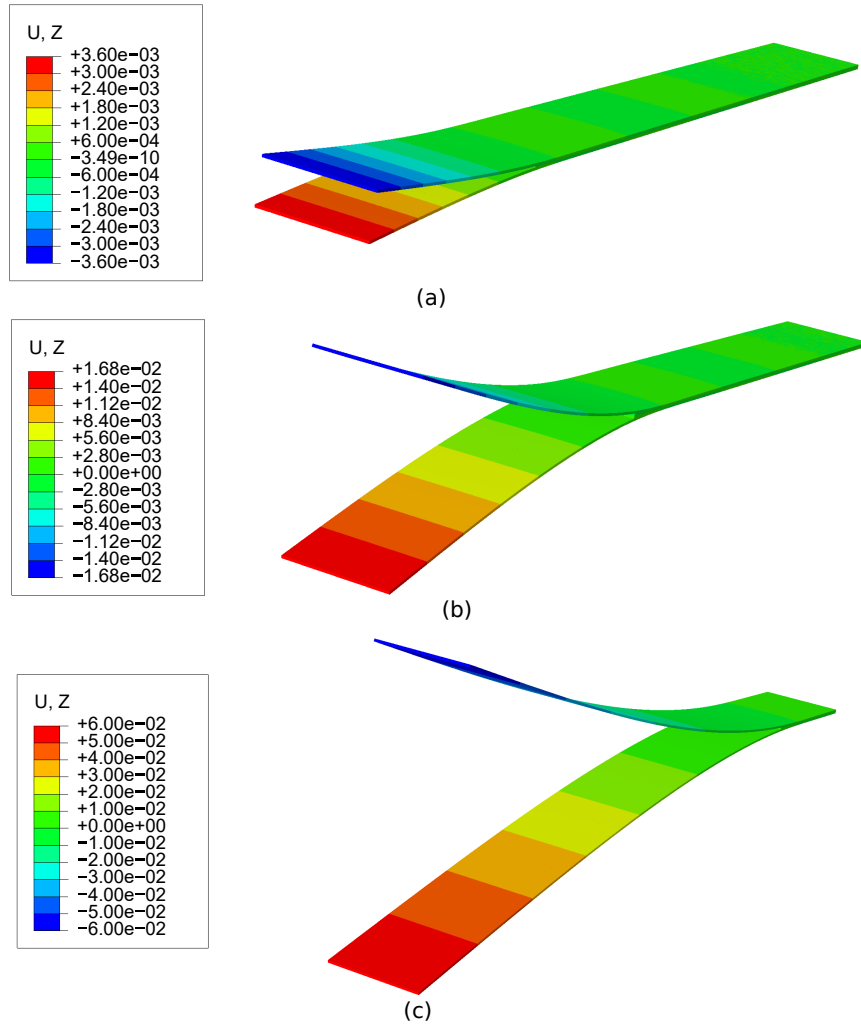


Fig. 6.8 Double cantilever test: Three-dimensional displacement contour plot for 8L9-4CS6 with 80B4 model at displacement of (a) 7.2 mm, (a) 33.6 mm and (c) 52.0 mm

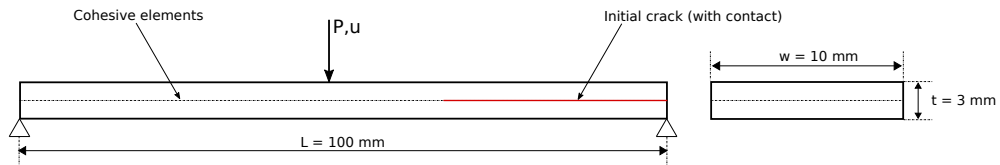


Fig. 6.9 Geometry and loading for end notch flexure test

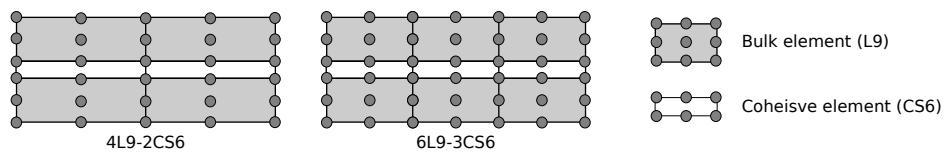


Fig. 6.10 End notch flexure test: Cross-section mesh configuration

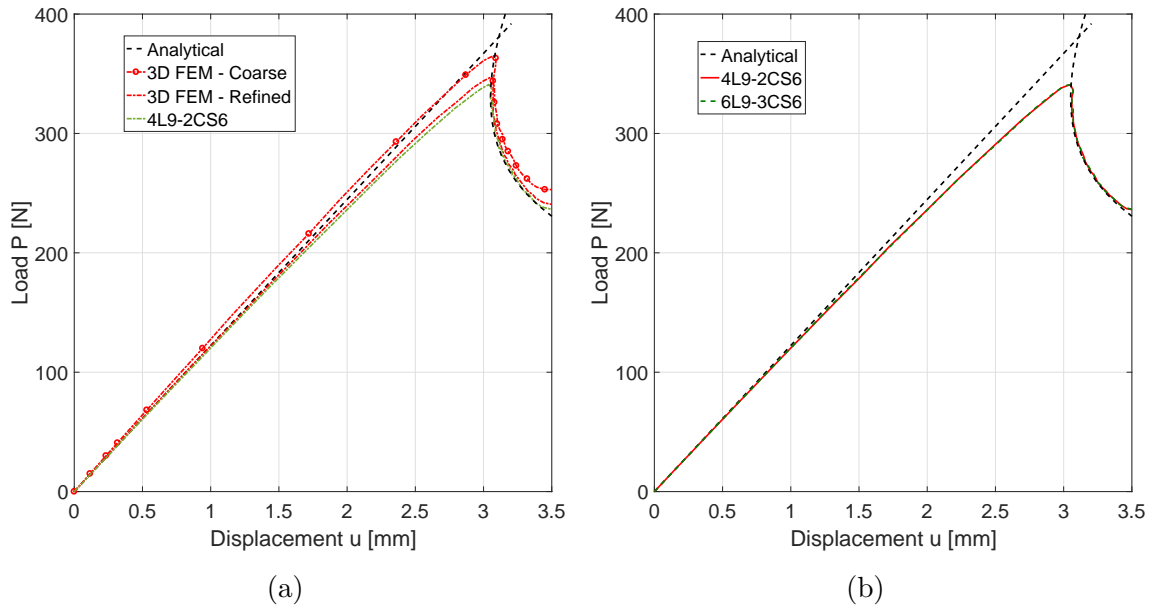


Fig. 6.11 End notch flexure test: Comparison of equilibrium curves for (a) linear (B2) and cubic (B4) beam elements using 8L9-4CS6 cross-section configuration and (b) different cross-section configuration using 80 cubic (B4) beam elements

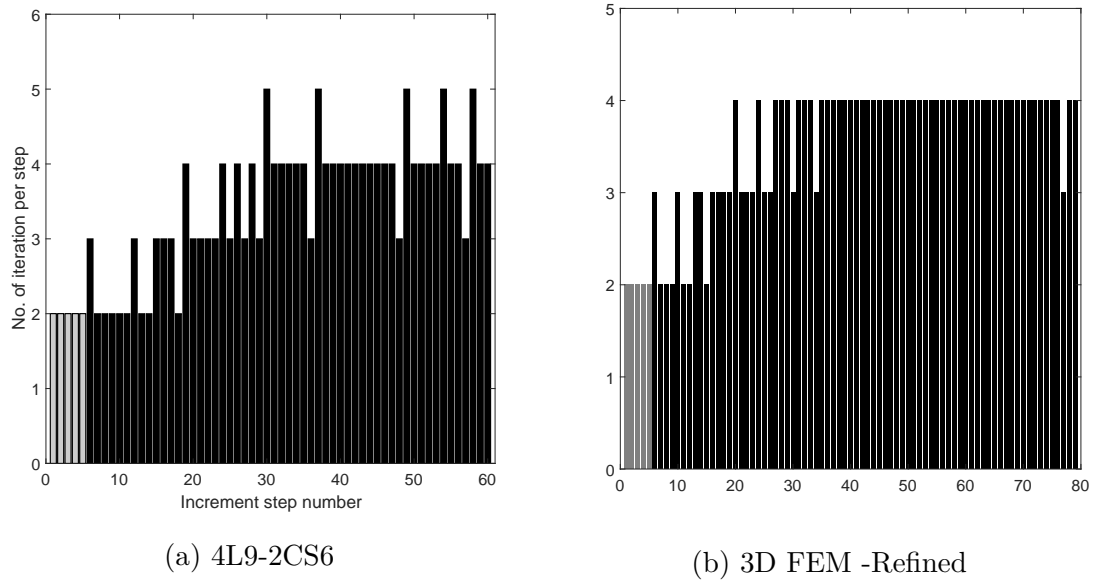


Fig. 6.12 End notch flexure test: Comparison of the no. of iteration required per increment for different models (Gray : Load controlled and Black: Energy-based arc length)

Table 6.4 Model information for ENF specimen test

Model	Information	DOF	Analysis time [s]
4L9-2CS6	Cross-section is modeled using 4L9 bulk elements with 2 CS6 cohesive elements (see Fig. 6.10). The beam is modeled using 80 B4 elements	21,690	383
6L9-3CS6	Cross-section is modeled using 6L9 bulk elements (three per each layer) with 3 CS6 cohesive elements (see Fig. 6.10). The beam is modeled using 80 B4 elements	30,366	666
3DFEM - Coarse	Linear brick element with a mesh density of $4 \times 240 \times 4$ along with 4×240 cohesive elements inserted between the layers. The mesh density is equivalent to 4L9-2CS6 configuration amounting to same degrees of freedom	21,690	420
3DFEM - Refined	Linear brick element with a mesh density of $4 \times 360 \times 4$ along with 4×360 cohesive elements inserted between the layers.	32,490	893

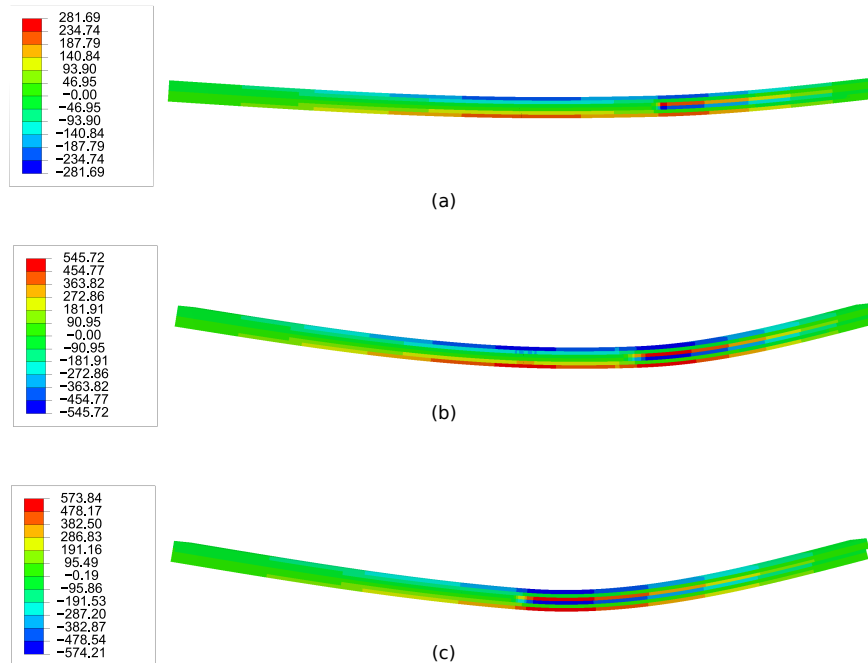


Fig. 6.13 End notch flexure test: Stress σ_{yy} contour plot for 4L9-2CS6 model at (a) $\lambda = 30.08$, (b) $\lambda = 228.4$ and (c) $\lambda = 280.3$

equilibrium path obtained by the models are compared against analytical solution developed by Mi et al. [128]. Figure 6.11a depicts the comparison of equilibrium curves between 3D FEM models and 4L9-2CS6 beam model. The equilibrium curve for CW models with different cross-section mesh configurations is depicted in Fig. 6.11b. Solver performance and convergence behavior of 4L9-2CS6 beam model is compared against 3DFEM-Refined model in Fig. 6.12. The deformed configuration along with stress σ_{yy} contour plot is depicted in Fig. 6.13 for 4L9-2CS6 CW model.

Following observations can be drawn:

1. It is evident from Fig. 6.11(b) that the CUF-CW models accurately captures the equilibrium as compared to the analytical solution
2. Even though 3D FEM - Coarse and 4L9-2CS6 configurations amounts to the same degrees of freedom, 3D FEM - Coarse exhibits a stiffer response in comparison to analytical solution whereas 4L9-2CS6 model accurately captures the equilibrium path.
3. Table 6.4 emphasizes the computational efficiency of CUF-CW models as compared to 3D FEM. The 4L9-2CS6 configuration and 3DFEM - Refined produces similar equilibrium path, but the former model requires only 383 s whereas the latter takes 893s to complete the simulation. Superior convergence behavior of the model is further highlighted in Fig. 6.12

6.4.3 Mixed-mode bending test

This section deals with numerical simulation of mixed-mode bending (MMB) test, a widely adopted standardized testing method (ASTM-D5528) for characterizing mixed-mode fracture toughness in laminated composites as the same experimental apparatus can be used for any mixed-mode ratio [16]. Different mode ratios are obtained by varying the loading arm length c with DCB and ENF test being the borderline of MMB test capabilities. Based on the experimental and numerical investigation undertaken by Camanho et al. [30], simulation of MMB test using CUF-CW framework is undertaken. Figure 6.14 depicts the geometry and boundary conditions for MMB test based on simplification of ASTM standards. A uni-directional AS4/PEEK carbon-reinforced composite with fibers oriented along the beam direction is considered (see Table 6.5 for properties).

Two mode-mix ratios are considered: (a) 0.5 and (b) 0.8. Table 6.6 enlists the geometric properties and applied loading conditions for different mode-mix ratios. As

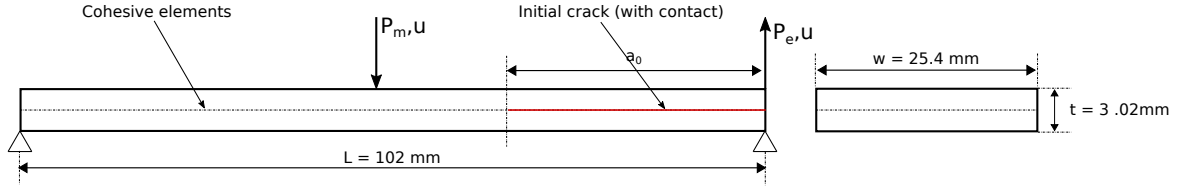


Fig. 6.14 Geometry and loading for mixed-mode bending test

Table 6.5 Material properties for MMB test

E_{11}	$E_{22}=E_{33}$	$G_{12}=G_{13}$	G_{23}	$\nu_{12} = \nu_{13}$	G_{IC}	G_{IIIC}	τ_3	τ_2	K_0
(GPa)	(GPa)	(GPa)	(GPa)	(-)	(Nmm ⁻¹)	(Nmm ⁻¹)	(MPa)	(MPa)	(Nmm ⁻³)
122.7	10.1	5.5	3.7	0.25	0.969	1.719	80	100	10 ⁶

tabulated in Table 6.7, two classes of CUF model with varying mesh density is utilized to model the problem in hand. Similar to the previous numerical case, additional 3D FEM models based on standard linear elements are developed for the sake of comparison (see Table 6.7). In addition, inter-penetration between initial crack is mitigated by placing contact elements along the crack surface. Based on the rigid body motion assumption for loading arm, the load-point displacement u is computed as [17, 30]:

$$u = \frac{2c + L}{L} u_m - \frac{2c}{L} u_e \quad (6.41)$$

where u_m and u_e are displacement obtained at middle and end of the specimen (see Fig. 6.14). Energy-based arc length method is employed to solve the numerical problem with an initial lambda λ_0 of 10 and 25 for mode-mix ratio of 0.5 and 0.8 respectively. The analysis is terminated when the load-point attains 6.5mm and 6.1mm for mode-mix ratio of 0.5 and 0.8 respectively.

Table 6.6 Geometric properties and load values for different mode-mix ratio for MMB test [17, 30]

G_{II}/G_T	G_c (Nmm ⁻¹)	a_0 (mm)	c (mm)	P_m (N)	P_e (N)
0.5	1.131	34.1	44.4	1.87P	0.87P
0.8	1.376	31.4	28.4	1.56P	0.56P

Balzani and Wagner used a three-dimensional FE models mixed-mode delamination using linear and exponential cohesive constitutive law[17]. Figure 6.15(a) compares equilibrium curve obtained using 8L9-4CS6-60B4 model against experimental and

Table 6.7 Model information for MMB test

Model	Information	DOF
8L9-4CS6-40B4	Cross-section is modeled using 8L9 continuum element (4 per each layer) with 4 CS6 cohesive elements. The beam is modeled using 40 B4 elements.	19,602
8L9-4CS6-60B4	Cross-section is modeled using 8L9 continuum element (4 per each layer) with 4 CS6 cohesive elements. The beam is modeled using 60 B4 elements.	29,322
3D FEM - Coarse	Linear brick element with mesh density of 8x120x4 with 8x120 linear cohesive elements inserted between the layers. The mesh density is equivalent to 8L9-4CS6-40B4 configuration amounting to same degrees of freedom.	19,602
3D FEM - Refined	Linear brick element with mesh density of 8x240x4 with 8x240 linear cohesive elements inserted between the layers. The fem element density is twice as 3D FEM coarse configuration.	39,042

numerical results of Camanho et al. and Balzani et al. for different mode-mix ratio [17, 30]. Comparison of equilibrium curves for different CUF-CW model against standard 3D FEM models are depicted in Fig. 6.15(b). Table 6.8 compares the maximum load obtained by CUF-CW model using 8L9-4CS6-60B4 configuration against experimental and numerical reference results. The analysis time along with total number of increments and iterations required for all numerical models are enlisted in Table 6.9.

Table 6.8 Comparison of maximum load obtained using 8L9-4CS6-60B4 model for MMB test against experimental and literature

G_{II}/G_T	Experimental [30]	Camanho et al. [30]		Balzani et al. [17]		CUF-CW	
		Value	Error	Value	Error	Value	Error
	(N)	(N)	(%)	(N)	(%)	(N)	(%)
0.5	275.35	236.6	14.1	251.2	8.8	261.0	5.2
0.8	518.66	479.9	7.5	438.3	15.5	494.5	4.7

Results suggests:

1. Equilibrium curves for different mode-mix ratios depicted in Fig. 6.15 (a) illustrates that effectiveness of CUF-CW models for modeling MMB test
2. It is evident from Fig. 6.15(b) that even 3D FEM models produces slightly stiffer response as compared CUF-CW model

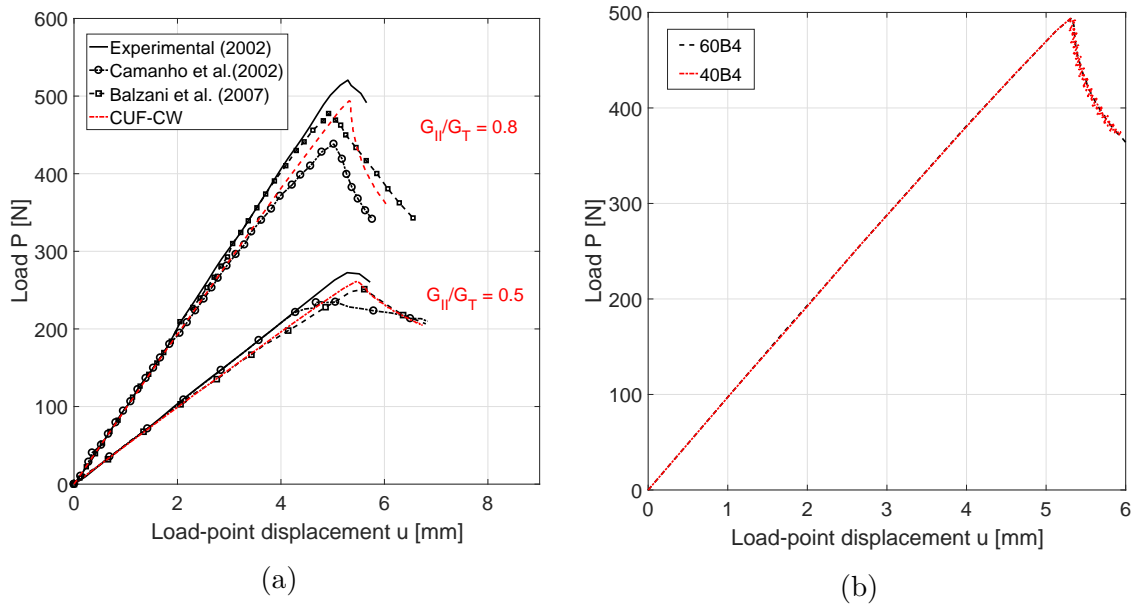


Fig. 6.15 Equilibrium curves for mixed-mode bending test: (a) Results from CUF-CW model using 8L9-4CS6-60B4 is compared against experimental and numerical results from the literature for different mode ratios [17, 30] (b) Comparison of different CUF-CW models against 3D FEM models with varying mesh density for 0.8 mode-mix ratio

Table 6.9 Numerical results for MMB test

Model	Total number of increments	Total number of iterations	Analysis time [hh:mm]
8L9-4CS6-40B4	91	548	0:27
8L9-4CS6-60B4	93	603	0:45
3D FEM - Coarse	300 ¹	2250	1:30
3D FEM - Refined	88 ²	468	0:48

¹ Maximum allowable increment is 300. Analysis terminated prematurely

² Convergence issues. Analysis terminated prematurely

3. Even though 8L9-4CS6-40B4 and 3D FEM - Coarse has similar size and exhibit oscillations in the equilibrium curve, 3D FEM - Coarse prematurely terminates due to convergence issues (see Table 6.9).
4. In comparison to experimental results, maximum load predictions by CUF-CW models are within an average error limit of 5% as compared to reference numerical results (see Table 6.8).

6.4.4 Multiple delamination of composite specimen

Robinson et al. investigated multiple mixed-mode delamination in a carbon-fiber laminate through numerical as well experimental study [170]. As illustrated in Fig. 6.16, the problem consists of two initial cracks with the first crack placed along the mid-plane on the left end of the specimen and the second initial crack is positioned two plies below and right of the first initial crack. The problem has been widely studied in literature as it exhibits complex equilibrium path, therefore serves as good benchmark example [12, 145]. The material properties of the specimen is tabulated in Table

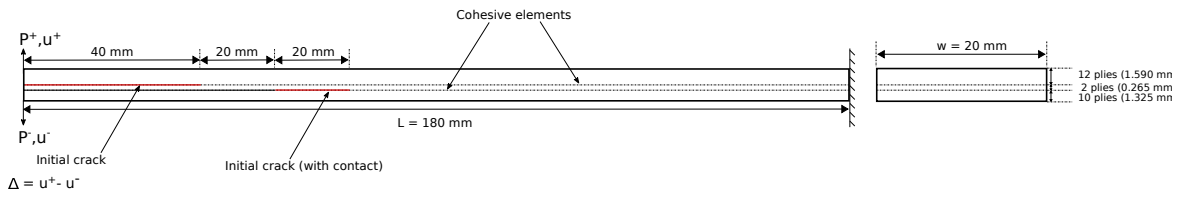


Fig. 6.16 Geometry and boundary condition for multiple delamination in composite specimen test

6.10. Figure 6.17 illustrated the modeling technique adopted using CUF-CW approach. Based on the position of initial crack, different cross-section configuration is allotted to each set of beams. Node compatibility is maintained at the interfaces of different set of beams (two-colored beam nodes in Fig. 6.17). As illustrated, CW modeling of the beam makes meshing process effortless by assigning different cross-section to individual beams whereas discretization and insertion of cohesive element within a 3D FEM model could be tedious and cumbersome process. To emphasis upon the efficiency of the CW models, three additional models based on standard linear brick elements with linear 3D cohesive elements with varying mesh density are developed as tabulated in Table 6.11. Energy-based arc length method is employed to solve the numerical problem with an initial lambda λ_0 of 1 with a unit force applied as P with a termination condition of δ equal to 24 mm. Alfano and Crisfield performed the multiple delamination analysis using 2D standard FEM elements equipped with

Table 6.10 Material properties for multiple delamination of composite specimen test [145, 170]

E_1 (GPa)	E_2/E_3 (GPa)	G_{12} (GPa)	ν_{12}/ν_{13} (-)	G_{IC} (Nmm ⁻¹)	G_{IIC} (Nmm ⁻¹)	τ_3 (MPa)	τ_1 (MPa)	K (Nmm ⁻³)
115.0	8.5	4.5	0.29	0.33	0.8	8.0	3.3	2.5×10^5

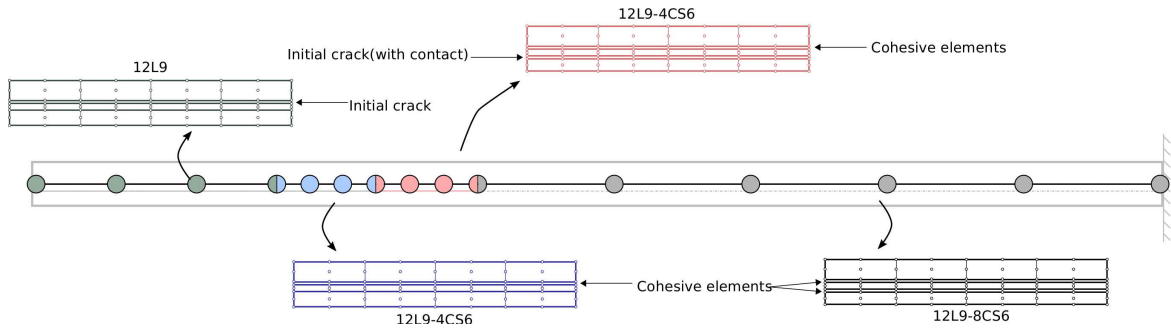


Fig. 6.17 Modeling Multiple delamination of composite specimen using CUF-CW model

Table 6.11 Model information for multiple delamination of composite specimen test

Model	Information	DOF
12L9-4CS6	Cross-section is modeled using 12L9 elements with a combination of 4CS6/8CS6 cohesive elements inserted between the layers based on position of crack (see Fig. 6.17). The beam is modeled using 77B4 elements.	56,376
3DFEM - Coarse	Linear brick element is a mesh density of 8x230x6. The mesh density is equivalent to that of 12L9-4CS6 configuration, amounting to similar degrees of freedom	56,133
3DFEM - Medium	Linear brick element is a mesh density of 8x458x6. Mesh density along the beam is doubled as compared to the 3DFEM -Coarse configuration	111,537
3DFEM - Refined	Linear brick element is a mesh density of 8x619x6. Mesh density along the beam is three times as compared to the 3DFEM -Coarse configuration	150,660

local arc-length and line search based numerical solver [12]. Nguyen and Nguyen-Xuan developed a two-dimensional higher-order Bèzier elements along with energy-based arc length method and efficiently solved the multiple delamination analysis of composite specimen [145]. Figure 6.18a compares the equilibrium curve obtained using CUF-CW model against the experimental and numerical results available from the literature [12, 145, 170]. Equilibrium curves obtained from CUF-CW model is compared against the results of 3D FEM models with varying mesh density in Fig. 6.18. Table 6.12 enlists the information pertaining to convergence behavior of various models along with the total analysis time. Figure 6.19 depicts the equilibrium curve of CUF-CW model along with deformation state at specific load instances. Contour plots for delaminated zones in the top and bottom surfaces of the specimen at various instances are in Fig. 6.20.

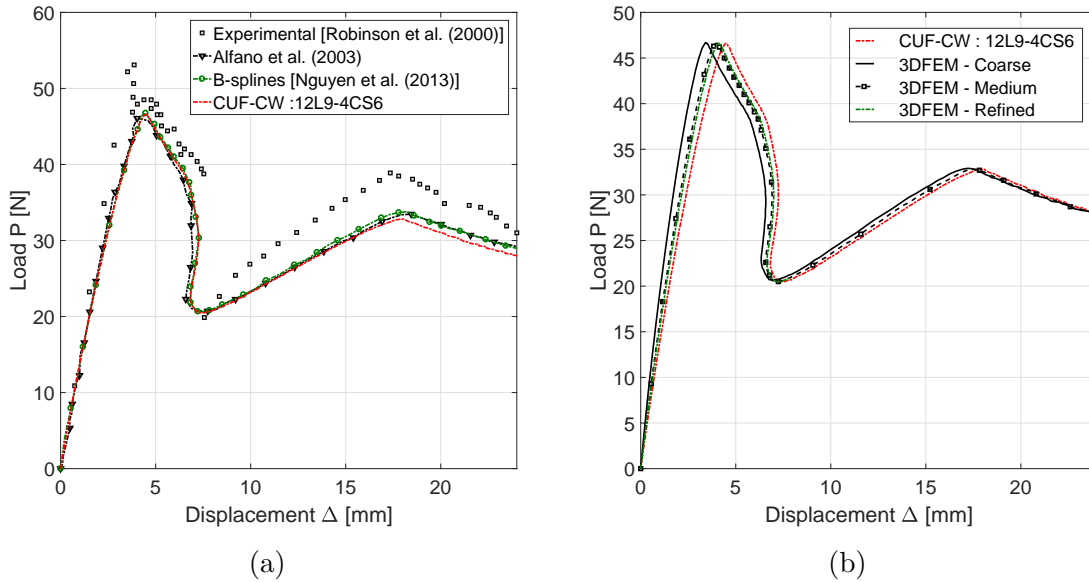


Fig. 6.18 Equilibrium curves for multiple delamination of composite specimen test: (a) Comparison of CUF-CW model with experimental and literature results [12, 145, 170] and (b) Comparison between CUF-CW model against 3D FEM results with varying mesh density

The results suggests that

1. As verified via reference solutions, CUF accurately captures the complex equilibrium curve for multiple delaminations.

Table 6.12 Numerical results for Multiple delamination of composite specimen test

Model	Total number of increment	Total number of iterations	Analysis Time [hh:mm]
12L9-4CS6	229	897	1:47
3DFEM- Coarse	213	835	1:25
3DFEM - Medium	298	1173	4:44
3DFEM - Refined	300	1188	7:15

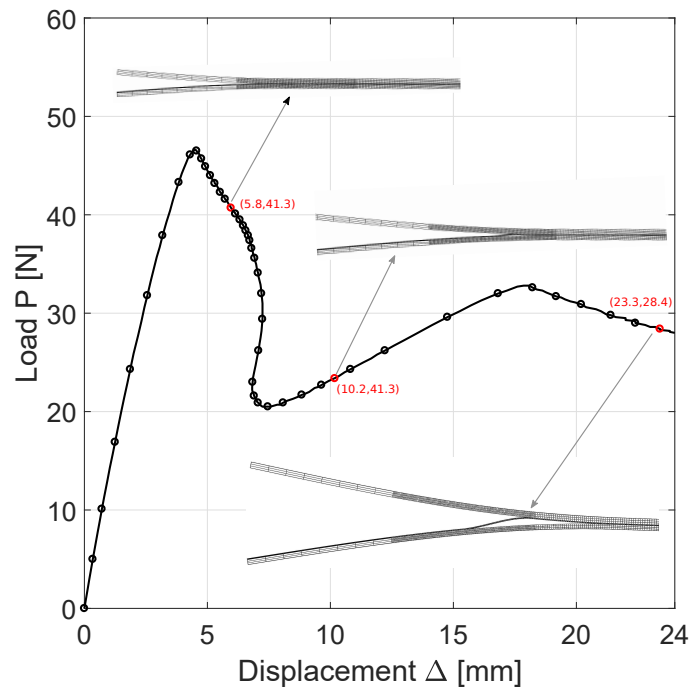


Fig. 6.19 Equilibrium curve along with deformed states for CUF-CW model for multiple delamination of composite specimen test

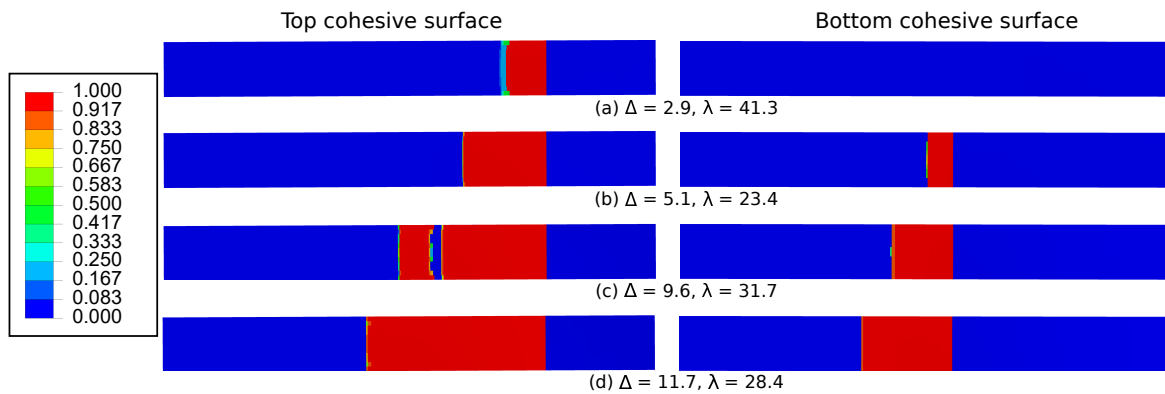


Fig. 6.20 Contour plots of the delamination index - 0: intact, 1: fully delaminated - at the top and bottom cohesive surfaces via CUF for multiple delaminations

2. The refining process of 3D models converges to CUF. In particular, although the size of the problem for 12L9-4CS6 and 3D FEM - Coarse configurations is similar, the 3D FEM - Coarse model presents visible differences in the equilibrium path.
3. CUF models have multi-fold better efficiency in terms of analysis times than standard 3D FEM.
4. The present formulation can capture the progressive delamination propagation along multiple fronts.
5. From a modeling standpoint, the CUF modeling improves the meshing process by assigning various cross-section configurations to individual beams whereas the discretization and insertion of cohesive elements within a 3D FEM model may lead to a cumbersome process due to the high number of FE elements.

6.5 Conclusion

The chapter extends the capabilities of 1D higher-order FE models for delamination modeling to increase the computational efficiency. Cohesive modeling capabilities make use of the CUF approach to exploit refined displacement field along the cross-section and obtain complete and accurate 3D stress and displacement fields. The approach makes use of the mixed-mode cohesive constitutive law and a global dissipation energy-based arc -length method and verified via various numerical examples including the double cantilever beam test, end-notch flexure test, mixed-mode bending test and composite specimen with multiple delamination fronts. The analysis of the results suggest that

- CUF tends to outperform standard 3D FEM with multi-fold efficiency in terms of analysis times. Such an outcome stems from the lower amounts of DOF required by CUF models.
- The absence of aspect ratio constraints in 1D models permits to enrich the modeling capabilities only by adopting refined structural theories instead of re-meshing.
- In the MMB test, CUF models provided significant improvements in terms of prediction of peak loads if compared to other numerical tests and experimental results.

- The use of cohesive elements within CUF may lead to more efficiency in the modeling as the elements are cross-section features and non-homogeneous 1D elements and compatibilities are enforceable straightforwardly.

Chapter 7

Impact modeling in CUF

The chapter presents an application of CUF 1D models for undertaking impact modeling. Formulation of boundary value problem and incorporation of contact modeling technique within CUF is briefly explained. The work considers normal, frictionless contact based on a node-to-node formulation and a penalty approach to enforce the constraints. Explicit time integration scheme is utilized to undertake initial assessment of the capabilities of CUF 1D models for impact simulation of elastic rods and wave propagation on impact in rectangular blocks

7.1 Contact modeling within CUF

7.1.1 Contact Kinematics

Consider two distinct bodies Ω_i , $i = 1, 2$, as shown in Fig. 7.1. Two distinct points X_1 and X_2 initially on the boundary of the respective bodies, come into contact due to the applied deformation φ . The position of the points X_i in the current configuration is given by

$$\mathbf{x}_i = \mathbf{X}_i + \mathbf{u}_i; \quad i = 1, 2 \quad (7.1)$$

where \mathbf{u}_i is the displacement of the reference point X_i . For the case of contact between the two bodies, the two points are said to occupy the same physical space, and thus $\mathbf{x}_1 = \mathbf{x}_2$.

Contact can be taken into consideration either through the application of geometric constraints, or via the use of constitutive laws at the contact interface resulting in a micromechanical approach [206]. In the current study, geometrical constraints have been considered, where a non-penetration condition is used to prevent the penetration

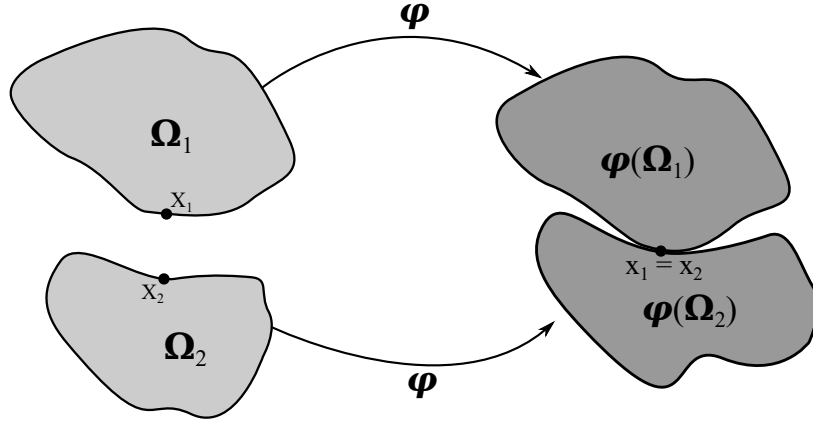


Fig. 7.1 Reference and current configuration of two distinct bodies coming into contact

of one body into the other. Such a condition is given in the form of a gap function g_N which is defined as

$$g_N = (\mathbf{x}_2 - \mathbf{x}_1) \cdot \mathbf{n}_1 \geq 0 \quad (7.2)$$

where n_1 is the normal vector w.r.t Ω_1 . For the case of geometrically linear kinematics, the gap function given in (Eq.7.2) can be written as

$$g_N = [(\mathbf{X}_2 + \mathbf{u}_2) - (\mathbf{X}_1 + \mathbf{u}_1)] \cdot \mathbf{n}_1 \geq 0 \quad (7.3)$$

$$= [(\mathbf{X}_2 - \mathbf{X}_1) + (\mathbf{u}_2 - \mathbf{u}_1)] \cdot \mathbf{n}_1 \geq 0 \quad (7.4)$$

The above results in an alternate definition of the gap function as

$$g_N = (\mathbf{u}_2 - \mathbf{u}_1) \cdot \mathbf{n}_1 + g_{init} \geq 0 \quad (7.5)$$

where the initial gap between the two bodies, g_{init} , is defined as

$$g_{init} = (\mathbf{X}_2 - \mathbf{X}_1) \cdot \mathbf{n}_1 \quad (7.6)$$

In such an approach, the normal component of the stress field relates to the contact pressure, and is obtained as a consequence of the contact constraint, i.e., it is not computed directly via constitutive equations. The system is then in a state of contact when the gap function $g_N = 0$. The normal component of the stress tensor is then the contact pressure p_N , which is equal and opposite for the two bodies at the point of contact. This leads to a set of Kuhn-Tucker type equations in the following form

$$g_N \geq 0, \quad p_N \leq 0, \quad g_N p_N = 0 \quad (7.7)$$

which in the context of constraint-based frictionless contact are termed as Hertz-Signorini-Moreau conditions [206].

7.1.2 Weak form of the contact BVP

According to the principle of virtual work, the equilibrium equation for a static structural problem is in the form given in (Eq. 2.16). This remains the same even for the case of static contact problems, except for the addition of a contact term, δL_c , which signifies the variation of the work done due to contact. However, since the contact term arises due to the non-penetration condition (Eq. 7.5) which is an inequality, the resulting variational form is also an inequality, as shown below

$$\delta L_{int} \geq \delta L_{ext} + \delta L_c \quad (7.8)$$

This inequality introduces a nonlinearity to the problem, even when both material and geometrical linearity are considered. Therefore cases involving contact constitute a new class of nonlinear problems based on nonlinear boundary conditions. In the current work, the nonlinear contact problem is implicitly solved using Newton's method. Furthermore, the penalty approach is considered for the treatment of the contact constraint using a variational approach. Thus, the work due to contact takes the form

$$L_c = \frac{1}{2} \int_{\partial\Omega_c} \epsilon_N g_N^2 dA \quad (7.9)$$

where $\partial\Omega_c$ is the contact surface, and ϵ_N is the penalty parameter for normal contact. The virtual variation is then given by

$$\delta L_c = \int_{\partial\Omega_c} \epsilon_N g_N \delta g_N dA \quad (7.10)$$

Equation 7.10 is then discretized and solved numerically using a finite element framework. The discretization and solution of the equations depend on the type of contact considered at the interface, for instance surface-based or node-based contact. The following section elaborates on the finite element formulation for the case of node-based contact.

7.1.3 Node-to-Node contact

In the node-to-node formulation, the contact constraints are enforced at the nodal level, for a given node pair. Such a contact treatment requires nodal compatibility

at the contact interface i.e. matching meshes for the two bodies in contact. Such an approach to contact is valid for the case of geometrical linear theory, where infinitesimal deformations ensure that the nodes remain aligned in the deformed configuration. Based on the penalty approach, the global equilibrium equation takes the following form

$$[\mathbf{K} + \mathbf{K}^p]\mathbf{u} = \bar{\mathbf{F}} \quad (7.11)$$

where \mathbf{K}^p is the penalty stiffness matrix, which enhances the structural stiffness matrix \mathbf{K} . The global penalty matrix is formed by the assembly of the penalty stiffness terms for a given node pair i , which is given by

$$\mathbf{k}_i^p = \epsilon_N \mathbf{n}_i^T \mathbf{n}_i \quad (7.12)$$

where $\mathbf{n}_i = \{n_x, n_y, n_z\}$ is the unit normal vector between the node pair i , and ϵ_N is the penalty parameter.

The contact pressure at the contact region takes the form of a nodal force for the case of node-based contact. Such a nodal contact force \mathbf{F}_i^c for the node pair i is a consequence of enforcing the contact constraint g_N between the nodes, and can be written from (Eq. 7.10) as

$$\mathbf{F}_i^c = \epsilon_N g_N \mathbf{n} \quad (7.13)$$

The contact force term is an addition to the external force vector, and the sum represents the right hand side of (Eq. 7.11), such that

$$\bar{\mathbf{F}} = \mathbf{F}^c + \mathbf{F}_{ext} \quad (7.14)$$

Equation 7.11 can then be solved incrementally using Newton's method.

7.2 Numerical results

7.2.1 Impact between two rods

The current numerical example provides an assessment of contact-impact using CUF. Two rods are considered, with one impacting the other, as shown in Fig. 7.2. The problem definition is based on [105]. Both rods consist of an isotropic material with Young's modulus $E = 100$, and a Poisson's ratio $\nu = 0.3$. The problem is analyzed using CUF-Explicit, and reference 3D solutions are obtained using ABAQUS - Explicit modules. Two solutions are generated using ABAQUS: (a) ABQ¹, modeled with the

same mesh configuration and degrees of freedom as used in the CUF-Explicit analysis, and (2) ABQ - Ref, with a refined mesh to provide a reference solution. A time period $T = [0, 1.0]$ has been considered, and a time step value $\Delta_t = 5.0 \cdot 10^{-4}$ has been considered in all the numerical approaches. Numerical damping via the Bulk Viscosity Method (BVM) has been toggled off in the current analysis.

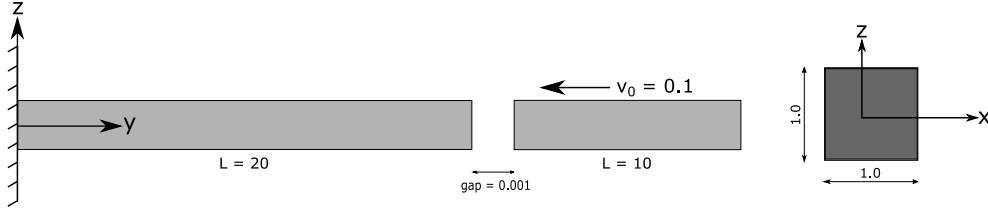


Fig. 7.2 Schematic representation of impact between two rods

The results of the various numerical analyses are as follows – the time history of the axial deflection u_y of the fixed rod, at the point $[0.5, 0.5, 20]$ i.e. the center of the contact region on the impacted end, is plotted in Fig. 7.3a. The time history of the axial stress σ_{yy} , at the same point, is given in Fig. 7.3b. The propagation of the axial stress σ_{yy} along the length of fixed rod has been plotted in Fig. 7.4 for various points of time during the analysis.

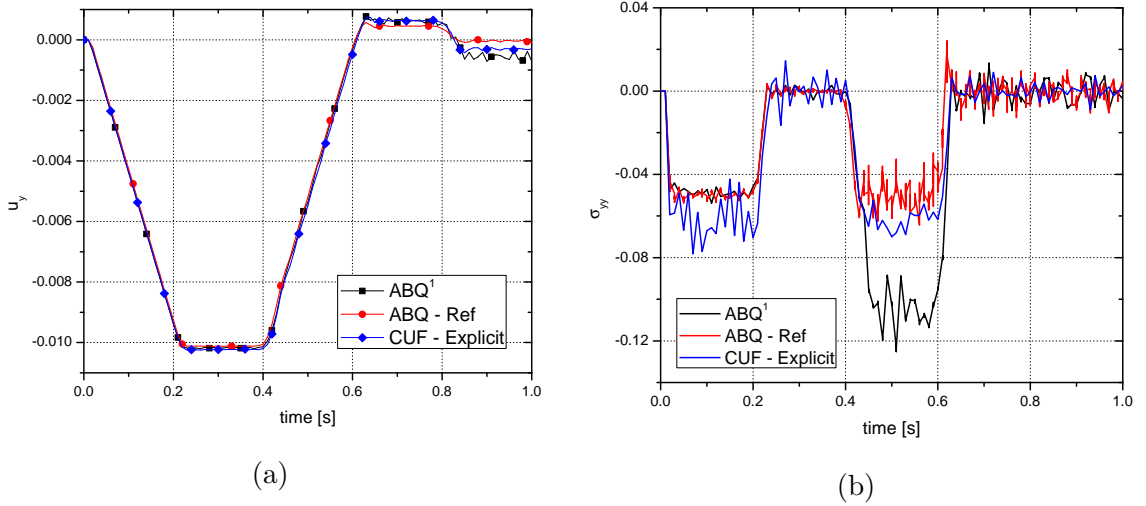


Fig. 7.3 Time history of (a) Axial deflection u_y and (b) Axial stress σ_{yy} at the free end of the first rod during the time period of the analysis

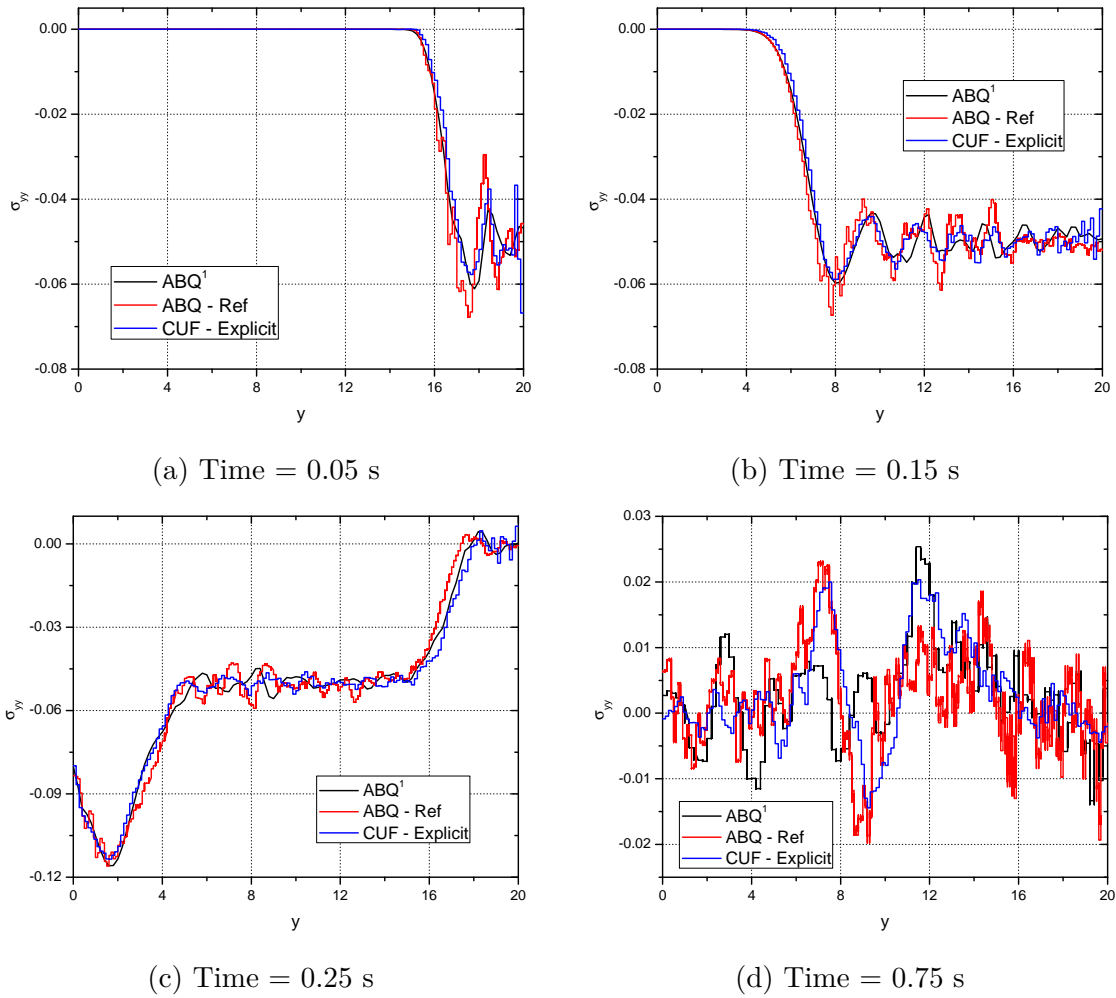


Fig. 7.4 Propagation of axial stress σ_{yy} at various points of time during the analysis.

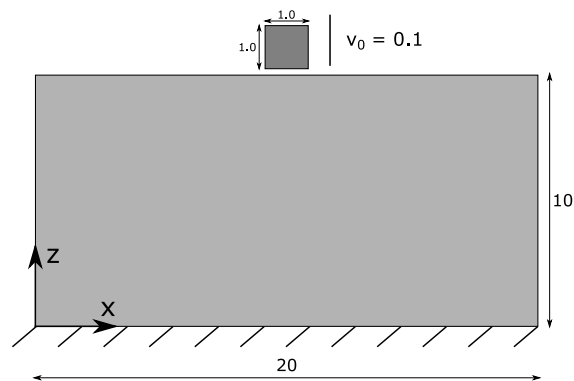


Fig. 7.5 Schematic representation of a rectangular block under impact

7.2.2 Impact of a rectangular block

The current example deals with the impact of a rectangular block. The geometry of the structure is shown in Fig. 7.5. A thickness of 0.1 units has been considered for both blocks, and an initial gap $g = 0.001$ exists between the block and the impactor. Both bodies consist of an isotropic material with a Young's modulus $E = 100$, and Poisson's ratio $\nu = 0.3$. As before, the analysis is performed with CUF - Explicit, and reference 3D results are obtained using ABAQUS - Explicit. A time period $T = [0, 0.5]$ has been considered, and the time step $\Delta_t = 1.0 \cdot 10^{-4}$ is used for all the analyses.

The results of the various analyses have been plotted in the following. Figure 7.6a shows the time history of the vertical displacement u_z at the point $[10.0, 10.0, 0.1]$. The time history of the transverse stress component σ_{zz} at the same point has been plotted in Fig. 7.6b. The propagation of the σ_{zz} component through the z-axis of the block, at specific points of time, has been plotted in Fig. 7.7.

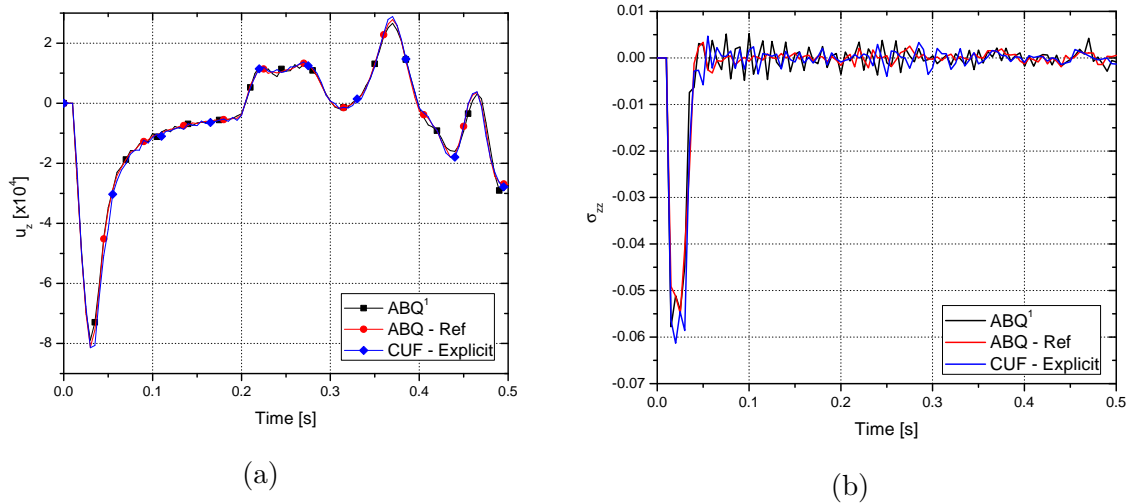


Fig. 7.6 Time history of (a) Transverse deflection u_z and (b) Transverse stress σ_{zz} at the point $[10.0, 10.0, 0.1]$ of the block

7.3 Conclusion

The chapter incorporates the capabilities of contact kinematics within CUF to undertake impact modeling. A normal, frictionless contact based on a node-to-node formulation is implemented along with a penalty approach to enforce the constraints. Initial numerical assessment on impact simulation of elastic rods and wave propagation on impact in rectangular blocks provide accurate resolution of displacement and

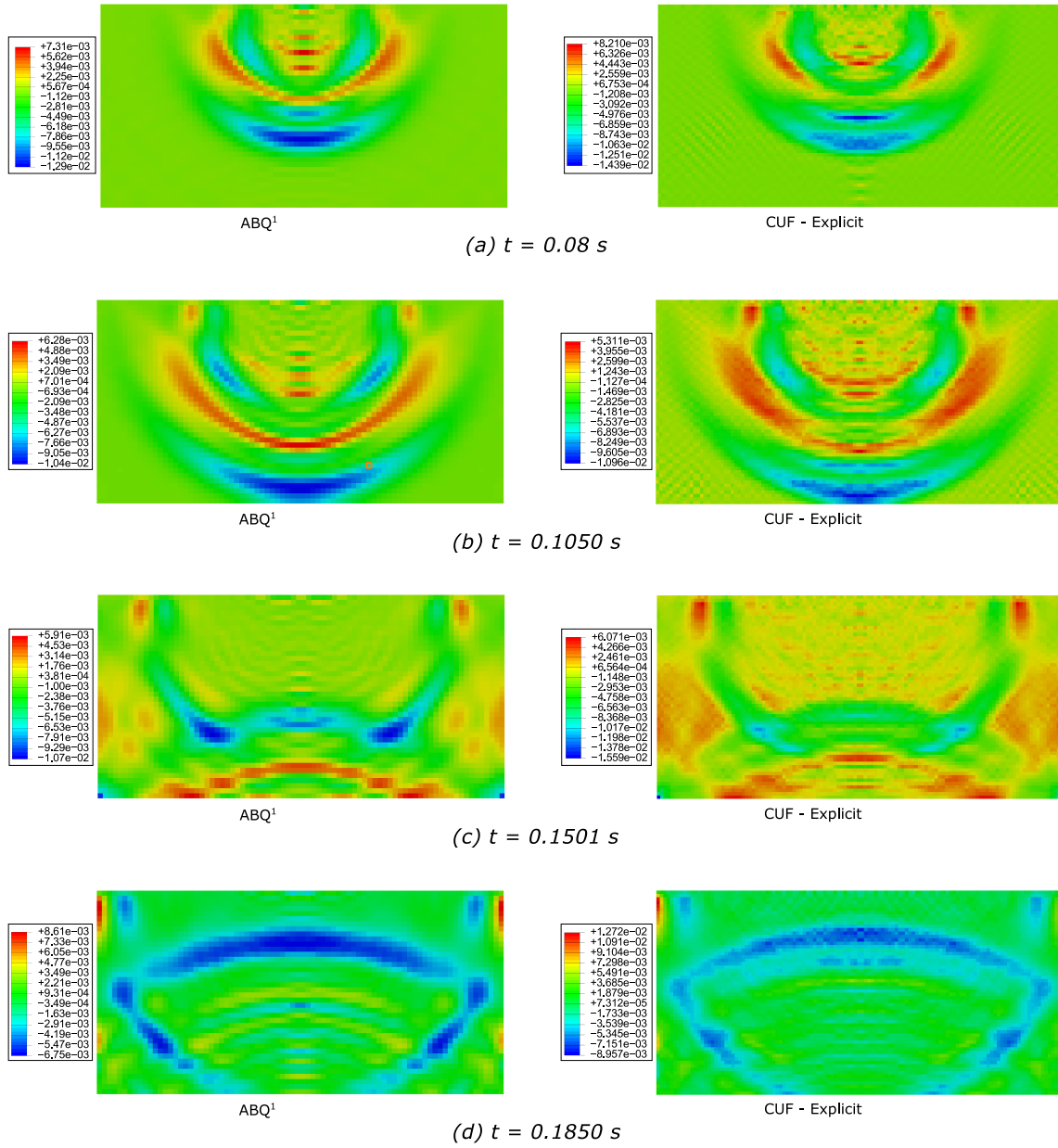


Fig. 7.7 Propagation of transverse stress σ_{zz} through the block at various points of time

stress fields in comparison to benchmark 3D FE simulations. Current ongoing work includes implementation of surface-based contact algorithms into CUF framework and integration of damage modeling constitutive modeling within the analysis to undertake impact modeling in composites.

Chapter 8

Summary and Outlook

The dissertation focused on the development of computationally-efficient, high-fidelity numerical tools for modeling various aspects of progressive failure in composite structures across scales. The framework is built within the scheme of Carrera Unified Formulation (CUF), a hierarchical scheme that provides computationally efficient structural models through variable kinematic definitions. The capability of one-dimensional to provide accurate 3D displacement and stress fields at a highly reduced computational cost is extended to a diverse set of nonlinear problem pertaining to composite structures. A class of tools is presented that can undertake various aspects virtual testing of composite across different stages of test pyramid including micromechanical progressive failure analysis, nonlinear multiscale modeling, delamination modeling and impact analysis.

Part I dealt with the formulation of one-dimensional CUF models for physically nonlinear simulations. Chapter 2 focussed on the formulation of 1D CUF models and emphasized on the importance of accurate resolution of fields as they serve as a prerequisite to accurate physically nonlinear simulations. The inability of standard modeling approaches such as the use of 3D linear FEM, to capture stresses highlights the importance of non-traditional higher-order models for high-fidelity analysis in composites. Chapter 3 highlighted the effectiveness of 1D CUF models to undertake physically nonlinear simulation using elasto-plastic models. Prohibitive computational cost associated with iterative nonlinear solutions can be mitigated by using proposed higher-order models. The effect on kinematic enrichment on the overall accuracy and computational efficiency is highlighted.

In Part II, a novel micromechanical and multiscale platform built within the scheme of CUF models are introduced. Chapter 4 presents a micromechanics platform to undertake nonlinear simulation of different classes of RVE architectures. Pre-peak nonlinearity within the matrix constituent is modeled using the von-Mises plasticity model and continuum damage based crack band model is employed to model progressive failure analysis. The predicted failure modes using CUF-CW corresponds well with the analogous FEM 3D model and observations made in the experiments. On average, CUF models were able to produce solutions in the range of 3D FE models with a three-fold decrease in terms of analysis time and ten-fold reduction in the memory requirement. A computationally efficient concurrent multiscale platform to undertake linear and nonlinear analysis is presented Chapter 5. The framework exploits CUF models at macroscale to model the structural level components (e.g: open-hole specimens, coupons etc) interfaced through concurrent modeling approach with an efficient CUF-micromechanics toolbox. A multi-fold improvement of efficiency with respect to analysis time and memory requirement as compared to traditional multiscale implementations based on 3D FE, thereby addressing the scalability issues associated with multiscale modeling. The variable kinematic nature of the formulation permits balancing the efficiency versus fidelity trade-off in a pragmatic manner.

Part III presented interfacial and impact modeling capabilities built within the CUF framework. The capabilities of the CUF model to undertake progressive delamination problems is discussed in Chapter 6. The approach makes use of the mixed-mode cohesive constitutive law and a global dissipation energy-based arc -length method for iterative solution. CUF tends to outperform standard 3D FEM with multi-fold efficiency in terms of analysis times. Chapter 7 presents an application of CUF 1D models for impact modeling in composites. Initial numerical assessment further emphasized on the applicability as well as efficiency of CUF 1D models to undertake impact problems.

A combination of above-mentioned tools is employed to obtain accurate overall structural response in the nonlinear regime at multiple scales i.e, macro-scale structural components to the material constituent level at micro-scale in a computationally efficient manner. Following sets of conclusion can be drawn:

1. The effectiveness of refined CUF 1D models in undertaking different structural nonlinear analysis is successfully demonstrated.
2. Detection of 3D fields is fundamental in capturing local effects such as damage initiation and delamination onset.

3. Hierarchical characteristics along with computational efficiency of the 1D CUF models is demonstrated with a class of nonlinear problems
4. The absence of aspect ratio constraints in 1D models permits to enrich the modeling capabilities only by adopting refined structural theories instead of re-meshing.
5. CUF tends to outperform standard 3D FEM with multi-fold efficiency regarding the analysis times as well as memory requirements for a class of nonlinear problems.
6. Within the class of fully-numerical methods, CUF micromechanics tool demonstrates excellent computational efficiency without any drop in accuracy. For micromechanical progressive failure analysis, the predicted failure modes using CUF-CW correspond well with the analogous FEM 3D model and observations made in the experiments.
7. In addition to computational efficiency, the ease of modeling the structure using 1D CUF model by assigning different cross-section to individual beams is also highlighted for delamination problem.
8. The capability of using the same 1D formulation at every scale independently of the complexity of the material system and geometry makes the present methodology appealing as a way to reduce the computational overhead of multiscale frameworks

Future Work

The applicability of CUF 1D models for modeling composite across multiple scales have been successfully demonstrated. In general, application of proposed methodologies for industry-relevant as well computationally intensive simulations is proposed. Specifically, following set of activities are slated for future work:

1. Extension of progressive failure crack band to account of compressive and shear driven damage propagation at micro scales
2. Integration of multiple nonlinear phenomena into a single analysis such as nonlinear micromechanical analysis accounting for pre-peak nonlinearity, post-peak damage progression along with fiber-matrix debonding with cohesive elements

3. Inclusion of geometrically nonlinear formulation into the framework along with material nonlinearity to model relevant computationally intensive problems such as micromechanical fiber kinking under compression and post-buckling analysis of large scale structures along with skin-stringer debonding
4. Extension of multiscale framework to different kinds of material nonlinearity (fracture and damage modeling) at the microscale and interfacing of CUF-CW micromechanics modules to commercial software packages such as ABAQUS through UMAT implementations
5. Undertaking high-fidelity impact simulation of composite using CUF-1D models accounting different level of material nonlinearity across multiple scales

References

- [1] Abambres, M., Camotim, D., and Silvestre, N. (2013). GBT-based first-order analysis of elastic-plastic thin-walled steel members exhibiting strain-hardening. *The IES Journal Part A: Civil & Structural Engineering*, 6(2):119–134.
- [2] ABAQUS (2014). *Abaqus Analysis User's Guide*. Dassault Systèmes.
- [3] Aboudi, J. (1982a). A continuum theory for fiber-reinforced elastic-viscoplastic composites. *International Journal of Engineering Science*, 20(5):605–621.
- [4] Aboudi, J. (1982b). A continuum theory for fiber-reinforced elastic-viscoplastic composites. *International Journal of Engineering Science*, 20(5):605–621.
- [5] Aboudi, J., Arnold, S. M., and Bednarczyk, B. A. (2013). *Micromechanics of Composite Materials: A Generalized Multiscale Analysis Approach*. Elsevier.
- [6] Aboudi, J., Pindera, M.-J., and Arnold, S. (1999). Higher-order theory for functionally graded materials. *Composites Part B: Engineering*, 30(8):777 – 832.
- [7] Aboudi, J., Pindera, M.-J., and Arnold, S. M. (2001). Linear Thermoelastic Higher-Order Theory for Periodic Multiphase Materials. *Journal of Applied Mechanics*, 68:697–707.
- [8] Abrate, S. (2001). Modeling of impacts on composite structures. *Composite Structures*, 51(2):129 – 138.
- [9] ACARE (2010). Beyond Vision 2020 (Towards 2050): Aeronautics and Air Transport. PDF.
- [10] Accorsi, M. L. and Nemat-Nasser, S. (1986). Bounds on the overall elastic and instantaneous elastoplastic moduli of periodic composites. *Mechanics of Materials*, 5(3):209 – 220.
- [11] Ahmad, S. and Zienkiewicz, B. M. I. O. C. (1970). Analysis of thick and thin shell structures by curved finite elements. *International Journal for Numerical Methods in Engineering*, 2(3):419–451.
- [12] Alfano, G. and Crisfield, M. A. (2003). Solution strategies for the delamination analysis based on a combination of local-control arc-length and line searches. *International Journal for Numerical Methods in Engineering*, 58(7):999–1048.

- [13] Allix, O. and Corigliano, A. (1999). Geometrical and interfacial non-linearities in the analysis of delamination in composites. *International Journal of Solids and Structures*, 36(15):2189 – 2216.
- [14] Allix, O., Kerfriden, P., and Gosselet, P. (2010). On the control of the load increments for a proper description of multiple delamination in a domain decomposition framework. *International Journal for Numerical Methods in Engineering*, 83(11):1518–1540.
- [15] Allix, O. and Ladeveze, P. (1992). Interlaminar interface modelling for the prediction of delamination. *Composite Structures*, 22:235–242.
- [16] ASTM (1994). Standard test method for mode i interlaminar fracture toughness of unidirectional fiber-reinforced polymer matrix composites. Technical report, ASTM.
- [17] Balzani, C. and Wagner, W. (2008). An interface element for the simulation of delamination in unidirectional fiber-reinforced composite laminates. *Engineering Fracture Mechanics*, 75:2597–2615.
- [18] Barenblatt, G. (1962a). The mathematical theory of equilibrium cracks in brittle fracture. *Advances in Applied Mechanics*, 7:55 – 129.
- [19] Barenblatt, G. I. (1962b). The mathematical theory of equilibrium cracks in brittle fracture. volume 7 of *Advances in Applied Mechanics*, pages 55 – 129. Elsevier.
- [20] Bathe, K. (1996). *Finite element procedure*. Prentice hall, USA.
- [21] Bathe, K. J. and Wilson, E. (1973). Stability and accuracy analysis of direct integration methods. *Earthquake Engineering and Structural Dynamics*, 1:283–291.
- [22] Bazant, Z. and Oh, B. H. (1983). Crack band theory of concrete. *Materials and Structures*, 16:155–177.
- [23] Bednarczyk, B. A., Aboudi, J., and Arnold, S. M. (2010). Micromechanics Modeling of Composites Subjected to Multiaxial Progressive Damage in the Constituents. *AIAA Journal*, 48(7):1367–1378.
- [24] Benson, D. J. (1992). Computational methods in lagrangian and eulerian hydrocodes. *Computer Methods in Applied Mechanics and Engineering*, 99:235–394.
- [25] Benzeggagh, M. and Kenane, M. (1996). Measurement of mixed-mode delamination fracture toughness of unidirectional glass/epoxy composites with mixed-mode bending apparatus. *Composites Science and Technology*, 56(4):439 – 449.
- [26] Berdichevsky, V., Armanios, E., and Badir, A. (1992). Theory of anisotropic thin-walled closed-cross-section beams. *Composites Engineering*, 2(5):411 – 432.
- [27] Bernoulli, D. (1751). De vibrationibus et sono laminarum elasticarum. *Commentarii Academiae Scientiarum Imperialis Petropolitanae*, Petropoli.
- [28] Brewer, J. and Lagace, P. (1988). Quadratic stress criterion for initiation of delamination. *Journal of composite materials*, 22(12):1141–1155.

-
- [29] Burton, W. and Noor, A. (1997). Assessment of continuum models for sandwich panel honeycomb cores. *Computer Methods in Applied Mechanics and Engineering*, 145(3):341 – 360.
- [30] Camanho, P. P., Davila, C. G., and Moura, M. F. D. (2003). Numerical Simulation of Mixed-mode Progressive Delamination in Composite Materials. *Journal of Composite Materials*, 37(16):1415–1438.
- [31] Carrera, E. (1994). A study on arc-length-type methods and their operation failures illustrated by a simple model. *Computers & Structures*, 50(2):217–229.
- [32] Carrera, E. (1995). A class of two dimensional theories for multilayered plates analysis. *Atti Accademia delle Scienze di Torino, Memorie Scienze Fisiche*, 19-20:49–87.
- [33] Carrera, E. (2003). Theories and finite elements for multilayered plates and shells: a unified compact formulation with numerical assessment and benchmarking. *Archives of Computational Methods in Engineering*, 10(3):216–296.
- [34] Carrera, E., Cinefra, M., Petrolo, M., and Zappino, E. (2014). *Finite Element Analysis of Structures through Unified Formulation*. John Wiley and Sons, Ltd.
- [35] Carrera, E., Filippi, E., and Zappino, E. (2013a). Analysis of rotor dynamic by one-dimensional variable kinematic theories. *Journal of engineering for gas turbines and power*, 135(9):092501.
- [36] Carrera, E., Filippi, M., and Zappino, E. (2013b). Laminated beam analysis by polynomial, trigonometric, exponential and zig-zag theories. *European Journal of Mechanics - A/Solids*, 41:58 – 69.
- [37] Carrera, E. and Giunta, G. (2010). Refined Beam Theories Based on a Unified Formulation. *International Journal of Applied Mechanics*, 02(01):117–143.
- [38] Carrera, E., Guarnera, D., and Pagani, A. (2018a). Static and free-vibration analyses of dental prosthesis and atherosclerotic human artery by refined finite element models. *Biomechanics and Modeling in Mechanobiology*, 17(2):301–317.
- [39] Carrera, E., Maiarú, M., and Petrolo, M. (2012). Component-wise analysis of laminated anisotropic composites. *International Journal of Solids and Structures*, 49:1839–1851.
- [40] Carrera, E., Pagani, A., and Petrolo, M. (2013c). Classical, Refined, and Component-Wise Analysis of Reinforced-Shell Wing Structures. *AIAA Journal*, 51(5):1255–1268.
- [41] Carrera, E., Pagani, A., Petrolo, M., and Zappino, E. (2015). Recent developments on refined theories for beams with applications. *Mechanical Engineering Reviews*, 2(2):14–00298–14–00298.
- [42] Carrera, E. and Petrolo, M. (2012). Refined beam elements with only displacement variables and plate/shell capabilities. *Meccanica*, 47(3):537–556.

- [43] Carrera, E. and Varello, A. (2012). Dynamic response of thin-walled structures by variable kinematic one-dimensional models. *Journal of Sound and Vibration*, 331(24):5268–5282.
- [44] Carrera, E., Zappino, E., and Li, G. (2018b). Analysis of beams with piezo-patches by node-dependent kinematic finite element method models. *Journal of Intelligent Material Systems and Structures*, 29(7):1379–1393.
- [45] Catapano, A. and Montemurro, M. (2014). A multi-scale approach for the optimum design of sandwich plates with honeycomb core . Part I : homogenisation of core properties. *Composite Structures*, 118:664–676.
- [46] Cesnik, C. E. S. and Hodges, D. H. (1997). VABS: A New Concept for Composite Rotor Blade Cross-Sectional Modeling. *Journal of the American Helicopter Society*, 42(1):27–38.
- [47] Chamis, C., Abdi, F., Garg, M., Minnetyan, L., Baid, H., Huang, D., Housner, J., and Talagani, F. (2013). Micromechanics-based progressive failure analysis prediction for WWFE-III composite coupon test cases. *Journal of Composite Materials*, 47(20-21):2695–2712.
- [48] Chiang, K. and Fulton, R. (1990). Concepts and implementation of parallel finite element analysis. *Computers & Structures*, 36(6):1039 – 1046.
- [49] Chinesta, F., Ammar, A., and Cueto, E. (2010). Recent advances and new challenges in the use of the proper generalized decomposition for solving multidimensional models. *Archives of Computational Methods in Engineering*, 17(4):327–350.
- [50] Clay, S. B. and Knoth, P. M. (2017). Experimental results of quasi-static testing for calibration and validation of composite progressive damage analysis methods. *Journal of Composite Materials*, 51(10):1333–1353.
- [51] Clech, J. P., Keer, L. M., and Lewis, J. L. (1983). A Crack Model of a Bone Cement Interface. *Journal of Biomechanical Engineering*, 106(3):235—243.
- [52] Council, N. R. (2008). *Integrated Computational Materials Engineering: A Transformational Discipline for Improved Competitiveness and National Security*. The National Academies Press, Washington, DC.
- [53] Crisfield, M. (1981). A fast incremental/iterative solution procedure that handles “snap-through”. *Computers & Structures*, 13(1):55 – 62.
- [54] Cui, W., Wisnom, M., and Jones, M. (1992). A comparison of failure criteria to predict delamination of unidirectional glass/epoxy specimens waisted through the thickness. *Composites*, 23(3):158 – 166.
- [55] Dagum, L. and Menon, R. (1998). Openmp: An industry-standard API for shared-memory programming. *IEEE Comput. Sci. Eng.*, 5(1):46–55.
- [56] Davenne, L., Ragueneau, F., Mazars, J., and Ibrahimbegovic, A. (2003). Efficient approaches to finite element analysis in earthquake engineering. *Computers and Structures*, 81:1223–1239.

-
- [57] de Borst, R. (1987). Computation of post-bifurcation and post-failure behavior of strain-softening solids. *Computers & Structures*, 25(2):211 – 224.
- [58] de Borst, R. (2003). Numerical aspects of cohesive-zone models. *Engineering Fracture Mechanics*, 70(14):1743 – 1757. Cohesive Models.
- [59] de Borst, R. and Nauta, P. (1985). Non-orthogonal cracks in a smeared finite element model. *Engineering Computations*, 2(1):35–46.
- [60] de Miguel, A., Kaleel, I., Nagaraj, M., Pagani, A., Petrolo, M., and Carrera, E. (2018). Accurate evaluation of failure indices of composite layered structures via various fe models. *Composite Science and Technology*, Accepted:–.
- [61] de Saint-Venant, A. (1856a). Mémoire sur la flexion des prismes. *Journal de Mathématiques pures et appliquées*, 1:89–189.
- [62] de Saint-Venant, A. (1856b). Mémoire sur la torsion des prismes. *Académie des Sciences de l'Institut Impérial de Frances*, 14:233–560.
- [63] DIGIMAT (2018). e-Xstream Engineering. Louvain-la-Neuve, Belgium.
- [64] D'Mello, R. J., Maiaru, M., and Waas, A. M. (2016). Virtual manufacturing of composite aerostructures. *Aeronautical Journal*, 120(1223):61–81.
- [65] Doghri, I., Ghezal, M. E., and Adam, L. (2016). Finite strain mean-field homogenization of composite materials with hyperelastic-plastic constituents. *International Journal of Plasticity*, 81:40 – 62.
- [66] Dugdale, D. (1960a). Yielding of steel sheets containing slits. *Journal of the Mechanics and Physics of Solids*, 8(2):100 – 104.
- [67] Dugdale, D. (1960b). Yielding of steel sheets containing slits. *Journal of the Mechanics and Physics of Solids*, 8(2):100 – 104.
- [68] El-Fatmi, R. (2007). Non-uniform warping including the effects of torsion and shear forces. part i: A general beam theory. *International Journal of Solids and Structures*, 44(18):5912 – 5929.
- [69] Engelstad, S. P. and Clay, S. B. (2017). Comparison of composite damage growth tools for static behavior of notched composite laminates. *Journal of Composite Materials*, 51(10):1493–1524.
- [70] Entezari, A., Filippi, M., and Carrera, E. (2017). Unified finite element approach for generalized coupled thermoelastic analysis of 3d beam-type structures, part 1: Equations and formulation. *Journal of Thermal Stresses*, 40(11):1386–1401.
- [71] Ernst, G., Vogler, M., Hühne, C., and Rolfes, R. (2010). Multiscale progressive failure analysis of textile composites. *Composites Science and Technology*, 70(1):61–72.
- [72] Eshelby, J. D. (1957). The determination of the elastic field of an ellipsoidal inclusion, and related problems. *Proceedings of the Royal Society of London A: Mathematical, Physical and Engineering Sciences*, 241(1226):376–396.

- [73] Euler, L. (1744). De curvis elasticis. *Methodus Inveniendi Lineas Curvas Maximi Minimive Proprietate Gaudentes, Sive Solutio Problematis Isoperimetrici Lattissimo Sensu Accepti*.
- [74] Falzon, B. G. and Tan, W. (2017). Virtual testing of composite structures: Progress and challenges in predicting damage, residual strength and crashworthiness. In *The structural integrity of carbon fiber composites*, pages 699–743. Springer.
- [75] Feyel, F. (1999). Multiscale FE² elastoviscoplastic analysis of composite structures. *Computational Materials Science*, 16(1):344 – 354.
- [76] Feyel, F. and Chaboche, J. L. (2000). Fe² multiscale approach for modelling the elastoviscoplastic behaviour of long fibre sic/ti composite materials. *Computer Methods in Applied Mechanics and Engineering*, 183(3):309 – 330.
- [77] Filippi, M., Carrera, E., and Zenkour, A. (2015). Static analyses of fgm beams by various theories and finite elements. *Composites Part B: Engineering*, 72:1–9.
- [78] Fish, J., Yu, Q., and Shek, K. (1999). Computational damage mechanics for composite materials based on mathematical homogenization. *International journal for numerical methods in engineering*, 45(11):1657–1679.
- [79] Fritzen, F., Hodapp, M., and Leuschner, M. (2014). Gpu accelerated computational homogenization based on a variational approach in a reduced basis framework. *Computer Methods in Applied Mechanics and Engineering*, 278:186 – 217.
- [80] Gamstedt, E. K. and Sjögren, B. A. (1999). Micromechanisms in tension-compression fatigue of composite laminates containing transverse plies. *Composites Science and Technology*, 59(2):167–178.
- [81] Gao, Y. F. and Bower, A. F. (2004). A simple technique for avoiding convergence problems in finite element simulations of crack nucleation and. *Modeling and Simulation in Material Science and Engineering*, 12:453–463.
- [82] Geers, M. G., Kouznetsova, V. G., Matouš, K., and Yvonnet, J. (2017). Homogenization methods and multiscale modeling: Nonlinear problems. In *Encyclopedia of Computational Mechanics Second Edition*, pages 1–34. American Cancer Society.
- [83] Gibson, L. J. and Ashby, M. F. (1999). *Cellular Solids: Structure and Properties*. Cambridge University Press.
- [84] Gigliotti, L. and Pinho, S. T. (2015). Virtual testing of large composite structures: A multiple length/time-scale framework. *Journal of Multiscale Modelling*, 6(03):1550008.
- [85] Glaessgen, E. and Stargel, D. (2012). The digital twin paradigm for future nasa and us air force vehicles. In *53rd AIAA/ASME/ASCE/AHS/ASC Structures, Structural Dynamics and Materials Conference 20th AIAA/ASME/AHS Adaptive Structures Conference 14th AIAA*, page 1818.

-
- [86] Gonçalves, R. and Camotim, D. (2012). Geometrically non-linear generalised beam theory for elastoplastic thin-walled metal members. *Thin-Walled Structures*, 51:121–129.
- [87] González, C. and LLorca, J. (2007). Mechanical behavior of unidirectional fiber-reinforced polymers under transverse compression: Microscopic mechanisms and modeling. *Composites Science and Technology*, 67(13):2795–2806.
- [88] Graff, K. F. (1975). *Wave Motion in Elastic Solids*. Dover Publications, Inc, USA.
- [89] Grediac, M. (1993). A finite element study of the transverse shear in honeycomb cores. *International Journal of Solids and Structures*, 30(13):1777 – 1788.
- [90] Gruttmann, F. and Wagner, W. (2001). Shear correction factors in timoshenko’s beam theory for arbitrary shaped cross-sections. *Computational Mechanics*, 27(3):199–207.
- [91] Gutiérrez, M. A. (2004). Energy release control for numerical simulations of failure in quasi-brittle solids. *Communications in Numerical Methods in Engineering*, 20:19–29.
- [92] Haj-Ali, R. and Aboudi, J. (2009). Nonlinear micromechanical formulation of the high fidelity generalized method of cells. *International Journal of Solids and Structures*, 46(13):2577–2592.
- [93] Hashin, Z. (1980). Failure criteria for unidirectional fiber composites. *Journal of applied mechanics*, 47(2):329–334.
- [94] Hashin, Z. and Rosen, B. W. (1964). The Elastic Moduli of Fiber-Reinforced Materials. *Journal of Applied Mechanics*, 31(2):223–232.
- [95] Hassani, B. and Hinton, E. (1998). A review of homogenization and topology optimization II—analytical and numerical solution of homogenization equations. *Computers & Structures*, 69(6):719–738.
- [96] Herakovich, C. T. (1997). *Mechanics of Fibrous Composites*.
- [97] Herakovich, C. T. (2012). Mechanics of composites: A historical review. *Mechanics Research Communications*, 41:1–20.
- [98] Hill, R. (1965). A self-consistent mechanics of composite materials. *Journal of the Mechanics and Physics of Solids*, 13(4):213 – 222.
- [99] Hillerborg, A., Modéer, M., and Petersson, P.-E. (1976). Analysis of crack formation and crack growth in concrete by means of fracture mechanics and finite elements. *Cement and Concrete Research*, 6(6):773 – 781.
- [100] Hinton, M., Soden, P., and Kaddour, A. (2004). *Failure Criteria in Fibre-Reinforced-Polymer Composites*. Elsevier, Oxford.
- [101] Hollister, S. J. and Kikuchi, N. (1992). A comparison of homogenization and standard mechanics analyses for periodic porous composites. *Computational Mechanics*, 10(2):73–95.

- [102] Homes, N. and Belytschko, T. (1976). Postprocessing of finite element transient response calculations by digital filters. *Computers and Structures*, 6:211–216.
- [103] Hosseini, S., Remmers, J. J. C., Verhoosel, C. V., and De Borst, R. (2015). Propagation of delamination in composite materials with isogeometric continuum shell elements. *International Journal for Numerical Methods in Engineering*, 102(3-4):159–179.
- [104] Huang, Y., Hu, K., Wei, X., and Chandra, A. (1994). A generalized self-consistent mechanics method for composite materials with multiphase inclusions. *Journal of the Mechanics and Physics of Solids*, 42(3):491 – 504.
- [105] Huněk, I. (1993). On a penalty formulation for contact-impact problems. *Computers & Structures*, 48(2):193–203.
- [106] Ibrahim, S., Carrera, E., Petrolo, M., and Zappino, E. (2012). Buckling of composite thin walled beams by refined theory. *Composite Structures*, 94(2):563–570.
- [107] Jiang, F. and Yu, W. (2015). Nonlinear variational asymptotic sectional analysis of hyperelastic beams. *AIAA Journal*, 54(2):679–690.
- [108] Jiang, F. and Yu, W. (2017). Damage analysis by physically nonlinear composite beam theory. *Composite Structures*, 182:652–665.
- [109] Kaddour, A., Hinton, M., Smith, P., and Li, S. (2013). A comparison between the predictive capability of matrix cracking, damage and failure criteria for fibre reinforced composite laminates: Part A of the third world-wide failure exercise. *Journal of Composite Materials*, 47(20-21):2749–2779.
- [110] Kaleel, I., Petrolo, M., and Carrera, E. (2018a). Elastoplastic and progressive failure analysis of fiber-reinforced composites via an efficient nonlinear microscale model. *Aerotecnica Missili and Spazio*.
- [111] Kaleel, I., Petrolo, M., Waas, A. M., and Carrera, E. (2017). Computationally efficient, high-fidelity micromechanics framework using refined 1d models. *Composite Structures*, 181:358–367.
- [112] Kaleel, I., Petrolo, M., Waas, A. M., and Carrera, E. (2018b). Micromechanical Progressive Failure Analysis of Fiber- Reinforced Composite Using Refined Beam Models. *Journal of Applied Mechanics*, 85(February):1–8.
- [113] Kanouté, P., Boso, D. P., Chaboche, J. L., and Schrefler, B. A. (2009). Multiscale methods for composites: A review. *Archives of Computational Methods in Engineering*, 16(1):31–75.
- [114] Kapania, R. K. and Raciti, S. (1989). Recent advances in analysis of laminated beams and plates. part i-sheareffects and buckling. *AIAA journal*, 27(7):923–935.
- [115] Kouznetsova, V., Brekelmans, W. A. M., and Baaijens, F. P. T. (2001). An approach to micro-macro modeling of heterogeneous materials. *Computational Mechanics*, 27(July 2000):37–48.

-
- [116] Krueger, R. (2004). Virtual crack closure technique : History , approach , and applications. *Applied Mechanics Reviews*, 57(2):109–143.
- [117] Ladevèze, P., Loiseau, O., and Dureisseix, D. (2001). A micro–macro and parallel computational strategy for highly heterogeneous structures. *International Journal for Numerical Methods in Engineering*, 52(1-2):121–138.
- [118] Ladevèze, P. and Simmonds, J. (1998). New concepts for linear beam theory with arbitrary geometry and loading. *European Journal of Mechanics - A/Solids*, 17(3):377 – 402.
- [119] Lapczyk, I. and Hurtado, J. A. (2007). Progressive damage modeling in fiber-reinforced materials. *Composites Part A: Applied Science and Manufacturing*, 38(11):2333–2341.
- [120] Levy, A. and Papazian, J. M. (1990). Tensile properties of short fiber-reinforced sic/al composites: Part ii. finite-element analysis. *Metallurgical Transactions A*, 21(1):411–420.
- [121] Liu, X., Furrer, D., Kusters, J., and Holmes, J. (2018). Vision 2040: A roadmap for integrated, multiscale modeling and simulation of materials and systems. NASA Glenn Research Center.
- [122] Maheo, L., Grolleau, V., and Rio, G. (2013). Numerical damping of spurious oscillations: A comparison between the bulk viscosity method and the explicit dissipative tchamwa-wielgosz scheme. *Computational Mechanics*, 51:109–128.
- [123] Maiarú, M., Petrolo, M., and Carrera, E. (2017). Evaluation of energy and failure parameters in composite structures via a Component-Wise approach. *Composites Part B: Engineering*, 108:53–64.
- [124] Maimí, P., Camanho, P., Mayugo, J., and Dávila, C. (2007). A continuum damage model for composite laminates: Part i – constitutive model. *Mechanics of Materials*, 39(10):897 – 908.
- [125] Mata, P., Oller, S., and Barbat, A. H. (2007). Static analysis of beam structures under nonlinear geometric and constitutive behavior. *Computer Methods in Applied Mechanics and Engineering*, 196:4458–4478.
- [126] McCarthy, C. T., O’Higgins, R. M., and Frizzell, R. M. (2010). A cubic spline implementation of non-linear shear behaviour in three-dimensional progressive damage models for composite laminates. *Composite Structures*, 92(1):173–181.
- [127] Meyer, P. and Waas, A. M. (2015). Mesh-objective two-scale finite element analysis of damage and failure in ceramic matrix composites. *Integrating Materials and Manufacturing Innovation*, 4(1):18.
- [128] Mi, Y., Crisfield, M. A., Davies, G. A. O., and Hellweg, H. B. (1998). Progressive delamination using interface elements. *Journal of Composite Materials*, 32(14):1246–1272.

- [129] Miehe, C. (1996). Numerical computation of algorithmic (consistent) tangent moduli in large-strain computational inelasticity. *Computer Methods in Applied Mechanics and Engineering*, 134(3):223 – 240.
- [130] Miehe, C. and Koch, A. (2002). Computational micro-to-macro transitions of discretized microstructures undergoing small strains. *Archive of Applied Mechanics*, 72(4):300–317.
- [131] Miglioretti, F. and Carrera, E. (2015). Application of a refined multi-field beam model for the analysis of complex configurations. *Mechanics of Advanced Materials and Structures*, 22(1-2):52–66.
- [132] Mirbagheri, Y., Nahvi, H., Parvizian, J., and Düster, A. (2015). Reducing spurious oscillations in discontinuous wave propagation simulation using high-order finite elements. *Computers and Mathematics with Applications*, 70:1640–1658.
- [133] Mises, R. V. (1913). Mechanics of solid bodies in the plastically-deformable state. *Mechanik der festen Körper in plastisch-deformablen Zustand*, 4:582–592.
- [134] Mises, R. V. and Pollaczek-Geiringer, H. (1929). Praktische verfahren der gleichungsauflösung. *Journal of Applied Mathematics and Mechanics / Zeitschrift für Angewandte Mathematik und Mechanik*, 9(2):152–164.
- [135] Moffat, A. J., Wright, P., Buffière, J.-Y., Sinclair, I., and Spearing, S. M. (2008). Micromechanisms of damage in 0 splits in a [90/0] s composite material using synchrotron radiation computed tomography. *Scripta Materialia*, 59(10):1043–1046.
- [136] Mori, T. and Tanaka, K. (1973). Average stress in matrix and average elastic energy of materials with misfitting inclusions. *Acta Metallurgica*, 21(5):571 – 574.
- [137] Naghipour, P., Arnold, S. M., Pineda, E. J., Stier, B., Hansen, L., Bednarczyk, B. A., and Waas, A. M. (2017). Multiscale static analysis of notched and unnotched laminates using the generalized method of cells. *Journal of Composite Materials*, 51(10):1433–1454.
- [138] Needleman, A. (1987). A Continuum Model for Void Nucleation by Inclusion Debonding. *Journal of Applied Mechanics*, 54(3):525–531.
- [139] Nemat-Nasser, S., Iwakuma, T., and Hejazi, M. (1982). On composites with periodic structure. *Mechanics of Materials*, 1(3):239 – 267.
- [140] Néron, D. and Ladevèze, P. (2010). Proper generalized decomposition for multi-scale and multiphysics problems. *Archives of Computational Methods in Engineering*, 17(4):351–372.
- [141] Neto, E. S., Peric, D., and Owen, D. (2008). *Computational Methods for Plasticity: Theory and Application*. John Wiley and Sons, Ltd.
- [142] Nguyen, V. P., Kerfriden, P., and Bordas, S. P. A. (2014). Two-and three-dimensional isogeometric cohesive elements for composite delamination analysis. *Composites Part B: Engineering*, 60:193–212.

-
- [143] Nguyen, V. P., Lloberas-Valls, O., Stroeven, M., and Sluys, L. J. (2011). Homogenization-based multiscale crack modelling: From micro-diffusive damage to macro-cracks. *Computer Methods in Applied Mechanics and Engineering*, 200:1220–1236.
- [144] Nguyen, V. P., Lloberas-Valls, O., Stroeven, M., and Sluys, L. J. (2012). Computational homogenization for multiscale crack modeling. implementational and computational aspects. *International Journal for Numerical Methods in Engineering*, 89(2):192–226.
- [145] Nguyen, V. P. and Nguyen-Xuan, H. (2013). High-order B-splines based finite elements for delamination analysis of laminated composites. *Composite Structures*, 102:261–275.
- [146] Noh, G., Ham, S., and Bathe, K. J. (2013). Performance of an implicit time integration scheme in the analysis of wave propagations. *Computers and Structures*, 123:93–105.
- [147] O’ Higgins, R. M. (2007). *An experimental and numerical study of damage initiation and growth in high strength glass and carbon fiber-reinforced composite materials*. PhD thesis, University of Limerick.
- [148] O’Higgins, R. M., McCarthy, C. T., and McCarthy, M. A. (2012). Effects of shear-transverse coupling and plasticity in the formulation of an elementary ply composites damage model, part i: Model formulation and validation. *Strain*, 48(1):49–58.
- [149] Orbison, J., McGuire, W., and Abel, J. (1982). Yield surface application in non-linear steel frame analysis. *Computer Methods in Applied Mechanics and Engineering*, 33:557–573.
- [150] Ortiz, M. and Pandolfi, A. (1999). Finite-deformation irreversible cohesive elements for three-dimensional crack-propagation analysis. *International Journal for Numerical Methods in Engineering*, 44(9):1267–1282.
- [151] Ozdemir, I., Brekelmans, W., and Geers, M. (2008). Fe2 computational homogenization for the thermo-mechanical analysis of heterogeneous solids. *Computer Methods in Applied Mechanics and Engineering*, 198(3):602 – 613.
- [152] Pagani, A. and Carrera, E. (2017). Large-deflection and post-buckling analyses of laminated composite beams by Carrera Unified Formulation. *Composite Structures*, 170:40–52.
- [153] Pagani, A., Miguel, A. G. D., Petrolo, M., and Carrera, E. (2016). Analysis of laminated beams via Unified Formulation and Legendre polynomial expansions. *COMPOSITE STRUCTURE*.
- [154] Pagani, A., Petrolo, M., Colonna, G., and Carrera, E. (2015). Dynamic response of aerospace structures by means of refined beam theories. *Aerospace Science and Technology*, 46:360–373.
- [155] Paley, M. and Aboudi, J. (1992a). Micromechanical analysis of composites by the generalized cells model. *Mechanics of Materials*, 14(2):127 – 139.

- [156] Paley, M. and Aboudi, J. (1992b). Micromechanical Analysis of Composites by the Method of Cells. *Applied Mechanics Reviews*, 14(0):127–139.
- [157] Paley, M. and Aboudi, J. (1992c). Micromechanical Analysis of Composites by the Method of Cells. *Applied Mechanics Reviews*, 14(0):127–139.
- [158] Patel, D. K., Waas, A. M., and Yen, C. (2018). Direct numerical simulation of 3d woven textile composites subjected to tensile loading: An experimentally validated multiscale approach. *Composites Part B: Engineering*, 152:102 – 115.
- [159] Petrolo, M. (2013). Flutter analysis of composite lifting surfaces by the 1d carrera unified formulation and the doublet lattice method. *Composite Structures*, 95:539–546.
- [160] Pineda, E., Bednarczyk, B., Waas, A. M., and Arnold, S. (2012). Progressive Failure of a Unidirectional Fiber-reinforced Composite Using the Method of Cells: Discretization Objective Computational Results. *53rd AIAA/ASME/ASCE/AHS/ASC Structures, Structural Dynamics and Materials Conference 20th AIAA/ASME/AHS Adaptive Structures Conference*, (April):1–46.
- [161] Pineda, E. J., Bednarczyk, B. A., Waas, A. M., and Arnold, S. M. (2013). Progressive failure of a unidirectional fiber-reinforced composite using the method of cells: Discretization objective computational results. *International Journal of Solids and Structures*, 50(9):1203–1216.
- [162] Pineda, E. J., Waas, A. M., Bednarczyk, B. A., Collier, C. S., and Yarrington, P. W. (2009). Progressive damage and failure modeling in notched laminated fiber reinforced composites. *International Journal of Fracture*, 158(2):125–143.
- [163] Pollayi, H. and Yu, W. (2014). Modeling matrix cracking in composite rotor blades within vabs framework. *Composite Structures*, 110:62–76.
- [164] Radermacher, A., Bednarczyk, B. A., Stier, B., Simon, J., Zhou, L., and Reese, S. (2016a). Displacement-based multiscale modeling of fiber-reinforced composites by means of proper orthogonal decomposition. *Advanced Modeling and Simulation in Engineering Sciences*, 0123456789:1–23.
- [165] Radermacher, A., Bednarczyk, B. A., Stier, B., Simon, J., Zhou, L., and Reese, S. (2016b). Displacement-based multiscale modeling of fiber-reinforced composites by means of proper orthogonal decomposition. *Advanced Modeling and Simulation in Engineering Sciences*, 3(1):29.
- [166] Ramm, E. (1981). Strategies for tracing the nonlinear response near limit points. In *Nonlinear Finite Element Analysis in Structural Mechanics*, pages 63–89. Springer Berlin Heidelberg.
- [167] Reuss, A. (1929). Berechnung der fließgrenze von mischkristallen auf grund der plastizitätsbedingung für einkristalle . *ZAMM - Journal of Applied Mathematics and Mechanics / Zeitschrift für Angewandte Mathematik und Mechanik*, 9(1):49–58.

-
- [168] Ricks, T. M., Lacy, T. E., Pineda, E. J., Bednarczyk, B. A., and Arnold, S. M. (2016). Computationally efficient High-Fidelity Generalized Method of Cells micromechanics via order-reduction techniques. *Composite Structures*, 156:2–9.
 - [169] Riks, E. (1972). The Application of Newton ' s Method to the Problem of Elastic Stability. *Journal of Applied Mechanics*, 39(4).
 - [170] Robinson, P., Besant, T., and Hitchings, D. (2000). Delamination growth prediction using a finite element approach. *European Structural Integrity Society*, 27:135–147.
 - [171] Rouchon, J. (1990). Certification of large airplane composite structures. In *Recent Progress and New Trends in Compliance Philosophy*.
 - [172] Rybicki, E. and Kanninen, M. (1977). A finite element calculation of stress intensity factors by a modified crack closure integral. *Engineering Fracture Mechanics*, 9(4):931 – 938.
 - [173] Schardt, R. (1994). Generalized beam theory—an adequate method for coupled stability problems. *Thin-walled structures*, 19(2-4):161–180.
 - [174] Schellekens, J. C. J. and de Borst, R. (1993). On the numerical integration of interface elements. *International Journal for Numerical Methods in Engineering*, 36(April 1992):43–66.
 - [175] Segurado, J., Llorca, J., and González, C. (2002). On the accuracy of mean-field approaches to simulate the plastic deformation of composites. *Scripta Materialia*, 46(7):525 – 529.
 - [176] Sherman, J. and Morrison, W. J. (1950). Adjustment of an inverse matrix corresponding to a change in one element of a given matrix. *Ann. Math. Statist.*, 21(1):124–127.
 - [177] Simo, J. and Ju, J. (1987). Strain- and stress-based continuum damage models—i. formulation. *International Journal of Solids and Structures*, 23(7):821 – 840.
 - [178] Simo, J. and Taylor, R. L. (1985). Consistent tangent operators for rate-independent elastoplasticity. *Computer Methods in Applied Mechanics and Engineering*, 48(1):101–118.
 - [179] Soden, P. D., Hinton, M. J., and Kaddour, a. S. (2002). Biaxial test results for strength and deformation of a range of E-glass and carbon fibre reinforced composite laminates: Failure exercise benchmark data. *Composites Science and Technology*, 62:52–96.
 - [180] Spahn, J., Andrä, H., Kabel, M., and Müller, R. (2014). A multiscale approach for modeling progressive damage of composite materials using fast Fourier transforms. *Computer Methods in Applied Mechanics and Engineering*, 268:871–883.
 - [181] Sullivan, R. W. and Arnold, S. M. (2010). An annotative review of multiscale modeling and its application to scales inherent in the field of icme. In *Models, Databases, and Simulation Tools Needed for the Realization of Integrated Computational Materials Engineering*. ASM International.

- [182] Sun, C. and K.J., Y. (1992). Elastic-Plastic Analysis of AS4/PEEK Composite Laminate Using a One-Parameter Plasticity Model. *Journal of Composite Materials*, 26(2):293–308.
- [183] Sun, C. T. and Vaidya, R. S. (1996). Prediction of composite properties from a representative volume element. *Composites Science and Technology*, 56(2):171–179.
- [184] Tay, T., Liu, G., Tan, V., Sun, X., and Pham, D. (2008). Progressive failure analysis of composites. *Journal of Composite Materials*, 42(18):1921–1966.
- [185] Tikarrouchine, E., Chatzigeorgiou, G., Praud, F., Piotrowski, B., Chemisky, Y., and Meraghni, F. (2018). Three-dimensional FE² method for the simulation of non-linear, rate-dependent response of composite structures. *Composite Structures*, pages 165–179.
- [186] Timoshenko, S. and Goodier, J. (1970). *Theory of Elasticity*. McGraw-Hill, London.
- [187] Timoshenko, S. P. (1921). On the correction for shear of the differential equation for transverse vibration of prismatic bars. *Philosophical Magazine Series*, 41:744–746.
- [188] Timoshenko, S. P. (1922). On the transverse vibrations of bars of uniform cross section. *Philosophical Magazine Series*, 43:125–131.
- [189] Timoshenko, S. P. and Gere, J. M. (1991). *Mechanics of Materials*. Springer-Science+Business Media, B.V.
- [190] Turon, A. (2006). *Simulation of delamination in composites under quasi-static and fatigue loading using cohesive zone models*. PhD dissertation, Universitat de Girona.
- [191] Turon, A., Camanho, P., Costa, J., and Dávila, C. (2006). A damage model for the simulation of delamination in advanced composites under variable-mode loading. *Mechanics of Materials*, 38(11):1072 – 1089.
- [192] Turon, A., Dávila, C., Camanho, P., and Costa, J. (2007). An engineering solution for mesh size effects in the simulation of delamination using cohesive zone models. *Engineering Fracture Mechanics*, 74(10):1665 – 1682.
- [193] Varello, A. (2013). *Advanced higher-order one-dimensional models for fluid-structure interaction analysis*. PhD thesis, POLITECNICO DI TORINO.
- [194] Varello, A., Lamberti, A., and Carrera, E. (2013). Static aeroelastic response of wing-structures accounting for in-plane cross-section deformation. *International Journal of Aeronautical and Space Sciences*, 14(4):310–323.
- [195] Varello, A., Pagani, A., Guarnera, D., and Carrera, E. (2018). Analysis of Stokes flows by Carrera unified formulation. *Advances in Aircraft and Spacecraft Science*, 5(3):363–383.
- [196] Vaughan, T. J. and McCarthy, C. T. (2011). Micromechanical modelling of the transverse damage behaviour in fibre reinforced composites. *Composites Science and Technology*, 71(3):388–396.

-
- [197] Verhoosel, C. V., Remmers, J. J. C., Gutiérrez, M. A., and de Borst, R. (2010). Computational homogenization for adhesive and cohesive failure in quasi-brittle solids. *International Journal for Numerical Methods in Engineering*, 83(8-9):1155–1179.
- [198] Verhoosel, C. V., Remmers, J. J. C., and Gutiérrez, M. A. (2009). A dissipation-based arc-length method for robust simulation of brittle and ductile failure. *International Journal for Numerical Methods in Engineering*, 77(9):1290–1321.
- [199] Vogler, M., Rolfes, R., and Camanho, P. P. (2013). Mechanics of Materials Modeling the inelastic deformation and fracture of polymer composites -Part I : Plasticity model. *Mechanics of Materials*, 59:50–64.
- [200] Voigt, W. (1889). Ueber die beziehung zwischen den beiden elasticitätsconstanten isotroper körper. *Annalen der Physik*, 274(12):573–587.
- [201] Walker, K. P., Freed, A. D., and Jordan, E. H. (1993). Accuracy of the Generalized Self-Consistent Method in Modelling the Elastic Behaviour of Periodic Composites. *Philosophical Transactions of the Royal Society A: Mathematical, Physical and Engineering Sciences*, 345(1677):545–576.
- [202] Washizu, K. (1968). *Variational Methods in Elasticity and Plasticity*. Pergamon press.
- [203] Wen, Y. and Zeng, Q. Y. (2010). A novel approach to elasto-plastic finite element analysis of beam structures using the concept of incremental secant stiffness. *Finite Element in Analysis and Design*, 46:982–991.
- [204] Williams, T. O. (2005). A three-dimensional, higher-order, elasticity-based micromechanics model. *International Journal of Solids and Structures*, 42(3-4):971–1007.
- [205] Wisnom, M. R. (2012). The role of delamination in failure of fibre-reinforced composites. *Philosophical Transactions of the Royal Society A: Mathematical, Physical and Engineering Sciences*, 370:1850–1870.
- [206] Wriggers, P. (2006). *Computational Contact Mechanics*. Springer-Verlag.
- [207] Wu, L., Doghri, I., and Noels, L. (2015). An incremental-secant mean-field homogenization method with second statistical moments for elasto-plastic composite materials. *Philosophical Magazine*, 95(28-30):3348–3384.
- [208] Wu, S. (2006). Lumped mass matrix in explicit finite element method for transient dynamics of elasticity. *Computer Methods in Applied Mechanics and Engineering*, 195:5983–5994.
- [209] Xia, Z., Zhang, Y., and Ellyin, F. (2003). A unified periodical boundary conditions for representative volume elements of composites and applications. *International Journal of Solids and Structures*, 40(8):1907–1921.

- [210] Xie, D. and Waas, A. M. (2006). Discrete cohesive zone model for mixed-mode fracture using finite element analysis. *Engineering Fracture Mechanics*, 73(13):1783 – 1796.
- [211] Yang, Q. D., Cox, B. N., Fang, X. J., and Zhou, Z. Q. (2011). Virtual testing for advanced aerospace composites: advances and future needs. *Journal of Engineering Materials and Technology*, 133(1):011002.
- [212] Ye, L. (1988). Role of matrix resin in delamination onset and growth in composite laminates. *Composites Science and Technology*, 33(4):257 – 277.
- [213] Yu, W. and Tang, T. (2010). Variational asymptotic method for unit cell homogenization. *Solid Mechanics and its Applications*, 168:117–130.
- [214] Zappino, E. and Carrera, E. (2017). Multidimensional model for the stress analysis of reinforced shell structures. *AIAA Journal*.
- [215] Zhang, D., Patel, D. K., and Waas, A. M. (2015a). A novel two-scale progressive failure analysis method for laminated fiber-reinforced composites. *56th AIAA/ASCE/AHS/ASC Structures, Structural Dynamics, and Materials Conference*, (January):1–19.
- [216] Zhang, D. and Waas, A. M. (2014). A micromechanics based multiscale model for nonlinear composites. *Acta Mechanica*, 225(4-5):1391–1417.
- [217] Zhang, D., Waas, A. M., and Yen, C. F. (2015b). Progressive damage and failure response of hybrid 3D textile composites subjected to flexural loading, part II: Mechanics based multiscale computational modeling of progressive damage and failure. *International Journal of Solids and Structures*, 75-76:321–335.
- [218] Zhao, B. and Yu, W. (2017). Multiscale structural analysis of honeycomb structure using mechanics of structure genome. In *Proceedings of the American Society for Composites Thirty-second Technical Conference*, pages 92–106.
- [219] Zhou, Y., Hou, C., Wang, W., Zhao, M., and Wan, X. (2015). A phenomenological intra-laminar plasticity model for frp composite materials. *IOP Conference Series: Materials Science and Engineering*, 87(1).

Part IV

Appendices

Appendix A

Publications

Book Chapter

Kaleel I., Petrolo M., Carrera E., Waas A., (2019) "On the effectiveness of higher-order models for physically non linear analysis", in “Advances in Predictive Models and Methodologies for Numerically Efficient Linear and Nonlinear analysis of Composites”

Journal Articles

Kaleel I., Carrera E., Petrolo M. (2018), "Novel structural models for the progressive delamination of laminated composites" (Under review)

Kaleel I., Petrolo M., Carrera E., Waas A.M. (2018), "A computationally efficient concurrent multiscale framework for the nonlinear analysis of composite structures" (Under review)

Kaleel I., Petrolo M., Carrera E., Waas A.M. (2018), "A computationally efficient concurrent multiscale framework for the linear analysis of composite structures" (Under review)

Kaleel I., Petrolo M., Waas A. M., Carrera E. (2017), Micromechanical Progressive Failure Analysis of Fiber-Reinforced Composite using Refined Beam Models. ASME. J. Appl. Mech. 85(2)
DOI: <http://dx.doi.org/10.1115/1.4038610>

Kaleel I., Petrolo M., Waas A.M., Carrera E. (2017), "Computationally efficient, high-fidelity micromechanics framework using refined 1D models", Composite

Structures 181:358-367.

DOI: <http://dx.doi.org/10.1016/j.compstruct.2017.08.040>

Carrera E., **Kaleel I.**, Petrolo M. (2017), "Elastoplastic analysis of compact and thin-walled structures using classical and refined beam finite element models", Mechanics of Advanced Materials and Structures .

DOI: <http://dx.doi.org/10.1080/15376494.2017.1378780>

Petrolo M., **Kaleel I.**, Pietro G. D., Carrera E. (2018), "Wave propagation in compact, thin-walled, and layered beams using refined finite element model", International Journal for Computational Methods in Engineering Science and Mechanics 19(3): 207-220

DOI: <http://dx.doi.org/10.1080/15502287.2018.1447048>

Petrolo M., Nagaraj M. H., **Kaleel I.**, Carrera E. (2018), "A global-local approach for the elastoplastic analysis of compact and thin-walled structures via refined models", Computers and Structures 206:54-65.

DOI: <https://doi.org/10.1016/j.compstruc.2018.06.004>

de Miguel A.G., **Kaleel I.**, Nagaraj M. H., Petrolo M. Pagani A., Carrera E. (2018), "Accurate evaluation of failure indices of composite layered structure via various FE models", Composite Science and Technology 167(2):174-189

DOI: <https://doi.org/10.1016/j.compscitech.2018.07.031>

Kaleel I., Petrolo M., Carrera E. (2018), "Elastoplastic and progressive failure analysis of fiber-reinforced composites via an efficient nonlinear microscale model", Aerotecnica Missili and Spazio 97(2):103-110

DOI: <http://dx.doi.org/10.19249/ams.v97i2.340>

Conference Proceedings

Guarnera D., Carrera E., **Kaleel I.**, Pagani A., Petrolo M., "Non-linear analysis of bio-structures through refined beam models", In: Proceedings of ASME 2018 International Mechanical Engineering Congress and Exposition (IMECE 2018), Pittsburgh, PA, USA, 9-15 November 2018.

Carrera E., **Kaleel I.**, Nagaraj M.H., Petrolo M., "A Global-Local Strategy for the Elastoplastic Analysis of Complex Metallic Structures via Component-Wise Approach", In: Proceedings of ASME 2018 International Mechanical Engineering

Congress and Exposition (IMECE 2018), Pittsburgh, PA, USA, 9-15 November 2018.

Kaleel I., Nagaraj M. H., Petrolo M., Carrera E., Waas A.M. (2018), "An efficient multiscale virtual testing platform for composite via component-wise models", In: Proceedings of the American Society for Composites - Thirty-Third Technical Conference, Seattle, WA (USA), 24-26 September 2018.

Kaleel I., Petrolo M., Carrera E. (2018), "Computationally efficient interface modeling in fiber-reinforced composites through displacement-based component-wise approach", In: Proceedings of the American Society for Composites – Thirty-Third Technical Conference, Seattle, WA (USA), 24-26 September 2018.

Carrera E., **Kaleel I.**, Nagaraj M. H., Petrolo M. (2018), "A Virtual Testing Framework for the Analysis of Damage in Composite Structures", In: Proceedings of the 13th World Congress in Computational Mechanics, New York (USA), 22-27 July 2018.

Kaleel I., Nagaraj M. H., Petrolo M., Carrera E. (2018), "Contact modeling within displacement-based refined one-dimensional beam models", In: Proceedings of the First International Conference on Mechanics of Advanced Materials and Structures (ICMAMS), Turin (Italy), 17-20 June 2018.

Nagaraj M.H., **Kaleel I.**, Petrolo M., Carrera E., "Global-local techniques for macroscale analysis and key performance indicator evaluation of composite structures", In: Proceedings of the First International Conference on Mechanics of Advanced Materials and Structures (ICMAMS), Torino, Italy, 17-20 June 2018.

Kaleel I., de Miguel A. G., Nagaraj M. H., Pagani A. Petrolo M., Carrera E. (2018), "A component-wise formulation for virtual testing of composites", In: Proceedings of the First International Conference on Mechanics of Advanced Materials and Structures (ICMAMS), Turin (Italy), 17-20 June 2018.

Kaleel I., Petrolo M., Carrera E., Giugno M., Linari M. (2018), "Micromechanics-based multiscale modeling for nonlinear analysis of fiber-reinforced composites using DIGIMAT", In: Proceedings of the First International Conference on Mechanics of Advanced Materials and Structures (ICMAMS), Turin (Italy), 17-20 June 2018.

Guarnera D., Carrera E., **Kaleel I.**, Pagani A., Petrolo M., "Advanced models for the nonlinear static response of biological structures", In: Proceedings of the First International Conference on Mechanics of Advanced Materials and Structures (ICMAMS), Torino, Italy, 17-20 June 2018.

Carrera E., Petrolo M., Pagani A., Zappino E., Fiordilino G.A., de Miguel A.G., Nagaraj M.H., **Kaleel I.**, "Local refinement of classical FEM solution using node-dependent kinematics elements", In: Proceedings of the European Conference on Spacecraft Structures, Materials and Environmental Testing - ECSSMET 2018, Noordwijk, The Netherlands, 28 May - 1 June 2018.

Kaleel I., Petrolo M., Carrera E. (2017), "Advanced Structural Models for Numerical Simulation of Delamination in Laminated Structures", In: Proceedings of International Conference on Composite Materials and Structures, Hyderabad (India), 27-29 December 2017.

Kaleel I., Petrolo M., Carrera E., Waas A.M. (2017), "Micromechanical progressive failure analysis of fiber-reinforced composite using refined beam models", In: Proceedings of the ASME 2017 International Mechanical Engineering Congress and Exposition (IMECE2017), Tampa, FL (USA), 3-9 November 2017.

Carrera E., Pagani A., Petrolo M., de Miguel A.G., **Kaleel I.** (2017), "Component-Wise method for macro-meso-micro modelling and failure analysis of composite structures", In: Proceedings of the American Society for Composites - Thirty-second Technical Conference, West Lafayette, IN (USA), 23-25 October 2017.

Carrera E., **Kaleel I.**, Petrolo M. (2017), "Numerical simulation of failure in fiber reinforced composites", In: Proceedings of the XXIV International Conference of the Italian Association of Aeronautics and Astronautics, AIDAA 2017, Palermo-Enna (Italy), 18-22 September 2017.

Kaleel I., Petrolo M., Carrera E., Waas A. (2017), "Efficient high-fidelity two-scale computational model for progressive failure analysis of fiber reinforced composites via refined beam models", In: Proceedings of the 6th ECCOMAS Thematic Conference on the Mechanical Response of Composites: COMPOSITES 2017, Eindhoven (Netherlands), 20-22 September 2017.

Kaleel I., Maiarú M., Petrolo M., Carrera E., Waas A. (2017), "Fast two-scale computational model for progressive damage analysis of fiber reinforced

composites", In: Proceedings of the 25th Annual International Conference on Composite/Nano Engineering, ICCE-25, Rome (Italy), 16-22 July 2017.

Carrera E., **Kaleel I.**, Petrolo M. (2016), "Progressive Damage Analysis of Composite Structures via One-Dimensional Carrera Unified Formulation", In: 19th International Conference on Composite Structures (ICCS19), Porto (Portugal), September 5-9, 2016.

Petrolo M., Carrera E., **Kaleel I.** (2016), "Efficient Component-Wise Finite Elements for the Dynamic Response Analysis of Metallic and Composite Structures", In: 1st International Conference on Impact Loading of Structures and Materials (ICILSM 2016), 23 May 2016, Torino, Italy.